Predicting Phase Stability in Nitrogen Steels with Density-Functional Theory

Het voorspellen van fasestabiliteit in stikstofstaal met dichtheids-functionaaltheorie

Sam De Waele

Supervisors: prof. dr. Stefaan Cottenier, dr. ir. Lode Duprez,
dr. ir. Kurt Lejaeghere
Dissertation submitted in fulfillment of the requirements for the degree of Doctor (Ph.D.) of Engineering Physics

Department of Electrical Energy, Metals, Mechanical Constructions and Systems
Chair: Luc Dupré
Faculty of Engineering and Architecture
Ghent University
Academic year 2019–2020

GHENT UNIVERSITY

Members of the Examination Committee

Chair

prof. dr. Hennie De Schepper (Ghent University)

Reading Committee

dr. Tilmann Hickel (Max-Planck-Institut für Eisenforschung GmbH)
prof. dr. Bart Partoens (University of Antwerp)
prof. dr. ir. Toon Verstraelen (Ghent University)
prof. dr. ir. Leo Kestens (Ghent University)

Other voting members

dr. ir. Elke Leunis (OCAS NV)

Supervisors

prof. dr. Stefaan Cottenier (Ghent University)
dr. ir. Lode Duprez (OCAS NV)
dr. ir. Kurt Lejaeghere (OCAS NV)

Contents

Contents i

List of Symbols v

List of Abbreviations ix

Samenvatting xi

Summary xv

I Predicting phase stability in nitrogen steels with Density-Functional Theory 1

1 Introduction 3

1.1 Steel: applications and market 3

1.2 From iron to advanced alloys 6

1.3 The role of nitrogen in the manufacturing of steel 9

1.3.1 Nitriding as a surface treatment 9

1.3.2 The iron-nitrides Fe_4N_{1-x} and $Fe_{16}N_2$ 12

1.4 Goals and outlook 15

1.4.1 Metallurgical 15

1.4.2 Methodological 16

2 Methods **19**

2.1 Density-functional Theory 20

2.1.1 General background 20

2.1.2 DFT for crystalline solids 23

2.1.3 DFT for magnetic systems 24

2.2 Finite temperatures 26

2.2.1 Electron temperature 27

2.2.2 Vibrational excitations 29

2.2.3 Magnetic excitations 31

2.2.4 Combining all contributions 33

3 The binary Fe-N system: thermodynamics from DFT **37**

3.1 Introduction 37

3.2 Technical details 38

3.3 Evaluation of the calculated thermodynamic properties 39

3.3.1 Free energy and heat capacity 40

3.3.2 Elastic properties 43

3.3.3 Magnetic properties 47

3.3.4 Equilibrium between $Fe_{16}N_2$ and Fe_4N 51

3.4 Constructing the phase diagram 52

3.4.1 An impurity in the solid at 0 K 53

3.4.2 Free energy of the impurity 53

3.4.3 Limit of solubility 55

3.5 Conclusion 57

4 Introducing ternary elements in the $Fe_{16}N_2$/Fe_4N equilibrium **61**

4.1 Introduction 61

4.2 The role of ternary elements in nitrided steels: background . . 63

4.3 Methodology: Work flow for the screening of ternary compounds 64

4.3.1 Energy of formation for ternary phases 64

I. The γ' crystal structure 64

II. The α'' crystal structure 65
4.3.2 Impurities in ferrite and their interactions 67
4.3.3 Free energy at finite temperature of selected ternary compounds 69
4.3.4 The study set 70
4.3.5 Technical details 71
4.4 Results 73
4.4.1 γ' and α'' ternary compounds at 0 K. 73
4.4.2 Solute interactions in the ferrite matrix 76
4.4.3 Influence of ternary alloying elements on the thermodynamic balance between α'' and γ' 79
4.5 Conclusions 82

5 Conclusions and perspectives 85
5.1 Conclusions 85
5.2 Perspectives 89

II Published Papers 93

A Publications in International Peer–Reviewed Journals 95
Paper I: A first–principles reassessment of the Fe–N phase diagram in the low–nitrogen limit 97
Paper II: Precipitation in simultaneously nitrided and aged Mo–containing maraging steel 111
Paper III: Error estimates for density-functional theory predictions of surface energy and work function 123

B List of Publications 151
Publications in international peer–reviewed journals 151
Conference contributions 152
Oral presentations 152
Poster presentations 152
Master's thesis 152

Appendices **155**

a Thermodynamic Data for the Ternary compounds **157**

Formation energy of solute complexes 158

Energy of formation of Ternary structures at 0 K 159

b Overview of computational resources **171**

c Supporting information for the Fe-N binary thermodynamics **175**

Free energy of Fe_4N: LDA and PBE comparison 176

Magnetic contributions 176

d List of utilized software **179**

Bibliography **183**

Acknowledgements **201**

List of Symbols

Alphanumeric symbols	
B_0	Bulk modulus
B_0'	Derivative of the bulk modulus with respect to pressure
C	Heat capacity
C_{magn}	Magnetic contribution to the heat capacity
C_{P}	Isobaric heat capacity
C_{V}	Isochoric heat capacity
c	Concentration
c_{lim}	Concentration at limit of solubility
c'	Ratio of impurity concentrations
c/a	Ratio of tetragonal axis
$c_{\boldsymbol{K}}^{n,\boldsymbol{k}}$	Expansion coefficient of the Bloch wave
$D_{i\alpha,j\beta}$	Element of the dynamical matrix
E	Energy
E_0	Electronic energy at 0 K
E_{f}	Energy of formation
E^{CE}	Cluster expansion energy
$f(T,\epsilon)$	Fermi-Dirac distribution
F	Helmholtz free energy
F_{conf}	Configurational contribution to the Helmholtz free energy
F_{imp}	Free energy of an impurity
F_{el}	Electronic contribution to the Helmholtz free energy
$\tilde{F}_{\mathsf{el}}$	Temperature-dependent part of the electronic free energy
F_{mag}	Magnetic contribution to the Helmholtz free energy
F_{vib}	Vibrational contribution to the Helmholtz free energy
$\mathsf{Fe}_{\mathsf{[N]}}$	Iron with nitrogen in solid solution
g	Number of interstitial sites per host atom

g'	Multiplicity of interstitial site around solute impurity
H	Hamiltonian for the Heisenberg model
$\hat{H}$	Hamiltonian operator
$\hat{H}_{\mathrm{KS}}$	Kohn-Sham Hamiltonian
$\hbar$	Reduced Planck constant
$\mathbf{J}$	Coupling matrix
J_{ij}	Heisenberg exchange constants
K_{max}	Convergence radius in reciprocal space
$\boldsymbol{K}$	Reciprocal vector with translation symmetry
$\boldsymbol{k}$	Vector in the first Brillouin zone
k_{B}	Boltzmann constant
M	Magnetization
M_0	Magnetization at 0 K
$\boldsymbol{M}_i$	Magnetization at atomic site i
m_{i}	Ion mass
N	Number of particles
N_{atoms}	Number of atoms
N_{el}	Electron density of states
N_{ph}	Number of phonons
$\tilde{N}$	Phonon sampling points
$\mathrm{N}_{\mathrm{sol}}$	Nitrogen atom in solid solution
n	Band number of the Bloch wave
P	Pressure
R	Number of atoms in the unit cell
R_{max}	Convergence radius in real space
S	Localized spin
S_{el}	Electronic entropy
T	Temperature
T_{C}	Curie temperature, critical temperature
$\hat{T}$	Kinetic energy operator
$\hat{T}_{\mathrm{e}}$	Electron kinetic energy operator
t	Normalized temperature
t_{s}	Temperature rescaling constant
U_0	Electronic energy at equilibrium volume
U_{sol}	Energy of solution of an impurity at $0\,\mathrm{K}$
V	Volume (per atom)
V_0	Equilibrium volume
$V_{\boldsymbol{i}}$	Effective cluster interaction for cluster with compound index $\boldsymbol{i}$
$\hat{V}$	Potential energy operator
$\hat{V}_{\mathrm{ext}}$	Static external potential
$\hat{V}_{\mathrm{xc}}$	Exchange-correlation functional

W	Number of configurations
X	Ternary alloy element
X_{sol}	Ternary alloy element in solid solution

Greek symbols

α	Body-centered cubic structure of iron (below 911 C°)
α''	Tetragonal structure of the iron-nitride $Fe_{16}N_2$
α_V	Thermal expansion
γ	Face-centered cubic structure of iron
γ'	Face-centered cubic structure of the iron-nitride Fe_4N
δ	Body-centered cubic structure of iron (above 1392 C°)
ϵ	Hexagonal iron-nitride phase Fe_3N_{1-z}
ρ_0	Ground state electron density
ρ_{in}	Input density for a single SCF step
ρ_{out}	Output density for a single SCF step
ρ_{new}	Density constructed from output and input density
σ	Smearing parameter
$\boldsymbol{\sigma}$	Cluster configuration vector
Φ	Potential energy of a solid as a Taylor's series of ion displacements
ϕ^+	Spin-up single-particle orbital
ϕ^-	Spin-down single-particle orbital
ϕ'	Steep partial wave defined in augmentation sphere
ϕ_i	Single-particle orbitals
$\tilde{\phi}$	Smooth wave function (plane waves)
$\tilde{\phi}'$	Smooth partial wave defined in augmentation sphere
Ψ	Many-body wave function
$\psi^n_{\boldsymbol{k}}$	Bloch wave
ω	Angular phonon frequency

Currency symbols

€	The official currency of the eurozone

Mathematical symbols

ϕ^*	Complex conjugate of ϕ

In general, vectors and matrices are printed in bold face throughout this work.

List of Abbreviations

3D	Three-dimensional
AHSS	Advanced high-strength steels
at. %	Atomic percentage
bcc	Body-centered cubic
BZ	Brillouin zone
cMC	classical Monte Carlo
CE	Cluster expansion (method)
cMC	classical Monte Carlo
CP	Complex Phase
CVM	Cluster variation method
DFT	Density-functional theory
DP	Dual Phase
ECI	Effective cluster interactions
fcc	Face-centered cubic
GDP	Global domestic product
GGA	Generalized gradient approximation
GP	Guinier-Preston (zone)
GS	Ground state
KKR	Korringa–Kohn–Rostoker
LDA	Local density approximation
LSDA	Local Spin density approximation
MC	Monte Carlo
MS	Martensitic steel
OR	Orientation Relationship
PAW	Projector-augmented waves
PBE	Perdew Burke Ernzerhof
p.p.p.	Price per pound
QHA	Quasi-harmonic approximation
QMC	Quantum Monte Carlo
rMC	rescaled Monte Carlo

SCF	Self-consistent field
SPR–KKR	Spin-polarized relativistic Korringa–Kohn–Rostoker
TRIP	Transformation induced plasticity
TTT	Time-Temperature-Transformation diagram
VASP	Vienna ab initio software package
wt. %	Weight percentage
XRD	X-ray diffraction
ZPE	Zero-point energy

Samenvatting

Het ontwerp en de productie van nieuwe materialen vormt al eeuwenlang de ruggengraat van onze technologische vooruitgang. Een van de meest impactvolle innovaties vond plaats in de negentiende eeuw, toen nieuwe productieprocessen resulteerden in consistent en goedkoop staal. Het gebruik van staal werd alomtegenwoordig in de transport- en constructiesector en bepaalde het uitzicht van de wereld in de twintigste eeuw. Dit is vooral het geval voor onze vervoersmiddelen, waarbij de verhouding tussen sterkte en gewicht cruciaal is. Vandaag ligt een groot deel van de focus in het materiaalonderzoek op de zoektocht naar steeds meer sterkte voor gewicht bij de productie van een component. Verbeteringen in staaltechnologie zijn er dus vooral op gericht om minder materiaal te gebruiken voor dezelfde functie. Dit speelt vooral in de transportsector, waar de emissienormen steeds strikter worden, en een verminderd gewicht een lager brandstofverbruik met zich mee brengt. In dit opzicht heeft staal een bijkomend voordeel: de productie kent een lage uitstoot van CO_2 in vergelijking met andere materialen zoals aluminium of composieten. Recente ontwikkelingen in staaltechnologie gaan dikwijls hand in hand met een verhoogde complexiteit op de microscopische schaal: het combineren van verschillende fasen, creëeren van extreme fijne korrels of zelfs vertrouwen op fasetransformaties wanneer het materiaal operationeel is. Deze worden tot stand gebracht via nauwkeurige en precieze legering en temperatuurbehandelingen. Met het oog op de ontwikkeling van nieuwe staalsoort is het van uitermate groot belang om te weten welke fase stabiel is gegeven een bepaalde samenstelling en temperatuur.

Het nitreren van staal wordt al meer dan een eeuw uitgevoerd, maar de focus ligt tot dusver voornamelijk op de verbeterde oppervlakte-eigenschappen. Tijdens het opstikken vormt er zich immers een samengestelde laag op het oppervlak, die bestaat uit ijzernitrides zoals Fe_4N en Fe_3N. Deze laag zorgt voor een verhoogde resistentie tegen corrosie en slijtage. Onder die laag is

stikstof als onzuiverheid aanwezig in de ferrietmatrix. Hierdoor kunnen er zich, tijdens het afkoelen na het opstikken, secundaire ijzer-stikstoffasen vormen zoals Fe_4N en $Fe_{16}N_2$. Vooral $Fe_{16}N_2$ helpen om de mechanische eigenschappen van de matrix, met name sterkte en slijtvastheid, te verbeteren. Welke mogelijke andere fasen zich kunnen vormen wanneer naast ijzer en stikstof andere chemische elementen aanwezig zijn, is minder geweten.

Door een gepaste opstikkingsprocedure kan de vorming van een samengestelde laag op het oppervlak van het genitreerde materiaal vermeden worden. Op die manier diffundeert doorheen het volledige specimen en worden de eigenschappen van de diffusiezone overgedragen naar het volledige materiaal. De mogelijkheden van deze behandeling zijn nog maar zelden overwogen en vormen dus een onderzoeksdomein met groot potentieel. Wanneer ternaire elementen naast ijzer en stikstof aanwezig zijn in het materiaal, wordt het uiterst belangrijk om te kunnen voorspellen welke andere fasen zich kunnen vormen.

In dit werk beogen we om de toekomstige ontwikkeling van stikstofstaal te sturen en ondersteunen door de fasestabiliteit te voorspellen van ijzer-stikstofmaterialen. Thermodynamische (meta)stabiliteit is immers een nodige voorwaarde voor een fase om te vormen in de ferrietmatrix. Wanneer zo'n analyse experimenteel zou worden uitgevoerd, dient men een groot aantal proeven te doorlopen om te besluiten welke fase stabiel is in functie van temperatuur en compositie, om zo uiteindelijk tot het fasediagram te komen. Dit is vooral het geval wanneer een groot aantal verschillende legeringselementen geëvalueerd moet worden. Voor het ijzer-stikstofsysteem zijn er daarbij nog bijkomende praktische verwikkelingen. Ten eerste zijn alle ijzer-stikstoffasen onstabiel ten opzichte van ontbinding in ijzer en stikstofgas. Ten tweede is het experimenteel zeer uitdagend om grote homogene stalen te maken van die fasen. Dit bemoeilijkt een experimentele karakterisatie en beperkt die meestal tot een nauw temperatuurbereik. Voor $Fe_{16}N_2$ bijvoorbeeld, is het experimenteel niet direct meetbaar waar de Curie temperatuur ligt, aangezien deze fase onstabiel wordt vooraleer de ferromagnetische orde verloren gaat.

Het gebruik van simulaties kan dit probleem helpen aanpakken door bijkomend inzicht te verwerven, vooraf interessante legeringselementen voor te selecteren of het experimentele werk te vermijden. Vooral methoden die geen experimentele input vergen verschaffen de mogelijkheid om onbevooroordeelde voorspellingen te maken. Deze methoden noemt men

in het algemeen *ab initio* methoden. Recent werd aangetoond dat een dergelijke methode, namelijk dichtheidsfunctionaaltheorie (DFT), accurate voorspellingen kan maken voor de vrije energie van ijzer en cementiet. Aangezien de vrije energie de bepalende grootheid is die fasestabiliteit bepaalt, wijst dit op de kracht van DFT om voorspellingen inzake stabiliteit te maken voor ijzerlegeringen.

Vooreerst stellen we als doel om de vrije energie van ferriet met stikstof in oplossing, Fe_4N en $Fe_{16}N_2$ te berekenen. Hieruit bepalen we vervolgens de fase-evenwichten voor temperaturen lager dan 592 °C. Uit die analyse kunnen we twee besluiten trekken. Ten eerste slaagt het gebruik van DFT erin om de oplossingslimiet van stikstof in ferriet accuraat te voorspellen. Dit valideert het gebruik van DFT om vrije energieën te bepalen voor ijzer-stikstofmaterialen. We vinden een evenwicht tussen Fe_4N en $Fe_{16}N_2$ bij 120 °C en ook dit resultaat is consistent met de experimentele waarnemingen. Ten tweede kunnen de berekende thermodynamische eigenschappen dienen als betrouwbare inputdata voor modellering op grotere schaal. Uit de berekende vrije energieën kan bijvoorbeeld de drijvende kracht voor dissociatie van $Fe_{16}N_2$ in Fe_4N en ferriet afgeleid worden voor elke temperatuur en stikstofconcentratie. Aangezien de precipitatie van Fe_4N voorafgegaan wordt door die van $Fe_{16}N_2$, dat fungeert als een precursor voor die laatste, is dit evenwicht van centraal belang voor het ijzer-stikstofsysteem.

Met een gevalideerde methodologie is het vervolgens mogelijk om de fasestabiliteit van meer complexe ijzer-stikstoflegeringen te bestuderen, door ternaire legeringselementen toe te voegen. Ten eerste onderzoeken we hoe een ternair element de oplosbaarheid en de mobiliteit van stikstof in de ferrietmatrix kan beïnvloeden. Ten tweede evalueren we welke legeringselementen stabiele ternaire fasen kunnen vormen in het kristalrooster van Fe_4N (γ') of $Fe_{16}N_2$ (α''), aangezien deze structuren van centraal belang zijn in de precipitatievorming. Voor de legeringselementen die ternaire fasen vormen in beide structuren, berekenen we verder ook de volledige vrije energie. Dit stelt ons uiteindelijk in staat om de ternaire elementen te classificeren. Deze classificatie is gebaseerd op het effect dat de ternairen kunnen voortbrengen: vorming in de γ'–structuur en/of vorming in de α''–structuur. Daaruit kunnen we besluiten dat Nb, Mo, Al en Cu mogelijke kandidaten zijn voor stabilisatie van de α''–structuur. Cu zal echter resulteren in de vorming van de binaire fase $Cu_{16}N_2$, die mogelijk niet het beoogde versterkende effect zal hebben op het materiaal. Voor Mo en Al geldt dat er zich alternatieve binaire stikstofhoudende fasen kunnen

vormen: MoN, Mo_2N en AlN. Als deze binaire fasen eerder vormen dan de ternairen, zal de vorming van die laatste niet optreden. Nb is de meest beloftevolle kandidaat om α''–structuren te bekomen, met $Fe_8Nb_8N_2$ als stabiel materiaal boven 400 K.

Dit werk toont aan dat DFT een gevalideerde en betrouwbare methodologie is voor het gebruik van eindige temperatuurseigenschappen binnen het ijzer-stikstofsysteem. Hoewel er nog steeds uitdaging overblijven, zoals de beschrijving van onzuiverheden en magnetische effecten, toont de vergelijking met experiment de accuraatheid aan. Verder stellen we een classificatie op van de ternaire legeringselementen op basis van de thermodynamische interactie met stikstof en ijzer. Deze biedt een leidraad voor de toekomstige ontwikkeling van stikstofstaal, zowel voor de samenstelling als voor de thermische behandeling.

Summary

The design and production of new materials has formed the backbone of human development throughout the ages. One of the most impactful innovations occurred in the 19th century, when new manufacturing techniques yielded consistent and cheap steels. Its ensuing application in transport and construction largely shaped our world in the 20th century, especially our most important modes of transportation, where strength-to-weight is crucial. Today's quest for new materials in transport and construction seeks ever more strength for per component weight. Improvements in steel technology are thus focused on the development of steel grades that result in the use of less material. This is especially true in light of ever more stringent emission standards in the automotive sector, where lighter weights result in reduced fuel consumption. In this respect, an increasingly important argument for the continued use of steel is its low carbon footprint during production. Recent progress in steel technology often consists in producing a more complex material on the microscopic level: coexistence of multiple phases, extreme grain refinements or even phase transformations during operation. This is achieved through carefully controlled alloying and thermal processing. In this light, knowing which phase is stable for a given composition and temperature is a crucial element for understanding and developing steel grades.

Of particular interest to this doctoral thesis is the addition of nitrogen to steel. Although the nitriding of steel has been an established process for over a century, research focus lies mainly with how it affects the surface of the material. During the nitriding process, a layer of iron-nitrides such as Fe_4N and Fe_3N are known to form at the surface. This compound layer results in an improved corrosion and wear resistance. Underneath the compound layer, nitrogen is present in solid solution. Upon cooling, iron-nitrogen phases such as Fe_4N and $Fe_{16}N_2$ are known to form secondary particles in the ferrite matrix. $Fe_{16}N_2$ precipitates in particular can improve the

strength and wear resistance. Knowledge is very limited on the conditions that trigger the formation of these phases, such as composition and cooling process, or what other possible phases can evolve when elements besides nitrogen and iron are present.

By selecting the appropriate nitriding conditions, the formation of a compound layer at the surface can be avoided. As such nitrogen is diffused through the entire thickness of the nitrided material and the properties of the diffusion zone extended throughout the entire specimen. The possibilities of such a treatment have rarely been considered and thus present a research avenue with large development opportunities. In case ternary alloying elements are present that form nitrides, precipitates can form during nitriding or cooling. In this respect, the ability to predict which phases can form in the ferrite matrix becomes key.

In this work, we aim to aid future development of nitriding steels by predicting the phase stability of iron-nitrogen compounds. Thermodynamic (meta)stability is a necessary condition for a phase to form in the ferrite matrix. Traditionally, such an analysis is dependent on extensive experimental research that determines the most stable phase for given conditions, from which a phase diagram is constructed. This requires a large amount of experimental work, especially if one wishes to screen many possible additional alloying elements to the iron-nitrogen composition. For iron–nitrogen compounds in particular, practical limitations hamper such a procedure. It is challenging to manufacture large homogeneous samples of iron-nitrogen phases such as Fe_4N and $Fe_{16}N_2$. Because of this, experimental characterization is difficult and mostly constrained to limited temperature ranges. For $Fe_{16}N_2$, for example, the Curie temperature is hard to determine, as the compound becomes unstable and dissociates before the ferromagnetic order is broken.

Atomistic simulations address this problem by providing further insight, by pre-selecting compositions and temperature ranges of interest, or by avoiding the experimental work altogether. In particular, methods that do not require any experimental input, called first-principles or *ab initio* methods, have the ability to provide unbiased predictions. In recent years, one such method, Density-Functional Theory (DFT), has been shown to provide accurate results for the heat capacity and free energy of iron and cementite. As the free energy is the key thermodynamic quantity determining phase stability, such successes point toward DFT as a powerful

tool to predict it for iron-based compounds.

First, we calculate the free energy of ferrite with nitrogen in solid solution and the iron-nitrogen phases Fe_4N and $Fe_{16}N_2$. This enables us to determine the phase equilibria between those three phases in the low nitrogen concentration limit for temperatures below 592 °C. Two main results can be deduced from this analysis. First, DFT successfully predicts the limit of solubility for nitrogen in ferrite, which validates its use for calculating free energies for the iron-nitrides. The equilibrium between Fe_4N and $Fe_{16}N_2$, found to be at 120 °C, is consistent with experimental findings as well. Secondly, we resolved experimental uncertainties concerning the metastable nature and magnetic properties of the $Fe_{16}N_2$ phase. Additionally, the calculated thermodynamic properties can serve as input for higher-order calculations, as they contain more information than the mere phase equilibria.

With an established and validated methodology available to predict the phase stability for the iron-nitrogen compounds, we proceed to extend the research to ternary compounds. First, we aim to determine which ternary alloying elements can form ternary phases in the crystal structure of Fe_4N (γ') or $Fe_{16}N_2$ (α''), in light of the importance of these two phases in precipitation formation. Second, we want to tackle the question of how a ternary alloying element dissolved in the ferrite matrix can affect the mobility and solubility of nitrogen. Finally, for those elements that form ternary phases in both structures, free energies are compared at finite temperatures. Ultimately, a classification of the ternary alloying elements is obtained. This classification is based on whether the addition of the alloying element can lead to the formation of α'' and/or γ' ternary phases. From this analysis, Nb, Mo, Al and Cu can be considered candidates for stabilizing the α'' structure. However, Cu forms the binary $Cu_{16}N_2$ compound, which might not result in precipitation strengthening. Also, Mo and Al are known to form the binary nitrides AlN, MoN and Mo_2N, which can impede the precipitation of ternary phases. Nb is a more promising candidate, however, as no binary Nb–N phases are known to form and we find the ternary phase $Fe_8Nb_8N_2$ to be stable with respect to dissociation above 400 K. As such, it is a potential candidate to improve the precipitation strengthening effects in nitrided steels.

This work demonstrates DFT as a valid methodology to determine phase stability in the iron-nitrogen system. Although some difficulties remain, such as the treatment of impurities and magnetism, comparisons with

experiment have shown good accuracy. Furthermore, a classification for the ternary alloying elements concerning possible precipitate formation in the α'' or γ' crystal structure is put forward. This can serve as a quantitative guideline during the future development of iron-nitrogen steels.

Part I

Predicting phase stability in nitrogen steels with Density-Functional Theory

1

Introduction

To make a complete carbon fiber road car would never be affordable for the everyday motorist.

Gordon Murray, Formula 1 design engineer.

1.1 Steel: applications and market

Steel making is one of the oldest industries in the world. Today, its applications are numerous, from high-precision medical equipment to freight containers, continuing to facilitate scientific progress and globalization alike. If a product is not made from steel, it is likely produced using a machine made from steel. The main consumption (Figure 1.1) takes place in the construction sector, where steel is used as standalone designs or incorporated into reinforced concrete.[1] Construction steels are generally low–cost and today, they are mostly manufactured from recycled steel.

In other markets, the material demands are higher and more specific. For automotive applications, a high strength-to-weight ratio is crucial to minimize the mass of the end product, especially in light of the ever more stringent CO_2 emission standards. Additionally, a high formability of the used steel grades is also desired for the design and manufacturing. In the case of machinery and tools, high surface hardness and resistance to

corrosion and abrasion are the desired properties. Because iron is a magnetic material, it is used in transformers, electric motors and generators. For such applications, a high magnetization and small hysteresis losses are of primary importance. These are all very different materials requirements, yet the core product, in all cases, is steel.

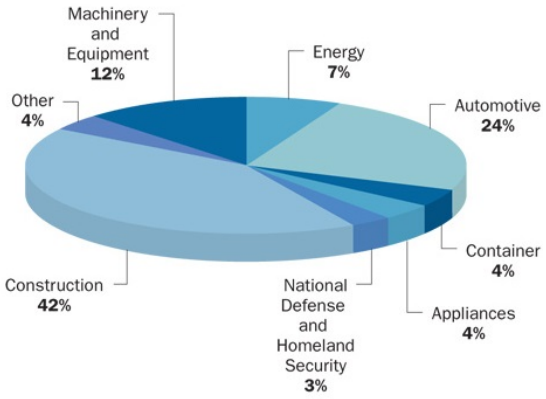

Figure 1.1: Steel use by market classification for 2010[1]

The widespread use of steel means that even the slightest of technological advancements result in an enormous impact. Innovation in materials research often focuses on novel materials such as carbon fibre, aluminum alloys, graphene or composite materials, proposing them as the materials of the future. Although this may be true for very specific applications, steel is still the main material of choice in most industrial endeavours. The total world production of steel in 2015 amounted to 1620 million metric tons,[2] compared to 64 million tons of aluminum and 117 thousand of carbon composites,[3, 4] highlighting its central industrial role.

The main reason for carbon steel's industrial prominence, is its relatively low price, resulting from the low cost of the raw materials. For example: at the time of writing, July 9 2019, the price per pound (p.p.p.) of A36 plate steel in the United States was €0.34, whereas the p.p.p. of aluminum plates was €1.37.[5] With such a low cost, it is hard to change the material for steel-based products without losing their affordability .

The global demand for steel is still very much on the rise (Figure 1.2).[6] One of the big driving factors behind the increasing steel demand is economic growth in developing countries.[7] In those economies, large investments in fixed assets, manufacturing and urbanization generate a spike in steel

consumption (Figure 1.3). With such an evolution in mind, long-term growth markets such as India and Africa are easily identified. However, the decreasing consumption in mature economies present a challenge for the steel industry. In China, the major growth market over the last 20 years, demand is expected to decline at $1.1\,\%$ per year by 2035.[7] Furthermore, the peak consumption per capita, as depicted in Figure 1.3, is decreasing and its occurrence (in GDP/per capita) is coming earlier. These factors all point towards a steel industry where more specific uses of the material, e.g. the automotive, energy, manufacturing and tools sectors, will become ever more important.

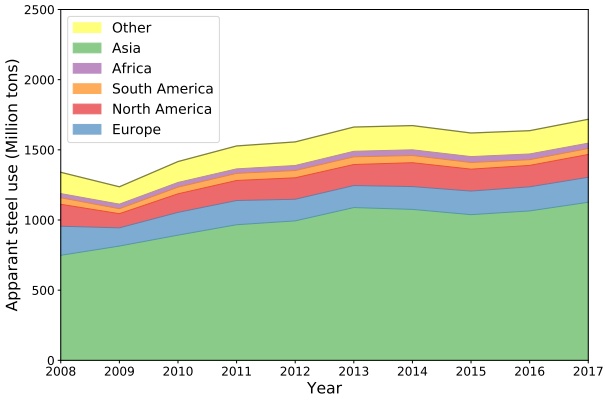

Figure 1.2: Evolution of steel consumption in millions of metric tons crude steel equivalent over the years 2008-2017. Apart from some years with an economic downturn, the global trend is upward. The increase between 2008 and 2017 can be mostly attributed to the growing consumption in Asia.[6]

One example of how current advancements can yield very significant progress is the development of advanced high-strength steels (AHSS). It reduces the environmental impact as less material is necessary to obtain similar strength in manufactured parts. The weight reduction in the manufacturing of body structural materials amounts to an estimate of 25% (Figure 1.4).[8] Combined with the lower part weight resulting in lower CO_2 emissions under operation, the use of steel also has the added benefit that it is much more environmentally friendly. Aluminum production generates at least 4 times the CO_2 emission of producing steel, and other lightweight materials such as magnesium or carbon fiber can generate even 5 times more than that.[9] As such, steel is still very much the main material of

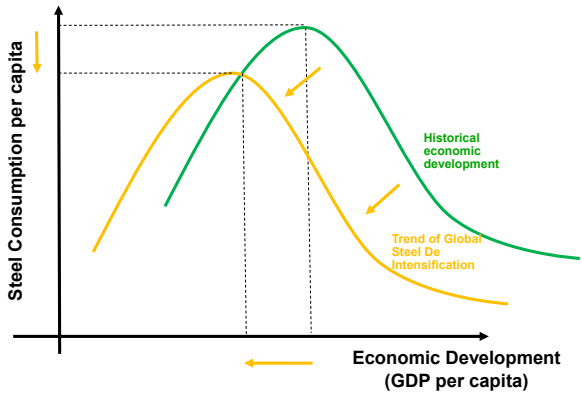

Figure 1.3: During economic development, the steel consumption initially increases drastically. Afterwards it declines again towards a steady-state situation.[7] As steel technology improves, however, the peak consumption is lower and it takes place earlier.

choice for vehicle manufacturing.

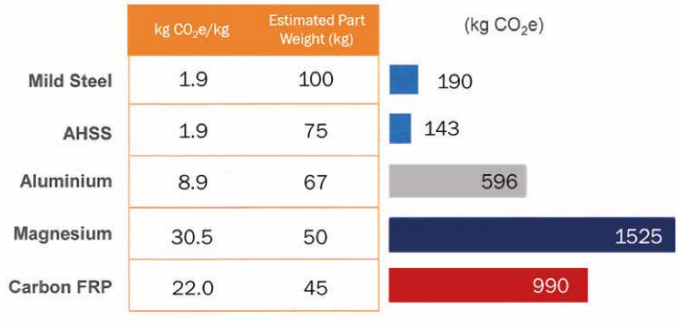

Figure 1.4: Comparison of CO_2 emission during the production process of body structurals depending on the choice of material. Even though carbon fibre composites and magnesium alloys require a significantly lower material weight, the greenhouse gas emissions are increased by an order of magnitude.[9]

1.2 From iron to advanced alloys

In materials science, the name “steel” is used to refer to materials from the family of iron-carbon-based alloys. The main ingredient, iron, is in itself a

material with a variety of interesting properties. Cooling from a melt, it first solidifies into the body-centered cubic (bcc) δ structure at $1536\,^{\circ}\mathrm{C}$. Upon further cooling, it transforms to the face-centered cubic (fcc) γ structure at $1392\,^{\circ}\mathrm{C}$, also referred to as austenite. At $911\,^{\circ}\mathrm{C}$, it transforms back to a bcc structure, the α phase, called ferrite. At $768\,^{\circ}\mathrm{C}$, there is also a second-order phase transformation, where the material becomes ferromagnetic. This critical point is called the Curie temperature.

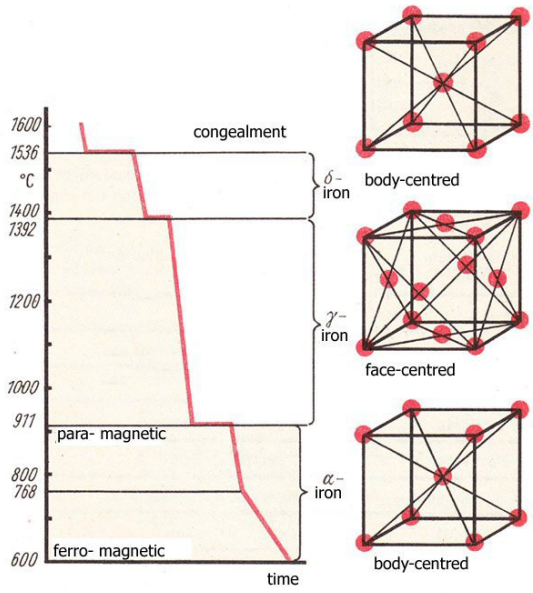

Figure 1.5: The allotropes of iron. Cooling from melt to room temperature first yields the bcc phase, followed by the fcc phase to finally transform to the bcc phase again. The latter phase is paramagnetic at higher temperatures, but becomes ferromagnetic below $768^{\circ}\mathrm{C}$.[10]

The history of steel making is as old as the melting of iron itself. At higher temperatures, the solubility of carbon in iron increases, especially when ferrite transforms to austenite (Figure 1.6). The historical burning of coal as a source of heat therefore resulted in carbon being diffused into the iron matrix, yielding carbon steel. Classically, this process was more of an art than science, as there was no understanding of the final carbon concentration. The carbon concentration, however, largely determines the properties of the steel. Higher concentrations yield increased hardness and tensile strength, but this reduces ductility and results in a more brittle

material.

Halfway through the 19th century, a number of process developments took place. First, the Bessemer process allowed the control of carbon content in iron production by blowing air through the melt, thus reducing the amount of impurities through oxidation. Subsequently, when manganese was added as a ternary element to remove the leftover oxygen it marked the real birth of mass steel production. When Sidney Gilchrist Thomas started adding limestone to remove phosphorus, iron ore from anywhere in the world could be used for the Bessemer process and prices duly dropped. This made steel one of the pillars of the industrial revolution in the 19th century.

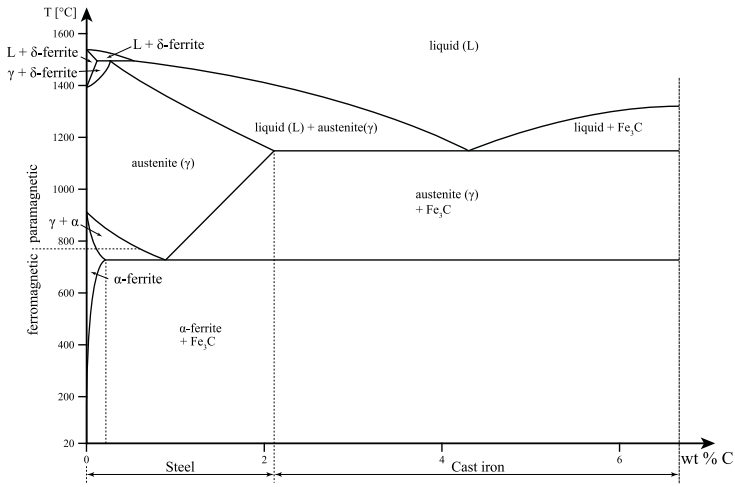

Figure 1.6: The Fe–C phase diagram up to 6.67 weight percentage carbon. In steels, an increasing carbon content lowers the melting temperature and stabilizes austenite, where the limit of carbon solubility is much higher than in ferrite.[11]

Today's addition of ternary alloying elements to the iron-carbon system has many more intricate objectives. Advanced High Strength Steels, for example, are characterized by the presence of multiple phases of iron coexisting in the material (Figure 1.7). These are achieved not only by their chemical composition, but also stem from more complex thermomechanical treatments.[12] To formulate the manufacturing protocols, *i.e.* chemical composition, processing and heat treatments, the interaction of the alloying elements with iron, carbon and each other needs to be known. Which phases can form if a certain element is added, what is the solubility of carbon in those phases and how does this change the steel's properties? These are just

some of the questions that need to be addressed to further metallurgical research. From a simple thermodynamic point of view, knowing the phase diagram for the entire composition range should provide the necessary background. However, steel making usually involves cooling and mechanical processes whereby the material is not in thermodynamic equilibrium. As such, knowing what phases can form in an alloy and in which temperature ranges is a hugely complex assignment.

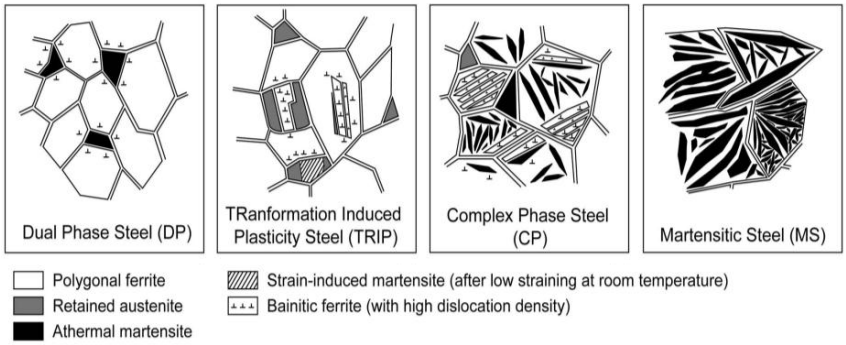

Figure 1.7: Microstructures of advanced high strength steels. These microstructures are markedly more complex compared to standard high strength steels.[10]

1.3 The role of nitrogen in the manufacturing of steel

1.3.1 Nitriding as a surface treatment

In conventional alloying of steels, additional elements are added to the liquid iron-carbon melt after the latter has been cleared of impurities and its carbon content regulated. The melt can then be cast and solidified into steel slabs. Nitriding of steels is a surface treatment that takes place afterwards on the solidified material. At the start of the 20^{th} century, in search of improved surface hardness, it was discovered that nitrogen in iron can result in a hard surface with good corrosion resistance.[13] It has since been used to improve the surface properties of parts and components made in forging and tool steels.[14–18] Today, nitrided steels can be found in many manufacturing industries, such as aircraft, bearings, automotive or turbine generation systems.[13]

During nitriding, nitrogen is diffused into the surface of steel, which usually remains in the ferrite phase, at temperatures of 490 to 580°C.[19] The diffusion process can be performed in a variety of ways: in an ammonia atmosphere, in a salt bath or even using a plasma. The end result, however, is usually quite similar: a nitride compound layer at the surface and a diffusion zone underneath are formed (Figure 1.8).[20]

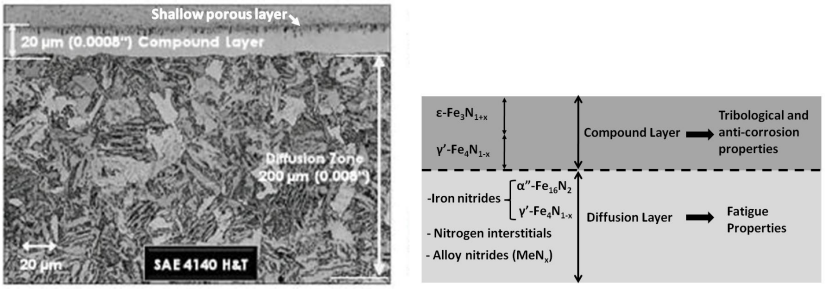

(a) Metallographic cross section of nitrocarburized AISI 4140 steel.

(b) Schematic overview of the compound and diffusion layer.

Figure 1.8: The nitriding process forms a compound and diffusion layer near the steel surface.[21]

In the compound layer, also called growth or white layer, the higher concentrations of nitrogen result in the formation of multiple phases, mainly the Fe_3N_{1+z} and Fe_4N_{1-x} (Figure 1.9a).[1] The thickness of this compound layer is controllable through the treatment time, temperature and nitriding potential used during the process. This layer can significantly increase the wear and corrosion resistance.[19] Whether its presence is desired, however, largely depends on the required performance under operating conditions, for which a testing procedure is necessary.

1. The inclusion of z and x serves to indicate the off-stoichiometry that is present in these phases.

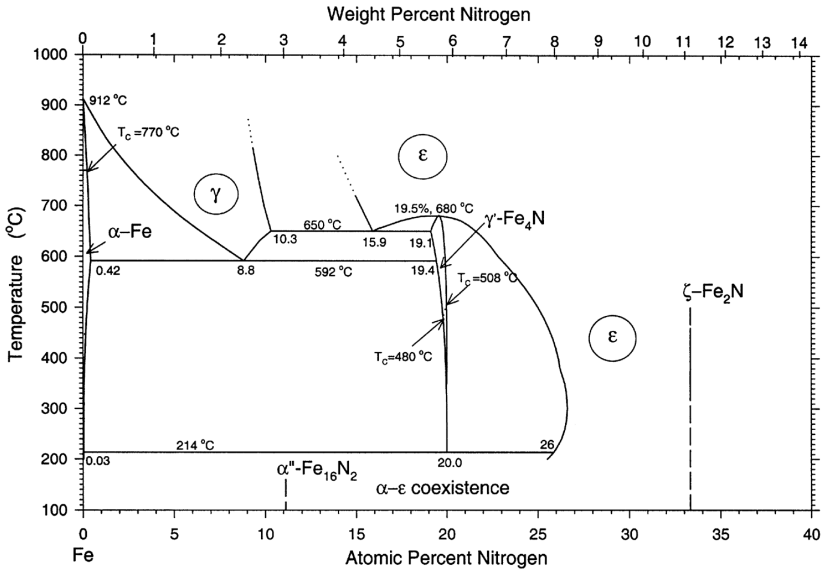

(a) The Fe-N phase diagram.[22]

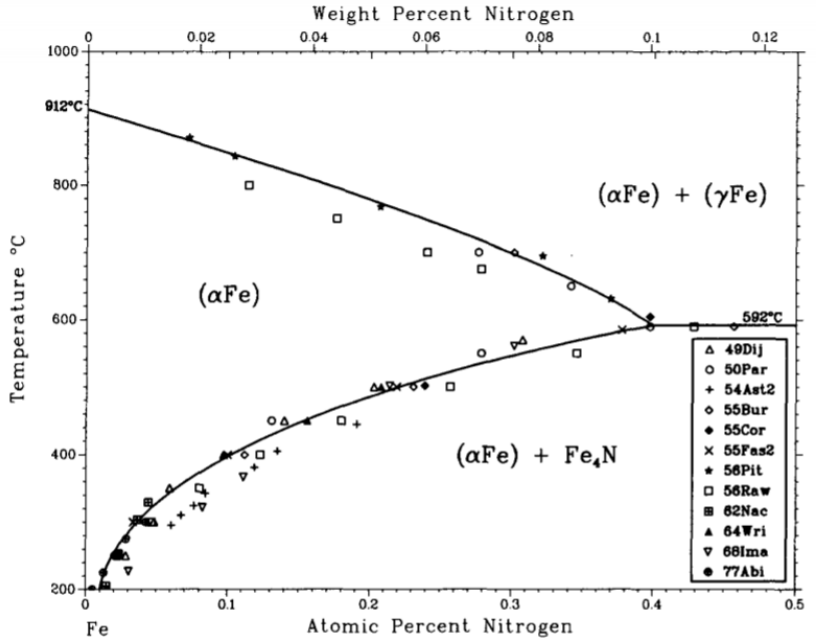

(b) The low–concentration limit of the Fe–N phase diagram, with the experimentally measured limits of solubility for nitrogen in ferrite.[23]

Figure 1.9: The phase diagram of Fe–N for different ranges of composition. Top: up to 40 at.% nitrogen showing all possible iron-nitrogen phases. Bottom: enlarged section of the low–concentration limit.

Below the compound layer lies the diffusion layer (Figure 1.8). There, nitrogen is present in solid solution in the ferrite matrix. As a result, a solid solution strengthening of 50 MPa per 0.01 wt% of added nitrogen can be achieved.[24] Also, ternary alloying elements such as Cr, Al, V, W or Mo can form stable nitrides during the process. These can further strengthen both the compound layer and the diffusion zone through precipitation hardening.[25]

As an impurity in ferrite, nitrogen occupies an interstitial position in an octahedral configuration [Figure 1.10].[26] In this position, the nitrogen impurity aligns with its nearest iron neighbors. This causes a local tetragonal distortion, where the aligned iron atoms undergo a large displacement from their original bcc position. This local lattice distortion results in solid solution strengthening by impeding dislocation motion.[27]

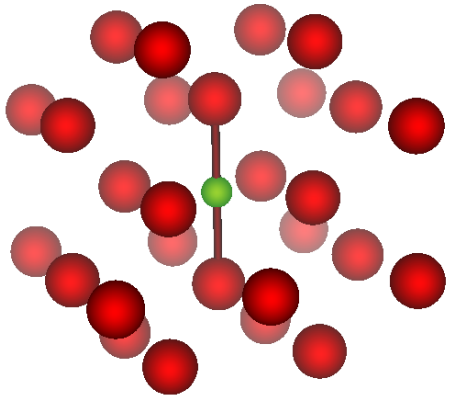

Figure 1.10: Nitrogen impurity in a ferrite lattice. It occupies an octahedral interstitial position. There are two nearest-neighbor iron atoms (red lines) that undergo a significant displacement, resulting in a local tetragonal distortion.

1.3.2 The iron-nitrides Fe_4N_{1-x} and $Fe_{16}N_2$

After the nitriding procedure, with nitrogen present in solid solution, precipitation of iron-nitrogen phases can occur upon cooling at temperatures where the nitrogen concentration exceeds the limit of solubility (Figure 1.9a)). This is provided the cooling is sufficiently slow. At temperatures above 230-250 °C, Fe_4N_{1-x} forms, whereas below that threshold $Fe_{16}N_2$ precipitates (Figure 1.11).[28] The formation of Fe_4N_{1-x} is usually determined by thermodynamic stability; *i.e.* given sufficient time in the right temperature

range, precipitates will form in the supersaturated matrix (Figure 1.11). $Fe_{16}N_2$, on the other hand, is not a stable Fe-N compound for any mole fraction of nitrogen. It is a metastable compound that forms at temperatures below 230-250 °C. Below that temperature, the activation energy for transformation of $Fe_{16}N_2$ to Fe_4N_{1-x} is too large and cannot be overcome, which is why the metastable $Fe_{16}N_2$ precipitates form.[29]

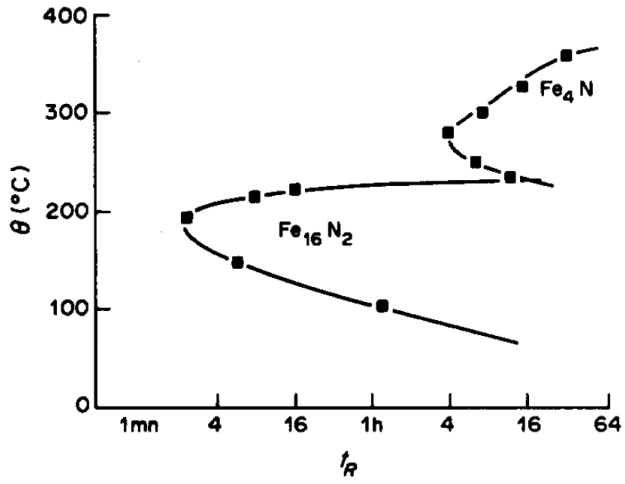

Figure 1.11: Fe-N Time Temperature Transformation (TTT) diagram.[28]

The iron-nitride $Fe_{16}N_2$ is ferromagnetially ordered and has the space group I4/mmm.[30] The nitrogen atoms occupy the regular octahedral interstitial positions $(0.0, 0.0, 0.0)$ and $(0.5, 0.5, 0.5)$ in a distorted ferrite supercell [Figure 1.12a]. The regular ordering of the nitrogen atoms causes a macroscopic tetragonal distortion. In this work, the name α'' is used to indicate the crystal structure of $Fe_{16}N_2$.

The structural similarity between ferrite and $Fe_{16}N_2$ is the reason why the latter phase precipitates, even at lower temperatures, as it only requires the diffusion of nitrogen atoms. Indeed, it has been found experimentally that the formation of $Fe_{16}N_2$ is preceded by the formation of planar nitrogen atom clusters, or Guinier-Preston (GP) zones, that form atomically thin platelets on the $\{001\}$ ferrite planes.[31–33] The precipitates are perfectly coherent with the matrix in their habit plane, but the tetragonal distortion due to the nitrogen accumulation results in a misfit with the matrix in the direction orthogonal to that plane. Therefore, these planar structures form disc-shaped precipitates with a cube-on-cube orientation relationship (OR) $(001)_{\alpha''}//(100)_{\alpha}$ with $\langle 100\rangle_{\alpha''}//[100]_{\alpha}$ and a (001) habit

plane.[34] Essentially, this means the iron bcc structure is continued, but distorted because of the regular presence of nitrogen at interstitial positions, constituting the $Fe_{16}N_2$ phase. These $Fe_{16}N_2$ precipitates can produce a hardness increase of about 10 to 20 %, especially when they are still small and in the early stages of precipitation.[35–38]

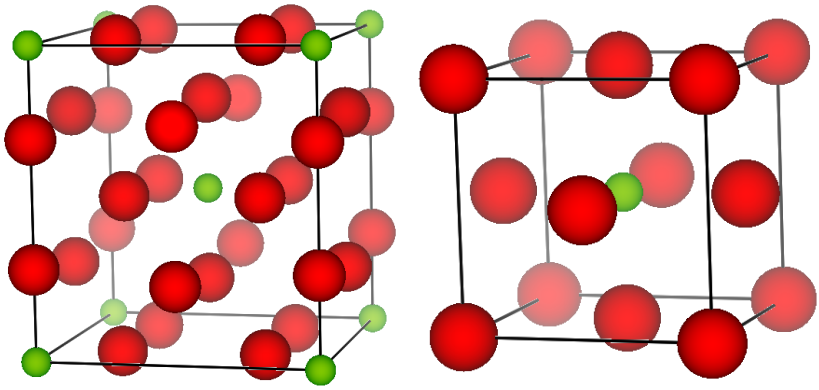

(a) The unit cell of $Fe_{16}N_2$. **(b)** The unit cell of Fe_4N.

Figure 1.12: Crystal structures of the Fe-N phases with the Fe atoms shown in red and the N atoms in green.

Fe_4N_{1-x} is a ferromagnetic material as well, but in contrast to $Fe_{16}N_2$ it has a cubic crystal structure (γ') with space group P m $\overline{3}$ m,[39] where iron atoms form a face-centered cubic sublattice, and nitrogen atom occupying the $(0.5, 0.5, 0.5)$ 1b Wyckoff position [Figure 1.12b]. The structural dissimilarities between ferrite (bcc) and Fe_4N_{1-x} (fcc) result in a higher activation barrier for the transformation. Hence, the Fe_4N_{1-x} precipitates only occur above 200°C.[34] They form V–shaped groups of large plates, where the shape serves to accommodate the shear strain of the precipitate. The stoichiometric coefficient $1\text{-}x$ of nitrogen indicates that there is usually a slight deficiency (19.5 at.% instead of 20 at.%) of nitrogen compared with the ideal crystal lattice of Fe_4N, shown in Figure 1.12b.[40] For the remainder of this work, however, we will consider the perfect crystal Fe_4N.

It has been proposed that the Fe_4N and $Fe_{16}N_2$ precipitates are linked via a precipitation chain.[34, 41–43] As such, $Fe_{16}N_2$ is a precursor for the formation of Fe_4N. Because the latter phase does not provide significant strength or hardness improvements, its presence is preferably avoided in favor of nitrogen in solid solution or $Fe_{16}N_2$ precipitation. Although, as seen above, a temperature range for the transformation and a time temperature

transformation (TTT) diagram (Figure 1.11) are available, few of the thermodynamic properties of Fe_4N or $Fe_{16}N_2$ are known. Because they mainly occur as precipitates in a ferrite, manufacturing large homogeneous samples of Fe_4N and especially $Fe_{16}N_2$ is very challenging. Most of the research on the iron-nitrogen system has thus focused on how the kinetics of the process influence the microstructure of the surface layer; in other words: control of the compound layer and diffusion layer characteristics.[19, 44–47]

1.4 Goals and outlook

1.4.1 Metallurgical

The main goal of this dissertation is first to better understand the thermodynamics of the binary Fe–N system and subsequently chart the possible effects of ternary alloying elements. These results are aimed at the development of through–thickness nitrided steels, which are rarely considered for the improvement of bulk properties. By selecting the appropriate nitriding conditions[2], the formation of a compound layer at the surface can be avoided and, for pure $\alpha-$Fe or for ferritic steels with no nitride forming elements present, the absorbed nitrogen will be in solid solution during nitriding. As such, the properties of the diffusion layer of a typical nitrided surface, *i.e.* increased hardness and strength, are extended throughout the bulk.

The lack of knowledge about the thermodynamics of Fe_4N and $Fe_{16}N_2$ severely hampers the understanding of their precipitation and the possibilities to model them. This hinders the further development of the process. The goal of this work thus consists in a two-step procedure. First, we aim to characterize the thermodynamic properties of both Fe_4N and $Fe_{16}N_2$, mainly obtaining the free energy. From the free energy, we can obtain quantitative knowledge of the driving force for both phase precipitations and the thermodynamic balance between them. Such information can aid significantly in improving the accuracy of diffusion-precipitation models.[48, 49]

In the second step, the impact of ternary alloying elements is investigated by calculating the energies of formation when these elements are included in the crystal structures of Fe_4N (γ') and $Fe_{16}N_2$ (α''), respectively. We evaluate three effects these elements can have on the iron-nitrogen system:

2. Gas composition and flow, nitriding temperature and surface pre-treatment

1. Stabilization of the nitrogen in solid solution through interaction with the ternary solute.
2. Formation of stable ternary compounds with Fe and N into the α'' crystal structure.
3. Formation of stable ternary compounds with Fe and N into the γ' crystal structure.

If ternary compounds are formed, the resulting shift in stability between the α'' and γ' precipitate structures will be investigated to evaluate what the impact is on the relative stability of both structures. Combining these insights will allow us to unravel the thermodynamic behavior of the iron-nitrogen system and aid the development of nitrided steels. For the purpose of this thesis, the role that carbon can play in the formation of iron–nitrides is not evaluated.

1.4.2 Methodological

It is not possible to directly measure the free energy of a material. Indeed, only the difference in free energy is a physically relevant quantity. Most commonly, it is derived through the analysis of equilibria between phases as a function of temperature and composition, combined with phenomenological models for the free energy. However, as first touched upon in Section 1.3, under some conditions iron–nitrogen binary phases form even though they are not the most stable ones. This metastability is a further complication to experimentally characterize those phases. The $Fe_{16}N_2$ crystal structure, crucial for precipitation hardening,[38] only exists as a precipitate in the Fe-N solid solution. Combined with the narrow temperature range of stability, it is very challenging to experimentally determine the thermodynamic properties.

From a computational point of view, this picture is inverted. The atomistic energy of the material that is modeled is often the primary output of the calculation. As a result, such calculations form an excellent starting point for a bottom-up approach, where essential thermodynamic properties are calculated on the atomic scale and subsequently serve higher-order modeling (Figure 1.13). In the case of a composition phase diagram, for example, this means calculating the energy of formation for all relevant phases at the desired temperatures and subsequently deriving the ranges of stability. Because modeling on an atomic level enables an isolated

treatment of each phase, the problem of metastability is circumvented. We will therefore perform electronic structure calculations on a quantum theoretical level, using Density Functional Theory (DFT),[50, 51] to study the iron-nitrogen system.

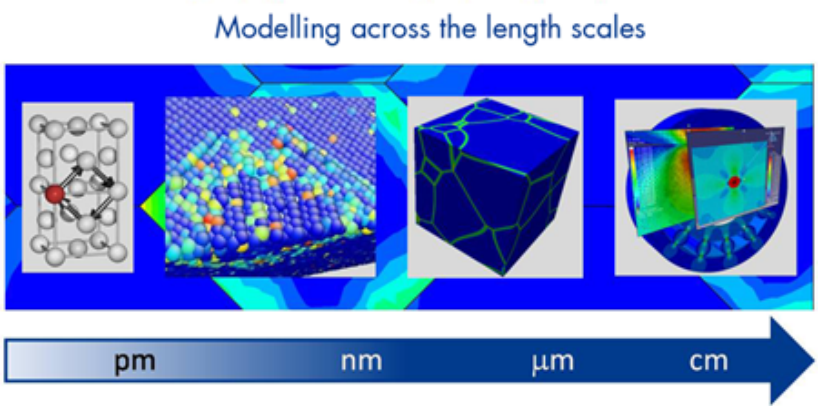

Figure 1.13: Materials properties are determined by a variety of its features, each of which can present themselves at a different length scale. At the atomic scale, generally the smallest modeling scale, basic properties can be calculated based on the chemical composition and the crystal structure. Not only does this result in better understanding of the material's behavior, but it also serves as input for higher-order simulations.[52]

In this work, we aim to calculate the free energy of $Fe_{16}N_2$, Fe_4N and Fe with N in solid solution ($Fe_{[N]}$) and use it to elucidate the Fe-N phase diagram in the low-nitrogen limit. To obtain these free energies, all relevant contributions should be taken into account: electronic, vibrational, magnetic and configurational. The electronic free energy is obtained using finite-electron temperature DFT,[53] the quasiharmonic approximation is used to compute the vibrational free energy and a rescaled Monte Carlo approach is applied for the magnetic excitations.[54, 55] The free energies can subsequently be used to evaluate the phase equilibria between the various phases, yielding the temperature/composition phase diagram of Fe_4N, $Fe_{16}N_2$ and bcc $Fe_{[N]}$ for N concentrations in the dilute concentration limit. From the calculated free energy, the heat capacity, thermal expansion and bulk modulus of Fe, Fe_4N and $Fe_{16}N_2$ as a function of temperature are obtained as well. A successful computational derivation of these thermodynamic properties sets a methodological base for further work on the Fe-N system.

When steelmaking involves multiple alloying elements, the number of phases

that can form quickly becomes a combinatorial nightmare. Setting up the large number of experiments required to determine the effects of different additions to the metal results in a huge investment. Indeed, methods that try to achieve consistent high-throughput combinatorial screenings form a research field in themselves.[56–59] Performing computer simulations can also present a low-cost alternative to experimental screenings. In an atomistic simulation, the researcher can perform alchemistic marvels, as swapping one atom for another usually yields a similar calculation. For example, if one is able to calculate the bulk modulus of an Fe-W alloy with 5 at.% W, the methodology can be quickly transferred to any Fe-X alloy by simply repeating the calculations with a different chemical element in place. As computational power has increased exponentially, computational high-throughput screenings have become ever more widespread.[60]

In this vein, this research will predict which impact the addition of ternary alloying elements can have on the precipitation of phase with an α'' or γ' crystal structure, extending the methodology used for the binary phases $Fe_{16}N_2$ and Fe_4N respectively. This is by no means an all-inclusive analysis into the possible effects of ternary elements. Rather, the goal is to identify the specific balance between the α'' and γ' structures that can precipitate in a ferrite matrix (*i.e.* below 590°C) at low nitrogen concentrations, which results in practical guidelines for future research in iron-nitrogen steels.

2

Methods

In this work, where we focus on the thermodynamic stability as a function of composition and structure, the free energy of the materials needs to be calculated. This free energy is determined at the atomic scale, as it directly derives from how atoms interact: do they form bonds and, if so, how strongly? To correctly describe these atomic interactions, a quantum mechanical approach is necessary. This means solving the Schrödinger equation. There is a large variety in approximate solution models to solve this equation, as exact solutions for real materials rarely exist. In recent years, Density-Functional theory (DFT) has become one of the most popular methods, for both computational chemistry and materials physics. Especially for crystalline solids, it offers a good trade-off between accuracy and performance.

In the following chapter, we first describe how to treat a static crystalline solid (Sec. 2.1), where the material is at 0 K. Afterwards, Sec. 2.2 explains the methodology to extend those calculations towards finite temperatures, specifically for magnetic materials.

2.1 Density-functional Theory

2.1.1 General background

A quantum mechanical calculation consists in solving the time–independent Schrödinger equation for all particles in a material by taking into account the interactions between them. In a traditional material, the considered particles are nuclei and electrons, which interact electrostatically. The Schrödinger equation thus takes the form:

$$\hat{H}\Psi = (\hat{T} + \hat{V})\Psi = E\Psi \tag{2.1}$$

This is an eigenvalue problem, where the energy E of the system and the wave function Ψ underlie all materials properties of interest. The wave function is a function of the position of all the nuclei and electrons, the operator $\hat{T}$ returns their kinetic energy and the operator $\hat{V}$ returns the potential energy, *i.e.* the pairwise electrostatic interactions.

There are two reasons why metallurgical problems are usually not solved using the Schrödinger equation:

- Because the operator $\hat{V}$ contains pairwise interactions, equation 2.1 is exponentially hard with respect to the number of particles N. Thus, it becomes unfeasible to solve it for systems where $N >> 10$. In practice, this means only small molecules can be tackled.[61]

- The many-body wavefunction, which is a function of the positions of all particles involved, requires an enormous amount of storage space on a computational platform. If a very crude 3D grid consisting of $10 \times 10 \times 10$ points is used, a simple nonmagnetic 4-electron system would require 8 terabytes of storage.

In order to describe larger systems on a quantum level, it is thus necessary to transform Equation 2.1 to a more practical one. This is achieved in 4 steps:

1. **Born-Oppenheimer approximation:**[62] Because the nuclei have a much larger mass than the electrons, their motion can be considered infinitely slow compared to the electronic motion. As such, it is

possible to separate the nuclear and the electronic part of the wave function. The positions of the nuclei, relevant for their electrostatic attraction of the electrons, enter the electronic Schrödinger equation as parameters generating a static external potential $\hat{V}_{\text{ext}}$. Forces can then be calculated by evaluating the derivative of the energy with respect to the nuclear positions, using the Hellmann-Feynman theorem.

2. **Hohenberg-Kohn theorems:**[50] The external potential $\hat{V}_{\text{ext}}$ is a unique functional of the total ground state electron density. As such, the entire Hamiltonian and all properties can be derived from that density. At this point, Density-Functional Theory (DFT) is born, where the electron density–not the wave function–becomes the central object. This results in a further reduction in complexity, as the density only depends on three spatial coordinates, whereas the electronic wave function depends on the positions of the individual electrons. Because the functional that delivers the ground state energy of the system gives the lowest energy if and only if the input density is the true ground state density, minimizing the energy is a necessary and sufficient condition to find the ground state density.

3. **Kohn-Sham theorem:[51]** The ground state density of an N-electron system can, without any loss of information, be written as

$$\rho_0 = \sum_{i=1}^{N} \phi_i^* * \phi_i. \tag{2.2}$$

where ϕ_i are the single-particle orbitals. Kohn and Sham showed that a hypothetical non-interacting system exists for which ϕ_i constitute the ground-state orbitals. As a result, solving the many-body equation is substituted with solving that surrogate Hamiltonian for N auxiliary single-particle orbitals ϕ_i. The Hamiltonian $\hat{H}_{\text{KS}}$ of this system introduces the exchange-correlation functional $\hat{V}_{\text{xc}}$. Consequently the sum of the kinetic energies of the non-interacting auxiliary orbitals can be used, circumventing the difficulty of obtaining it from the density itself.

4. Finally, the Kohn-Sham orbitals ϕ_i are expanded in terms of a basis set of functions to allow dealing with a continuous function within

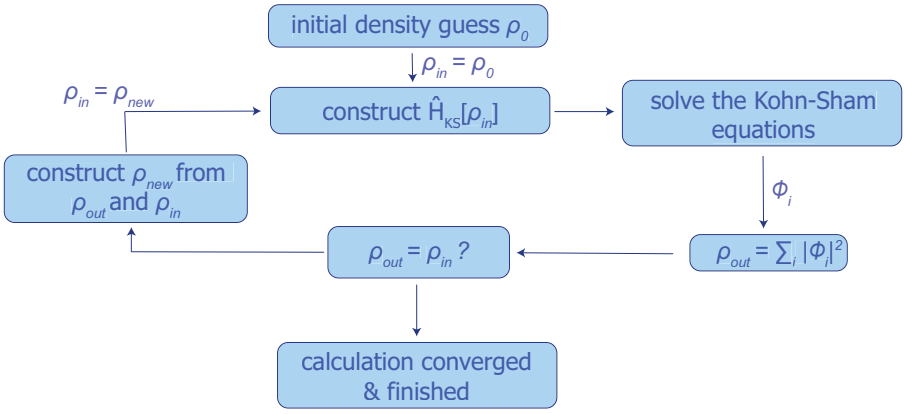

Figure 2.1: Flow chart for a DFT calculation. In each cycle the Kohn-Sham orbitals ϕ_i are calculated, from which a density ρ_{out} can be derived. Each cycle requires an input density ρ_{in} to construct the equations. For the first iteration this is an initial guess ρ_0, for the subsequent iterations a linear combination of the previous ρ_{in} and ρ_{out} is used. After each iteration the new density is compared with the input density. If the energy of these densities is sufficiently close, the calculation is finished.

a numerical calculation. Assuming this basis set is complete, the single-particle differential equations transform to a matrix-form eigenvalue equation, yielding the expansion coefficients of the orbitals and their energy.

To construct the single-particle Hamiltonian functional $\hat{V}_{\text{xc}}$, the electron density is required. However, the density is what we are trying to calculate in the first place. This circularity is tackled by starting with an initial density, from which a new one will be found by solving the Kohn-Sham equations. Using this new density to create an input for a new calculation and repeating the process eventually leads to a point where input and output density are the same. At that point the calculation is self-consistent and the correct density is found (Figure 2.1).

There are two levels of approximation present in a single DFT calculation. One aspect is the presence of numerical errors that result primarily from the choice of the basis set for the Kohn-Sham orbitals. Today, the use of DFT codes in materials science has resulted in a variety of implementations which by now have matured sufficiently towards very small numerical errors as

long as sufficiently stringent settings are used.[63] A second, more important issue, however, is the necessity of an exchange-correlation functional for the Kohn-Sham orbitals. This functional is not exactly known and today there is a large variety of choice available for the materials scientist. In this research, the Perdew–Burk–Ernzerhof parametrization within the Generalized Gradient Approximation is used for the majority of the calculations,[64] unless stated explicitly otherwise. This is for two reasons. First, it is one of the most accurate functionals for describing transition metals in general and in particular the magnetism of ferrite with good accuracy.[65] Second, it is today the most widely used functional in solid state physics.[66] Although this latter point does not imply it is the most reliable functional, it does offer the widest range of possibilities to compare with other computational results.

2.1.2 DFT for crystalline solids

In the case of molecules, the system size is defined by the atomic composition and the resulting number of electrons. The interactions and number of Kohn-Sham orbitals follow directly. Consequently, the functions in the basis sets for molecular DFT are usually centered around the atomic positions. To tackle crystalline solids with DFT, a more intricate computational recipe is necessary. For this, Bloch's theorem is of invaluable use.[67] It states that any eigenfunction $\psi_{\boldsymbol{k}}^{n}(\boldsymbol{r})$ of a periodic Hamiltonian can be expressed in a basis of plane waves:

$$\psi_{\boldsymbol{k}}^{n}(\boldsymbol{r}) = \sum_{\boldsymbol{K}} c_{\boldsymbol{K}}^{n,\boldsymbol{k}} \exp^{i(\boldsymbol{k}+\boldsymbol{K})\cdot\boldsymbol{r}}, \tag{2.3}$$

where n (the band number of the orbital)[67] and k (a vector in the first Brillouin zone)[67] are the quantum numbers that determine the eigenfunction. The summation in equation 2.3 is taken over the infinite set of reciprocal vectors $\boldsymbol{K}$ that adhere to the crystal's translational symmetry. In practice, it is truncated at some point by setting a maximum energy for the plane waves, *i.e.* a cut-off energy. Furthermore, only a finite number of $\boldsymbol{k}$-points are sampled. These two approximations are usually treated in a pragmatic manner: the cut-off energy and number of $\boldsymbol{k}$-points are increased to evaluate their impact on the material and its property that is calculated. Ultimately, they are increased to the point where the calculated result has achieved its desired precision.

Now it is possible to grasp the quantum nature of an infinite crystalline solid on a computational platform. However, near the nuclei, the Kohn-Sham

orbitals ϕ_i oscillate strongly, requiring plane waves with a very high wave number to describe them. The cut-off energy that would be required to capture this behavior near the core prohibits feasible computation times. Moreover, these regions near the nuclei are not of interest for chemical interactions. A large variety of methods have been put forward over the past decades that tackle this problem. Most of the methods that remain today have, by now, matured sufficiently and they are very comparable in performance.[63] In this work, for the majority of the time, the projector-augmented plane-wave method is used as implemented in the Vienna ab initio software package.[68–71] This method uses plane waves for the wave function in the region between atoms, as in equation 2.3. In the neighborhood of the atoms, however, the plane waves are augmented with their projection onto pseudo partial waves, that are able to capture the strong oscillating behavior of the wave functions around the atomic cores (Figure 2.2). In this way, the variable behavior of the wave functions, *i.e.* smooth in the interstitial regions but steep near the atoms, can be described efficiently.

2.1.3 DFT for magnetic systems

So far the Kohn-Sham DFT that was presented assumes that every occupied orbital, is doubly occupied by an electron pair of opposite spin. Using this restriction simplifies a DFT calculation, but in some cases this is too limiting. With every electron paired, no magnetization can occur except for the small orbital magnetization. Obviously, describing iron–let alone steel–with such a restriction is downright incorrect.

Formally, since all possible information of the system can be extracted from the density, a functional of the density exists that renders the magnetization. To actually perform a magnetic DFT calculation, however, it is necessary to adapt the Kohn-Sham single-particle equations. This is done by assuming spin-up single-particle orbitals ϕ_i^+ and spin-down orbitals ϕ_i^-.[73] It follows that all operators in the Kohn-Sham equations are then 2-dimensional tensors. In theory, such a spin-polarized calculation increases the calculation time 8-fold. In practice, however, this can be much more, as the numerical tools utilized to speed up the self-consistent cycle become less powerful. It would be a significant simplification if the operators only had diagonal elements. In that case, the computational load would only be twice that of a regular DFT calculation. This is usually done by assuming collinear magnetism only, in which case there is a transformation that diagonalizes

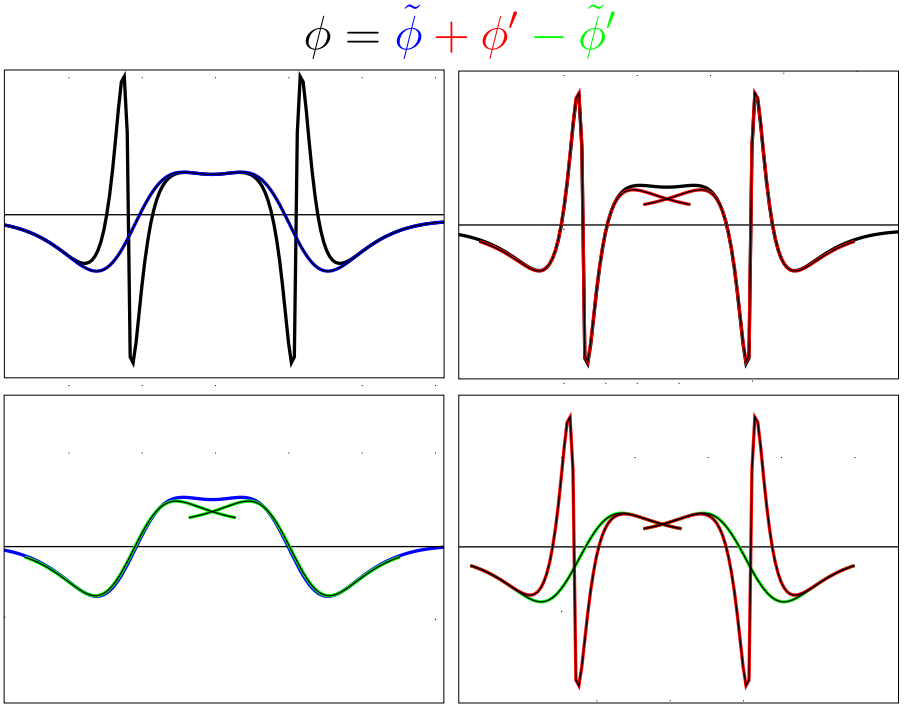

Figure 2.2: One-dimensional schematic of how the Kohn-Sham orbitals are treated around an atom (figure from [72]). The total wave function ϕ is the sum of a smooth wave $\tilde{\phi}$ that extends into the entire solid and a steep function ϕ' that is defined only round the atom (partial wave). A smooth partial wave $\tilde{\phi}'$, only defined around the atom, is subtracted to achieve the correct total wave function.

the operators and identifies a preferential spin direction. The corresponding orbitals are then decoupled and have a different energy. Consequently, it is possible to have a majority spin, resulting in a net magnetic moment. Furthermore, these local magnetic moments inside the unit cell can be associated to the atoms therein present. By setting a sphere around each atom (the Wigner-Seitz sphere) and summing over the magnetic moments inside each sphere, the total magnetization of the unit cell is (in large part) divided across its atoms.

Just as was the case for regular Kohn-Sham theory, the difficulty lies with finding a good approximation for the exchange-correlation functional, which is now dependent on the spin channel. In this work, unless mentioned otherwise, the Perdew-Burke-Ernzerhof (PBE) functional is used, mainly for

the following two reasons:

- As a Generalized Gradient Approximation (GGA), it has the lowest level of complexity which succeeds in predicting the correct magnetic ground state of ferrite. Indeed, the local spin density approximation (LSDA) fails to predict the correct ground state for bcc Fe.[74]

- It has been successfully used to calculate the free energy of ferrite up to 1200 K, including electronic, vibrational and magnetic excitations.[75] This includes the correct prediction of the ferromagnetic to paramagnetic phase transformation, which is vital for a correct description of the magnetic excitations.

2.2 Finite temperatures

DFT, as explained in the previous section (2.1), yields the cohesive energy of a crystal with volume V, the stress on the structure and the forces on its atoms at 0 K. To determine the Helmholtz free energy F of a crystal at a finite temperature T, however, the electronic, vibrational and magnetic excitations need to be taken into account. If a concentration c of impurities are present,[1] their configurational entropy is a required component as well (Section 3.4.2). The common assumption is that these contributions are all adiabatically decoupled, *i.e.* $F(V,T,c)$ can then be written as:[76]

$$F(V,T,c) = F_{\text{el}}(V,T) + F_{\text{vib}}(V,T) + F_{\text{mag}}(V,T) + F_{\text{conf}}(T,c), \qquad (2.4)$$

where F_{el}, F_{vib}, F_{mag} and F_{conf} are the electronic, vibrational, magnetic and configurational contributions, respectively.

Using DFT calculations to analyze and predict phase boundaries has mainly focused on thermodynamic stability at 0 K and pressure-driven phase transitions.[77] Obtaining the free energy at finite temperatures is, however, essential to determine the full phase stability of a material. This requires the explicit inclusion of thermal excitations. Of these, the lattice vibrations are usually the largest. Including this vibrational free energy with DFT has

1. In general, the configurational entropy is determined by the number of all constituents. In this work, however, the configurational entropy of an impurity is always limited to the dilute concentration limit. As such, the entropy is determined by the concentration c of the impurity alone.

enabled a computational description of, for example, the closed-packed to bcc phase transition of Li and the thermodynamic stabilization of Au-Cu alloys.[78, 79] Nowadays, obtaining the vibrational free energy within the quasiharmonic approximation knows widespread use and has become a validated methodology.[80]

For steel applications, the presence of impurities and the magnetic nature of the material present two challenges for obtaining finite-temperature properties. The modeling of the former, with the inclusion of vibrational free energy, requires a large allocation of computational resources, which is in reach of today's supercomputers. Consequently, over the past decade, impurity properties such as the limit of solubility in aluminum–rare-earth alloys have been obtained from DFT calculations.[81] To model the magnetic excitations, there exist a number of different methods which have matured towards practical use over the past decade.[82] This has resulted in the successful derivation of the heat capacity of Fe and Fe_3C using DFT,[54, 55] along with the thermodynamic stability of Fe_3C.[83] The computational description of phase transitions between allotropes of magnetic materials, such as the hcp to fcc transition in Co and the bcc to fcc transition in Fe, have also become more accurate.[84, 85] As such, today the methodology to derive the phase boundaries in the Fe-N system is available and largely validated. In the next sections, we present the specifics of how the thermal excitations are taken into account throughout this work.

2.2.1 Electron temperature

Although DFT was conceived as a ground state theory, it has since been extended to nonzero temperature.[53] Concretely, this means that, for a crystal with N electrons in the unit cell, more than N bands are included in the spin-polarized calculation. The occupation of those bands is determined by the Fermi-Dirac distribution. As such, an electron temperature can be set for the calculation. The electronic contribution $F_{\text{el}}(V, T)$ is obtained from a set of DFT calculations at different volumes and electron temperatures. In our calculations, we first perform an initial optimization of the atomic positions and volume, after which the total energy is calculated for volumes ranging from $94\,\%$ to $106\,\%$ of the initial equilibrium volume and for electron temperatures between $2\,\text{K}$ to $1000\,\text{K}$. Following the approach proposed by Grabowski *et al.*,[86] the electronic free energy is separated into two contri-

butions:

$$F_{\text{el}}(V,T) = E_0(V) + \widetilde{F}_{\text{el}}(V,T). \tag{2.5}$$

The different contributions to $F_{\text{el}}(V,T)$ are subsequently parametrized into an analytical form, which facilitates the derivation of entropy and heat capacity. The energies for the different volumes at the lowest temperature ($T = 2\,\text{K}$) are used to fit the $0\,\text{K}$ volume-dependent behavior $E_0(V)$ to a Birch-Murnaghan equation of state:[87]

$$E_0(V) = U_0 + \frac{9V_0B_0}{16}\left\{B_0'\left[\left(\frac{V_0}{V}\right)^{\frac{2}{3}} - 1\right]^3 + \left[\left(\frac{V_0}{V}\right)^{\frac{2}{3}} - 1\right]^2\left[6 - 4\left(\frac{V_0}{V}\right)^{\frac{2}{3}}\right]\right\}. \tag{2.6}$$

This determines the equilibrium volume, the internal energy U_0 at V_0, bulk modulus B_0 and the derivative of the bulk modulus B_0' with respect to the pressure. For the temperature dependence one uses

$$\begin{aligned}\widetilde{F}_{\text{el}}(V,T) =& \frac{1}{2}Tk_{\text{B}}\left\{\sum_{i=1}^{3}(\alpha_i + V\beta_i)T^i\right\} \\ &\times \int d\epsilon\big[f(T,\epsilon)\ln f(T,\epsilon) + (1-f(T,\epsilon))\ln(1-f(T,\epsilon))\big],\end{aligned} \tag{2.7}$$

which is based on the general electronic entropy [68]

$$\widetilde{F}_{\text{el}}(V,T) \approx -\frac{1}{2}TS_{\text{el}}(V,T) \tag{2.8}$$

and

$$S_{\text{el}}(V,T) = -k_{\text{B}}\int d\epsilon\, N_{\text{el}}(V,T,\epsilon)[f(T,\epsilon)\ln f(T,\epsilon) + (1-f(T,\epsilon))\ln(1-f(T,\epsilon))] \tag{2.9}$$

The function f is the band occupation described by the Fermi-Dirac distribution. The electronic density of states N_{el} is replaced by the energy-independent average

$$N_{\text{el}}(V,T) = \sum_{i=1}^{3}(\alpha_i + V\beta_i)T^i. \tag{2.10}$$

Here, α_i and β_i are six fitting parameters that fully describe the temperature-dependent part of F_{el} and the temperature-induced volume dependence. The linear parametrization in volume combined with the third-order polynomial parametrization in temperature produces a maximum residual error of well below 0.1 meV/atom.

2.2.2 Vibrational excitations

As a material heats up, the kinetic energy of its atoms increases. The Born-von Kármán model assumes the nuclei as the only significant masses in the system, whereby the electrons determine the forces between these nuclei as a function of the interatomic distances. The total potential energy of the solid can then be expanded as a Taylor's series in powers of the atomic displacements $x_{i\alpha}$, where i indicates the atom and α the (cartesian) direction of displacement:[88]:

$$\Phi = \Phi_0 + \sum_{i\alpha} \Phi_{i\alpha} x_{i\alpha} + \frac{1}{2} \sum_{i\alpha,j\beta} \Phi_{i\alpha,j\beta} x_{i\alpha} x_{j\beta} + ... \tag{2.11}$$

with

$$\begin{aligned} \Phi_{i\alpha} &= \frac{\partial \Phi}{\partial x_{i\alpha}} \\ \Phi_{i\alpha,j\beta} &= \frac{\partial^2 \Phi}{\partial x_{i\alpha} \partial x_{j\beta}} \\ &= \frac{\partial F_{j\beta}}{\partial x_{i\alpha}} \end{aligned} \tag{2.12}$$

Within harmonic lattice dynamics, each displacement of an atom generates a force F on all atoms that is linearly proportional to the displacement. This means equation 2.11 is truncated after the second order term. Because the potential energy is determined up to a constant, Φ_0 can be set to zero. Furthermore, if all atoms are in mechanical equilibrium, the first derivatives, *i.e.* the forces on these atoms, are zero as well. As such, only the second order terms enter the equations of motion:

$$m_i \frac{\partial^2 x_{i\alpha}}{\partial t^2} = -\frac{\partial \Phi}{\partial x_{i_alpha}} = -\sum_{j\beta} \Phi_{i\alpha,j\beta} x_{j\beta} \tag{2.13}$$

For a solid, these form a practically infinite set of linear differential equations. However, these are simplified by the periodicity of the lattice which implies Bloch waves as solutions to this equation. For a wave vector $\boldsymbol{k}$ these eigenmodes are then found by diagionalizing the dynamical matrix with elements

$$D_{i\alpha,j\beta}(\boldsymbol{k}) = \frac{1}{\sqrt{m_i m_j}} \sum_l \Phi_{i\alpha,j\beta l} \exp^{i\boldsymbol{k}\cdot(\boldsymbol{r}_{jl}-\boldsymbol{r}_i)} . \tag{2.14}$$

Where m are the masses and $\boldsymbol{r}$ the positions of the atoms, respectively. Now, the indices α and β are restricted to the unit cell and the index l is used to sum over all unit cells in the entire solid. As such, the matrix has dimensions $3R \times 3R$, where R is the number of atoms in the unit cell. For each wave vector $\boldsymbol{k}$ there are thus $3R$ eigenmodes with each a positive eigenvalue $\omega_i^2(\boldsymbol{k})$ of the mode.

In quantum mechanics, these elementary vibrational motions are associated with quasiparticles called phonons. In a harmonic approximation, the phonons can be superimposed indefinitely and, as such, they can be regarded as a collection of single harmonic oscillators. It follows that the temperature-dependent vibrational free energy of the periodic crystal then becomes:

$$F_{\text{vib}}(T) = \frac{1}{N_{\text{ph}}} \sum_{i=1}^{N_{\text{ph}}} \left\{ \frac{1}{2}\hbar\omega_i + k_{\text{B}} T \ln\left[1 - \mathrm{e}^{-\hbar\omega_i/k_{\text{B}}T}\right] \right\}, \tag{2.15}$$

where $\hbar$ is Planck's constant, k_{B} Boltzmann's constant and ω_i are the angular frequencies of the oscillators. The summation is taken over all phonons (N_{ph}).

The atomic force constants $\Phi_{i\alpha,j\beta l}$ are obtained using DFT calculations where the displacement $x_{i\alpha}$ is introduced. Theoretically, the sum in equation 2.14 is infinite. However, if for each displacement $x_{i\alpha}$ a large enough supercell is constructed, the force responses $\Phi_{i\alpha,j\beta}$ are sufficiently attenuated for the summation to be precise. Typically, this means a separation of $7 - 12\,\text{Å}$ of the periodic images, which corresponds to supercells of the order of 100 atoms. For the construction of these supercells, which involves setting up all symmetrically inequivalent displacements in the reference unit cell, the software package Phonopy is used.[89] For each displacement, a DFT calculation is performed using VASP. Afterwards, constructing the dynamical matrix and determining its eigenvalues for the desired values of $\boldsymbol{k}$ is done with phonopy again.

With the DFT-obtained frequencies, it is now possible to determine the free energy of the crystal using equation 2.15. All that is left, is to determine

the limits of the summation. In principle, this sum is a combination of an integral across all $\boldsymbol{k}$ in the first Brillouin zone and a discrete sum over the $3R$ eigenvalues for each $\boldsymbol{k}$. In practice, the eigenvalues are determined for a large but discrete number of $\boldsymbol{k}$, densely sampling the first Brillouin zone, which makes calculating equation 2.15 feasible.

The above derivation of the free energy is limited to a harmonic approximation of the force response. To try and recover a part of the *an*harmonic contributions to the vibrational free energy, it is possible to take the phonon approach one step further. The lattice vibrations in this work are included using the quasiharmonic approximation. To account for thermal expansion, phonon spectra are computed for volumes relevant to the thermal expansion; *i.e.* ranging from $99\,\%$ to $106\,\%$ of the equilibrium volume. The volume-dependent frequencies $\omega_i(V)$ thus obtained are used to calculate the vibrational free energy:[76]

$$F_{\text{vib}}(V,T) = \frac{1}{3\tilde{N}} \sum_{i=1}^{3\tilde{N}} \left\{ \frac{1}{2}\hbar\omega_i(V) + k_{\text{B}}T \ln\left[1 - \mathrm{e}^{-\hbar\omega_i(V)/k_{\text{B}}T}\right] \right\}. \quad (2.16)$$

Here, $\tilde{N}$ is the number of sampled points in reciprocal space multiplied by the number of atoms in the unit cell. The volume-dependent behavior of each frequency from the different phonon spectra is fitted to a quadratic function of volume. This use of a second-order polynomial is sufficient to limit the maximum residual error to 0.01 THz for all frequencies. Even for the smallest frequencies, this results in an error below $1\,\%$ for the vibrational free energy.

2.2.3 Magnetic excitations

Most of the materials in this work are magnetically ordered. As the electron temperature increases, this order is broken and the material becomes paramagnetic, no longer exhibiting a macroscopic magnetization. The temperature at which this transition occurs is called the Curie temperature and the free energy increase associated with this excitation yields a significant contribution to the total free energy.

Directly calculating magnetic free energies with DFT is not yet possible. Instead, utilizing an atom-centered model for the magnetic moments has

proven to be a successful approximation for iron and its alloys. More specifically, the Heisenberg model will be used as magnetic Hamiltonian:[55, 75, 90–95]

$$H = -\frac{1}{2}\sum_{i\neq j} J_{ij}\, \boldsymbol{M}_i \cdot \boldsymbol{M}_j \tag{2.17}$$

The sum in Eq. 2.17 is taken for all atom pairs in the solid, with M_i the local magnetic moments and J_{ij} the Heisenberg exchange coupling parameters. The former are easily obtained from DFT calculations, as explained in Section 2.1.3, but the J_{ij} require a somewhat more involved derivation. There are multiple ways of obtaining the coupling parameters. In this work, they are derived from DFT calculations based on a spin-polarized relativistic version of the Korringa-Kohn-Rostoker Green's function method,[96, 97] as implemented in the the SPR-KKR software.[98, 99] This framework allows direct access to the J_{ij} using the formulation of Liechtenstein *et al.*,[100] with only one surplus calculation necessary for each crystal structure.

To determine $F_{\text{mag}}(T)$ from Eq. 2.17, classical Metropolis Monte Carlo (cMC) calculations are performed with the ALPS software.[101–103] To do this, the sum in equation 2.17 is truncated at a threshold for the J_{ij}. This truncation is determined by evaluating the convergence of the mean-field Curie temperature as a function of the threshold value. The mean-field Curie temperature is equal to the largest eigenvalue of the coupling parameters matrix **J** with[104]

$$\mathbf{J}_{\alpha,\beta} = \sum_{\beta_i} J_{\alpha,\beta_i} \boldsymbol{M}_\alpha \cdot \boldsymbol{M}_{\beta_i} \tag{2.18}$$

Here, α and β are atoms in the crystallographic unit cell and β_i are all the periodic images of the atom β for which a J_{ij} has been calculated. Now, a finite form of the Hamiltonian (equation 2.17) is available to perform the Monte Carlo simulations. Each simulation is performed at a given temperature, and the heat capacity at that temperature is derived from the cMC calculations via the fluctuation-dissipation theorem.[105, 106]

The use of cMC, in which the magnetizations in Eq. 2.17 are not quantized, only approximates the correct quantum mechanical result. However, performing Quantum Monte Carlo (QMC)[107] for frustrated systems is generally infeasible because of the negative sign problem.[108] To approximate

the correct heat capacity, the cMC results can be transformed according to the scaling proposed by Körmann *et al.*:[54]

$$\frac{C_{\mathrm{V,QMC}}(t,S)}{C_{\mathrm{V,cMC}}(t,S)} \approx \left(\frac{2t_{\mathrm{s}}/t}{\exp(t_{\mathrm{s}}/t)-\exp(-t_{\mathrm{s}}/t)}\right). \tag{2.19}$$

Here, t is the normalized temperature $T/T_{\mathrm{C,cMC}}$, where the cMC Curie temperature is determined by the peak in the heat capacity $C_{\mathrm{V,cMC}}$, and

$$1/t_{\mathrm{s}} \approx 0.54S + 0.54, \tag{2.20}$$

where S is the localized spin. For a system with more than one atom in its unit cell, the average S is used. Finally, the rescaled heat capacity can be numerically integrated to obtain the entropy and free energy. The latter is fitted to a function of the form

$$F_{\mathrm{mag}}(T) = A\exp(B/T) + CT^4, \tag{2.21}$$

where A, B and C are fitting parameters. This ensures interpolation errors smaller than 0.1 meV/atom. F_{mag} is 0 at $0\,\mathrm{K}$ because the energy of the ferromagnetic ordering is contained in the DFT calculations.

2.2.4 Combining all contributions

The methodology described in this section is summarized into the applied work flow (Figure 2.3) to achieve the total free energy $F(V,T,c)$. Both F_{vib} and F_{elec} have an explicit volume dependence, as these are the results of DFT calculations performed at multiple volumes. For F_{mag}, a different approach is utilized. First, the equilibrium volume $V_0(T)$ with $F = F_{\mathrm{vib}} + F_{\mathrm{elec}}$ is calculated:

$$\left.\frac{\partial F(V,T)}{\partial V}\right|_{V=V_0} = 0, \tag{2.22}$$

The most significant contributions to F_{mag} are found around the Curie temperature, where there is a peak in heat capacity. To minimize the error at these conditions, the J_{ij} are therefore recalculated at the volume associated with T_{C}, obtained from Eq. 2.22. This is done in an iterative way, until a self-consistent T_{C} is reached (Fig 2.3). For numerical stability, the derivative of F_{mag} with respect to volume is not included in the optimization.

The methodology described in this section does not take into account explicit anharmonic contributions or electron-phonon coupling. These are deemed to be of negligible magnitude, because our temperature range of interest lies below half of the melting temperature for the materials that were studied.[109, 110] The magnon-phonon coupling contributions were not taken into account either. This can potentially lead to larger uncertainties, especially for Fe_4N, which has a Curie temperature of around 750 K. Indeed, in the paramagnetic state the force response and thus, the vibrational properties of the material can differ significantly with respect to the ferromagnetic state. For ferrite, for example, it was shown that some phonon branches are softened by as much as 10 meV.[111]

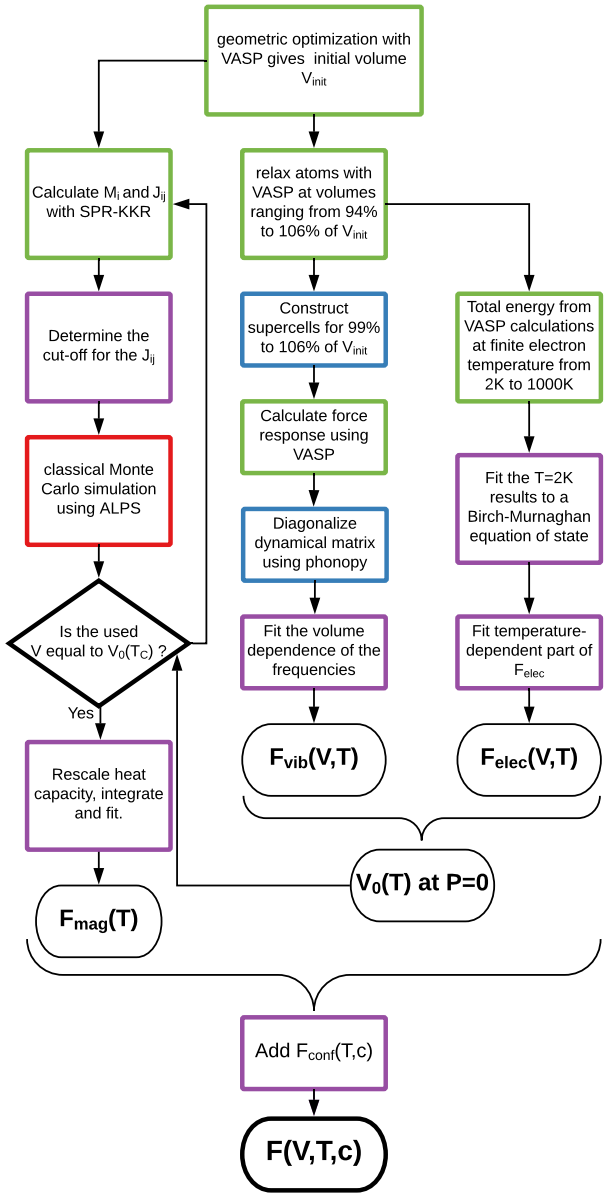

Figure 2.3: Flowchart indicating the different calculations performed to obtain the free energy. Green indicates a DFT calculation, red an ALPS simulation, blue indicates use of the phonopy software and purple is for standard post-processing.

3

The binary Fe-N system: thermodynamics from DFT

3.1 Introduction

As introduced in section 1.3, the cooling of ferrite with nitrogen in solid solution can introduce secondary phases in the ferrite matrix, which impact the mechanical properties of the material. This chapter investigates their thermodynamic properties, focusing on low nitrogen concentrations ($< 1\,\text{at.}\%$) and temperatures below the ferrite-austenite temperature ($< 865\,\text{K}$). At these conditions, Fe_4N and $Fe_{16}N_2$ are known to precipitate. Fe_4N tends to occur for slower cooling rates, as it forms above $500\,\text{K}$, whereas at lower temperatures $Fe_{16}N_2$ precipitates (Figure 1.11).[28]

Thermodynamic properties such as the heat capacity and the thermal expansion are essential to describe the iron-nitrides in large-scale approaches, such as phase field models,[49] but they require the knowledge of free energies for each phase. Previous derivations of the free energy for Fe_4N were based on solvus lines in the phase diagram[112] or the cluster variation method (CVM) combined with the Debye-Grüneisen model.[113] In contrast to such (semi-)empirical methods, using density-functional theory (DFT) provides a non-empirical approach for modeling the iron-nitrides.[50, 51] This avoids the process of extrapolating phase stability from narrow temperature ranges and provides insight into the relative

stability of Fe with nitrogen in solid solution ($Fe_{[N]}$), Fe_4N and $Fe_{16}N_2$ from 0 K up to 1000 K. On the other hand, the complexity and size of crystal structures that are feasible to tackle with DFT calculations are limited. Consequently, this work is restricted to the line compounds Fe_4N and $Fe_{16}N_2$ and does not take into account the disorder associated with possible off-stoichiometries.[40, 114]

The driving forces for the precipitation are the differences in free energy between the Fe-N phases. These are obtained using DFT calculations as described in Chapter 2. The first step in the evaluation of these thermodynamic DFT-derived data is the accurate calculation of the binary phase diagram. The presence of $Fe_{16}N_2$ into the thermodynamic comparison already highlights one of the main motivations for performing such an analysis with DFT: $Fe_{16}N_2$ is a metastable phase and, in reality, only occurs as a nanosized precipitate in the ferrite matrix. It is therefore very challenging to measure properties such as heat capacity, magnetization or thermal expansion. Because in a DFT calculation a single infinitely large crystallographic phase can be modeled, its quantities become readily available through the work flow described in Chapter 2.

3.2 Technical details

All calculations of F_{el} were performed with the Vienna Ab Initio Simulation Package (VASP), [68, 69] using VASP 5.4 recommended PAW potentials.[70, 71] For the Fe atoms, the PAW potential with 8 valence electrons was used ([Ar] $3d^6$ $4s^2$), while for N the potential with 5 valence electrons was used ([He] $2p^3$ $2s^2$). These potentials were recently shown to provide a similar precision as all-electron calculations. [63] The Perdew-Burke-Ernzerhof (PBE) exchange-correlation functional was used in most cases,[64] but the local density approximation (LDA) as parametrized by Perdew and Zunger[115] was, where useful, evaluated as well. The Brillouin zone integration grid always contained at least $27\,648/N_{\text{atoms}}$ $\boldsymbol{k}$-points, with N_{atoms} the number of atoms in the unit cell. Fermi smearing, with the smearing parameter σ determined by the required temperature (Section 2.2.1), was used for the electronic self-consistent field cycle with a convergence criterion of 10^{-9} eV. A conjugate-gradient algorithm was used for the geometric optimization with a convergence criterion of 10^{-8} eV. An energy cutoff of 500 eV was used for the plane wave basis sets, with the grid for fast Fourier transform able to capture reciprocal vectors twice as large as the vectors included in the

basis set. These numerical settings ensured a computational precision of at least 0.5 meV/atom.

The phonon spectra were constructed using the direct force constant method (Section 2.2.2).[116] Various supercells with atomic displacements of 0.01 Å were set up using the phonopy software package.[89] The forces in response to the displacements were calculated with DFT using VASP. Compared to the calculations of F_{el} an additional support grid was used for the augmentation charges. Moreover, instead of Fermi smearing, first-order Methfessel-Paxton smearing with $\sigma = 0.2$ eV was used for electronic convergence.[117] The simulated supercells were made large enough so that the minimum distance between periodic images was at least 11 Å. The diagonalization of the dynamical matrix was performed with the phonopy software again,

SPR-KKR version 6.3 was used with the PBE functional to compute the Heisenberg coupling parameters (Section 2.2.3). The atomic-sphere approximation was applied. The number of E-mesh points was 40 for all calculations with a minimum E-value of -0.2 Ry. The Brillouin zone integration was performed on a $57 \times 57 \times 57$ grid for bulk Fe, a $36 \times 36 \times 36$ grid for Fe_4N and $25 \times 25 \times 25$ grid for $Fe_{16}N_2$. The structure constants R_{max} and G_{max} were set to 2.9 $a.u.$ and 3.3 $a.u.^{-1}$ respectively. The electronic self-consistent field cycle had a convergence criterion of 10^{-5} Ry.

The ALPS classical Monte Carlo calculations were performed with cluster updates for temperatures ranging from $2\,\text{K}$ to $1000\,\text{K}$ or higher, with the maximum temperature always exceeding T_C by at least $10\,\%$ to accurately determine the maximum in the magnetic heat capacity. Periodic boundary conditions were used with a unit cell size of 1000 atoms for Fe, 2560 for Fe_4N and 2250 for $Fe_{16}N_2$. The nitrogen atoms were never accounted for in the Heisenberg Hamiltonian, because their magnetic moments, and hence the coupling parameters with neighbors, were negligible. For initial thermalization, $30\,000$ MC steps were needed. The production phases contained $1\,500\,000$ MC steps for all materials.

3.3 Evaluation of the calculated thermodynamic properties

Because of their limited temperature range of stability and the inability to manufacture isolated specimens, there is very little thermodynamic data available for the Fe_4N and $Fe_{16}N_2$ compounds, especially for the latter. Apart

from free energies and heat capacities (Section 3.3.1), we have therefore also calculated structural properties, thermal expansion and bulk moduli (Section 3.3.2), which we have validated with the limited available experimental data where possible. The magnetic contribution to the heat capacity is evaluated separately in Section 3.3.3. Finally, the free energies of both phases are compared and the phase equilibrium between them is discussed in Section 3.3.4.

3.3.1 Free energy and heat capacity

The calculated free energies and heat capacities are shown in Figure 3.1 for all three bulk phases at their equilibrium volume at zero pressure. The vibrational, electronic and magnetic contributions are plotted separately to indicate their size. The temperature-dependent equilibrium volumes at zero pressure are obtained by minimizing the free energy for each temperature in the range of $0 - 1000\,\mathrm{K}$. This temperature interval was chosen because it is the most relevant for nitriding ferritic steels. [47]

To assess the accuracy of the DFT-derived free energy of ferrite, it is compared to the data derived from experimental phase equilibria and thermochemical properties.[118] These experimental and our DFT free energies are set equal at room temperature ($298\,\mathrm{K}$). The accuracy of the DFT prediction is very good, with a difference of less than 0.1 meV/atom up to $750\,\mathrm{K}$. This confirms the correctness of the methodology, which was previously used to obtain the various contributions to the free energy for Fe and Fe_3C.[54, 55] The excellent accuracy is also the main argument for utilizing the same approach for Fe_4N and $Fe_{16}N_2$. As can be seen in Figure 3.1a, for the free energy of ferrite a somewhat more significant discrepancy starts to occur beyond $850\,\mathrm{K}$, leading to a difference in F of 6 meV/atom between theory and experiment at $1000\,\mathrm{K}$. This is because the quasiharmonic approximation often overestimates anharmonic contributions to the free energy, which typically become important at about half of the melting temperature.[109] For the phase equilibria with Fe_4N and $Fe_{16}N_2$, temperatures above $850\,\mathrm{K}$ are not relevant, and the overestimation of the anharmonic contributions poses no problem.

For ferrite, ample experimental data for the isobaric heat capacity C_P are available over its entire range of stability. Comparing experimental data[119] with calculated results shows a very good correspondence up to $800\,\mathrm{K}$ (Figure 3.1d). For higher temperatures, towards the Curie temperature T_C, where the transition between the ferromagnetic and the paramagnetic

state occurs, the heat capacity is somewhat underestimated.

For all three phases, the contribution of the electronic entropy to the free energy is the smallest. For Fe, it amounts to a contribution of 4 meV/atom at $750\,\mathrm{K}$, which is nevertheless much larger than the inaccuracy of 0.1 meV/atom at that temperature. This shows the importance of taking all three excitations into account for all materials. For Fe_4N the magnetic contribution to the heat capacity and free energy are larger than for bulk Fe. In contrast, $Fe_{16}N_2$ has a smaller magnetic heat capacity because this material is predicted to have the highest Curie temperature.

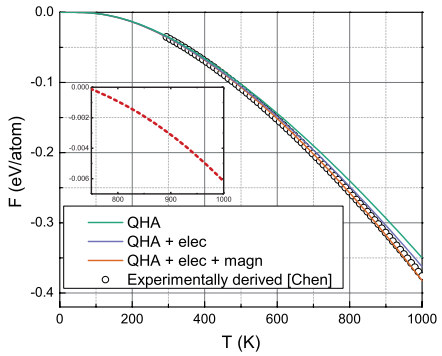

(a) Free energy of Fe

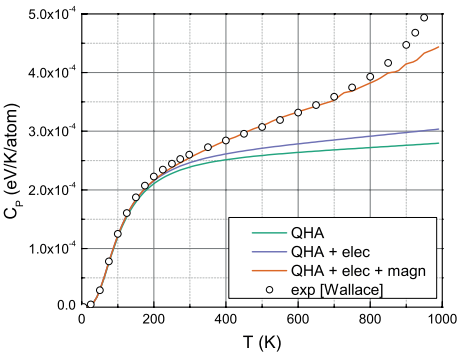

(d) Heat capacity of Fe

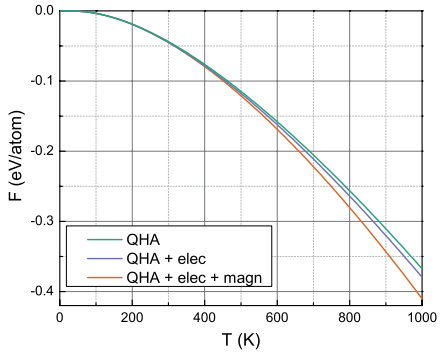

(b) Free energy of Fe_4N

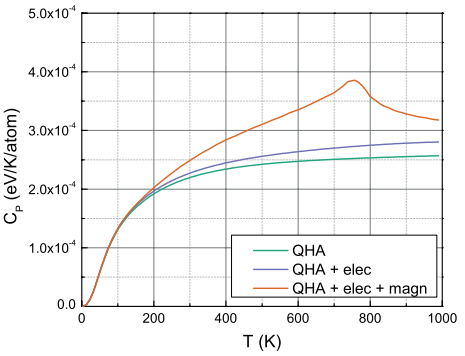

(e) Heat capacity of Fe_4N

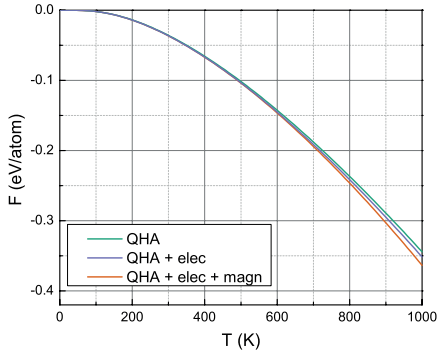

(c) Free energy $Fe_{16}N_2$

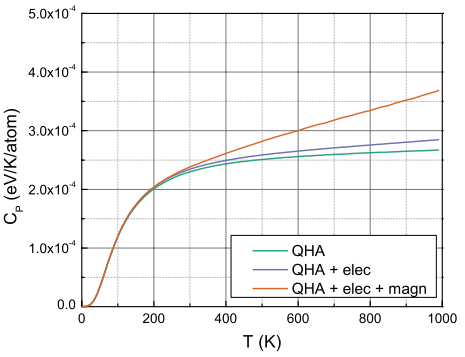

(f) Heat capacity of $Fe_{16}N_2$

Figure 3.1: The free energies F [left, (a)-(c)] and isobaric heat capacities C_P [right, (d)-(f)] of the bulk phases Fe, Fe_4N and $Fe_{16}N_2$ from 0 to 1000 K. The vibrational contributions within the quasiharmonic approximation (QHA), the electronic contributions (elec) and the magnetic contributions (magn) are shown incrementally. For ferite, the free energy is compared to the one experimentally derived by Chen *et al.*[118] and the heat capacity is compared to the one recommended by Desai.[119] Inset in a: The difference between the total calculated free energy and the experimentally derived free energy.

3.3.2 Elastic properties

The (volumetric) thermal expansion coefficient is defined as

$$\alpha_V = \frac{1}{V}\left(\frac{\partial V}{\partial T}\right)_P . \tag{3.1}$$

It can be calculated from the derived equilibrium volumes using finite differences over sufficiently small temperature intervals (10 K), using finite differences. In Figure 3.2 this calculated coefficient is shown for Fe, Fe_4N and $Fe_{16}N_2$ as a function of temperature.

The DFT expansion coefficient of bulk Fe compares very well with experimental data, certainly considering the typical error of $0.7\times10^{-5}\,K^{-1}$ for expansion coefficients derived with QHA.[121] The slight bump in the experimental coefficient that is not accounted for in the DFT result, stems

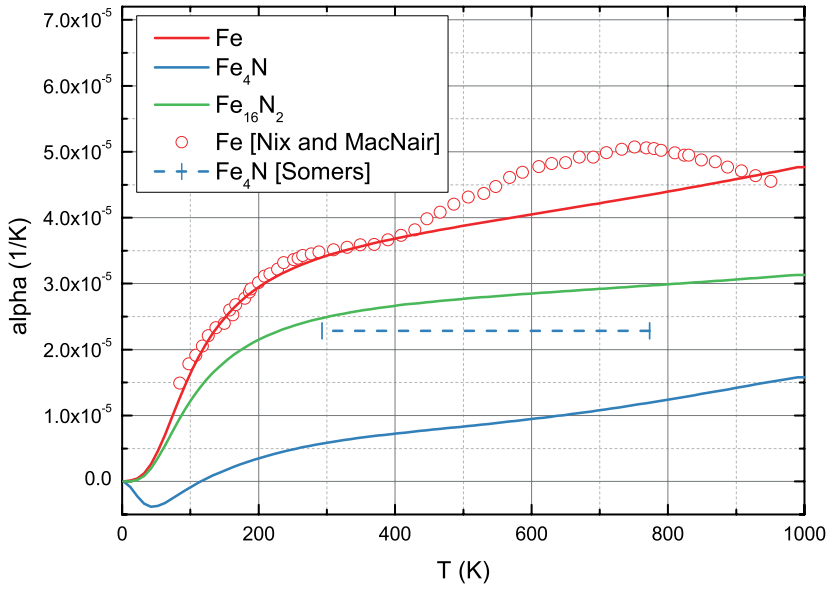

Figure 3.2: DFT-calculated volumetric thermal expansion coefficients of Fe (red), Fe_4N (blue) and $Fe_{16}N_2$ (green). For ferrite, the experimental data from Nix and MacNair enable a comparison for almost the entire temperature interval.[120]. For Fe_4N, there is only an average expansion coefficient between 293 and 773 K available. At all temperatures, however, the DFT-derived expansion coefficient for Fe_4N constitutes a severe underestimation.

from the volume dependence of the magnetic heat capacity,[120] which is not taken into account in the calculations.

In the case of Fe_4N, an average expansion coefficient was derived experimentally from XRD measurements on powder samples.[40] It is seen that the DFT-obtained expansion severely underestimates that experimental one. Possibly, inaccuracies might be present in the experimental measurement because it was taken on a powder sample created from a deposited layer, whereas the calculated expansion is valid for an infinitely large bulk. Because the difference between experiment and DFT is so large, however, a critical assessment of the calculated result is needed to identify the various sources of theoretical inaccuracies.

The argument made for bulk Fe, that the volume dependence of the magnetic heat capacity is not accounted for in the QHA method as employed in this work, can be made for Fe_4N as well. This might be even more pronounced since it has a lower Curie temperature; $T_C = 750\,K$ compared to $1044\,K$ for ferrite.[122] However, the error with respect to the experiment is so large that it cannot be solely explained by such a minor magnetic effect, which is usually secondary to lattice vibrational effects. If the deviation cannot be attributed to the thermodynamic approach, it must be rooted in the calculated energies and forces. For DFT calculations, the exchange-correlation functional is the main source of deviations from experiment. In this case, the main cause of the large deviation of the PBE functional in predicting the thermal expansion of Fe_4N is most likely the material's unique magneto-volume behavior. A large increase in magnetization occurs close to the equilibrium volume, which PBE is unable to describe well.[123], This volume-dependent magnetic effect can be explained by the covalent nature of the Fe-N bond. As the bond length shortens, the overlap of the $2p$ orbitals of the N atom with the $4s$ orbitals of the nearest-neighbor Fe atoms increases, causing more electron transfer to the N atom.[124] This in turn reduces the screening effect of the $4s$ shell on the $3d$ Fe electrons, causing electron transfer from the $3d$ orbitals of the second nearest-neighbor Fe atoms to those of the Fe atoms nearest to the N atom. Ultimately, compression thus results in a lower magnetic moment on the nearest-neighbor Fe atoms that bond with the N atom.[125] It moreover causes the Fe_4N to be very rigid in the direction of the Fe-N bond, *i.e.* the $< 100 >$ direction.[126]

In an effort to verify that the functional is indeed the source of the discrepancy of the Fe_4N thermal expansion coefficient with respect to

experiment, the PBE exchange-correlation functional was swapped for the LDA one. The latter functional differs from PBE in that it positions the LDA equilibrium volume of Fe_4N in the low-magnetization regime rather than at the crossing between low and high magnetization.[123] As can be seen in Figure 3.3, the LDA functional does produce a much larger thermal expansion compared to the PBE functional. As expected, the experimental value lies between the LDA and PBE predictions, but the difference between them is much larger than for metals without any covalent character.[80] Although the observed inaccuracy of the Fe_4N thermal expansion might also be due to experimental errors, the large impact of the exchange-correlation functional on the calculated expansion coefficient remains a methodological problem. At this point, it is not clear whether there is another functional or another (feasible) level of theory that can provide a better description of both the covalent nature of the Fe-N bond, the unique magnetic behavior of Fe_4N and the $Fe_{16}N_2$ and bulk Fe phases.

Note that the large discrepancy between LDA and PBE regarding the volume-dependent behavior is not reflected in the QHA free energy. The LDA and PBE free energy only differ by about 3 meV/atom at $400\,\mathrm{K}$, which implies that phase stabilities are much more accurately obtained than the thermal expansion.

The temperature-dependent bulk modulus, or inverse of the compressibility,

$$B(T) = V_0 \left(\frac{\partial^2 F}{\partial V^2} \right)_T \Bigg|_{V=V_0} \tag{3.2}$$

can be directly obtained from the above results and the derivatives of the analytic expressions for the various contributions to the free energy (Eqs. 2.7-2.16). In Figure 3.4 the bulk modulus is shown for all three phases. As far as Fe is concerned, the calculated bulk modulus at $0\,\mathrm{K}$ is too high by about 15 GPa compared to experimental data. This is in contrast to the typical trend for PBE, which usually underestimates bulk moduli by about 5%.[129] On the other hand, it is typical for magnetic materials to buck this trend, as a generalized-gradient approximation (GGA) such as PBE tends to overestimate the magnetic energy.[130] The slope of the Fe bulk modulus is reproduced quite well, with the experimental one being overall slightly less steep compared to the DFT result. Much fewer data are available on bulk moduli for Fe_4N and $Fe_{16}N_2$, because these phases usually only exist as precipitates or as a deposited layer. In fact, there are no experimental data for $Fe_{16}N_2$ whatsoever and the experimentally determined bulk

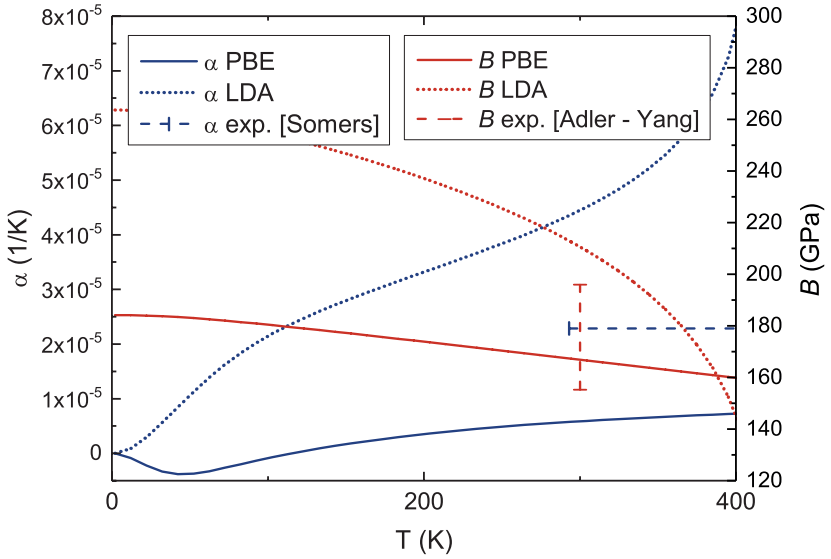

Figure 3.3: A comparison between LDA (dotted lines) and PBE (solid lines) for the calculation of the bulk moduli B (red) and volumetric thermal expansion coefficients α_V (blue) of Fe_4N. For the bulk modulus, a large range of experimental values exists (dashed red bar).[127, 128] For the thermal expansion, the value determined by Somers *et al.* is an average for the temperature range 293 to $773\,K$.[40]

moduli that are available for Fe_4N have a large spread (Figure 3.4). A possible reason for these large experimental deviations, is the difference in measurement methodology. It varies from nanoindentation to high-pressure X-ray diffraction (XRD) measurements, both on powdered samples and on bulk-like samples.[127, 128, 131] The combination with the difficulty of obtaining pure samples makes it very cumbersome to compare different experimental procedures. The calculated Fe_4N bulk modulus falls in the range of the experimental values. The strong dependence on temperature moreover confirms the volume-sensitive behavior of Fe_4N compared to the other two materials. Just as was the case for the thermal expansion, this volume-sensitive behavior causes a large discrepancy between the LDA and PBE functionals (Figure 3.3).

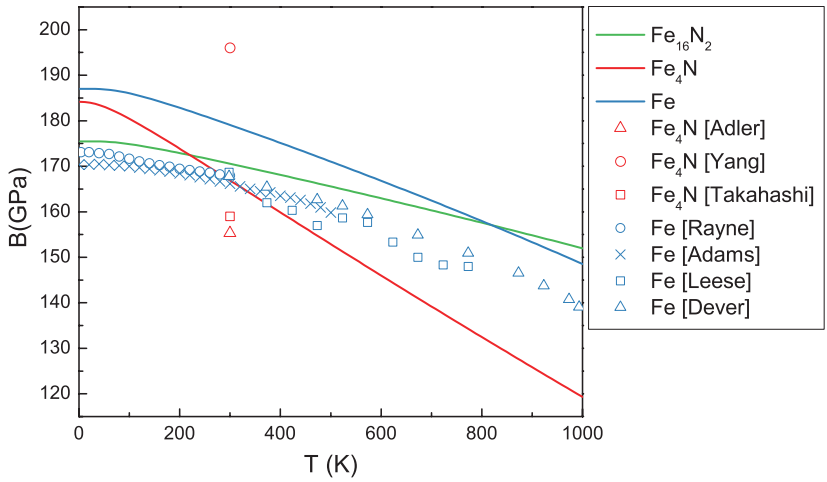

Figure 3.4: DFT-calculated (line) and experimental (symbol) bulk moduli B for Fe, Fe_4N and $Fe_{16}N_2$. For Fe, a combination of data from different authors is made to cover the temperature range from 0 to $1000\,\mathrm{K}$.[132–135] For Fe_4N, the three experimental data points are all at room temperature and cover a relatively large range (red symbols).[127, 128, 131]

3.3.3 Magnetic properties

The magnetic contribution to the free energy is significant, even at temperatures well below the Curie temperature (Figure 3.1), and thus requires a high degree of accuracy. It was found that this high accuracy can be reached through the rescaling procedure of Körmann *et al.* (Section 2.2.3), provided the Curie temperature is predicted accurately.[54] For this reason, effective nearest-neighbor magnetic exchange coefficients J_{ij} are sometimes fit to the experimental Curie temperature to obtain the magnetic heat capacity.[55, 136] This work, however, aims to use a methodology also able to predict the Curie temperature. Therefore, the J_{ij} were determined from first principles and the Curie temperature was identified as the temperature at which the resulting heat capacity reaches its peak.[137] The quality of the predicted Curie temperature is then a measure for the accuracy of the magnetic free energy.

For Fe and Fe_4N, the DFT-derived Curie temperature (Figure 3.5) corresponds very well with the experimental one. It is evident that the disappearance of the magnetization in the simulation is a poor measure to determine the transition to the paramagnetic state. The finite size of the simulation

cells is responsible for some remanent magnetization above the critical temperature. This remanent magnetization, however, is an experimental issue as well.[138] For $Fe_{16}N_2$ the experimental Curie temperature is much lower than the one derived from the simulations. The experimental magnetization goes to zero when $800\,\mathrm{K}$ is reached, but with the exchange coefficients and magnetization derived from DFT, a critical temperature of about $1300\,\mathrm{K}$ is found. In an extensive evaluation of different methods to obtain the Curie temperature for $Fe_{16}N_2$, Ke *et al.* concluded that the experimental value is most likely significantly too low. [139] Instead, it is proposed that $Fe_{16}N_2$ has a higher Curie temperature than the one experimentally derived and also higher than the one found for Fe. For this reason, unfilled symbols are used to show the experimental results for the magnetization of $Fe_{16}N_2$ in Figure 3.5.

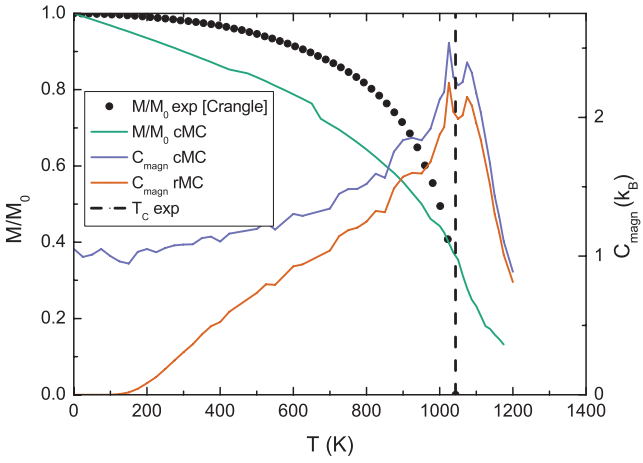
M/M0 exp [Crangle]
M/M0 cMC
Cmagn cMC
Cmagn rMC
TC exp
M/M0
Cmagn (kB)
T (K)

(a) Fe

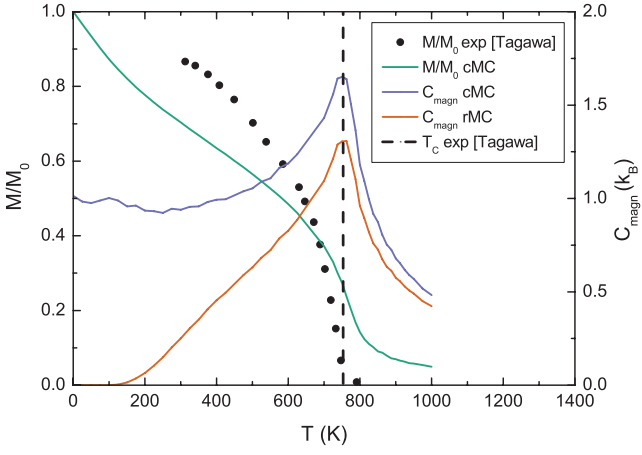
M/M0 exp [Tagawa]
M/M0 cMC
Cmagn cMC
Cmagn rMC
TC exp [Tagawa]
M/M0
Cmagn (kB)
T (K)

(b) Fe_4N

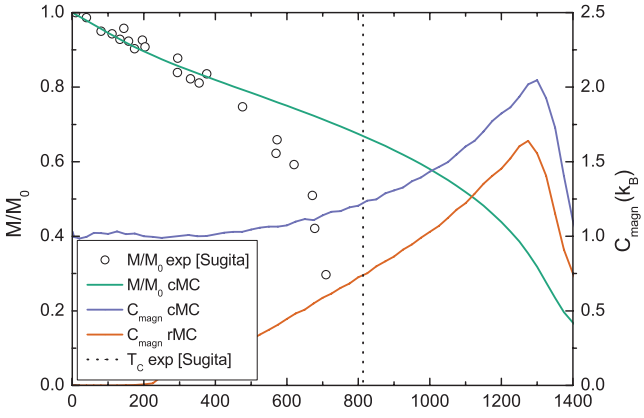

(c) $Fe_{16}N_2$

Figure 3.5: Calculated magnetization (M/M_0) and magnetic contribution C_{magn} to the heat capacity for Fe, Fe_4N and $Fe_{16}N_2$. Experimentally measured magnetizations and subsequently derived Curie temperatures are included for all three phases (black).[122, 140, 141] The experimental data for the magnetization of $Fe_{16}N_2$ are shown in unfilled circles to emphasize their problematic nature (see text). To compare the experimental magnetizations with those derived from the classical Monte Carlo (cMC) simulations, both are normalized to their respective magnetizations at $0\,K$. For the heat capacity, both the direct result from the cMC simulations (blue) and the rescaled result (rMC)(red) are presented, the latter serving as approximation for the quantum Monte Carlo result.

3.3.4 Equilibrium between $Fe_{16}N_2$ and Fe_4N

The question of the (meta)stability of $Fe_{16}N_2$ is still a contemporary topic.[142] The transformation governing the stability is:

$$Fe_{16}N_2 \leftrightarrow A\ Fe_4N + B\ Fe_{[N]}. \tag{3.3}$$

If one assumes the transformation takes place in a large environment of bulk Fe with interstitial N present in equilibrium concentration c_{lim} (see further), the coefficients must fulfill the conditions

$$\begin{aligned} 4A + B &= 16 \\ A + Bc_{\text{lim}} &= 2 \end{aligned} \tag{3.4}$$

The driving force ΔF for the formation of $Fe_{16}N_2$ from Fe_4N and $Fe_{[N]}$ is then

$$\Delta F(T) = F_{Fe_{16}N_2}(T) - \frac{2 - 16c_{\text{lim}}}{1 - 4c_{\text{lim}}} F_{Fe_4N}(T) - \frac{8}{1 - 4c_{\text{lim}}} F_{Fe_{[N]}}(T, c_{\text{lim}}), \tag{3.5}$$

The free energy difference can be obtained from the calculated free energies at equilibrium volumes V_0 in this work and is presented in Figure 3.6. We find that $Fe_{16}N_2$ is stable at low temperatures ($\Delta F < 0$) and decomposition becomes energetically favorable above $390\,\text{K}$ ($\Delta F > 0$). This is consistent with the experimental finding that decomposition starts between $470\,\text{K}$ and $520\,\text{K}$. The experimentally higher decomposition temperature is explained by the required activation energy for N diffusion.[139, 143] In experiment too, there is an indication that $Fe_{16}N_2$ becomes thermodynamically unstable around $400\,\text{K}$, *i.e.* before decomposition occurs. The temperature-dependent change in c/a-ratio, measured very precisely by Widenmeyer *et al.*,[143] shows a sharp rise starting from $400 - 450\,\text{K}$ (Figure 3.6). Widenmeyer *et al.* proposed that this stems from a loss of order of the N atoms on the interstitial sublattice of $Fe_{16}N_2$, thus suggesting a transition to a disordered Fe_8N phase. As shown in Figure 3.6, the temperature-dependent QHA $c/a-$ratio, derived from the $c/a-$ratio of the cell optimized at the temperature-dependent equilibrium volume, is practically invariant with temperature. This strengthens the argument that the experimentally observed variation is caused by loss of N ordering, as the N-atoms were kept ordered on their sublattice in the calculations. It also sheds a new light on the experimentally derived Curie temperature for $Fe_{16}N_2$.[144] The

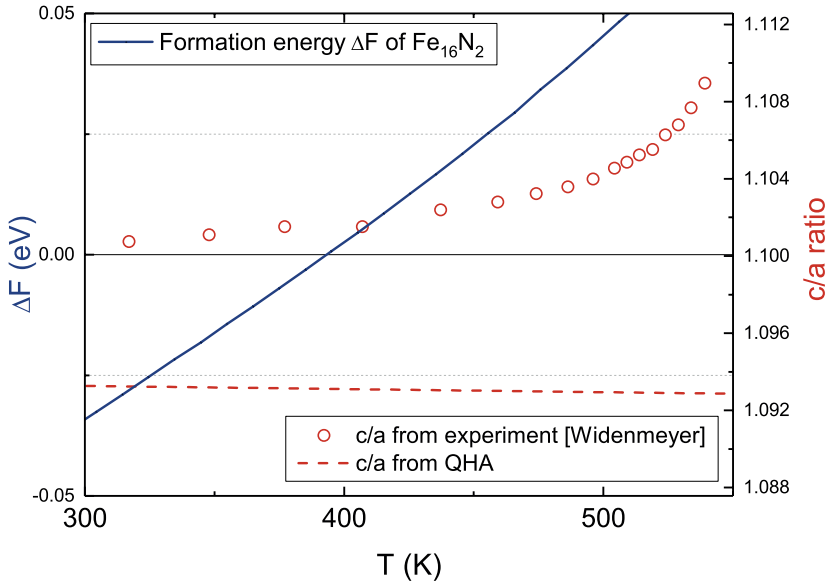

Figure 3.6: Left axis (blue): from the DFT calculations, it can be concluded that $Fe_{16}N_2$ becomes thermodynamically unstable with respect to dissociation into Fe_4N and bulk Fe (solid line) above $390\,K$. Right axis (red): a comparison of the experimental c/a ratio of $Fe_{16}N_2$ (circles)[143] with the one derived via the quasiharmonic approximation (dashed line). The sharp increase starting at 400-$450\,K$ measured in experiment is not observed computationally (see text for interpretation).

measured drop in magnetization becomes more pronounced from $400\,K$ onward (Figure 3.5), the point where $Fe_{16}N_2$ becomes thermally unstable according to the DFT result. Consequently, the magnetizations measured above $400\,K$, and the derived Curie temperature, should be associated with the disordered Fe_8N structure.

3.4 Constructing the phase diagram

The most important validation of the DFT-obtained free energies is the comparison with the experimental phase diagram. More precisely, we focus on the phase stability between the ferrite matrix with nitrogen in solid solution on the one hand, and Fe_4N and $Fe_{16}N_2$ on the other hand. In other words, we are calculating the limit of solubility of nitrogen in ferrite. Along with the free energies of Fe_4N and $Fe_{16}N_2$ that are already discussed

in section 3.3.1, the energy of the nitrogen atom as an impurity in iron is required as well.

3.4.1 An impurity in the solid at 0 K

The energy of interstitial nitrogen is obtained using the supercell method. In this approach, the crystallographic unit cell of the bulk material is multiplied and a nitrogen atom is inserted. In the case of the nitrogen interstitial, a N atom is inserted in the bulk Fe supercell on an octahedral position (see Figure 1.10). The local distortion caused by the nitrogen atom is captured by optimizing all atomic positions. Thus, the goal of the supercell method is to model an isolated impurity, *i.e.* the dilute concentration limit. It is debatable whether the volume and shape of the supercell should be optimized as well. On the one hand, maintaining the bulk geometry helps to isolate the impurity from its periodic images, as it cuts out long-range elastic interactions. However, this imposes a stress on the supercell which depends on the N concentration. On the other hand, if one wishes to remove those stresses by allowing full optimization of the shape and size of the unit cell, a larger computational investment might be necessary. Both approaches were evaluated for different supercell sizes. The energy of solution U_{sol} is obtained by subtracting the DFT-obtained total energy of the impurity-free supercell and the isolated N_2 molecule from the total energy of the supercell with the nitrogen impurity. In Figure 3.7 the dependence of U_{sol} on the used supercell size is shown. It shows that the constant-pressure (stress-free) and constant-volume approach converge towards a common limit, ultimately yielding the same energy as supercell size is increased. Using a 250-atom supercell for either method a precision of the calculation of about 10 meV/impurity can be achieved for U_{sol}. The 250-atom $U_{\text{sol}} = 0.133\ eV$ of the constant-volume approach was used in the remainder of this work, because that approach converges somewhat more rapidly.

3.4.2 Free energy of the impurity

The contribution of the nitrogen interstitial is not limited to U_{sol} alone. Describing the phase equilibrium between Fe_4N, $Fe_{16}N_2$ and $Fe_{[N]}$ requires accounting for the entropy of as well. For ferrite with nitrogen in solid solution, the configurational contribution as a function of the N concentration c must be taken into account as well. The $Fe_{[N]}/Fe_4N$ and $Fe_{[N]}/Fe_{16}N_2$ phase equilibria lie in the nitrogen concentration regions below 1 at.%.[23]

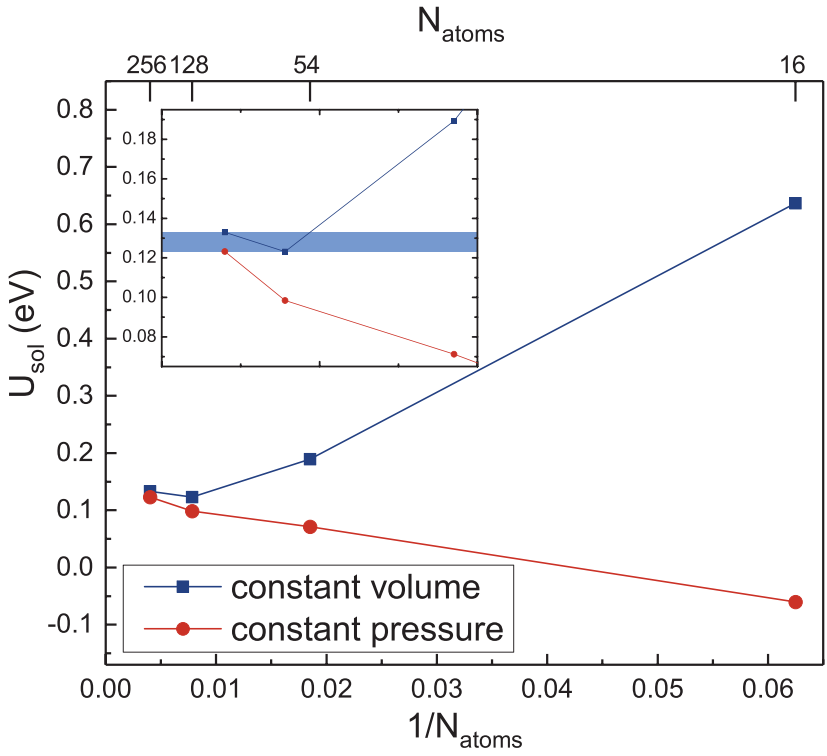

Figure 3.7: Convergence of the N interstitial energy at $0\,\mathrm{K}$ as a function of inverse supercell size. The absolute value of the energy is with reference to the N_2 gaseous state: $Fe_{solid} + \frac{1}{2}N_2 \rightarrow Fe_{[N],solid}$. Inset: The convergence for the larger supercells in more detail. A residual uncertainty of $10\,\mathrm{meV/impurity}$ remains (blue rectangle).

Consequently, F_{conf} can be calculated from the configurational entropy for a dilute solution:[145]

$$F_{conf}(T, c) = -T k_B \left[c - c\ln(c) + c\ln(g)\right], \tag{3.6}$$

where k_B is the Boltzman constant, c is the nitrogen concentration and $g = 3$ the number of interstitial sites per host atom. In Figure 3.8 the configurational contribution is shown to be largest, but both the vibrational and the electronic entropy have to be taken into account as well. The electronic part can be obtained in a similar way as for bulk materials. For the vibrational contribution, full phonon spectra are calculated for the supercells containing the impurity and QHA is used. Because the presence of the N atom in the Fe matrix breaks most of the symmetry, a large number of force

calculations is then necessary to obtain the phonon spectra. Alternatively, the less expensive partial Hessian method can be used, which only requires the frequencies of the N atom in a fixed Fe matrix. The three frequencies obtained can be used to apply a simplified form of Eq. 2.16. From Figure 3.8 it can be seen the differences between feasible supercell sizes are still quite large. An uncertainty of 0.2 eV/impurity remains for a 54-atom cell, which is as large as for the partial Hessian method that is also not sufficiently precise. This large uncertainty is not surprising; it is the same order of magnitude as for U_{sol} (see Figure 3.7).

We have chosen to use the largest supercells possible for both U_{sol} (250 atoms) and the finite-temperature contributions (128 atoms). Ultimately, by using a highly converged U_{sol} from a 250-atom cell and the vibrational and electronic entropies from a 128-atom supercell, one expects a remaining uncertainty of 10 meV/atom for the vibrational contribution. Combined with the uncertainty for U_{sol} (10K), this results in a total uncertainty of $14 - 20$ meV/atom.

3.4.3 Limit of solubility

With the free energies of Fe, Fe_4N, $Fe_{16}N_2$ and $Fe_{[N]}$, all information is available to predict their phase equilibria, resolving the experimental uncertainties that have hindered insight and further development of the Fe-N system.

To complete the phase diagram for $Fe_{[N]}$, Fe_4N and $Fe_{16}N_2$, the concentration limit of solubility $c_{\text{lim}}(T)$ can be derived from the free energy of the N interstitial F_{imp}, the free energy of Fe, the free energy of Fe_4N and the free energy of $Fe_{16}N_2$:

$$4F_{\text{Fe}}(T) + F_{\text{imp}}(T, c_{\text{lim}}(T)) = F_{\text{Fe}_4\text{N}}(T). \tag{3.7}$$

$$16F_{\text{Fe}}(T) + 2F_{\text{imp}}(T, c_{\text{lim}}(T)) = F_{\text{Fe}_{16}\text{N}_2}(T). \tag{3.8}$$

The final phase diagram, with all three phase equilibria, is presented in Figure 3.9. The computationally derived solubility limit of N in bulk Fe is compared to the experimental data assembled by Wriedt *et al.*[23]. In the case of the solvus, good correspondence with experimental data is achieved by using the impurity free energy from the 128-atom supercell. The large discrepancy with the 54-atom thus shows the importance of using this larger

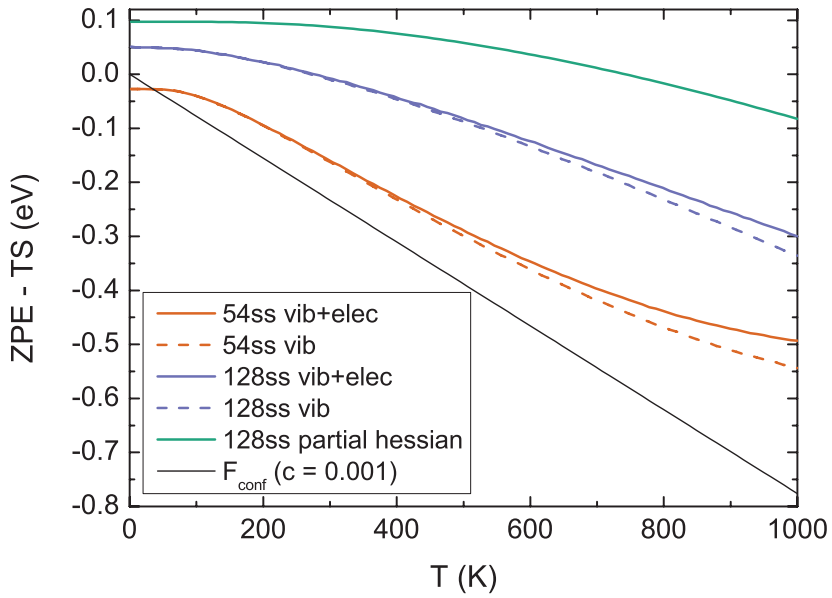

Figure 3.8: A comparison of the different methods to obtain the finite-temperature energetic contributions for N in solid solution in Fe. The configurational part, shown here for a typical concentration of 0.1 at.$\%$ is always the largest, but both the electronic and vibrational free energies cannot be neglected. In comparison with the 128-atom supercell, the simple partial Hessian approach (see text) yields frequencies that are overestimated, whereas a 54-atom supercell underestimates the frequencies.

supercell. For the phase boundary between $Fe_{16}N_2$ and its dissociation in Fe_4N and bulk Fe, no experimental data are available, but the accuracy is expected to be very high. As discussed in Section 3.3.1, the free energy for Fe is very accurate below half of its melting temperature. Because of the similarity of Fe_4N and $Fe_{16}N_2$ and the correct calculation of the Curie temperatures, the same is expected for these bulk phases.

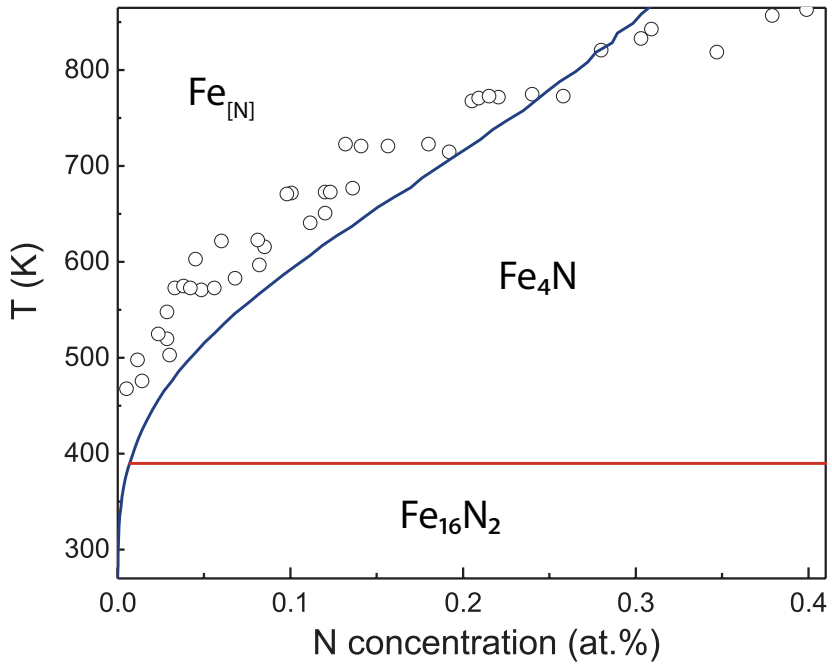

Figure 3.9: The DFT-obtained phase diagram of $Fe_{[N]}$, Fe_4N and $Fe_{16}N_2$. Experimental data for the limit of solubility of N in Fe are included for comparison (circles).[23]

3.5 Conclusion

Despite the industrial importance of nitriding for the post-treatment of steel, there is still a lack of understanding with respect to the properties of the governing Fe-N phases. In this chapter, the DFT-obtained free energies of $Fe_{16}N_2$, Fe_4N and Fe with N in solid solution were used to elucidate the Fe-N phase diagram in the low-nitrogen limit. From the free energy, the heat capacity, thermal expansion and bulk modulus were derived, which provided further insight into the thermal behavior of these phases. This is particularly useful for Fe_4N and $Fe_{16}N_2$, for which large homogeneous samples are not experimentally available and deriving these quantities experimentally is challenging at best.

The methodology to obtain the full free energy provides accurate results for ferrite (section 3.3.1), with a difference of less than 0.1 meV/atom up to 750 K. The only significant sources of inaccuracy are the (volume-independent) anharmonic contributions and the sharp increase of the heat capacity around the magnetic phase transition. In our temperature range of interest,

below 865 K, these inaccuracies are very small. The thermal expansion coefficient for ferrite is reproduced quite accurately as well, but for Fe_4N, a strong underestimation of the experimental result is found (section 3.3.2). A comparison of the LDA and PBE exchange-correlation functional revealed that the unique coupling between magnetism and crystal volume increases the sensitivity to the functional inadequacies. A better description of the volume dependence of Fe_4N therefore requires the development of improved exchange-correlation functionals that are able to capture both the covalent and magnetic characteristics correctly. This is in line with the conclusion from Blancá *et al.*[123]

For ferrite and Fe_4N, the calculated Curie temperature corresponds to the experimental one, but this was not the case for $Fe_{16}N_2$ (section 3.3.3). On the contrary, we concluded that the experimentally established Curie temperature for $Fe_{16}N_2$ cannot be attributed to the pure $Fe_{16}N_2$ phase, but is affected by the experimentally observed loss of nitrogen order between 400 and 450 K. This is also supported by a comparison between experimental measurements of the c/a-ratio as a function of temperature and our quasiharmonic DFT results.

Based on DFT-calculated free energies, the phase diagram of $Fe_{[N]}$,Fe_4N and $Fe_{16}N_2$ could be constructed, yielding an accurate representation of the nitrogen solvus and providing a closer view on the stability of $Fe_{16}N_2$ (section 3.3.4). We find $Fe_{16}N_2$ to be thermodynamically stable at low temperatures and to decompose into Fe_4N and Fe around 390 K. Experimental dissociation happens above 470 K, with the difference attributed to the required activation energy for nitrogen mobility. In addition, we note that the largest error bar originates from the supercell size used to model the free energy of interstitial nitrogen; this error is about $14 - 20$ meV/impurity at 0 K using a 128-atom supercell.

Three main takeaways can be distilled from this chapter:

1. Our results fill in a long-standing gap in the knowledge on the Fe-N system. The free energies of the Fe_4N and $Fe_{16}N_2$ phases were determined and used to quantify the metastability of $Fe_{16}N_2$.

2. The methodology used to derive the free energies from DFT has been validated and it can now be applied to ternary Fe-N-X compounds (Chapter 4).

3. The predicted free energies, heat capacities, equilibrium volumes and bulk moduli can now be used in larger-scale approaches, such as phase field models.[49] These approaches can aid in describing precipitation.

4

Introducing ternary elements in the $Fe_{16}N_2$/Fe_4N equilibrium

4.1 Introduction

For through-thickness nitriding, improving strength and fatigue resistance of the bulk material are the main goals. The addition of nitrogen into ferritic steels can induce precipitation hardening through the formation of nitrogen-containing secondary phases in the ferrite matrix.[25, 35] The thermodynamic balance between these precipitating phases, Fe_4N and $Fe_{16}N_2$, which was computationally derived in Chapter 3, is crucial for the formation of precipitates from the iron-nitrogen matrix. Indeed, it has been shown that both phases are part of a precipitation chain, whereby the formation of $Fe_{16}N_2$ precedes the formation of Fe_4N.[35, 41] As such, the dissociation energy of $Fe_{16}N_2$ is the driving force in the final step towards precipitation of Fe_4N. Precipitation hardening is, however, very much dependent on precipitate number and size.[146, 147] In the case of the binary Fe-N system, where both Fe_4N and $Fe_{16}N_2$ precipitate in the ferrite matrix, only the latter results in significant precipitation hardening.[38, 146] The Fe_4N particles are generally too large and consequently too sparse to significantly impede dislocation movement. Consequently, stabilizing the small $Fe_{16}N_2$ precipitates can further their strengthening effects on the material. We aim to search for possible (meta)stable ternary compounds in

the Fe_4N (γ') and $Fe_{16}N_2$ (α'') crystal structures[1] by substituting Fe for an alloying element. Thus, the goal is to identify those ternary elements that can stabilize the α'' precipitates.

First, in **step 1** we will identify which ternary compounds can form in the α'' and γ' crystal structures out of ferrite, interstitial nitrogen and an additional alloying element in solid solution by calculating the energies of formation (E_f) at $0\,K$ using DFT. For this, the thermodynamic reference state for the solutes must be correctly modeled. Both the ternary alloying elements and the interstitial nitrogen impurity are supposed to be in dilute solid solution. This is modeled with the supercell method, similar to the methodology presented in Section 3.4.1 Additionally, in **step 2**, to understand whether the ternary elements in solid solution can inhibit nitrogen diffusion or affect the solubility of nitrogen in the matrix, the pairwise interaction of nitrogen and the ternary element is calculated as well. This analysis is performed for alloying elements most commonly used in steel production. Attractive interactions between the solutes can lead to trapping or an increase in the solubility; Mn and V, for example, are known to immobilize nitrogen in such a way.[148] Finally, in **step 3**, temperature is taken into account by calculating the free energy for the ternary compounds showing both α'' and γ' formation and that are of interest from a metallurgical perspective. The methodology presented in Chapter 2, and successfully applied in Chapter 3, will be used to obtain the needed contributions to the free energy. From these free energies, the goal is to identify those ternary compounds that have the potential to swing the balance in the precipitation of the α'' structure in favor of the γ' structure, which was shown to lie around $400\,K$ (Chapter 3) for the binary Fe–N system.

In the next section (Section 4.2), we present a brief overview of the most important alloying effects known in iron-nitrogen steels. The methodology that is needed in each step of our research is presented in section (Section 4.3). First, we discuss the details of in-depth investigation of the $0\,K$ DFT calculations and the free energy calculations. Then, the study set selection is presented; *i.e.* which calculations will be performed for which ternary elements. Subsequently, for each ternary alloying element the results are presented in Section 4.4. At that point, interesting ternary compounds are discussed with respect to possible improved precipitation.

1. From here, the symbol α'' indicates a general $Fe_{16-2y}X_{2y}N$ ternary compound with alloying element X and the symbol γ' is used for a general compound $Fe_{4-x}X_xN$

4.2 The role of ternary elements in nitrided steels: background

When commercial alloys are used for nitriding, the interaction of the alloying elements with nitrogen can have a number of different effects. The most important is the formation of stable binary nitrides, which occurs for most early transition metals.[149] Most notable are Ti, V, Cr and Mo, which can form both XN and X_2N (X=Ti,V,Cr,Mo) precipitates during nitriding.[150] Because of the volume misfit between the nitrides and the ferrite matrix, these precipitates can produce a significant increase in hardness and fatigue resistance, especially if they are small and numerous.[151, 152] However, a lattice dilation occurs in the matrix surrounding the precipitate which in turn stabilizes interstitial nitrogen , resulting in excess nitrogen.[153, 154] This increased concentration of nitrogen enlarges the driving force for precipitation of iron-nitrides upon cooling, which can result in large (and undesired) Fe_4N precipitates. Moreover, the misfit at the matrix/precipitate interface creates a preferential occupation site for nitrogen, resulting in a second source of excess nitrogen. Manganese can combine with nitrogen and form Mn_6N_5, increasing the material's hardness.[25] However, Mn_4N is a stable compound as well,[155] which is ferrimagnetic and has a high Curie temperature,[156] making it a potentially interesting electrode material.[157] The addition of Mn can also result in a complex ferrite-austenite duplex structures, stemming from the austenite–stabilizing effects of Mn, yielding improved mechanical properties.[155]

Apart from the transition metals, Al and Si, two common substitutional impurities in ferritic steel, can interact with nitrogen as well. Aluminum can form incoherent AlN precipitates with a hexagonal crystal structure, or coherent precipiates with a cubic crystal structure, depending on the mechanical treatment.[158] As is the case for Ti, V, Cr and Mo, excess nitrogen is generated by lattice distortion.[159] For a sufficient supersaturation of nitrogen in the ferrite matrix, silicon forms nitrides as well. In contrast to the other nitrides discussed in this section, the silicon nitrides are amorphous, although they exhibit a fixed stoichiometry of Si_3N_4.[155]

There is a limited amount of experimental information on ternary Fe-X-N nitrides. Most of the research on the formation of ternaries has been focused on the γ' and α'' crystal structures, where a ternary element substitutes for Fe. In this respect, the inclusion of Ni into the γ' structure

has received much attention. A multitude of $Fe_{1-x}Ni_xN$ compounds have been synthesized[160–163] This results in a decrease in magnetization and Curie temperature.[163] Moreover, the addition of Ni improves the mechanical ductility of the brittle Fe_4N compound.[162] This has resulted in further experimental interest and synthesis of Fe_3PtN,[160] Fe_3OsN, Fe_3RuN and Fe_3IrN[164]; electronic structure calculations investigated Fe_3RhN,[165], Fe_3CoN,[166], Fe_3PdN, Fe_3MnN and Fe_3SnN.[167] Less attention has been given to possible ternary compounds in the α'' crystal structure. It was shown experimentally by Wang *et al.* that it is possible to stabilize the α'' phase in films by adding Ti.[168] From electronic structure calculations, Benea *et al.* concluded that Ti preferentially substitutes the Fe lattice sites nearest to the N atoms in the α'' crystal structure.[169] Further theoretical research has highlighted the potential of Mn or Co addition in $Fe_{16}N_2$ thin films towards magnetic applications,[139, 170] but very little is mentioned regarding the stability of these phases.

4.3 Methodology: Work flow for the screening of ternary compounds

4.3.1 Energy of formation for ternary phases

I. The γ' crystal structure

For the γ' crystal structure (Figure 4.1), when restricting to the conventional unit cell, there are 6 different ternary crystals possible when substituting one or more Fe atoms for a ternary element X (Table 4.1). In **step 1**, for each of these 6 phases, as well as for the binary phase X_4N, the 0 K energy of formation is obtained using DFT. In addition, the energy of formation of Fe_4N was already calculated in Chapter 3. From those data, combined with the nitrogen impurity energies (Section 4.3.2), it is possible to conclude whether the alloying element X can form a ternary phase with Fe and N within the γ' crystal structure that is stable with respect to decomposition into Fe with nitrogen and the element X in solid solution. Note that this analysis does not yield a sufficient condition for formation, as a stabilizing energy of formation at $0\,$K will still be in competition with the configurational entropy of the substitional impurity in solid solution.

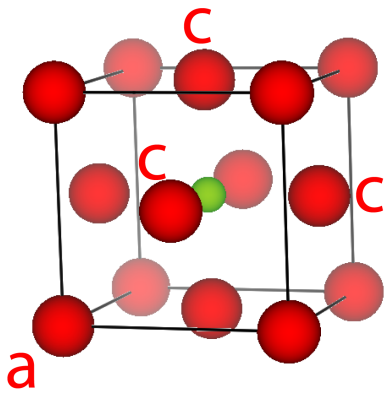

Figure 4.1: The Fe_4N unit cell. The indicated Fe sites a and c are possible locations for replacement with a ternary element.

stoichiometry	X at site(s)	name
Fe_4N	N/A	0
Fe_3XN	a	I.A
	c	I.C
Fe_2X_2N	a and c	II.AC
	2 × c	II.CC
FeX_3N	3 × c	III.A
	a and 2 × c	III.C
X_4N	N/A	IV

Table 4.1: List of possible stoichiometries and their respective configurations. Each of the 8 structures is given a name, which is used throughout this work.

II. The α'' crystal structure

The primitive unit cell of $Fe_{16}N_2$ contains 9 atoms. There are thus many more different stoichiometries and configurations to form ternary compounds in this crystal structure compared to the γ' one. Instead of the brute force approach applied for the γ' structure, we opted to utilize a shortcut that only evaluates structures that are likely to be the most stable ones for a given stoichiometry. The cluster expansion (CE) method presents us with a tool to make this preselection.[171–173] In this method, a physical property of a crystal, *e.g.* its total energy E, is expanded using a basis set of atomic clusters. The coefficients are called effective cluster interactions (ECIs) ϵ. For the CE energy, the expressions is thus

$$E^{\mathrm{CE}} = \epsilon_0 + \sum_i \epsilon\sigma_i + \sum_{i,j} \epsilon_{ij}\sigma_i\sigma_j + \sum_{i,j,k} \epsilon_{ijk}\sigma_i\sigma_j\sigma_k + \dots \qquad (4.1)$$

where the σ_i are the variables indicating the occupation at each site. For example, in our $Fe_{16-y}X_yN_2$ phase, $\sigma_i = -1$ could indicate an Fe atom at lattice site i and $\sigma_i = 1$ would indicate an X atom at that site. The ECIs are derived from fitting to DFT-calculated energies for varying configurations. Today, optimized protocols are available to efficiently select the configurations to be included in the fitting procedure, minimizing their number while resulting in an as precise CE model as possible. In Figure 4.2,

the outline of such a fitting procedure is presented.[174] An initial small set of clusters is gradually expanded until an adequate model is obtained. This model can predict the energy of structures that have not been put through DFT calculations. For each stoichiometry, one thus obtains a set of structures, whereby the most stable structure is called the ground state structure (Figure 4.3). For each stoichiometry, the ground state structure and those close to it in energy are calculated with DFT, to obtain a more accurate energy of formation.

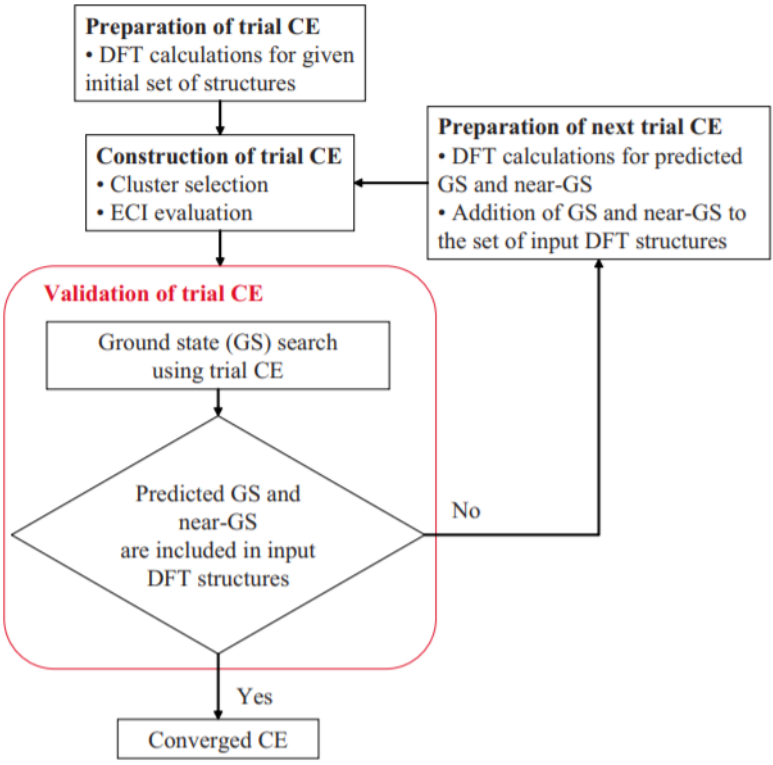

Figure 4.2: Flow chart depicting the fitting of a CE model. Clusters are added in an iterative fashion to the fitting process until adequate precision and prediction of the most stable structures is obtained. (Image taken from Seko *et al.*)[174]

Whereas a CE model is most often generated to perform Monte Carlo simulations with the aim to derive thermodynamic properties of a disordered lattice, our use of the model stops at the identification of the most stable structures. For this, we use the fitting procedures present in the

Alloy-Theoretic Automated Toolkit (ATAT).[175–177] For each substitutional impurity that we considered, a CE model was used to expedite the search for the most stable ternary compound.

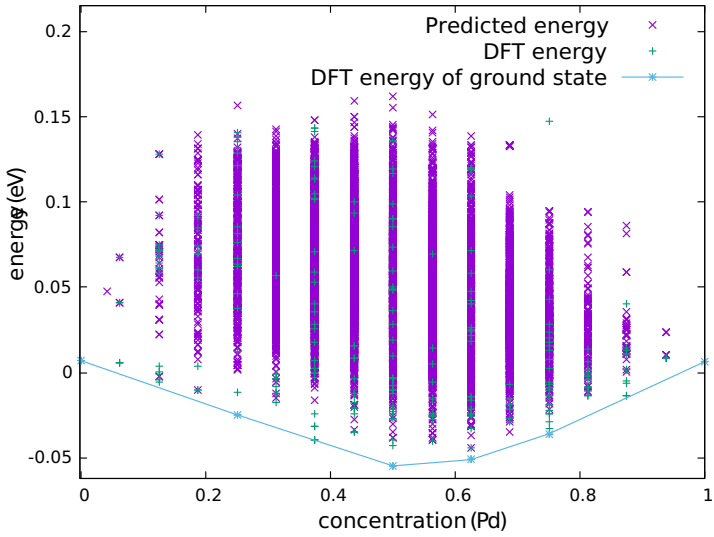

Figure 4.3: DFT and CE-predicted energies (eV per atom) for Pd-containing compounds in the α'' structure for increasing substitution of Fe for Pd.

4.3.2 Impurities in ferrite and their interactions

The thermodynamic reference states for the formation of the ternary compounds are bulk ferrite, nitrogen as impurityin ferrite and a ternary alloying element as substitutional impurity, also in the ferrite matrix. This represents a ferritic material without any secondary phase particles and all alloying elements X in solid solution, from which possible ternary compounds can form:

$$Fe_{\alpha} + X_{sol} + N_{sol} \rightarrow \text{Fe-X-N} \tag{4.2}$$

Ferrite and the nitrogen impurity were extensively treated in Chapter 3 and those results are used in this chapter. The supercell approach, which was used in Section 3.4.1 to describe the nitrogen impurity in dilute concentrations, is once more applied to model the substitutional impurity

as well.

The choice of supercell size in which to embed the impurity can have a large impact on the calculated energy of solution. Larger cells increase the distance and interaction between the periodic images, but come at a computational cost that rapidly makes calculations unfeasible. Furthermore, because numerical errors per atom increase for increasing supercell size, there often is a residual uncertainty on the energy of solution that cannot be resolved. In the case of the nitrogen impurity, this amounted to 10 meV/impurity, one of the largest uncertainties in the computationally predicted Fe-N phase diagram (Section 3.4.1). In this chapter, the supercells of 250 atoms were used as the reference state for the solute atoms. To estimate the size of the supercell model uncertainty for ternary solutes, however, we calculated all substitutional energies of solution in ferrite cells of 54 128 and 250 atoms. The evolution of the (absolute) error for increasing supercell size is shown in Figure 4.4, relative to the largest supercell size of 250 atoms. For most alloying elements, a decrease in the error is observed for increasing supercell size. An average uncertainty of 17 meV/impurity remains. The worst-performing elements are mostly the 5d elements. For these, the average error for the 128-atom supercells is 20 meV/impurity, whereas for all the other elements, that error is 15 meV/impurity. In that last category, Ti, Al, Ag and Zr and Nb show the largest errors with an average of 38 meV/impurity for a 128–atom cell.

The supercell size of 128 atoms is used to calculate the interaction between nitrogen and a ternary substitutional solute in **step 2**.[2] For most elements the supercell error at 128 atoms is acceptably small. Throughout the remainder of this chapter, however, it will be important to take into account the (typical) size of the supercell errors when interpreting the results.

For the X–N interactions, three possible configurations are considered, *i.e.* substitution of the alloying element X at the three Fe positions nearest to the nitrogen interstitial impurity. The X–N configurations are shown in Figure 4.5, with the substitutional impurity shown in blue and its connectivity to the nitrogen atom (green) indicated with a bond.

2. In our calculations, the computational resources required for a cell of 250 atoms are about 10 times larger than for a cell of 128 atoms.

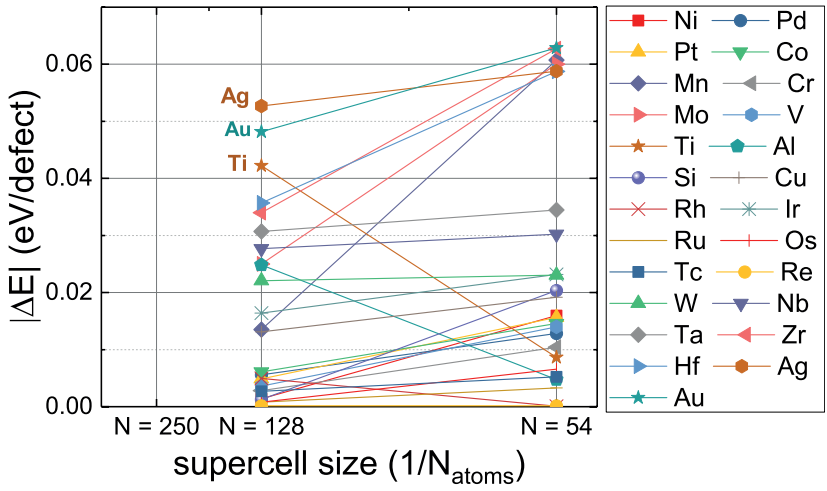

Figure 4.4: Evolution of the error on the energy of solution with respect to supercell size. With increasing supercell size (right to left), the relative error to the reference (250–atom supercell) generally decreases. Three alloying elements that showed unusually large errors are labeled: Ti, Ag and Au.

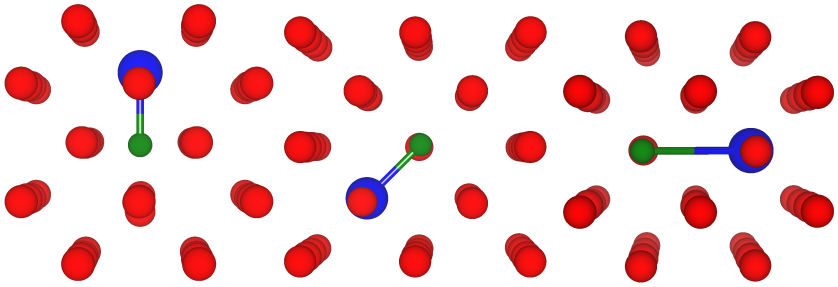

(a) nearest neighbor **(b)** second nearest neighbor **(c)** third nearest neighbor

Figure 4.5: Three configurations for which the X–N interaction has been calculated. The nitrogen atom is in its usual interstitial octahedral configuration in all structures.(note the crystal orientation is different for each configuration)

4.3.3 Free energy at finite temperature of selected ternary compounds

For those alloying elements that form binary or ternary α''/γ' compounds, the free energy up to 1000 K is calculated for the most stable α'' and γ' configurations in **step 3**. These calculations rely on the same methodology

as validated for the Fe-N binary system in Chapter 4 (Figure 2.3). Although the ternary compounds are configurationally more complex and are less symmetrical than Fe_4N or $Fe_{16}N_2$, calculating the necessary contributions to the total free energy does not necessitate any changes to the approach.

Having obtained the relevant free energies for the ternary structures for a given alloying element X, the dissociation of the α'' into the γ' structure and ferrite[3]

$$Fe_{16}N_2 \rightarrow Fe_4N + Fe \tag{4.3}$$

as discussed in Section 3.3.4, is now generalized and evaluated for

$$Fe_{16-x}X_xN_2 + Fe_{16}N_2 \rightarrow Fe_{4-y}X_yN + Fe_4N + Fe \tag{4.4}$$

where $Fe_{16-x}X_xN_2$ and $Fe_{4-y}X_yN$ are the most stable (ternary) compounds for the α'' and γ' structures, respectively. The presence of the binary phases $Fe_{16}N_2$ and Fe_4N, along with bulk Fe, is conditionally dependent on the stoichiometry and therefore indicated in gray. These phases serve to balance the stoichiometry of the dissociation. As such, *all* of the nitrogen and ternary element X is considered to be in either the α'' or γ' phase.

Our aim in this analysis is to focus on how ternary alloying elements can alter the thermodynamics of the precipitation process of ferrite $\rightarrow Fe_{16}N_2 \rightarrow Fe_4N$. Hence, this analysis does not aim, to cover the full phase stability spectrum as a function of ternary solute concentration. Indeed, this would require free energy calculations for the ternary solute - a computationally very expensive procedure which entails significant numerical uncertainties (Section 3.4.2)- and all possible binary and ternary phases. Instead, we focus only on the ground state structures in the α'' and γ' crystal structures.

4.3.4 The study set

All transition metals, barring the first and last column, are considered as substitutional solutes in this chapter, supplemented with Si and Al (red in Figure 4.6). For this entire study set, the solute impurity and the possible α'' and γ' crystal structures are evaluated with DFT at $0\,K$ for **step 1**. For

3. In principle, this balance has to account for a small portion of the nitrogen dissolving into the ferrite as was done in Equation 3.3. However, for equilibrium nitrogen concentrations this fraction is negligibly small.

step 2, the calculation of X–N interactions, only the elements most relevant for metallurgical purposes are considered (dark red in Figure 4.6), *i.e.* they are commonly used in steel production. Calculation of the free energies at finite temperatures (**step 3**) are only performed for the most relevant elements that form in both the α'' and γ' crystal structures (dark red with white highlight in Figure 4.6).

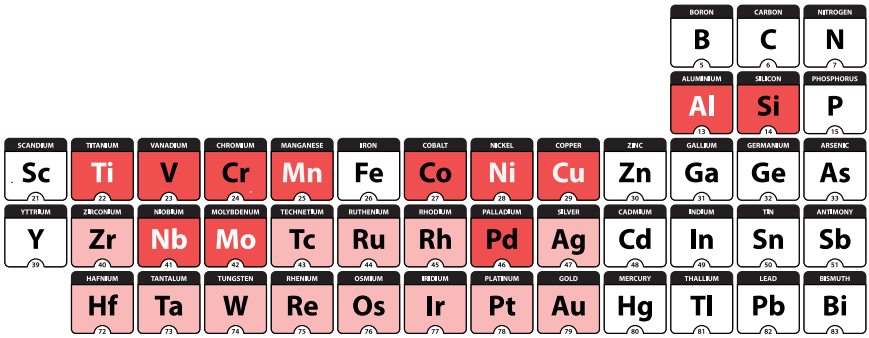

Figure 4.6: The possible alloying elements that are evaluated with DFT calculations. For the elements indicated in light red, only 0 K isolated impurities and crystal structures were performed. Dark red indicates X–N interactions were studied as well. For, an element with a highlighted name, finite temperature free energy calculations were performed.

4.3.5 Technical details

The specifics of the DFT and Monte Carlo calculations performed for this chapter are largely similar to those described in Section 3.2.

All DFT calculations for 0 K energies, F_{el} and F_{vib} were performed with the Vienna Ab Initio Simulation Package (VASP), [68, 69] using VASP 5.4 recommended PAW potentials.[70, 71] The Perdew-Burke-Ernzerhof (PBE) exchange-correlation functional was used in all cases.[64] The Brillouin zone integration grid always contained at least $20\,736/N_{\text{atoms}}$ $\boldsymbol{k}$-points, with N_{atoms} the number of atoms in the unit cell. For F_{el}, Fermi smearing, with the smearing parameter σ determined by the required temperature (Section 2.2.1), was used for the electronic self-consistent field cycle with a convergence criterion of 10^{-9} eV. For geometric optimizations, first-order Methfessel-Paxton smearing with $\sigma = 0.2$ eV was used for electronic convergence.[117] A conjugate-gradient algorithm was used for

the geometric optimization itself with a convergence criterion of 10^{-8} eV. An energy cutoff of 500 eV was used for the plane wave basis sets, with the grid for fast Fourier transform able to capture reciprocal vectors twice as large as the vectors included in the basis set. For the energies of solution using the supercell approach, where numerical errors need stringent control, and for the final energies of the crystal structures at 0 K, $63\,488/N_{\text{atoms}}$ $\boldsymbol{k}$-points were used with an energy cutoff of 650 eV and tetrahedron smearing with Blöchl corrections.[178]

The phonon spectra were constructed using the direct force constant method (Section 2.2.2).[116] The supercells with atomic displacements of 0.01 Å were set up using the phonopy software package.[89] The forces in response to the displacements were calculated with DFT using VASP. For these force calculations an additional support grid was used for the augmentation charges. First-order Methfessel-Paxton smearing with $\sigma = 0.2$ eV was used for electronic convergence.[117] In most cases, the simulated supercells were made large enough so that the minimum distance between periodic images was at least 11 Å. For $FeMn_7N$ and Fe_2Ni_6N, this was not feasible and this distance was 7.2 Å along one direction. The diagonalization of the dynamical matrix was performed with the phonopy software again.

SPR-KKR version 6.3 was used with the PBE functional to compute the Heisenberg coupling parameters (Section 2.2.3). The atomic-sphere approximation and Lloyd's corrections were applied. The number of E-mesh points was 40 for all calculations. The Brillouin zone integration was performed with at least $135\,000/N_{\text{atoms}}$ $\boldsymbol{k}$–points for the γ' structures and $35\,280$ for the α'' structures. The structure constants R_{max} and G_{max} were set to 2.9 $a.u.$ and 3.3 $a.u.^{-1}$ respectively. The electronic self-consistent field cycle had a convergence criterion of 10^{-5} Ry.

The ALPS classical Monte Carlo calculations were performed with cluster updates for temperatures ranging from 2 K to 1000 K or higher, with the maximum temperature always exceeding T_{C} by at least $10\,\%$ to accurately determine the maximum in the magnetic heat capacity. Periodic boundary conditions were used with a unit cell size of 2560 for Fe_4N and 3888 for $Fe_{16}N_2$. For initial thermalization, $30\,000$ MC steps were needed. The production phases contained $1\,500\,000$ MC steps for all materials.

4.4 Results

4.4.1 γ' and α'' ternary compounds at 0 K.

The possible formation of α'' and γ' ternary phases is assumed to start from the elements in solid solution. The energy of formation E_f for those phases is thus deduced from the transformation:

$$(4-x)\mathrm{Fe}_\alpha + x\mathrm{X}_\mathrm{sol} + \mathrm{N}_\mathrm{sol} \rightarrow \mathrm{Fe}_{4-x}\mathrm{X}_x\mathrm{N} \tag{4.5}$$

for the γ' structure, and

$$(16-y)\mathrm{Fe}_\alpha + y\mathrm{X}_\mathrm{sol} + 2\mathrm{N}_\mathrm{sol} \rightarrow \mathrm{Fe}_{16-y}\mathrm{X}_y\mathrm{N}_2 \tag{4.6}$$

for the α'' structure.

The results for all elements that can lead to γ' formation are summarized in Figure 4.7, where $E_\mathrm{f} = 0$ means the ternary compound has the same energy of formation as Fe_4N. Therefore, a driving force for formation is present if $E_\mathrm{f} < 0$. In the case of W, Re, Ru, Os, Co, Ir and Si there are no crystal structures that will form based on E_f. As such, these are not included in Figure 4.7. The full numerical data set can be found in table form in appendix a.

The DFT-obtained energies of formation for the most stable α'' structures at each stoichiometry (following the selection based on the CE model) are shown in Figure 4.8. $E_\mathrm{f} = 0$ means the ternary compound has the same energy of formation as $Fe_{16}N_2$. The alloying elements for which no negative E_f is obtained for any structure are not included in Figure 4.8. These were the same as for the γ' structure, with the addition of V, Cr, Rh and Pt. Ru, which did not form any γ' structure, does form α'' structures.

Those ternary compounds that are experimentally observed to form are confirmed to be stable by our results. Mn_4N is an observed stable phase,[156, 160] and precipitates in an Fe-Mn alloy.[179] We also find, however, that Mn takes part in the possible formation of α'' phases as well, with $Fe_2Mn_{14}N_2$ the most stable one. Experimentally, a multitude of $Fe_{4-x}Ni_xN$ compounds have been synthesized,[160–163] which is consistent with our results, where all possible stoichiometries in the γ' structure are stable. Wiener *et al.* found that Fe_3PtN can be synthesized as well, but

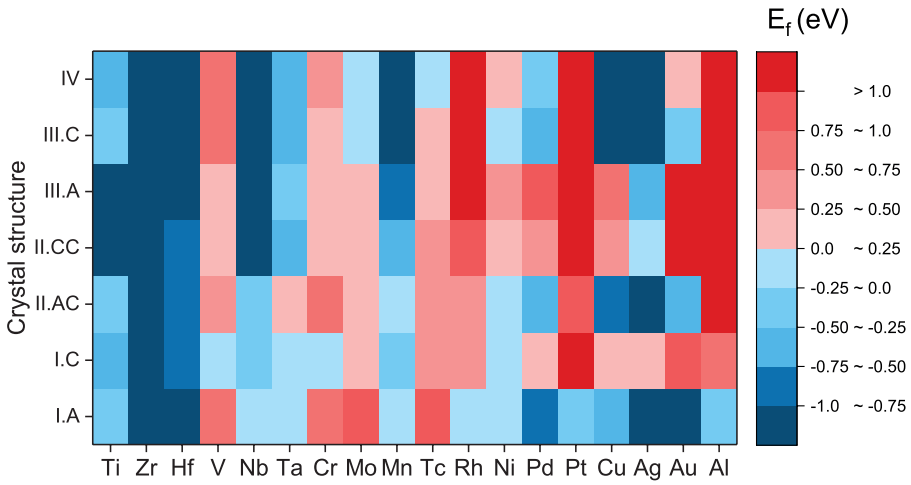

Figure 4.7: Color chart for the energy of formation E_f for the ternary compounds in the γ' crystal structure. The ternary alloying element is shown on the x-axis and the crystal structure on the y-axis (*cf.* Table 4.1). Blue indicates a negative E_f, meaning there is a driving force for forming the compound, whereas red indicates that that structure will not form. $E_\mathrm{f} = 0$ means the ternary compound is as stable as Fe_4N.

Fe_3CoN can not.[160] We draw a similar conclusion from our 0 K results.

The first main conclusion from these results is that W, Re, Os, Co, Ir and Si are completely non-bonding elements: $E_\mathrm{f} > 0$ for all structures considered. As such, these will not influence the precipitation of either the α'' or the γ' structure by forming ternary compounds. Similarly, the addition of V and Cr results in very little driving force towards ternary compounds: there are no stable α'' structures and the γ' compounds that can form have only a small negative E_f. In light of the fact that both Cr and V form strongly bound cubic CrN and VN precipitates, the formation of the ternary compounds will not occur.[25, 180]

For those elements that do form ternary compounds, multiple stable structures with differing stoichiometries exist in most cases. This indicates that the formation of ternaries is primarily determined by the element. Exceptions to this rule are Cr, V, Pt and Rh, which only form in the Fe_3XN stochiometry for γ' structures and form no α'' structures. Ternary compounds with Al are limited in substitutional concentration is well, with only Fe_3AlN, $Fe_{14}Al_2N_2$ and $Fe_{12}Al_4N_2$ forming.

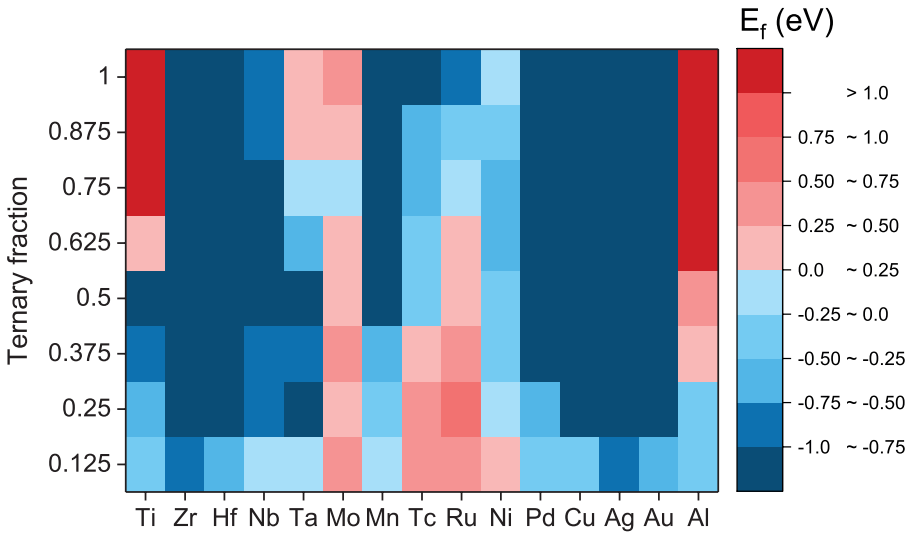

Figure 4.8: Color chart for the energy of formation E_f for the ternary compounds in the α'' crystal structure. The ternary alloying element is shown on the x-axis and the fraction of Fe sites occupied by the ternary element on the y-axis. Blue indicates a negative energy of formation, meaning there is a driving force for forming the compound, whereas red indicates the structure will not form. $E_f = 0$ means the ternary compound is as stable as $Fe_{16}N_2$.

When comparing different structures (see Figure 4.1) for a given element, it is observed that the I.A structure, whereby the ternary element substitutes Fe at the corner position ($1a$) in the γ' unit cell, is more stable than the I.C structure. However, our results indicate 5 exceptions: Ti, V, Nb, Cr and Mn. These atoms all have a larger atomic radius than Fe, which challenges the proposition that the favoured substitution at the $1a$ site is a consequence of the larger atomic radius of a substitutional atom.[165] So although the $1a$ site is larger in radius size (1.42 Å) compared to the $1c$ site (1.28 Å), the interaction with the nitrogen atom is an important consideration as well.

If a certain element forms stable ternary compounds, the other elements in the same group usually follow suit. Group 4 and 5 all form strongly bound ternaries in both the α'' and the γ' structure, except for V, which only forms Fe_3VN. In groups 8 and 9, few ternary compounds are formed, with only Ru resulting in $Ru_{16}N_2$ and Rh forming Fe_3RhN. All elements in groups 10 and 11 form multiple stable nitrides in both the α'' and the γ' structure, with the exception of Pt, which only results in γ' formation. In groups 6 and 7, a more varied behavior is observed. The 5d elements W and Re form no nitrides,

but the others do.

4.4.2 Solute interactions in the ferrite matrix

Additionally to the formation of crystallographic ternary phases, we wish to evaluate whether the solute atoms, *i.e.* nitrogen and a ternary substitutional solute X, interact in the ferrite matrix. Using the supercell approach, we calculated the energies of formation for the three configurations shown in Figure 4.5. The alloying elements for which an attractive interaction is obtained, are listed in Table 4.2, along with the magnitude of the formation energy of the solute pair and the configuration(s) for which the stabilization takes place (a, b or c, cf. Figure 4.5). Most of the attractive interactions occur for configurations a and b. Only in the case of Ti a large stabilizing effect is observed in configuration c and, even in that case, configuration b is much more stable. The most significant chemical interactions between the ternary substitutional solutes and nitrogen are thus accounted for within these calculations.

Eight of the twelve evaluated ternary elements show some bonding with the nitrogen interstitial in the ferrite matrix. However, most of these interactions are negligible in size, when taking into account the typical numerical errors using the supercell approach. These are on the order of 10 meV/atom, *cf.* Section 4.3.2. Additionally, one has to account for the loss of entropy when an X–N solute pair is formed out of two separate impurities. The configurational

Ternary element	E_f (meV)	Configuration
Pd	-30	c
Mn	-271	a
Cr	-35	a
V	-32	b
Ti	-312, -103	b,c
Al	-71	c
Cu	-71	c
Nb	-148, -26	b,c

Table 4.2: Stabilizing solute interactions between nitrogen and a ternary solute in the ferrite matrix (in meV per solute pair). Letters a, b and c in the final column indicate the configuration of the solutes as shown in Figure 4.5

free energy for nitrogen in concentration c in ferrite without any preferential sites is

$$F_{\text{conf}}(c) = -k_{\text{B}}T(1 - \ln(c) + \ln(g)), \tag{4.7}$$

where k_{B} is Boltzman's constant and g the number of interstitial sites per Fe bulk atom. When nitrogen is pinned to the substitutional solute atom, however, the configurational entropy changes. The number of configurations for n interstitial nitrogen atoms with respect to N substitutional atoms in the dilute limit is

$$W = \frac{(g'N)!}{(g'N - n)!\,(n)!}, \tag{4.8}$$

where g' is the symmetrical multiplicity of the nitrogen impurity site around the substitutional impurity. For the three X–N configurations we consider, $g' = 6$,12 and 24 for configurations a, b and c, respectively. Using Stirling's formula, and introducing the X/N ratio $c' = n/N$, the configurational free energy per nitrogen atom is

$$F'_{\text{conf}}(c') = -k_{\text{B}}T\ln(W) = -k_{\text{B}}T\left(\frac{g'}{c'}\ln\left(\frac{g'}{g' - c'}\right) + \ln\left(\frac{g' - c'}{c'}\right)\right). \tag{4.9}$$

To grasp the possible loss in configurational free energy when a solute pair is formed, the difference in F_{conf} for a nitrogen atom in the ferrite matrix with one pinned to a solute atom is shown in Figure 4.9. For $F_{\text{conf}}(c)$ a typical concentration of $c = 0.1$ at.% is assumed. From this, it is clear that in most situations, an X–N bonding of more than 100 meV is required to stabilize it at relevant temperatures. This means only Mn, Ti and Nb have a strong potential for nitrogen trapping in the configurations presently evaluated, with Al and Cu possible acting as slight trapping sites if the ratio of substitional impurities to the nitrogen atoms is sufficiently high (low c').

That Ti shows a strong affinity for N is already well–known through its formation of Ti-N platelets,[153], the interaction of N with Ti plates,[181] and previous DFT analysis of the interaction between the atoms in solution.[182]. It also helps explain why in our search for ternary compounds (Section 4.4.1), Ti formed strongly bound ternary phases in both the γ' and α'' structures.

The same observation can be made for Mn and Nb. Mn has been reported to act as a trapping site for nitrogen, with Kamminga *et al.* reporting a trapping

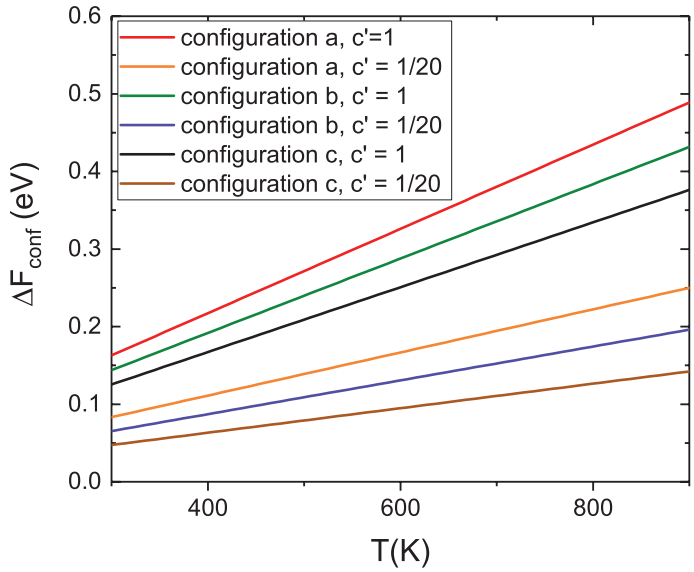

Figure 4.9: The difference in configurational entropy between an impurity in the ferrite matrix and one specifically pinned to a substitutional impurity. A range of X/N concentration ratios c' is shown for the three different configurations of the solute clustering.

depth of -0.30 eV, which is close to our energy of formation of -0.271 eV.[148] In the same study, however, V was also identified as a trapping agent with a depth of -0.55 eV, which is not confirmed by the present calculations. This points towards a more complex cluster formation of V, Fe and N.

For most alloying elements besides Ti, Nb and Mn, there is a repulsive interaction between the substitutional solute and nitrogen. Even for those elements in Table 4.2 that have a small attractive interaction in one configuration, the other configurations yield a large positive energy of formation. Consequently, these alloying elements can reduce the solubility of nitrogen in the material, certainly when their concentration is higher. For V and Cr, the results are more mixed, as some configurations are stable (Table 4.2) but others equally unstable. An overview of all calculated X–N interactions is given in Appendix a.

4.4.3 Influence of ternary alloying elements on the thermodynamic balance between α'' and γ'

The 0 K DFT results from the previous section warrant further investigation for some elements. Ni, Nb, Cu, Mo, Al, Mn and Ti all lead to formation of both α'' and γ' structures and are regularly used in common steel grades. For those elements, we aim to calculate the free energy to evaluate which phase is most stable at what temperatures. This is done using Equation 4.4, where both nitrogen and the ternary element are considered in either the γ' or α'' phase.

Ni

Ni forms stable phases for a range of stoichiometries in the γ' structure. The energies of formation for Fe_3NiN (both I.A and I.C), Fe_2Ni_2N (II.AC) and $FeNi_3N$ (III.C) are all less than 0.1 eV apart. To evaluate how this close balance evolves with increasing temperatures, we calculated the free energy of all four phases, shown in Figure 4.10. Fe_3NiN in the I.A structure and Fe_2Ni_2N remain the most stable ones, with Fe_3NiN-I.C becoming relatively less stable. The latter is in line with the experimental finding that Ni occupies the corner position in the γ' structure.[160]

Based on our calculations of the α''/γ' equilibrium, $Fe_4Ni_{12}N$ possesses stable ranges with respect to decomposition into γ'-$FeNi_3N$, but not with respect to Fe_3NiN or Fe_2Ni_2N. Thus, adding Ni will result in a driving force for γ' precipitation at all temperatures. Although for strengthening purposes, growth of the γ' phase is generally undesired, Ni does have the ability to improve the mechanical ductility of the normally brittle Fe_4N phase.[162]

Nb

$Fe_8Nb_8N_2$ and $FeNb_3N$ are the two most stable α'' and γ' phases, respectively. In Figure 4.11, the driving force for decomposition (eV per nitrogen atom) of the α'' phase

$$\frac{3}{8}Fe_8Nb_8N_2 + \frac{1}{8}Fe_{16}N_2 \rightarrow FeNb_3N + 4Fe \tag{4.10}$$

is shown, where negative values indicate a driving force for decomposition. Above 300 K, the α'' structure becomes the stable one, increasingly so for

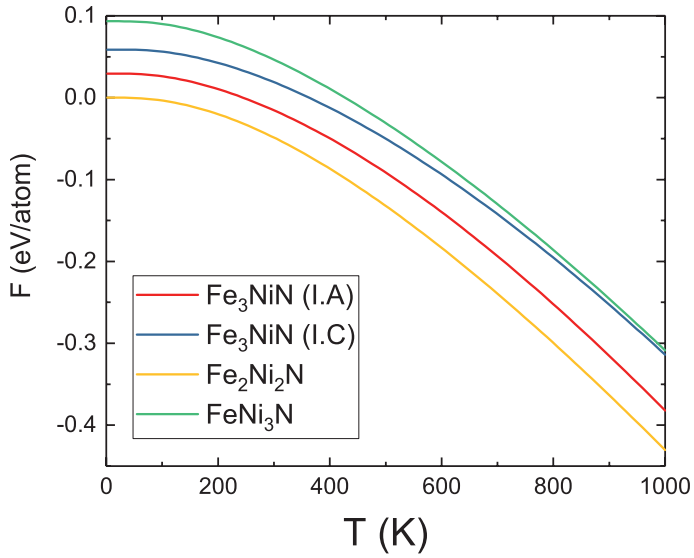

Figure 4.10: Free energies of the 4 different $Fe_{4-x}Ni_xN$ compounds. The total free energy of Fe_2Ni_2N at 0 K, as the most stable compound at 0 K, is used as the zero reference. The difference between the four compounds at 0 K stems from the difference in formation energy from the solid solution as described in Section 4.4.1

higher temperatures. This points to the strong α''–stabilizing effects of Nb, which can result in the suppression of the γ' phase. It is a notable fact that the stabilization occurs for higher temperatures, which is the reverse behavior compared with the binary Fe-N case.

Cu

In the case of Cu, the most stable α'' phase is the binary $Cu_{16}N_2$ compound. On the γ' side, Cu_4N and $FeCu_3N$ are the most stable compounds. Regardless of the decomposition path considered for $Cu_{16}N_2$, it is more stable than the γ' structures at all temperatures. This means Cu-N precipitates can form in an $Fe_{16}N_2$-like configuration, although the tetragonal lattice has a contracted c/a ratio (*i.e.* < 1), whereas $Fe_{16}N_2$ has an expanded one. The formation of $Cu_{16}N_2$ might thus not necessarily have the same beneficial precipitation strengthening effects.

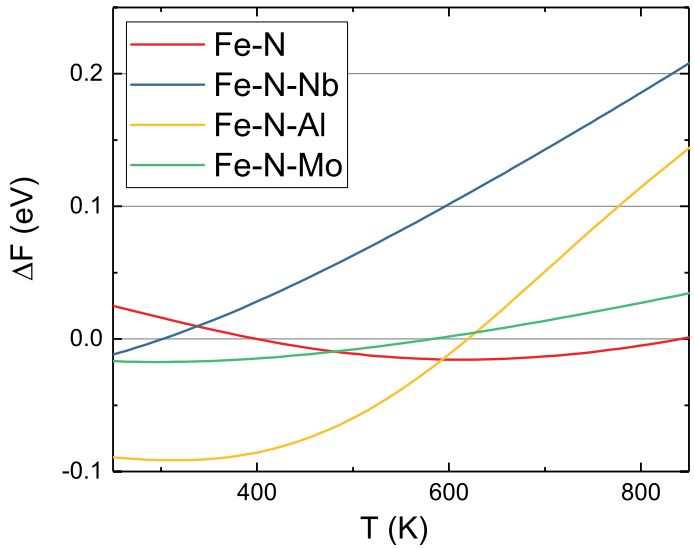

Figure 4.11: Driving forces for the decomposition of the α'' $Fe_8Nb_8N_2$, $Fe_{12}Al_4N_2$ and $Fe_4Mo_{12}N_2$ phases into $FeNb_3N$, Fe_3AlN and Mo_4N, respectively. For negative values, there is a driving force for decomposition towards γ' structures. To compare with the binary case, the decomposition energy for $Fe_{16}N_2$ into Fe_4N is shown as well.

Mo and Al

The stable compounds for Mo and Al are $Fe_4Mo_{12}N_2$, $Fe_{12}Al_4N_2$ for the α'' structure and Mo_4N, Fe_3AlN for the γ' structure. For both alloying elements, the α'' phase becomes stable around $580 - 600$ K (Figure 4.11), once more reversing the thermal stabilization compared to the binary Fe-N case. Above that temperature, γ' precipitation is thus suppressed. However, it is unlikely that either of the α'' compounds will form, in light of Mo-N and Al-N binary nitrides that are known to be stable.

Ti

In the α'' structure, $Fe_8Ti_8N_2$ is clearly the most stable phase, whereas in the γ' structure, Fe_2Ti_2N and $FeTi_3N$ are close in E_f. At 0 K, the α'' structure is more stable by 12 meV/atom. Unfortunately, no finite temperature analysis is possible, because all γ' Fe-Ti-N compounds were mechanically unstable

according to the calculated phonon spectra.[4] It is possible that the α'' structure remains stable at higher temperatures, as it has been shown that addition of Ti might stabilize it up to 700 K.[168] However, this is only for lower concentrations of Ti (< 5%) and it is not clear whether any ternary crystallographic phase could be stabilized at all in light of the dominant formation of Ti-N.

Mn

In the γ' structure, Mn does not form a ternary compound but the known stable Mn_4N. In the α'' structure, on the other hand, $Fe_2Mn_{14}N_2$ is the most stable phase. However, this phase is unstable with respect to decomposition in Fe and Mn_4N at all temperatures. This makes Mn_4N the dominating phase upon Mn alloying. Its experimentally measured Curie temperature of 720 K[156]-738 K[160] is confirmed by a DFT-obtained Curie temperature of 700 K.

4.5 Conclusions

The aim in this chapter was to chart how ternary elements, starting as substitutional impurities in ferrite, can influence the thermodynamics of the $Fe_{16}N_2$ and Fe_4N precipitation. This was done by substituting the Fe atoms in the α'' structure of $Fe_{16}N_2$ and in the γ' structure of Fe_4N by a ternary alloying element.

First, DFT calculations were used to evaluate which ternary phases have the potential to form in the γ' or α'' structure (Figure 4.12). For the majority of the elements, ternary phases in the γ' structure can form. Fewer elements resulted in formation of a ternary α'' phase. Most notably, Cr and V, which did form a γ' ternary compound, did not do so in the α'' crystal structure. Three main groups can be identified:

1. V, Cr, Pt, Rh (weakly) form ternary compounds in the γ' structure, but none in the α'' crystal structure. These elements will have very little effect on the formation of either. Certainly no stable ternary α'' compound can form.

4. This is suspected to be a numerical problem, for which no solution has been found.

2. W, Re, Ru, Os, Co, Ir and Si do not form any ternary phases at all in either crystal structure.

3. Ti, Zr, Hf, Nb, Ta, Mo, Mn, Tc, Ni, Pd, Cu, Ag, Au and Al all form both stable γ' and α'' phases. Because of their metallurgical relevance, Ti, Nb, Mo, Mn, Ni, Cu and Al warrant further investigation at finite temperature.

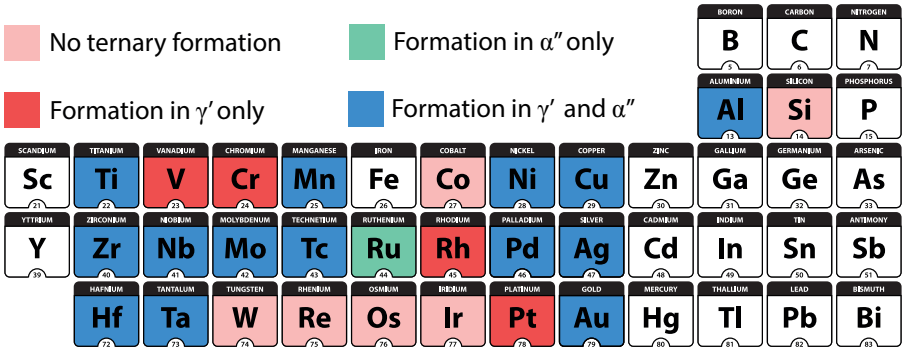

Figure 4.12: Summary of the 0 K results, identifying each element as neutral (light red), forming γ' compounds (red), α'' compounds (green) or both (blue).

Additionally, we sought to identify those ternary elements that could possibly interact with nitrogen in solid solution and thus affect the solubility or inhibit interstitial nitrogen diffusion by trapping. The solute interactions for three different configurations of the substitutional–interstitial complex were calculated with DFT using the supercell approach. It was found that very few ternary alloying elements show a strong bonding interaction with nitrogen in solid solution. Only Ti, Nb and Mn form a strong solute complex with the interstitial. Consequently, these three elements will inhibit the diffusion of nitrogen in ferrite. However, the binding interaction also means these elements can increase the solubility of nitrogen in ferrite, provided there is no formation of secondary phases. All other elements decrease the solubility of nitrogen, apart from V and Cr, which have a mixed character.

Finally, we calculated the free energy of the most stable γ' and α'' phases for Ti, Nb, Mo, Mn, Ni, Cu and Al, which enables us to classify them further. Mn and Ni drive the balance toward γ' structures. As such, their presence drives the precipitation of Mn_4N, Fe_3NiN and Fe_2Ni_2N. Cu stabilizes the

α'' structure at all temperatures. However, Cu forms a binary $Cu_{16}N_2$ structure of which the mechanical impact on the ferrite matrix is unknown. For Mo and Al, the α'' is stable above 600 K, but both these elements are known to form other, stable nitrides at temperatures of 580 °C and 500 °C, respectively. This makes it unlikely the α'' structures could be metastable.

Nb does show promise as a candidate for stabilizing the α'' structure, as $Fe_8Nb_8N_2$ is stable from 400 K upwards. This is especially the case since it also shows a binding interaction with nitrogen in solid solution, potentially increasing the solubility of nitrogen in the ferrite matrix.

5

Conclusions and perspectives

5.1 Conclusions

This PhD dissertation reported on a broad computational study of iron-nitrogen phases with the aim to improve understanding and advance the development of nitrided steels at low nitrogen concentrations. Nitriding of steels is a treatment performed on the solid material, generally at temperatures between 490 °C and 580 °C. It can result in the formation of a hardened surface, which consists of iron-nitrogen phases. Underneath the surface layer, diffused nitrogen is present as a solute in the ferrite matrix. For pure Fe, upon cooling, secondary iron-nitrogen particles can precipitate if the nitrogen concentration is sufficiently high and the cooling not too rapid. In this diffusion layer, both nitrogen in solid solution and the precipitates can improve the strength and fatigue resistance.

Given the appropriate nitriding conditions, *i.e.* the nitriding potential and temperature, the formation of a compound surface layer can be avoided. As such, nitrogen can be dissolved throughout the ferrite matrix and through–thickness nitriding is achieved. Developing bulk nitrided steels requires insight into the Fe-N phase diagram, however, on which current knowledge is very limited. This is because for Fe_4N and especially for $Fe_{16}N_2$, homogeneous samples are difficult to manufacture experimentally. As a result, their properties are hard to measure experimentally. Yet, these are precisely the phases that can form in through–thickness nitrided material, with $Fe_{16}N_2$ resulting in precipitation strengthening. A better grasp on the

thermodynamic behavior of these phases is thus crucial to better understand their formation and formulate heat treatment protocols. The aim was to use computer simulations to determine the phase equilibria in the Fe–N system for a wide range of temperatures. When the goal is to perform nitriding on more complex alloys, the effect of ternary alloying elements must be taken into account as well. Meeting this problem by performing an experimental investigation for each possible ternary element is costly and time-consuming. As such, the goal was to use computer simulations to predict which nitrogen–containing phases can form for different alloy compositions and under which temperature conditions.

To predict phase formation, the thermodynamic stability of that phase must be addressed first. This requires calculating its free energy for the relevant temperature range. Density-functional theory (DFT) calculations were used to obtain both the free energy at 0 K and all relevant contributions to the finite-temperature free energy. This theory strikes the balance between a quantum mechanical treatment of the materials at an atomic level and the need for calculating system sizes of 100–200 atoms per unit cell.

In the first step (Chapter 3), the free energy for ferrite, Fe_4N, $Fe_{16}N_2$ and nitrogen as an impurity in the dilute limit was calculated. This enabled to establish the binary phase diagram for low nitrogen concentrations for temperatures from 0 K to 865 K. The diagram was validated by comparing the calculated limit of solubility of nitrogen in ferrite with the experimental one available from literature (Figure 5.1). These calculations moreover revealed new information concerning $Fe_{16}N_2$. First, this phase is known to be metastable at temperatures below 470 K. The current results, however, indicate that it also becomes stable with respect to decomposition into Fe_4N and ferrite below 400 K. Second, the experimental Curie temperature of $Fe_{16}N_2$ (around 800 K) was found to be an underestimation, resulting from its instability above 400 K. The calculated Curie temperature, in contrast, is 1300 K. The thermodynamic data that were calculated for the binary Fe–N phases can serve purposes beyond the phase stability. They can serve as input for higher-order calculations, e.g. phase field simulations, as the differences in free energies give the driving force for precipitation of either Fe_4N or $Fe_{16}N_2$.

When processing the DFT results for the Fe-N phases, two methodological shortcoming were identified as the largest contributors to prediction uncertainty. The ferromagnetic nature of these compounds can result in non-negligible errors when calculating finite-temperature properties. This

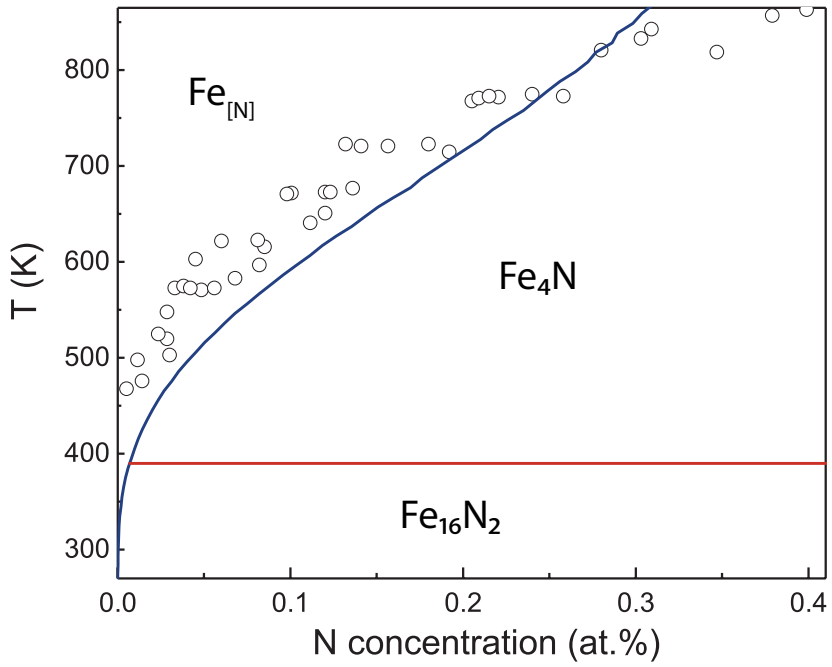

Figure 5.1: (Color online) The DFT-obtained phase diagram of $Fe_{[N]}$, Fe_4N and $Fe_{16}N_2$. Experimental data for the limit of solubility of N in Fe are included for comparison (circles).[23]

was most apparent for Fe_4N, which is known to show a steep volume-dependent increase in magnetization around the equilibrium volume. Because this increase is very sensitive to the approximations used in DFT, volume-dependent properties present a problem. Most noteworthy, the thermal expansion coefficient was underestimated with PBE-GGA and overestimated with LDA, although this had little impact on the free energy of Fe_4N. Another methodological problem concerns the free energy of the nitrogen impurity in ferrite. The supercell method that was used implies significant numerical errors of up to 20 meV. Because these error bars correspond with an uncertainty of 100–200 K on the transition temperatures, they can significantly limit the predictive power of the DFT calculations.

Because the balance between Fe_4N and $Fe_{16}N_2$ is crucial for the mechanical properties of the ferrite matrix, with the latter resulting in precipitation strengthening, the further aim was to investigate how the addition of ternary alloying compounds can influence this balance. This work on possible ternary compounds involved three parts. First, an evaluation was made as to which possible compounds can form in the crystal structure

of Fe_4N (γ') and the crystal structure of $Fe_{16}N_2$ (α'') at 0 K. The possible phases in the α'' and γ' structure were found using the energy of formation when adding either a transition metal element (except for the first and last columns), Al or Si. From these results, it was possible to identify those alloying elements that have the ability to stabilize either crystal structure (Figure 5.2). In addition, supercell calculations were performed to evaluate whether the ternary element can possibly influence the diffusion or solubility of nitrogen in ferrite by interacting with the interstitial impurity in solid solution. It was found that Ti, Mn and Nb interact with nitrogen to potentially form an impurity cluster, which inhibits diffusion but increases the solubility.

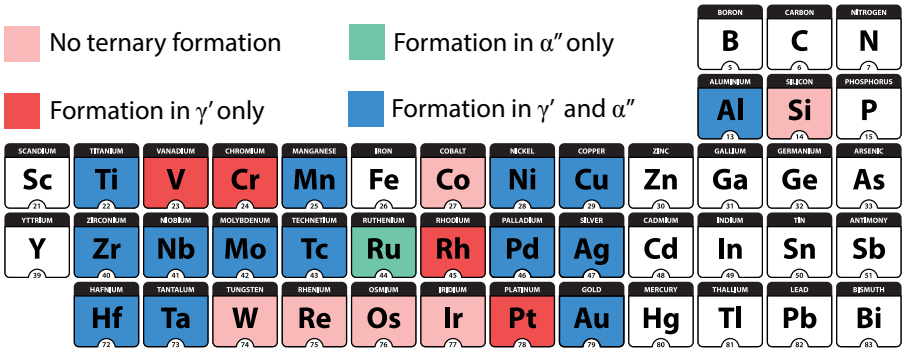

Figure 5.2: Summary of the 0 K results, identifying each element as neutral (light red), forming γ' compounds (red), α'' compounds (green) or both (blue).

In the final part of the research on ternary compounds, the goal was to evaluate the balance between the α'' and γ' phases of those ternary alloying elements that stabilized both and that are commonly used in steel alloys; this was the case for Nb, Mo, Mn, Ni, Cu and Al. For these elements, the free energy at finite temperatures was calculated in order to evaluate the temperature-dependent relative phase stability. It was found that for Ni and Mn the γ' structures were most stable at all temperatures. For Cu, the opposite was found and the α'' phase turned out to be the most stable at all temperatures. For Nb, Mo and Al, a transition was found to occur. At low temperatures (below 350 K for Nb and below 600 K for Mo and Al) the γ' phase was more stable, but at higher temperatures the α'' phase was stabilized. This is the inverse thermal behavior compared to the binary case, where $Fe_{16}N_2$ is stabilized *below* 400 K. Especially for Nb, this result points towards a potentially interesting stabilization of the α'' structure. As such, it

is a candidate to improve the precipitation strengthening effects in nitrided steels.

5.2 Perspectives

In this work, a DFT-based methodology has been applied and validated to calculate the free energy of binary and ternary iron-nitrogen phases. The calculated data can be used to model the Fe-N phases out of equilibrium with accurate input data. For example, simulating the (rate of) growth of $Fe_{16}N_2$ and Fe_4N phases in a ferrite matrix using phase field modeling can now benefit from accurate free energies for any desired nitrogen concentration or annealing temperature.

Using DFT to calculate the thermodynamic stability and properties also revealed two main methodological challenges. First, the large uncertainty in the prediction of the thermal expansion coefficient of Fe_4N showed how magnetism, and especially its volume dependence, still presents a tall hurdle for DFT calculations. There is at the moment no clear argument for any exchange-correlation to be recognized as the superior one for magnetic properties. This element of arbitrariness hampers the credibility of DFT predictions. To address this issue, a continued development of functionals that aim to improve the description of magnetic properties in a consistent fashion is required.

The second main issue encountered was the large numerical uncertainty when treating impurities in a crystal. These calculations are crucial to derive solubilities, but the numerical impact of using the supercell method results in error bars that often are too large when phase equilibria are concerned (100–200°C). A large–scale analysis of these errors is crucial for the further use of the supercell method in all DFT research and would aid in tackling them as well. In a similar way, the calculation of phonon spectra – or, more generally, forces – could benefit greatly from an error analysis. Although the numerical errors for calculating vibrational free energies are much smaller than for impurity energies, computational difficulties are often encountered when obtaining phonon spectra. Because these can often result in incorrect mechanical instabilities, it is paramount that more is learned about how numerical issues on forces propagate towards phonon spectra and free energies.

Although a good description of the thermodynamics of the binary Fe-N phases was achieved in this work, further research, both computational and experimental, can still advance the insight into the materials properties. Computationally, it would be interesting to calculate the magnitude of the anharmonic contributions to the vibrational free energy. Also, the impact of phonon-magnon interactions on the free energy should be investigated. Experimentally, a renewed effort for measuring the expansion coefficients and bulk moduli of both Fe_4N and $Fe_{16}N_2$ could provide useful information. Because experimental data is so sparse, any additional information can provide validation of the computational result, or unveil theoretical shortcomings.

The results for the ternary compounds can serve as a first guideline of what effect an alloying element can have on the precipitation behavior for experimental research. The presence of Nb, for example, shows promise if one wishes to increase the solubility and α'' stability. An especially interesting study would be evaluating whether the addition of Nb, Mo or Al can result in the formation of ternary α'' precipitates and thus increase precipitation strengthening effects. Also, for those alloying elements known to stabilize (ternary) compounds in the γ' structure, assessing whether these phases can perhaps improve the mechanical properties of the material (in contrast to the binary Fe_4N) is an interesting avenue of experimental research.

The approach taken in this work for ternary formation serves as a first estimate. The formation of the ternary phases from the elements in solution was only considered at 0 K and the subsequent evaluation at finite temperatures did not consider the elements in solid solution. A logical next step from a modeling perspective, specifically for those elements that showed to form ternary compounds with iron and nitrogen, is to include other (known) crystal structures in the finite temperature analysis and model the impurities in the ferrite matrix at finite temperatures. Ultimately, this would enable the calculation of the full ternary phase diagram. Moreover, the ternary compounds were considered as regular periodic crystals. Including disordered structures can result in a more accurate description of the possible precipitating phases.

Finally, this work focused on the thermodynamics of nitrogen-containing compounds, isolated from the effects of carbon. Whether carbon is soluble in any of the compounds discussed in this work, or if it prohibits their formation, is a necessary evaluation to describe the complete metallurgical

issue.

Part II

Published Papers

A

Publications in International Peer–Reviewed Journals

Paper I

A first-principles reassessment of the Fe-N phase diagram in the low-nitrogen limit

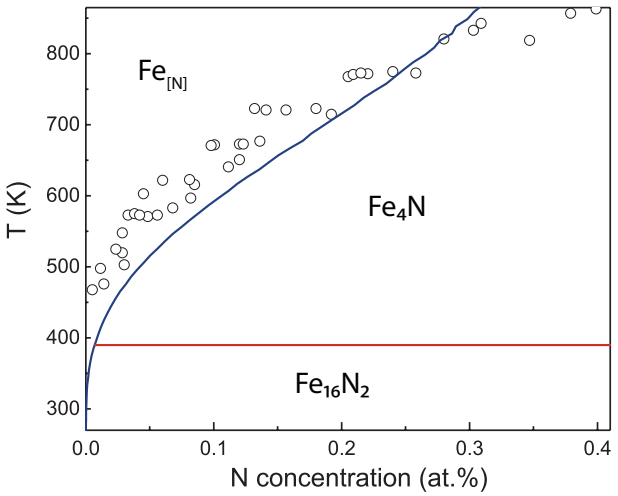

S. De Waele, K. Lejaeghere, E. Leunis,
L. Duprez and S. Cottenier

Journal of Alloys and Compounds, **2019**, *775*, 758–768

S. De Waele performed the calculations to obtain the free energies, interpreted the results and prepared the manuscript.

Journal of Alloys and Compounds 775 (2019) 758–768

Contents lists available at ScienceDirect

Journal of Alloys and Compounds

journal homepage: http://www.elsevier.com/locate/jalcom

A first-principles reassessment of the Fe-N phase diagram in the low-nitrogen limit

Sam De Waele [a, b, *], Kurt Lejaeghere [a], Elke Leunis [c], Lode Duprez [c], Stefaan Cottenier [a, b, **]

[a] Center for Molecular Modeling, Ghent University, Technologiepark 903, 9052 Zwijnaarde, Belgium
[b] Department of Electrical Energy, Metals, Mechanical Constructions and Systems, Ghent University, Tech Lane Ghent Science Park, Campus A, Building 903, 9052 Zwijnaarde, Belgium
[c] OCAS, Pres. J. F. Kennedylaan 3, 9060, Zelzate, Belgium

ARTICLE INFO

Article history:
Received 14 March 2018
Received in revised form
25 September 2018
Accepted 27 September 2018
Available online 1 October 2018

Keywords:
Nitride materials
Thermodynamic properties
Precipitation
Magnetization
Density-functional theory

ABSTRACT

Nitriding of steels has been widely used for almost a century. However, insight in two important precipitating phases for low concentration through-thickness nitriding is still lacking, hindering further development of the process. Due to their metastable nature, manufacturing large homogeneous samples of Fe_4N and $Fe_{16}N_2$ is very challenging. Consequently, measuring thermodynamic properties, such as heat capacity and free energy, has proven difficult at best. In this work, we have calculated those thermodynamic properties using density-functional theory (DFT) for Fe_4N, $Fe_{16}N_2$ and ferrite with nitrogen in solid solution. This information is a prerequisite to improve the accuracy of larger-scale modeling approaches of iron nitrides. We used the free energies to construct the temperature/concentration phase diagram for low nitrogen concentrations from 0 K to 865 K. Both the range of metastability for $Fe_{16}N_2$ and the nitrogen solvus confirm the experimental data. On the other hand, it was concluded that the experimental Curie temperature for $Fe_{16}N_2$ is severely underestimated because of the thermodynamic instability above 400 K.

1. Introduction

Nitrogen is present in all steels as a residual element. In some cases, nitrogen is even added intentionally as an alloying element. Nitriding is a gaseous thermochemical treatment that is widely used to improve the surface properties of parts and components made in forging and tool steel [1–5]. Indeed, during nitriding, a compound layer at the surface and a diffusion zone underneath are formed. In contrast, through-thickness nitriding for improvement of bulk properties is rarely considered. By selecting the appropriate nitriding conditions, the formation of a compound layer at the surface can be avoided and, for pure α – Fe or for ferritic steels with no nitride forming elements present, the absorbed nitrogen will be in solid solution during nitriding. If the cooling is fast enough, the nitrogen will stay in solid solution up to room temperature, resulting in a solid solution strengthening of 50 MPa per 0.01 wt% of added nitrogen [6]. For low nitrogen concentrations, slow cooling can lead to bulk precipitation of Fe_4N or $Fe_{16}N_2$ [7].

The knowledge of the thermodynamic stability and nucleation rate of precipitates or phases is essential to fully understand the thermal and mechanical properties of the manufactured steel. With respect to these aspects, the Fe-C system is relatively well studied, but such information is not generally available for the Fe-N system, due to the metastability of the Fe-N phases or the unavailability of the phases in pure form [8]. Because experimental data on phase equilibria in the Fe-N system are often limited to narrow temperature ranges, a computational approach offers a complementary approach.

Thermodynamic properties such as the heat capacity and the thermal expansion are essential to describe the iron nitrides in large-scale approaches, such as phase field models [9], but they require the knowledge of free energies for each phase. Previous derivations of the free energy for Fe_4N were based on solvus lines in

* Corresponding author. Center for Molecular Modeling, Ghent University, Technologiepark 903, 9052 Zwijnaarde, Belgium.
** Corresponding author. Center for Molecular Modeling, Ghent University. Technologiepark 903, 9052 Zwijnaarde, Belgium.
E-mail addresses: sdwaele.dewaele@ugent.be (S. De Waele), stefaan.cottenier@ugent.be (S. Cottenier).

https://doi.org/10.1016/j.jallcom.2018.09.356
0925-8388/

the phase diagram [10] or the cluster variation method (CVM) combined with the Debye-Grüneisen model [11]. In contrast to such (semi-)empirical methods, using density-functional theory (DFT) provides a non-empirical approach for modeling the iron nitrides [12,13]. This avoids the process of extrapolating phase stability from narrow temperature ranges and provides insight into the relative stability of Fe with N in solid solution ($Fe_{[N]}$), Fe_4N and $Fe_{16}N_2$ from 1000 K down to 0 K. On the other hand, the complexity and size of crystal structures that are feasible to tackle with DFT calculations are limited. Consequently, this work is restricted to the line compounds Fe_4N and $Fe_{16}N_2$ and does not take into account the disorder associated with possible off-stoichiometries [14,15]. To capture said off-stoichiometric disorder, a dedicated approach, such as the Gorsky-Bragg-Williams method [16], as employed by Kooi et al. [17], the cluster variation method used by Pekelharing et al. [18,19], the use of special quasirandom structures [20] or the cluster expansion model [21] would be necessary. However, reported off-stoichiometries are related to the equilibrium with a gaseous nitrogen environment while the focus of this article is on through-thickness nitriding and bulk phase equilibria. Our excellent agreement with experimental results (see Sec. 3)suggests that in such cases the impact of off-stoichiometries is less pronounced.

To obtain the free energies for Fe and iron nitrides, all relevant contributions should be taken into account: electronic, vibrational, magnetic and configurational. The electronic free energy is obtained using finite-electron temperature DFT [22], the quasi-harmonic approximation is used to compute the vibrational free energy and a rescaled Monte Carlo approach is applied for the magnetic excitations [23,24]. The free energies can subsequently be used to evaluate the phase equilibria between the various phases, yielding the temperature/composition phase diagram of Fe_4N, $Fe_{16}N_2$ and bcc $Fe_{[N]}$ for N concentrations below 1 at.%.

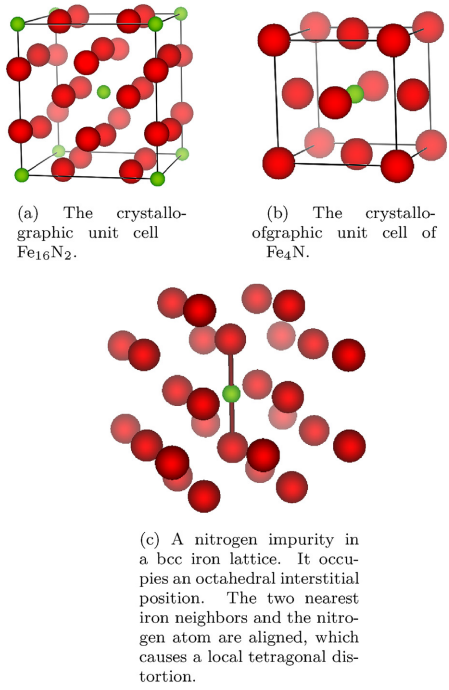

(a) The crystallographic unit cell $Fe_{16}N_2$.

(b) The crystallofgraphic unit cell of Fe_4N.

(c) A nitrogen impurity in a bcc iron lattice. It occupies an octahedral interstitial position. The two nearest iron neighbors and the nitrogen atom are aligned, which causes a local tetragonal distortion.

Fig. 1. Crystallography of the three considered Fe-N phases with the Fe atoms shown in red and the N atoms in green. (For interpretation of the references to colour in this figure legend, the reader is referred to the Web version of this article.)

2. Methodology

The free energy is determined for bcc iron (Fe), iron with N in solid solution ($Fe_{[N]}$), Fe_4N and $Fe_{16}N_2$. The iron nitride $Fe_{16}N_2$ is ferromagnetically ordered and has the space group $I4/mmm$ [25]. The nitrogen atoms occupy the regular octahedral interstitial positions $(0.0, 0.0, 0.0)$ and $(0.5, 0.5, 0.5)$ in a distorted bcc iron supercell (Fig. 1a), which is the 1b Wyckoff position. This regular ordering of the nitrogen atoms causes a macroscopic tetragonal distortion. Fe_4N is a ferromagnetic material as well, but in contrast to $Fe_{16}N_2$ it has a cubic crystallography with space group P m $\overline{3}$ m [26]. The iron atoms form a face-centered cubic sublattice, with the nitrogen atom occupying the $(0.5, 0.5, 0.5)$ 1b Wyckoff position (Fig. 1b).

To completely describe the equilibria between these phases, the defect free energy of nitrogen in solid solution is needed as well. As an impurity in body-centered iron, nitrogen forms an interstitial defect in an octahedral configuration (Fig. 1c) [27]. In this position, the nitrogen impurity aligns with its nearest iron neighbors. This causes a local tetragonal distortion, where especially the aligned iron atoms undergo a large displacement from their original bcc position. For every Fe host atom, there are 3 interstitial octahedral sites.

To determine the volume- and temperature-dependent Helmholtz free energy F for every phase, the electronic, vibrational and magnetic excitations are determined. For bcc Fe with N in solid solution, the configurational contribution as a function of the N concentration c must be taken into account as well. The common assumption is that these contributions are all adiabatically decoupled, *i.e.* $F(V, T, c)$ can be written as [28].

$$F(V,T,c) = F_{el}(V,T) + F_{vib}(V,T) + F_{mag}(V,T) + F_{conf}(T,c), \tag{1}$$

where F_{el}, F_{vib}, F_{mag} and F_{conf} are the electronic, vibrational, magnetic and configurational contributions, respectively. For the $Fe_{[N]}$/Fe_4N and $Fe_{[N]}$/$Fe_{16}N_2$ phase equilibria, the nitrogen concentrations in iron are below 1 at.% [29]. Consequently, F_{conf} can be calculated from the configurational entropy for a dilute solution [30],

$$F_{conf}(T,c) = -k_b T[c - c\ln(c) + c\ln(g)], \tag{2}$$

where k_b is the Boltzman constant, c is the nitrogen concentration and $g = 3$ the number of interstitial sites per host atom. Including all contributions eventually allows the derivation of the equilibrium volume $V_0(T)$ at a given pressure P and temperature T:

$$\frac{\partial F(V,T)}{\partial V} = -P, \tag{3}$$

which ultimately yields the free energy under (P, T) conditions.

2.1. Electronic free energy

The electronic contribution $F_{el}(V, T)$ is obtained from a set of DFT calculations at different volumes and electron temperatures [22]. After an initial optimization of the atomic positions and volume,

the total energy is calculated for volumes ranging from 94 % to 106 % of the initial equilibrium volume and for electron temperatures between 2 K to 1000 K. Following the approach proposed by Grabowski et al. [31], the electronic free energy is separated into two contributions:

$$F_{el}(V,T) = E_0(V) + \tilde{F}_{el}(V,T). \tag{4}$$

The different contributions to $F_{el}(V,T)$ are subsequently parametrized into an analytical form, which facilitates the derivation of entropy and heat capacity. The energies for the different volumes at the lowest temperature ($T = 2$ K) are used to fit the 0 K volume-dependent behavior $E_0(V)$ to a Birch-Murnaghan equation of state [32]. This determines the equilibrium volume, internal energy, bulk modulus and the derivative of the bulk modulus with respect to the pressure. For the temperature dependence one uses

$$F^{\sim}{}_{el}(V,T) = \frac{1}{2}k_bT\left\{\sum_{i=1}^{3}(\alpha_i + V\beta_i)T^i\right\} \times \int d\varepsilon[f(T,\varepsilon)\ln f(T,\varepsilon) + (1 - f(T,\varepsilon))\ln(1 - f(T,\varepsilon))], \tag{5}$$

which is based on the general electronic entropy [33].

$$\tilde{F}_{el}(V,T) \approx -\frac{1}{2}TS_{el}(V,T) \tag{6}$$

and

$$S_{el}(V,T) = -k_b\int d\varepsilon\, N_{el}(V,T,\varepsilon)[f(T,\varepsilon)\ln f(T,\varepsilon) + (1 - f(T,\varepsilon))\ln(1 - f(T,\varepsilon))] \tag{7}$$

The function f is the level occupation described by the Fermi-Dirac distribution. The electronic density of states N_{el} is replaced by the energy-independent average

$$N_{el}(V,T) = \sum_{i=1}^{3}(\alpha_i + V\beta_i)T^i. \tag{8}$$

Here, α_i and β_i are six fitting parameters that fully describe the temperature-dependent part of F_{el} and the temperature-induced volume dependence. The linear parametrization in volume combined with the third-order polynomial parametrization in temperature produces a maximum residual error of well below 0.1 meV/atom.

All calculations of F_{el} were performed with the Vienna Ab Initio Simulation Package (VASP) [33,34], using VASP 5.4 recommended PAW potentials [35,36]. For the Fe atoms, the PAW potential with 8 valence electrons was used ([Ar] $3d^6\,4s^2$), while for N the potential with 5 valence electrons was used ([He] $2p^3\,2s^2$). These potentials were recently shown to provide a similar precision as all-electron calculations [37]. The Perdew-Burke-Ernzerhof (PBE) exchange-correlation functional was used in most cases [38], but the local density approximation (LDA) as parametrized by Perdew and Zunger [39] was, where useful, evaluated as well. The Brillouin zone integration grid always contained at least 27 648/N_{atoms} $\vec{k}$-points, with N_{atoms} the number of atoms in the unit cell. Fermi smearing, with the smearing parameter σ determined by the required temperature, was used for the electronic self-consistent field cycle with a convergence criterion of 10^{-9} eV. A conjugate-gradient algorithm was used for the geometric optimization with a convergence criterion of 10^{-8} eV. An energy cutoff of 500 eV was used for the plane wave basis sets, with the grid for fast Fourier transform able to capture reciprocal vectors twice as large as the vectors included in the basis set. These numerical settings ensured a computational precision of at least 0.5 meV/atom. The input files for all the calculations used in this work can be found in the supplementary information.

2.2. Vibrational free energy of $Fe_{[N]}$, Fe_4N and $Fe_{16}N_2$

The lattice vibrations are included using the quasiharmonic approximation. To account for thermal expansion, phonon spectra are computed for volumes relevant to the thermal expansion; *i.e.* ranging from 99 % to 106 % of the equilibrium volume. The volume-dependent frequencies $\omega_i(V)$ thus obtained are used to calculate the vibrational free energy [28].

$$F_{vib}(V,T) = \frac{1}{3N}\sum_{i=1}^{3N}\left\{\frac{1}{2}\hbar\omega_i(V) + k_BT\ln\left[1 - e^{-\hbar\omega_i(V)/k_bT}\right]\right\} \tag{9}$$

Here, N is the number of sampled points in reciprocal space multiplied by the number of atoms in the unit cell.

The phonon spectra were constructed using the direct force constant method [40]. Various supercells with atomic displacements of 0.01 Å were set up using the phonopy software package [41]. The forces in response to the displacements were calculated with DFT using VASP. Compared to the calculations of F_{el} an additional support grid was used for the augmentation charges. Moreover, instead of Fermi smearing, first-order Methfessel-Paxton smearing with $\sigma = 0.2$ eV was used for electronic convergence [42]. The simulated supercells were made large enough so that the minimum distance between periodic images was at least 11 Å. The diagonalization of the dynamical matrix was performed with the phonopy software again, after which each frequency from the different phonon spectra was fitted to a quadratic function of volume. This use of a second-order polynomial is sufficient to limit the maximum residual error to 0.01 THz for all frequencies. Even for the smallest frequencies, this results in an error below 1 % for the vibrational free energy.

2.3. Magnetic contribution

Directly calculating magnetic free energies with DFT is not yet possible. Instead, utilizing an atom-centered model has proven to be a successful approximation for iron and its alloys. More specifically, the Heisenberg model will be used as magnetic Hamiltonian [24,43–49]

$$H = -\frac{1}{2}\sum_{i\neq j}J_{ij}\,\vec{M}_i\cdot\vec{M}_j \tag{10}$$

The sum in Eq. (10) is taken for all atom pairs in the solid, with M_i the local magnetic moments and J_{ij} the Heisenberg exchange coupling parameters. The former are easily obtained from DFT calculations, but the latter require a somewhat more involved derivation. There are multiple ways of obtaining the coupling parameters. In this work, a DFT calculation based on the Korringa-Kohn-Rostoker Green's function method [50,51] was performed using the SPR-KKR software [52,53]. This allows direct access to the J_{ij} using the formulation of Liechtenstein et al. [54].

To determine $F_{mag}(T)$ from Eq. (10), classical Metropolis Monte Carlo (cMC) calculations were performed with the ALPS software

[55–57]. To do this, the sum in Eq. (10) is truncated at a threshold for the J_{ij}. This truncation was determined by evaluating the mean-field Curie temperature as a function of the threshold value. The mean-field Curie temperature is equal to the largest eigenvalue of the coupling parameters matrix **J** with [58].

$$\mathbf{J}_{\alpha,\beta} = \sum_{\beta_i} J_{\alpha,\beta_i} \vec{M}_\alpha \cdot \vec{M}_{\beta_i} \tag{11}$$

Here, α and β are atoms in the crystallographic unit cell and β_i are all the periodic images of the atom β for which a J_{ij} has been calculated.

The use of cMC, in which the magnetizations in Eq. (10) are not quantized, only approximates the correct quantum mechanical result. However, performing Quantum Monte Carlo (QMC) [59] for frustrated systems is generally infeasible because of the negative sign problem [60]. To approximate the correct heat capacity, the value derived from the cMC calculations via the fluctuation-dissipation theorem [61,62] was transformed according to the scaling proposed by Körmann et al. [23]:

$$\frac{C_{V,QMC}(t,S)}{C_{V,cMC}(t,S)} \approx \left(\frac{2t_s/t}{\exp(t_s/t) - \exp(-t_s/t)} \right). \tag{12}$$

Here, t is the normalized temperature $T/T_{C,cMC}$, where the cMC Curie temperature is determined by the peak in the heat capacity $C_{V,cMC}$, and

$$1/t_s \approx 0.54S + 0.54, \tag{13}$$

where S is the localized spin. For a system with more than one atom in its unit cell, the average S is used. Finally, the rescaled heat capacity was numerically integrated to obtain the entropy and free energy. The latter was fitted to a function of the form

$$F_{mag}(T) = A \exp\left(B/T\right) + CT^4, \tag{14}$$

where A, B and C are fitting parameters. This ensures interpolation errors smaller than 0.1 meV/atom. F_{mag} is 0 at 0 K because the energy of the ferromagnetic ordering is contained in the DFT calculations.

The most significant contributions to F_{mag} are found around the Curie temperature, where there is a peak in heat capacity. To minimize the error at these conditions, the J_{ij} are therefore recalculated at the volume associated with T_C, obtained from Eq. (3). This was done in an iterative way, until a self-consistent T_C was reached (Fig. 2). For numerical stability, the derivative of F_{mag} with respect to volume was not included in the optimization.

Magnetic coupling parameters were obtained with spin-polarized scalar-relativistic DFT calculations in SPR-KKR 6.3 using the PBE functional. The atomic-sphere approximation was applied. The number of E-mesh points was 40 for all calculations with a minimum E-value of $-$ 0.2 Ry. The Brillouin zone integration was performed on a $57 \times 57 \times 57$ grid for bulk Fe, a $36 \times 36 \times 36$ grid for Fe_4N and $25 \times 25 \times 25$ grid for $Fe_{16}N_2$. The structure constants R_{max} and G_{max} were set to 2.9 $a.u.$ and 3.3 $a.u.^{-1}$ respectively. The electronic self-consistent field cycle had a convergence criterion of 10^{-5} Ry.

The ALPS classical Monte Carlo calculations were performed with cluster updates for temperatures ranging from 2 K to 1000 K or higher, with the maximum temperature always exceeding T_C by at least 10 % to accurately determine the maximum in the magnetic heat capacity. Periodic boundary conditions were used with a unit cell size of 1000 atoms for Fe, 2560 for Fe_4N and 2250 for $Fe_{16}N_2$. The nitrogen atoms were never accounted for in the Heisenberg Hamiltonian, because their magnetic moments, and hence the coupling parameters with neighbors, were negligible. For initial thermalization, 30 000 MC steps were needed. The production phases contained 1 500 000 MC steps for all materials. The input files for all the calculations used in this work can be found in the supplementary information.

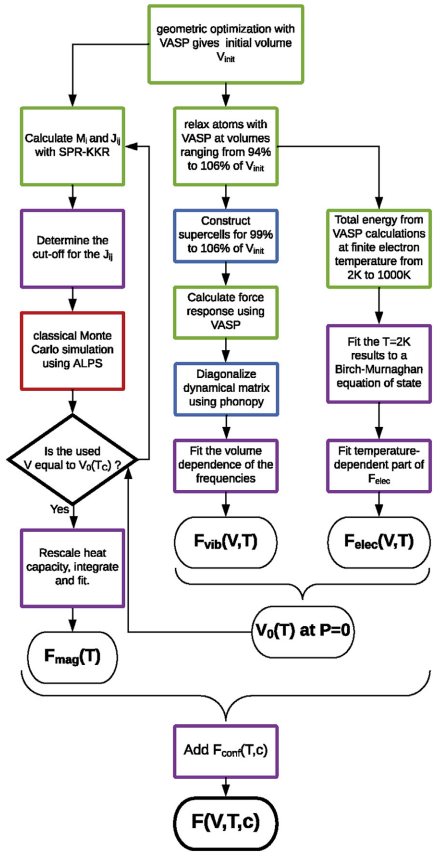

Fig. 2. Flowchart indicating the different calculations performed to obtain the free energy. Green indicates a DFT calculation, red an ALPS simulation, blue indicates use of the phonopy software and purple is for standard post-processing. (For interpretation of the references to colour in this figure legend, the reader is referred to the Web version of this article.)

The methodology described in this section does not take into account explicit anharmonic contributions or electron-phonon coupling. These were deemed to be of negligible magnitude, because our temperature range of interest lies below half of the melting temperature for the materials that were researched [63,64]. The magnon-phonon coupling contributions were not taken into account either. Based on the phonon mode softening for iron at 773 K, their size was estimated to be 1 – 2 meV/atom at the most for our temperature range of interest.

3. Results and discussion

Because of their limited temperature range of stability and the inability to manufacture isolated specimens, there is very little thermodynamic data available for the Fe_4N and $Fe_{16}N_2$ compounds, especially for the latter. Apart from free energies and heat capacities (Sec. 3.1), we have therefore also calculated structural properties, thermal expansion (Sec.3.2) and bulk moduli (Sec. 3.3), which we have validated with the limited available experimental data where possible. The magnetic contribution to the heat capacity is evaluated separately in Sec. 3.4 and the defect free energy of the N interstitial is discussed in Sec. 3.5. Finally, all the calculated free energies are combined into the phase diagram (Sec. 3.6).

3.1. Free energies and heat capacities

The calculated free energies and heat capacities are shown in Fig. 3 for all three bulk phases at their equilibrium volume at zero pressure. The vibrational, electronic and magnetic contributions are plotted separately to indicate their size. The equilibrium volumes at zero pressure are obtained from minimizing the free energy for the entire temperature range of 0 – 1000 K. This temperature interval was chosen because it is the most relevant for nitriding ferritic steels [65].

For bulk Fe, ample experimental data are available over its entire range of stability for the isobaric heat capacity C_P. To assess the accuracy of the DFT-derived free energy, it is compared to the data derived from experimental phase equilibria and thermochemical properties [66]. These experimental and our DFT free energies are set equal at room temperature (298 K). The accuracy of the DFT prediction is very good, with a difference of less than 0.1 meV/atom up to 750 K. This confirms the correctness of the methodology, which was previously used to obtain the various contributions to the free energy for Fe and Fe_3C [23,24]. The excellent accuracy is also the main argument for utilizing the same approach for Fe_4N and $Fe_{16}N_2$. As can be seen in Fig. 3a, for the free energy of ferrite a somewhat more significant discrepancy starts to occur beyond 850 K, leading to a difference in F of 6 meV/atom between theory and experiment at 1000 K. This is because the quasiharmonic approximation often overestimates anharmonic contributions to the free energy, which typically become important at about half of the melting temperature [63]. For the phase equilibria with Fe_4N and $Fe_{16}N_2$, temperatures above 850 K are not relevant, and the overestimation of the anharmonic contributions poses no problem. In case of the heat capacity of Fe, comparing experimental data [67] with calculated results shows a very good correspondence up to 800 K (Fig. 3d). For higher temperatures, towards the Curie temperature T_C, where the transition between the ferromagnetic and the paramagnetic state occurs, the heat capacity is somewhat underestimated.

For all three phases, the contribution of the electronic entropy to the free energy is the smallest. For Fe, it amounts to a contribution of 4 meV/atom at 750 K, which is nevertheless much larger than the inaccuracy of 0.1 meV/atom at that temperature. This shows the importance of taking all three excitations into account for all materials. For Fe_4N the magnetic contribution to the heat capacity and free energy are larger than for bulk Fe. In contrast, $Fe_{16}N_2$ has a smaller magnetic heat capacity because this material is predicted to have the highest Curie temperature.

3.2. Thermal expansion

The (volumetric) thermal expansion coefficient is defined as

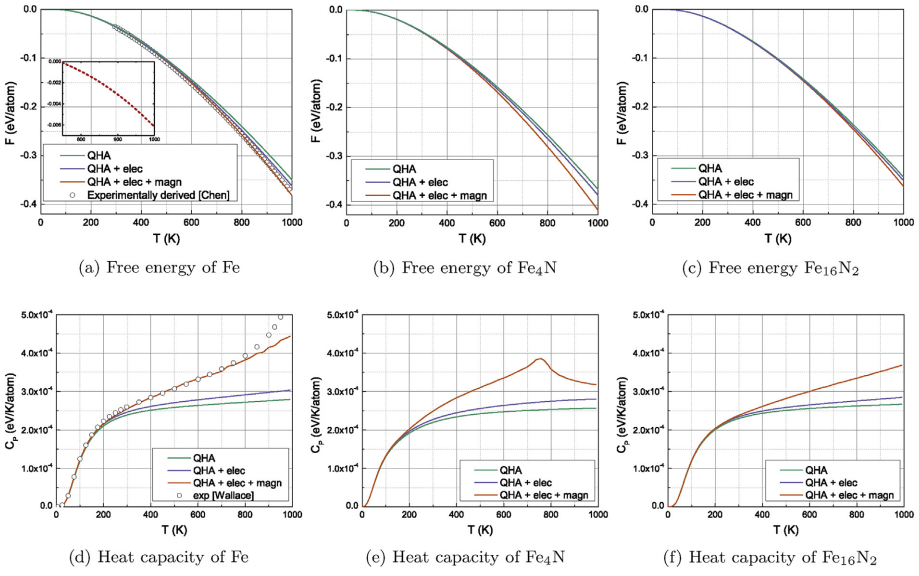

(a) Free energy of Fe (b) Free energy of Fe_4N (c) Free energy $Fe_{16}N_2$

(d) Heat capacity of Fe (e) Heat capacity of Fe_4N (f) Heat capacity of $Fe_{16}N_2$

Fig. 3. The free energies F [top row, (a)–(c)] and isobaric heat capacities C_P [bottom row, (d)–(f)] of the bulk phases Fe, Fe_4N and $Fe_{16}N_2$ from 0 to 1000 K. The vibrational contributions within the quasiharmonic approximation (QHA), the electronic contributions (elec) and the magnetic contributions (magn) are shown incrementally. For iron, the free energy is compared to the one experimentally derived by Chen et al. [66] and the heat capacity is compared to the one recommended by Desai [67]. Inset in a: The difference between the total calculated free energy and the experimentally derived free energy.

$$\alpha_V = \frac{1}{V}\left(\frac{\partial V}{\partial T}\right)_P. \quad (15)$$

It can be calculated from the derived equilibrium volumes over sufficiently small temperature intervals (10 K), using finite differences. In Fig. 4 this calculated coefficient is shown for Fe, Fe_4N and $Fe_{16}N_2$ as a function of temperature.

The DFT expansion coefficient of bulk Fe compares very well with experimental data, certainly considering the typical error of 0.7×10^{-5} K^{-1} for expansion coefficients derived with QHA [69]. The slight bump in the experimental coefficient that is not accounted for in the DFT result, stems from the volume dependence of the magnetic heat capacity [68], which is not taken into account in the calculations.

In the case of Fe_4N, an average expansion coefficient was derived experimentally from XRD measurements on powder samples [15]. It is seen that the DFT-obtained expansion severely underestimates that experimental one. Possibly, inaccuracies might be present in the experimental measurement because it was taken on a powder sample created from a deposited layer, whereas the calculated expansion is valid for an infinitely large bulk. Because the difference between experiment and DFT is so large, however, a critical assessment of the calculated result is needed to identify the various sources of theoretical inaccuracies.

The argument made for bulk Fe, that the volume dependence of the magnetic heat capacity is not accounted for in the QHA method as employed in this work, can be made for Fe_4N as well. This might be even more pronounced since it has a lower Curie temperature; $T_C = 750$ K compared to 1044 K for iron [70]. However, the error with respect to the experiment is so large that it cannot be solely explained by such a minor magnetic effect, which are usually secondary to lattice vibrational effects. If the deviation cannot be attributed to the thermodynamic approach, it must be rooted in the calculated energies and forces. For DFT calculations, the exchange-correlation functional is the main source of deviations from experiment. In this case, the main cause of the large deviation of the PBE functional in predicting the thermal expansion of Fe_4N is most likely the material's unique magneto-volume behavior. A large increase in magnetization occurs close to the equilibrium volume, which PBE is unable to describe well. [71], This volume-dependent magnetic effect can be explained by the covalent nature of the Fe-N bond. As the bond length shortens, the overlap of the 2*p* orbitals of the N atom with the 4*s* orbitals of the nearest-neighbor Fe atoms increases, causing more electron transfer to the N atom [72]. This in turn reduces the screening effect of the 4*s* shell on the 3*d* Fe electrons, causing electron transfer from the 3*d* orbitals of the second nearest-neighbor Fe atoms to those of the Fe atoms nearest to the N atom. Ultimately, compression thus results in a lower magnetic moment on the nearest-neighbor Fe atoms that bond with the N atom [73]. It moreover causes the Fe_4N to be very rigid in the direction of the Fe-N bond, *i.e.* the $<100>$ direction [74].

In an effort to verify that the functional is indeed the source of the discrepancy of the Fe_4N thermal expansion coefficient with respect to experiment, the PBE exchange-correlation functional was swapped for the LDA one. The latter functional differs from PBE in that it positions the LDA equilibrium volume of Fe_4N in the low-magnetization regime rather than at the crossing between low and high magnetization [71]. As can be seen in Fig. 5, the LDA functional does produce a much larger thermal expansion compared to the PBE functional. As expected, the experimental value lies between the LDA and PBE predictions, but the difference between them is much larger than for metals without any covalent character [75]. Although the observed inaccuracy of the Fe_4N thermal expansion might also be due to experimental errors, the large impact of the exchange-correlation functional on the calculated expansion coefficient remains a methodological problem. At this point, it is not clear whether there is another functional or another (feasible) level of theory that can provide a better description of both the covalent nature of the Fe-N bond, the unique magnetic behavior of Fe_4N and the $Fe_{16}N_2$ and bulk Fe phases.

Note that the large discrepancy between LDA and PBE regarding the volume-dependent behavior is not reflected in the QHA free energy. The LDA and PBE free energy only differ by about 3 meV/atom at 400 K (see Fig. 1 in supplementary information), which implies that phase stabilities are much more accurately obtained than the thermal expansion.

3.3. Bulk modulus

The temperature-dependent bulk modulus, or inverse of the

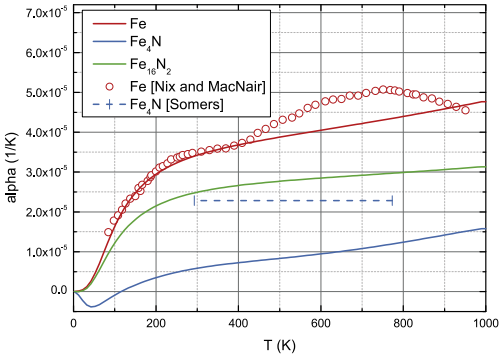

Fig. 4. DFT-calculated volumetric thermal expansion coefficients of Fe (red), Fe_4N (blue) and $Fe_{16}N_2$ (green). For iron, the experimental data from Nix and MacNair enable a comparison for almost the entire temperature interval [68]. For Fe_4N, there is only an average expansion coefficient between 293 and 773 K available. At all temperatures, however, the DFT-derived expansion coefficient for Fe_4N constitutes a severe underestimation. (For interpretation of the references to colour in this figure legend, the reader is referred to the Web version of this article.)

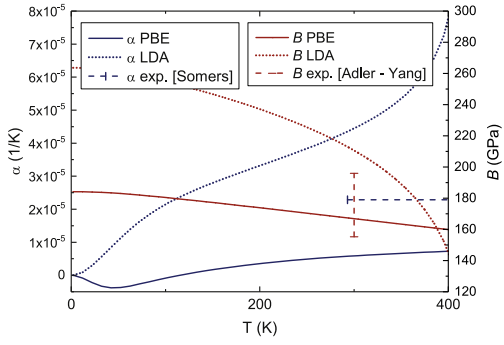

Fig. 5. A comparison between LDA (dotted lines) and PBE (solid lines) for the calculation of the bulk moduli B (red) and volumetric thermal expansion coefficients α (blue) of Fe_4N. For the bulk modulus, a large range of experimental values exists (dashed red bar) [76,77]. For the thermal expansion, the value determined by Somers et al. is an average for the temperature range 293 to 773 K [15]. (For interpretation of the references to colour in this figure legend, the reader is referred to the Web version of this article.)

compressibility,

$$B(T) = V_0 \left(\frac{\partial^2 F}{\partial V^2} \right)_T |_{V=V_0} \quad (16)$$

can be directly obtained from the above results and the derivatives of the analytic expressions for the various contributions to the free energy (Eqs. (5)–(9)). In Fig. 6 the bulk modulus is shown for all three phases. As far as Fe is concerned, the calculated bulk modulus at 0 K is too high by about 15 GPa compared to experimental data. This is in contrast to the typical trend for PBE, which usually underestimates bulk moduli by about 5% [78]. On the other hand, it is typical for magnetic materials to buck this trend, as a generalized-gradient approximation (GGA) such as PBE tends to overestimate the magnetic energy [79]. The slope of the Fe bulk modulus is reproduced quite well, with the experimental one being overall slightly less steep compared to the DFT result. Much fewer data are available on bulk moduli for Fe_4N and $Fe_{16}N_2$, because these phases usually only exist as precipitates or as a deposited layer. In fact, there are no experimental data for $Fe_{16}N_2$ whatsoever and the experimentally determined bulk moduli that are available for Fe_4N have a large spread (Fig. 6). A possible reason for these large experimental deviations, is the difference in measurement methodology. It varies from nanoindentation to high-pressure X-ray diffraction (XRD) measurements, both on powdered samples and on bulk-like samples [77]. The combination with the difficulty of obtaining pure samples makes it very cumbersome to compare different experimental procedures. The calculated Fe_4N bulk modulus falls in the range of the experimental values. The strong dependence on temperature moreover confirms the volume-sensitive behavior of Fe_4N compared to the other two materials. Just as was the case for the thermal expansion (Sec. 3.2), this volume-sensitive behavior causes a large discrepancy between the LDA and PBE functionals (Fig. 5).

3.4. Magnetic properties of the bulk phases

The magnetic contribution to the free energy is significant, even at temperatures well below the Curie temperature (Fig. 3), and thus requires a high degree of accuracy. It was found that this high accuracy can be reached through the rescaling procedure of Körmann et al., provided the Curie temperature is predicted accurately [23]. For this reason, effective nearest-neighbor magnetic exchange coefficients J_{ij} are sometimes fit to the experimental Curie temperature to obtain the magnetic heat capacity [20,24]. This work, however, aims to use a methodology also able to predict the Curie temperature. Therefore, the J_{ij} were determined from first principles and the Curie temperature was identified as the temperature at which the resulting heat capacity reaches its peak [85]. The quality of the predicted Curie temperature is then a measure for the accuracy of the magnetic free energy.

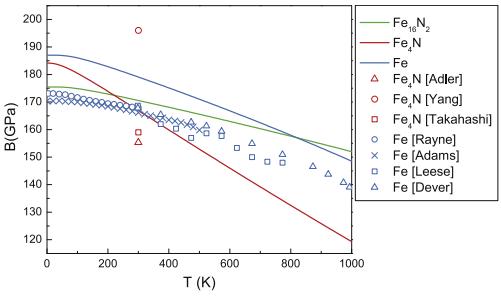

Fig. 6. DFT-calculated (line) and experimental (symbol) bulk moduli B for Fe, Fe_4N and $Fe_{16}N_2$. For Fe, a combination of data from different authors is made to cover the temperature range from 0 to 1000 K [81–84]. For Fe_4N, the three experimental data points are all at room temperature and cover a relatively large range (red symbols) [76],[77],[80]. (For interpretation of the references to colour in this figure legend, the reader is referred to the Web version of this article.)

For Fe and Fe_4N, the DFT-derived Curie temperature (Fig. 7) corresponds very well with the experimental one. It is also evident that the disappearance of the magnetization is a poor measure to determine the transition to the paramagnetic state; this is an experimental issue as well [86]. The finite size of the simulation cells is responsible for some remanent magnetization above the critical temperature. For $Fe_{16}N_2$ the experimental Curie temperature is much lower than the one derived from the simulations. The experimental magnetization goes to zero when 800 K is reached, but with the exchange coefficients and magnetization derived from DFT, a critical temperature of about 1300 K is found. In an extensive evaluation of different methods to obtain the Curie temperature for $Fe_{16}N_2$, Ke et al. concluded that the experimental value is most likely significantly too low [87]. Instead, it is proposed that $Fe_{16}N_2$ has a higher Curie temperature than the one experimentally derived and also higher than the one found for Fe. For this reason, unfilled symbols are used to show the experimental results for the magnetization of $Fe_{16}N_2$ in Fig. 7.

3.5. Interstitial nitrogen defect

The defect free energy of interstitial nitrogen is obtained using the supercell method. In this approach, the crystallographic unit cell of the bulk material is multiplied and a defect is inserted. In the case of the nitrogen interstitial, a N atom is inserted in the bulk Fe supercell on an octahedral position (see Fig. 1c). The local distortion caused by the defect is captured by optimizing all atomic positions. It is debatable whether the volume and shape of the defect supercell should be optimized as well. On the one hand, maintaining the bulk geometry helps to isolate the defect from its periodic images, as it cuts out long-range elastic interactions. However, this imposes a stress on the supercell which depends on the N concentration. On the other hand, if one wishes to remove those stresses by allowing full optimization of the shape and size of the unit cell, a larger computational investment might be necessary. Both approaches were evaluated for different supercell sizes. The energy of solution U_{sol} is obtained by subtracting the DFT-obtained total energy of the defect-free supercell and the isolated N_2 molecule from the total energy of the supercell with the defect. In Fig. 8 the dependence of U_{sol} on the used supercell size is shown. It shows that the constant-pressure (stress-free) and constant-volume approach converge towards a common limit, ultimately yielding the same defect energy as supercell size is increased. Using a 250-atom supercell for either method a precision of the calculation of about 10 meV/defect can be achieved for U_{sol}. The 250-atom $U_{sol} = 0.133\ eV$ of the constant-volume approach was used in the remainder of this work, because that approach converges somewhat more rapidly.

Insight in the phase equilibrium between Fe_4N, $Fe_{16}N_2$ and $Fe_{[N]}$ (Sec. 3.6) requires accounting for the entropy of the defect as well. In Fig. 9 the configurational contribution is shown to be largest, but both the vibrational and the electronic free energy have to be taken into account as well. The electronic part can be obtained in a similar way as for bulk materials. For the vibrational contribution, full phonon spectra are calculated for the supercells containing the defect and QHA is used. Because the presence of the N atom in the

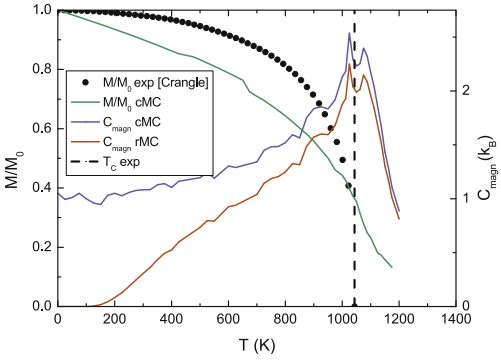

(a) Fe

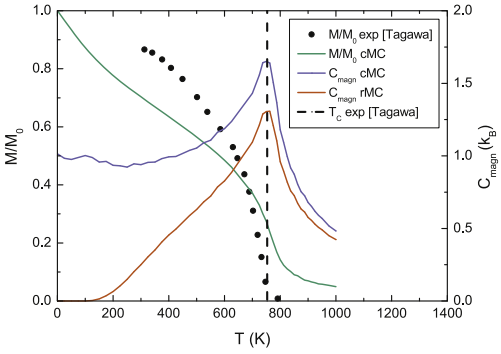

(b) Fe_4N

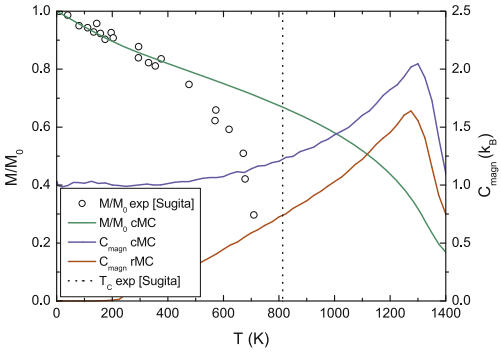

(c) $Fe_{16}N_2$

Fig. 7. Calculated magnetization (M/M_0) and magnetic contribution C_{magn} to the heat capacity for Fe, Fe_4N and $Fe_{16}N_2$. Experimentally measured magnetizations and subsequently derived Curie temperatures are included for all three phases (black) [70,88,89]. The experimental data for the magnetization of $Fe_{16}N_2$ are shown in unfilled circles to emphasize their problematic nature (see text). To compare the experimental magnetizations with those derived from the classical Monte Carlo (cMC) simulations, both are normalized to their respective magnetizations at 0 K. For the heat capacity, both the direct result from the cMC simulations (blue) and the rescaled result (rMC), (red) are presented, the latter serving as approximation for the quantum Monte Carlo result. (For interpretation of the references to colour in this figure legend, the reader is referred to the Web version of this article.)

Fe matrix breaks most of the symmetry, a large number of force calculations is then necessary to obtain the phonon spectra. Alternatively, the less expensive partial Hessian method can be used, which only requires the frequencies of the N atom in a fixed Fe matrix. The three frequencies obtained can be used to apply a simplified form of Eq. (9). From Fig. 9 it can be seen the differences between feasible supercell sizes are still quite large. An uncertainty of 0.2 eV/defect remains for a 54-atom cell, which is as large as for the partial Hessian method that is also not sufficiently precise. This large uncertainty is not surprising; it is the same order of magnitude as for U_{sol} (see Fig. 8). Ultimately, by using a highly converged U_{sol} 250-atom and the vibrational and electronic entropies from a 128-atom supercell, one expects a remaining uncertainty of 10 meV/atom for the vibrational contribution. Combined with the uncertainty for 10K (U_{sol}), this results in a total uncertainty of 14 – 20 meV/atom.

3.6. Phase equilibria

With the free energies of Fe, Fe_4N, $Fe_{16}N_2$ and $Fe_{[N]}$, all information is available to predict their phase equilibria, resolving the experimental uncertainties that have hindered insight and further development of the Fe-N system. The question of the (meta)stability of $Fe_{16}N_2$, for example, is still a contemporary topic [90]. The driving force ΔF for the formation of $Fe_{16}N_2$ from Fe_4N and $Fe_{[N]}$ is

$$\Delta F(T) = F_{Fe_{16}N_2}(T) - \frac{2-18c_{lim}}{1-5c_{lim}}F_{Fe_4N}(T) - \frac{8}{1-5c_{lim}}F_{Fe}(T), \tag{17}$$

if one assumes the transformation takes place in a large environment of bulk Fe with interstitial N present in equilibrium concentration c_{lim} (see further). The free energy difference can be obtained from the calculated free energies at equilibrium volumes V_0 in this work and is presented in Fig. 10. We find that $Fe_{16}N_2$ is stable at low temperatures ($\Delta F < 0$) and decomposition becomes energetically favorable above 390 K ($\Delta F > 0$). This is consistent with the experimental finding that decomposition starts between 470 K and 520 K. The experimentally higher decomposition temperature is explained by the required activation energy for N diffusion [87,91]. In experiment too, there is an indication that $Fe_{16}N_2$ becomes thermodynamically unstable around 400 K, *i.e.* before decomposition occurs. The temperature-dependent change in c/a ratio, measured very precisely by Widenmeyer et al. [91], shows a sharp rise starting from 400 – 450 K (Fig. 10). Widenmeyer et al. proposed that this stems from a loss of order of the N atoms on the interstitial sublattice of $Fe_{16}N_2$, thus suggesting a transition to a disordered Fe_8N phase. As shown in Fig. 10, the temperature-dependent QHA c/a ratio, derived from the c/a ratio of the cell optimized at the temperature-dependent equilibrium volume, is practically invariant with temperature. This strengthens the argument that the experimentally observed variation is caused by loss of N ordering, as the Natoms were kept ordered on their sublattice in the calculations. It also sheds a new light on the experimentally derived Curie temperature for $Fe_{16}N_2$ [92]. The measured drop in magnetization becomes more pronounced from 400 K onward (Fig. 7), the point where $Fe_{16}N_2$ becomes thermally unstable according to the DFT result. Consequently, the magnetizations measured above 400 K, and the derived Curie temperature, should

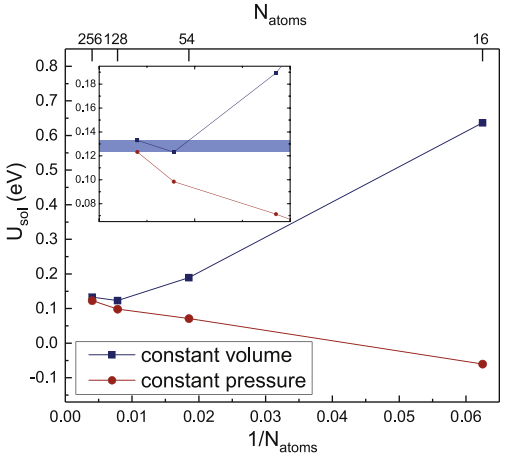

Fig. 8. Convergence of the N interstitial defect energy at 0 K as a function of inverse supercell size. The absolute value of the defect energy is with reference to the N_2 gaseous state: $Fe_{solid} + \frac{1}{2}N_2 \rightarrow Fe_{[N],solid}$. Inset: The convergence for the larger supercells in more detail. A residual uncertainty of 10 meV/defect remains (blue rectangle). (For interpretation of the references to colour in this figure legend, the reader is referred to the Web version of this article.)

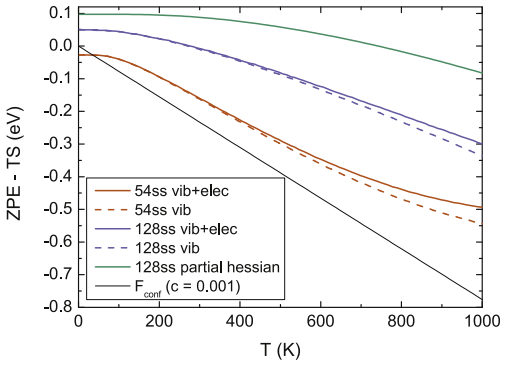

Fig. 9. A comparison of the different methods to obtain the finite-temperature energetic contributions for N in solid solution in Fe. The configurational part, shown here for a typical concentration of 0.1 at.% is always the largest, but both the electronic and vibrational free energies cannot be neglected. In comparison with the 128-atom supercell, the simple partial Hessian approach (see text) yields frequencies that are overestimated, whereas a 54-atom supercell underestimates the frequencies. (For interpretation of the references to colour in this figure legend, the reader is referred to the Web version of this article.)

be associated with the disordered Fe_8N structure.

To complete the phase diagram for $Fe_{[N]}$, Fe_4N and $Fe_{16}N_2$, the concentration limit of solubility $c_{lim}(T)$ can be derived from the defect free energy of the N interstitial F_{def}, the free energy of Fe, the free energy of Fe_4N and the free energy of $Fe_{16}N_2$:

$$4F_{Fe}(T) + F_{def}(T, c_{lim}(T)) = F_{Fe_4N}(T). \quad (18)$$

$$16F_{Fe}(T) + 2F_{def}(T, c_{lim}(T)) = F_{Fe_{16}N_2}(T). \quad (19)$$

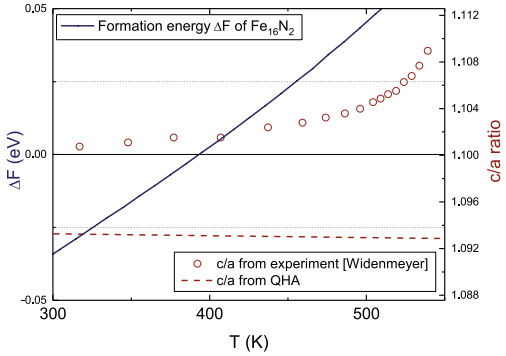

Fig. 10. Left axis (blue): from the DFT calculations, it can be concluded that $Fe_{16}N_2$ becomes thermodynamically unstable with respect to dissociation into Fe_4N and bulk Fe (solid line) above 390 K. Right axis (red): a comparison of the experimental c/a ratio of $Fe_{16}N_2$ (circles) [91] with the one derived via the quasiharmonic approximation (dashed line). The sharp increase starting at 400–450 K measured in experiment is not observed computationally (see text for interpretation). (For interpretation of the references to colour in this figure legend, the reader is referred to the Web version of this article.)

The final phase diagram, with all three phase equilibria, is presented in Fig. 11. The computationally derived solubility limit of N in bulk Fe is compared to the experimental data assembled by Wriedt et al. [29]. In the case of the solvus, good correspondence with experimental data is achieved by using the defect free energy from the 128-atom supercell. The large discrepancy with the 54-atom thus shows the importance of using this larger supercell. For the phase boundary between $Fe_{16}N_2$ and its dissociation in Fe_4N and bulk Fe, no experimental data are available, but the accuracy is expected to be very high. As discussed in Sec. 3.1, the free energy for Fe is very accurate below half of its melting temperature. Because of the similarity of Fe_4N and $Fe_{16}N_2$ and the correct calculation of the Curie temperatures, the same is expected for these bulk phases.

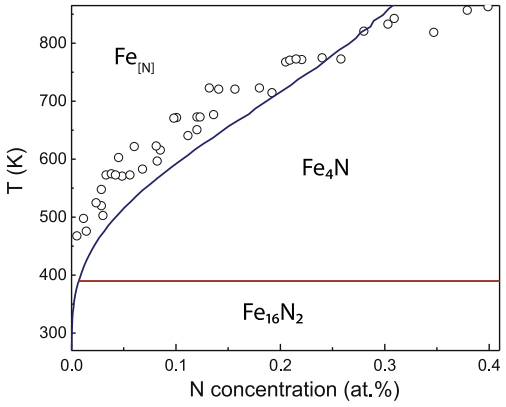

Fig. 11. The DFT-obtained phase diagram of $Fe_{[N]}$, Fe_4N and $Fe_{16}N_2$. Experimental data for the limit of solubility of N in Fe are included for comparison (circles) [29]

4. Conclusion

Despite the industrial importance of nitriding for the post-treatment of steel, there is still a lack of understanding with respect to the properties of the governing Fe-N phases. In this work, we established the thermodynamic behavior of $Fe_{16}N_2$, Fe_4N and Fe with N in solid solution and used it to elucidate the Fe-N phase diagram in the low-nitrogen limit (see Fig. 10). Phase equilibria were determined using density-functional theory, which avoids the need for any experimental input. This is particularly useful for Fe_4N and $Fe_{16}N$, for which large homogeneous samples are not experimentally available. Vibrational contributions to the free energy were derived with the quasiharmonic approximation, while the magnetic free energy was calculated using Monte Carlo simulations based on a Heisenberg model. Several potential sources of numerical errors were identified in the process, leading in most cases to limited errors. The largest error bar originates from the supercell size used to model the free energy of interstitial nitrogen; this error is about 14 – 20 meV/defect at 0 K using a 128-atom supercell.

Using our calculations, we were able to determine the free energy, heat capacity, thermal expansion and bulk modulus of Fe, Fe_4N and $Fe_{16}N_2$ as a function of temperature. While experimental data are available for Fe which allowed us to check the validity of our first-principles approach, these quantities are mostly not available for the Fe_4N and $Fe_{16}N_2$ phases, as these materials are experimentally hard to manufacture in bulk. Only for the thermal expansion coefficient of Fe_4N, a strong underestimation of the experimental result was found. A comparison of the LDA and PBE exchange-correlation functional revealed that the unique coupling between magnetism and crystal volume exacerbates the impact of functional inadequacies. A better description of the volume dependence of Fe_4N therefore requires the development of improved exchange-correlation functionals, which are able to capture both the covalent and magnetic characteristics correctly. This is in line with the conclusion from Blancá et al. [71] Furthermore, minor improvements can be made by evaluating the phonon-magnon coupling contributions for Fe_4N and $Fe_{16}N_2$ and explicit anharmonicity for the nitrogen defect.

Based on DFT-calculated free energies, the phase diagram of $Fe_{[N]}$-Fe_4N and $Fe_{16}N_2$ was constructed, yielding an accurate representation of the nitrogen solvus and providing a closer view on the stability of $Fe_{16}N_2$. We find $Fe_{16}N_2$ to be thermodynamically stable at low temperatures and to decompose into Fe_4N and Fe around 390 K. Experimental dissociation happens above 470 K, with the difference attributed to the required activation energy for nitrogen mobility. In addition, we note that the experimentally established Curie temperature for $Fe_{16}N_2$ cannot be attributed to the pure $Fe_{16}N_2$ phase, but is affected by the experimentally observed loss of nitrogen order between 400 and 450 K. This is also supported by a comparison between experimental measurements of the c/aratio as a function of temperature and our quasiharmonic DFT results.

Our results fill in a long-standing gap in the knowledge on the Fe-N system. The predicted free energies, heat capacities, equilibrium volumes and bulk moduli can now be used in larger-scale approaches, such as phase field models [9]. These approaches can aid in describing precipitation and transformation in the Fe-N system from a more macroscopic point of view. This is essential to increase the applicability of nitriding and lays the foundations to understand ternary nitrogen-containing compounds.

Acknowledgments

Sam De Waele and Stefaan Cottenier acknowledge financial support from OCAS NV by an OCAS–endowed PhD position and by an OCAS–endowed chair at Ghent University, respectively. This work moreover benefited from the Research Foundation Flanders (FWO) through the personal postdoctoral fellowship of Kurt Lejaeghere and project Nr. G0E0116N. The computational resources and services used in this work were provided by the VSC (Flemish Supercomputer Center), funded by the Research Foundation Flanders (FWO) and the Flemish Government – department EWI.

Appendix A. Supplementary data

Supplementary data to this article can be found online at https://doi.org/10.1016/j.jallcom.2018.09.356.

References

[1] G. Miyamoto, Y. Tomio, H. Aota, K. Oh-ishi, K. Hono, T. Furuhara, Mater. Sci. Technol. 27 (2011) 742.
[2] E.J. Mittemeijer, in: E.J. Mittemeijer, M.A.J. Somers (Eds.), Thermochemical Surface Engineering of Steels, Woodhead Publishing, Oxford, 2015, pp. 313–340.
[3] M.A.J. Somers, T.L. Christiansen, in: E.J. Mittemeijer, M.A.J. Somers (Eds.), Thermochemical Surface Engineering of Steels, Woodhead Publishing, Oxford, 2015, pp. 557–579.
[4] O. Singh, H.K. Malik, R.P. Dahiya, P.K. Kulriya, J. Alloys Compd. 710 (2017) 253.
[5] W. Dal'Maz Silva, J. Dulcy, J. Ghanbaja, A. Redjaïmia, G. Michel, S. Thibault, T. Belmonte, Mater. Sci. Eng., A 693 (2017) 225.
[6] X.C. Xiong, Élaboration et genèse des microstructures dans les "aciers" fer-azote, Vandoeuvre-les-Nancy, INPL, 2008.
[7] L.C. Gontijo, R. Machado, E.J. Miola, L.C. Casteletti, P.A.P. Nascente, Surf. Coating. Technol. 183 (2004) 10.
[8] H. Göhring, A. Leineweber, E.J. Mittemeijer, Metall. Mater. Trans. A 46 (2015) 3612.
[9] H. Liu, Y. Gao, J.Z. Liu, Y.M. Zhu, Y. Wang, J.F. Nie, Acta Mater. 61 (2013) 453.
[10] H. Göhring, O. Fabrichnaya, A. Leineweber, E.J. Mittemeijer, Metall. Mater. Trans. A 47 (2016) 6173.
[11] S. Shang, A.J. Böttger, Acta Mater. 53 (2005) 255.
[12] P. Hohenberg, W. Kohn, Phys. Rev. 136 (1964) B864.
[13] W. Kohn, L. Sham, Phys. Rev. 140 (1965) 1133.
[14] H. Grabke, Ber. Bunsen Ges. Phys. Chem. 73 (1969) 596.
[15] M.A.J. Somers, N.M. van der Pers, D. Schalkoord, E.J. Mittemeijer, Metall. Trans. A 20 (1989) 1533.
[16] G. Ceder, M. De Graef, L. Delaey, J. Kulik, D. de Fontaine, Phys. Rev. B 39 (1989) 381.
[17] B.J. Kooi, M.A.J. Somers, E.J. Mittemeijer, Metall. Mater. Trans. A 27 (1996) 1063.
[18] M.I. Pekelharing, A.J. Böttger, E.J. Mittemeijer, Phil. Mag. 83 (2003) 1775.
[19] M.I. Pekelharing, A.J. Böttger, Comput. Mater. Sci. 45 (2009) 561.
[20] F. Körmann, Y. Ikeda, B. Grabowski, M.H.F. Sluiter, npj Comput. Mater. 3 (2017) 36.
[21] G. Bonny, N. Castin, C. Domain, P. Olsson, B. Verreyken, M.I. Pascuet, D. Terentyev, Phil. Mag. 0 (2016) 1.
[22] N.D. Mermin, Phys. Rev. 137 (1965) A1441.
[23] F. Körmann, A. Dick, T. Hickel, J. Neugebauer, Phys. Rev. B 81 (2010), 134425.
[24] A. Dick, F. Körmann, T. Hickel, J. Neugebauer, Phys. Rev. B 84 (2011), 125101.
[25] K.H. Jack, J. Alloys Compd. 222 (1995) 160.
[26] K.H. Jack, Acta Crystallogr. 3 (1950) 392.
[27] C. Domain, C.S. Becquart, J. Foct, Phys. Rev. B 69 (2004), 144112.
[28] D.C. Wallace, Thermodynamics of Crystals, Courier Corporation, 1998.
[29] H.A. Wriedt, N.A. Gokcen, R.H. Nafziger, Bull. Alloy Phase Diagrams 8 (1987) 355.
[30] H.V. Keer, Principles of the Solid State, New Age International, 1993.
[31] B. Grabowski, P. Söderlind, T. Hickel, J. Neugebauer, Phys. Rev. B 84 (2011) 214107.
[32] F. Birch, Phys. Rev. 71 (1947) 809.
[33] G. Kresse, J. Furthmüller, Comput. Mater. Sci. 6 (1996a) 15.
[34] G. Kresse, J. Furthmüller, Phys. Rev. B 54 (1996b) 11169.
[35] G. Kresse, D. Joubert, Phys. Rev. B 59 (1999) 1758.
[36] G. Kresse, M. Marsman, J. Furthmüller, VASP the GUIDE, 2015.
[37] K. Lejaeghere, G. Bihlmayer, T. Björkman, P. Blaha, S. Blügel, V. Blum, D. Caliste, I.E. Castelli, S.J. Clark, A.D. Corso, S. di Gironcoli, T. Deutsch, J.K. Dewhurst, I. di Marco, C. Draxl, M. Dułak, O. Eriksson, J.A. Flores-Livas, K.F. Garrity, L. Genovese, P. Giannozzi, M. Giantomassi, S. Goedecker, X. Gonze, O. Grånäs, E.K.U. Gross, A. Gulans, F. Gygi, D.R. Hamann, P.J. Hasnip, N.A.W. Holzwarth, D. Iuşan, D.B. Jochym, F. Jollet, D. Jones, G. Kresse, K. Koepernik, E. Küçükbenli, Y.O. Kvashnin, I.L.M. Locht, S. Lubeck, M. Marsman, N. Marzari, U. Nitzsche, L. Nordström, T. Ozaki, L. Paulatto, C.J. Pickard, W. Poelmans, M.I.J. Probert, K. Refson, M. Richter, G.-M. Rignanese, S. Saha, M. Scheffler, M. Schlipf, K. Schwarz, S. Sharma, F. Tavazza, P. Thunström, A. Tkatchenko, M. Torrent, D. Vanderbilt, M.J. van Setten, V. Van Speybroeck, J.M. Wills, J.R. Yates, G.-

X. Zhang, S. Cottenier, Science 351 (2016) aad3000.
[38] J.P. Perdew, K. Burke, M. Ernzerhof, Phys. Rev. Lett. 77 (1996) 3865.
[39] J.P. Perdew, A. Zunger, Phys. Rev. B 23 (1981) 5048.
[40] K. Kunc, R.M. Martin, Phys. Rev. Lett. 48 (1982) 406.
[41] A. Togo, I. Tanaka, Scripta Mater. 108 (2015) 1.
[42] M. Methfessel, A.T. Paxton, Phys. Rev. B 40 (1989) 3616.
[43] N.M. Rosengaard, B. Johansson, Phys. Rev. B 55 (1997) 14975.
[44] M. Pajda, J. Kudrnovský, I. Turek, V. Drchal, P. Bruno, Phys. Rev. B 64 (2001), 174402.
[45] M. Ležaić, P. Mavropoulos, S. Blügel, Appl. Phys. Lett. 90 (2007), 082504.
[46] A.V. Ruban, S. Khmelevskyi, P. Mohn, B. Johansson, Phys. Rev. B 75 (2007), 054402.
[47] G.Y. Gao, K.L. Yao, E. Şaşoğlu, L.M. Sandratskii, Z.L. Liu, J.L. Jiang, Phys. Rev. B 75 (2007), 174442.
[48] F. Körmann, A. Dick, B. Grabowski, B. Hallstedt, T. Hickel, J. Neugebauer, Phys. Rev. B 78 (2008), 033102.
[49] F. Körmann, A. Dick, T. Hickel, J. Neugebauer, Phys. Rev. B 83 (2011), 165114.
[50] J. Korringa, Physica 13 (1947) 392.
[51] W. Kohn, N. Rostoker, Phys. Rev. 94 (1954) 1111.
[52] H. Ebert et al., The Munich SPR-KKR package.
[53] H. Ebert, D. Ködderitzsch, J. Minár, Rep. Prog. Phys. 74 (2011), 096501.
[54] A.I. Liechtenstein, M.I. Katsnelson, V.A. Gubanov, J. Phys. F Met. Phys. 14 (1984) L125.
[55] N. Metropolis, A.W. Rosenbluth, M.N. Rosenbluth, A.H. Teller, E. Teller, J. Chem. Phys. 21 (1953) 1087.
[56] A.F. Albuquerque, F. Alet, P. Corboz, P. Dayal, A. Feiguin, S. Fuchs, L. Gamper, E. Gull, S. Gürtler, A. Honecker, R. Igarashi, M. Körner, A. Kozhevnikov, A. Läuchli, S.R. Manmana, M. Matsumoto, I.P. McCulloch, F. Michel, R.M. Noack, G. Pawłowski, L. Pollet, T. Pruschke, U. Schollwöck, S. Todo, S. Trebst, M. Troyer, P. Werner, S. Wessel, J. Magn. Magn. Mater. 310 (2007) 1187.
[57] B. Bauer, L.D. Carr, H.G. Evertz, A. Feiguin, J. Freire, S. Fuchs, L. Gamper, J. Gukelberger, E. Gull, S. Guertler, A. Hehn, R. Igarashi, S.V. Isakov, D. Koop, P.N. Ma, P. Mates, H. Matsuo, O. Parcollet, G. Pawłowski, J.D. Picon, L. Pollet, E. Santos, V.W. Scarola, U. Schollwöck, C. Silva, B. Surer, S. Todo, S. Trebst, M. Troyer, M.L. Wall, P. Werner, S. Wessel, J. Stat. Mech. Theor. Exp. 2011 (2011) P05001.
[58] P.W. Anderson, Solid State Phys. 14 (1963) 99.
[59] A.W. Sandvik, J. Kurkijärvi, Phys. Rev. B 43 (1991) 5950.
[60] P. Henelius, A.W. Sandvik, Phys. Rev. B 62 (2000) 1102.
[61] H. Nyquist, Phys. Rev. 32 (1928) 110.
[62] H.B. Callen, T.A. Welton, Phys. Rev. 83 (1951) 34.
[63] A. Glensk, B. Grabowski, T. Hickel, J. Neugebauer, Phys. Rev. Lett. 114 (2015), 195901.
[64] T. Hickel, B. Grabowski, F. Körmann, J. Neugebauer, J. Phys. Condens. Matter 24 (2012), 053202.
[65] Mittemeijer, Fundamentals of Nitriding and Nitrocarburizing - Heat Treating Society.
[66] Q. Chen, Z. Jin, Metall. Mater. Trans. A 26 (1995) 417.
[67] P.D. Desai, J. Phys. Chem. Ref. Data 15 (1986) 967.
[68] F.C. Nix, D. MacNair, Phys. Rev. 60 (1941) 597.
[69] K. Lejaeghere, J. Jaeken, V. Van Speybroeck, S. Cottenier, Phys. Rev. B 89 (2014), 014304.
[70] K. Tagawa, E. Kita, A. Tasaki, Jpn. J. Appl. Phys. 21 (1982) 1596.
[71] E.L. Peltzery y Blancá, J. Desimoni, N.E. Christensen, H. Emmerich, S. Cottenier, Phys. Status Solidi (B) 246 (2009) 909.
[72] W. Zhou, L.-J. Qu, Q.-M. Zhang, D.-S. Wang, Phys. Rev. B 40 (1989) 6393.
[73] D. Li, J.W. Roh, K.J. Jeon, Y.S. Gu, W. Lee, Phys. Status Solidi (B) 245 (2008) 2581.
[74] T. Gressmann, M. Wohlschlögel, S. Shang, U. Welzel, A. Leineweber, E.J. Mittemeijer, Z.K. Liu, Acta Mater. 55 (2007) 5833.
[75] B. Grabowski, T. Hickel, J. Neugebauer, Phys. Rev. B 76 (2007), 024309.
[76] J.F. Adler, Q. Williams, J. Geophys. Res. Solid Earth 110 (2005), B01203.
[77] C.L. Yang, M.M. Abd-Elmeguid, H. Micklitz, G. Michels, J.W. Otto, Y. Kong, D.S. Xue, F.S. Li, J. Magn. Magn. Mater. 151 (1995) L19.
[78] K. Lejaeghere, V. Van Speybroeck, G. Van Oost, S. Cottenier, Crit. Rev. Solid State Mater. Sci. 39 (2013) 1.
[79] D.J. Singh, J. Ashkenazi, Phys. Rev. B 46 (1992) 11570.
[80] T. Takahashi, J. Burghaus, D. Music, R. Dronskowski, J.M. Schneider, Acta Mater. 60 (2012) 2054.
[81] J.A. Rayne, B.S. Chandrasekhar, Phys. Rev. 122 (1961) 1714.
[82] J.J. Adams, D.S. Agosta, R.G. Leisure, H. Ledbetter, J. Appl. Phys. 100 (2006), 113530.
[83] J. Leese, A.E. Lord, J. Appl. Phys. 39 (1968) 3986.
[84] D. Dever, J. Appl. Phys. 43 (1972) 3293.
[85] J. Weber, Phys. Rev. 101 (1956) 1620.
[86] R.G. Harrison, J. Appl. Phys. 115 (2014), 033901.
[87] L. Ke, K.D. Belashchenko, M. van Schilfgaarde, T. Kotani, V.P. Antropov, Phys. Rev. B 88 (2013), 024404.
[88] J. Crangle, G.M. Goodman, Proc. Roy. Soc. Lond. A 321 (1971) 477.
[89] Y. Sugita, H. Takahashi, M. Komuro, K. Mitsuoka, A. Sakuma, J. Appl. Phys. 76 (1994) 6637.
[90] S. Yamamoto, R. Gallage, Y. Ogata, Y. Kusano, N. Kobayashi, T. Ogawa, N. Hayashi, K. Kohara, M. Takahashi, M. Takano, Chem. Commun. 49 (2013) 7708.
[91] M. Widenmeyer, T.C. Hansen, R. Niewa, Z. Anorg. Allg. Chem. 639 (2013) 2851.
[92] Y. Sugita, J. Appl. Phys. 70 (1991) 5977.

Paper II

Precipitation in simultaneously nitrided and aged Mo–containing maraging steel

A. Verdiere, C. Hofer, S. De Waele, V. Bliznuk, S. Primig,
S. Cottenier, M.D. Tran, B. Pennings, L.A.I. Kestens and R.H. Petrov

Materials Characterization, **2017**, *131*, 21–30

S. De Waele perfomed the DFT calculations, interpreted the obtained calculated structures and aided in preparing the manuscript.
Reprinted with permission.

Materials Characterization 131 (2017) 21–30

Contents lists available at ScienceDirect

Materials Characterization

journal homepage: www.elsevier.com/locate/matchar

Precipitation in simultaneously nitrided and aged Mo-containing maraging steel

An Verdiere[a,*], Christina Hofer[b], Sam De Waele[a,c], Vitaliy Bliznuk[a], Sophie Primig[b,d], Stefaan Cottenier[a,c], Minh Duc Tran[e], Bert Pennings[e], Leo A.I. Kestens[a,f], Roumen H. Petrov[a,f]

[a] Department of Materials Science and Engineering, UGent, Belgium
[b] Department of Physical Metallurgy and Materials Testing, Montanuniversität Leoben, Austria
[c] Center for Molecular Modeling, UGent, Belgium
[d] School of Materials Science and Engineering, University of New South Wales, Australia
[e] Bosch Transmission Technology, Advanced Engineering, Tilburg, The Netherlands
[f] Department of Materials Science and Engineering, TUDelft, The Netherlands

ARTICLE INFO

Keywords:
Nitriding
Maraging steel
Precipitation
Transmission electron microscopy (TEM)
Atom probe tomography (APT)
Density functional theory (DFT)

ABSTRACT

The excellent mechanical properties of maraging steels are ascribed to nanometer-sized intermetallics which precipitate during aging in the ductile very low carbon Ni-martensite. Their wear and fatigue properties can be improved by nitriding. The non-equilibrium precipitation reactions in Fe-Ni-Co-Mo maraging steels are studied during an aging heat treatment executed in a nitriding atmosphere. The precipitates formed during the initial stages of precipitation are characterized with transmission electron microscopy and atom probe tomography. Spherical intermetallic precipitates having a diameter of around 3 nm were detected in the aged, bulk material. These ω-type precipitates formed during the early stages of aging, have a trigonal crystal lattice and their chemical composition is close to $(Fe,Ni)_7Mo_2$. In the nitrided layer, Mo-N disc-shaped nitrides on the {100} martensitic lattice having a diameter of 3 to 4 nm were found but their exact crystal structure could not be determined with microstructural characterization techniques. Density functional theory calculations confirmed that a single layer of Mo atoms, substituting Fe on the {100} plane of the Fe-matrix, is stable and showed that the N atoms prefer to be in the Mo-layer, on the octahedral sites with Fe as nearest neighbors.

1. Introduction

One of the best combinations of high strength and toughness in engineering alloys can be found in maraging steels. These very low carbon Fe-Ni alloys are strengthened by homogeneously distributed nanometer-sized intermetallics which are formed during the final aging step [1]. After quenching, soft and ductile lath martensite containing a high density of dislocations is formed. Nucleation of intermetallic precipitates during the aging step can occur quickly on these dislocations and the growth can proceed by dislocations serving as diffusion channels for solute atoms from the matrix [2]. However, randomly distributed precipitates throughout the matrix were also reported in maraging steels aged below 450 °C [3]. For several high performance applications such as aerospace and tooling, Fe-Ni-Co-Mo maraging steels are used due to their excellent mechanical properties and especially fatigue response even in the very high cycle fatigue domain [4].

A number of studies on aging in Fe-Ni-Co-Mo maraging steels have been carried out [3,5,6], but the current knowledge concerning the precursor phases formed during the early stages of precipitation is not yet complete. Main difficulties in the characterization are the ultrafine scale of the microstructure, absence of stable equilibrium phases and closely matching crystal structures and interplanar spacings of the phases [6]. Observed intermetallics in these Ti-free maraging steels are initially the metastable and coherent ω-phase, followed by Ni_3Mo at the earlier aging stage [1,7], and more stable Fe_7Mo_6 after prolonged aging [8].

Due to the absence of carbides, one of the limitations of maraging steels is the moderate wear resistance in comparison to conventional tool steels [9]. To improve their performance in severe loading conditions, the case can be additionally hardened e.g. by nitriding. During this low temperature thermochemical treatment, atomic N diffuses into the material, resulting in an increased surface hardness, wear and fatigue resistance. In general, a compound layer consisting of ε and/or γ' Fe-nitrides and an underlying nitrogen diffusion zone are formed during nitriding. The compound layer improves tribological and anticorrosion properties but it can be undesirable due to its porosity and brittleness.

* Corresponding author.
E-mail address: an.verdiere@ugent.be (A. Verdiere).

http://dx.doi.org/10.1016/j.matchar.2017.06.014
Received 29 October 2016; Received in revised form 12 June 2017; Accepted 12 June 2017
Available online 13 June 2017
1044-5803/

Therefore, in many industrial applications the formation of this compound layer is minimized or avoided by controlling the process parameters, especially the nitriding potential in the case of gas nitriding [10,11].

Steels containing alloying elements with a high affinity for nitrogen form finely dispersed and hard alloying element nitrides in the diffusion zone. These nitrides effectively contribute to the strengthening, while diffused nitrogen in the supersaturated diffusion zone is only responsible for a very small solid-solution strengthening effect [12]. Due to the volumetric misfit between the matrix and these fine nitrides, strain fields surrounding the precipitates develop. In order to counteract the desired expansion, compressive residual stresses evolve and contribute significantly to improving the fatigue resistance [13]. The alloying elements are classified by the Me-N interaction parameter, defined as the ratio (per unit volume of precipitate) of the Gibbs energy of formation of the precipitate and the misfit-strain energy induced in the precipitate/matrix system [10]. Alloying elements such as Ti, V and Cr having a strong Me-N interaction can instantaneously precipitate [14], while alloying elements such as Al, Si and Mo have a weaker interaction because of a large volume misfit. The latter will only precipitate when the N supersaturation in the surface layer is high enough [12] and the precipitation proceeds through a sequence of metastable phases until the equilibrium phase is reached [15]. Besides, the precipitation can be enhanced by the presence of dislocations in the matrix [10].

Several studies on nitriding of Mo-containing steels have been conducted and many different compositions of intermediate and equilibrium nitrides were identified. It is reported that during nitriding, the morphology of the precipitates changes from thin coherent platelets through semi-coherent plates to incoherent spheres [16]. The sequence of precipitation is proposed in [15] as changing respectively from bct $(Fe,Mo)_{16}N_2$ [17], to fcc $(Fe,Mo)_6N_2$ and finally fcc $(Mo,Fe)_2N$ or (Mo,Fe)N. Different compositions for the metastable interstitial-substitutional solute-atom clusters $Fe_xMo_yN_z$ can be found [18]. However, some authors suggest that the presence of Fe in the nitrides might be due to the limited spatial resolution of the field ion microscopy-atom probe analyses, on which most of the composition data are based [19–21]. The interaction of nitride precipitation and precipitation of intermetallic compounds in the depth direction, e.g. [22] will not be discussed in this paper.

Although the nitriding process is very well studied, there is little research on the precipitation behavior of Mo-nitrides in Mo-containing maraging steels, especially for short nitriding times. This is also the case for the formation of the precursor phases during aging in these steels. Information about the degree of coherency and the composition of the precipitates helps to understand the microstructure-property relationships in nitrided maraging steels. In this study, the precipitates formed during an aging heat treatment executed in a nitriding atmosphere during the initial stages of precipitation, are characterized with transmission electron microscopy (TEM) and atom probe tomography (APT). Density functional theory (DFT) calculations are used to confirm and specify the atomic structure of the nitrides.

2. Experimental Setup and Calculation Details

The studied maraging steel has the following nominal composition (wt%): 18 Ni, 16.5 Co, 5 Mo and balance Fe. Thin strips of this steel were 50% cold rolled from the as-delivered sheet and air-quenched after annealing at 840 °C in a protective atmosphere. This heat treatment generates a fully martensitic structure without retained austenite. In order to determine the peak-hardness, aging heat treatments were performed in a salt bath for various aging times at a temperature of 470 ± 5 °C. Vickers hardness was measured on a Zwick hardness tester with a load of 200 g (HV 0.2). Based on these results, the nitriding conditions were selected. After cleaning and degreasing, the as-quenched samples were aged and simultaneously gas nitrided at 470 °C for 50 min in a N_2-H_2 atmosphere containing 7% NH_3. The nitriding potential was 3.8 $atm^{-1/2}$.

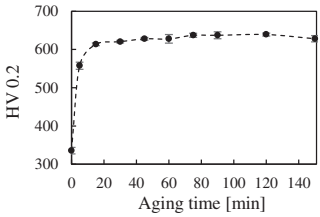

Fig. 1. Vickers hardness of the studied maraging steel as a function of aging time at an aging temperature of 470 ± 5 °C.

Glow discharge optical emission spectroscopy depth profiles were recorded with a Spectruma GDA 750 GD-OES analyzer. The samples for electron backscatter diffraction (EBSD) examination were prepared by electropolishing with A2 Struers electrolyte, followed by mechanical polishing with OP-U for 40 min. EBSD data were collected by an Oxford-HKL EBSD system attached to a FEI Nova 600 Nanolab Dual Beam FIB-SEM (Focussed Ion Beam - Scanning Electron Microscope) with field emission gun. The EBSD patterns were acquired with an acceleration voltage of 18 kV, a beam current of 2.2 nA, and a step size of 60 nm. The EBSD data were postprocessed with the OIM-TSL Data Analysis 7 commercial software.

Two different types of specimens were prepared for atom probe tomography experiments. The first type of samples was prepared to study the aged material. They were prepared from the central part of the nitrided sample with a standard two-step electropolishing technique [23]. The second type of samples was prepared in order to study the nitrided layer. In this case site-specific sample preparation with the focussed ion beam scanning electron microscope (FIB-SEM FEI Versa 3D DualBeam) using the lift-out technique [24] was applied to extract samples from the nitrided diffusion zone at the sample's surface. The last step of the annular milling was done at 5 kV followed by a cleaning step at 2 kV to minimize Ga implantation. The atom probe tomography experiments were carried out on a local electrode atom probe (LEAP 3000X HR) from Cameca at a temperature of 60 K in voltage mode with a pulse repetition rate of 200 kHz and a pulse fraction of 20%. The Imago Visualization and Analysis Software (IVAS) version 3.6.6 was used for data reconstruction and analysis. Several peak overlaps in the mass-to-charge-state ratio spectrum are present in this highly alloyed material. Peak deconvolution was considered for the overlapping peaks based on the natural abundance of the present elements: for the Ni^{2+} and Fe^{2+} overlap at 29 Da, for Mo^{3+} and Ni^{2+} at 32 Da, for N^+ and Si^{2+} at 14 and 15 Da, and the N_2^+ and Fe^{2+} overlap at 28 Da.

In order to study the aged material with TEM, the nitrided layers were removed by grinding and polishing up to 60 µm, keeping the central and aged material. Subsequently, the samples were thinned by means of a twin-jet electropolishing setup (Struers Tenupol-5) using a mixture of 4 vol% perchloric acid and 96 vol% acetic acid at room temperature. In order to study the nitrided layer, the Focused Ion Beam and lift-out method (FIB-SEM, FEI Nova 600 Nanolab DualBeam) was applied on the outer layer of the nitrided part. High-resolution transmission electron microscopy (HRTEM) and selected area electron diffraction (SAED) were performed using an objective lens C_s corrected JEOL JEM-2200FS FEG TEM operating at 200 kV. The images were analyzed with the Digital Micrograph™ software (Gatan, USA). To interpret the SAED patterns, diffraction patterns were simulated with the JEMS software [25].

Density Functional Theory (DFT) [26,27] calculations were performed at 0 K and zero pressure to study the atomic structure of the nitrides. The ACONVASP software package [28] was used to construct the starting unit cells. All DFT calculations were carried out on the

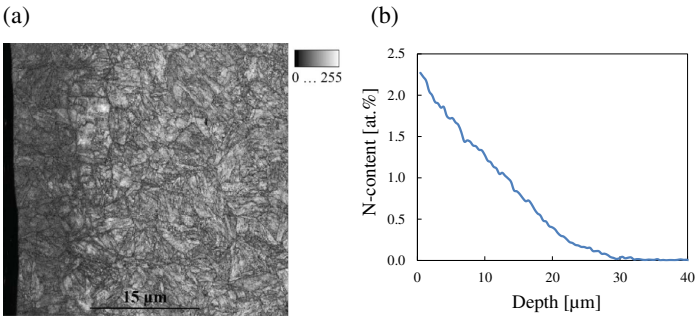

Fig. 2. (a) Band slope parameter map. Dark pixels correspond to distorted crystal lattices. (b) GD-OES N profile of the studied nitrided maraging steel.

Table 1
Chemical analysis of the maraging steel (optical emission spectroscopy) and chemical analysis measured by APT (at.%).

at.%	Fe	Co	Ni	Mo	C	Al	Si	Cr	Mn	Cu
Comp.	Bal.	16.25	18.03	3.23	0.024	0.054	0.091	0.066	0.075	0.072
APT	61.6 ± 0.25	16.5 ± 0.19	18.1 ± 0.42	3.4 ± 0.01	0.01 ± 0.002	0.06 ± 0.002	0.05 ± 0.06	0.09 ± 0.001	0.08 ± 0.001	0.05 ± 0.001

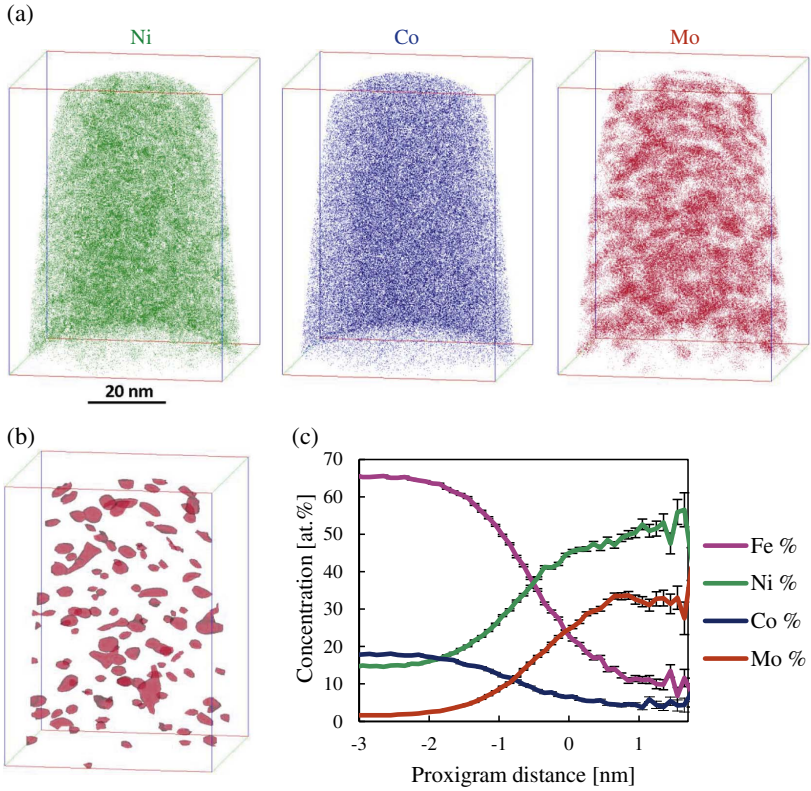

Fig. 3. Maraging steel aged at 470 °C for 50 min: (a) 3D reconstruction of the atom positions of Ni, Co and Mo; (b) Isoconcentration surfaces for 15 at.% Mo; (c) Proximity histogram according to isosurfaces with 15 at.% Mo. Zero distance on the x-axis corresponds to the precipitate/matrix interface, positive values to the precipitate.

Table 2
Chemical composition of the precipitates of aged maraging steel, based on the volumes in the isoconcentration surfaces of certain at.% Mo.

at.%	all	Inside 15 at.% Mo	Inside 18 at.% Mo	Inside 21 at.% Mo
Fe	61.6 ± 0.25	18.9 ± 1.53	15.3 ± 3.20	13.7 ± 5.66
Co	16.5 ± 0.19	5.8 ± 0.42	5.2 ± 0.81	5.0 ± 1.35
Mo	3.4 ± 0.01	29.2 ± 0.79	32.9 ± 0.98	35.9 ± 1.93
Ni	18.1 ± 0.42	45.0 ± 2.95	45.3 ± 5.40	43.8 ± 10.12
$Ni_{x=...}Mo$		1.6 ± 0.14	1.4 ± 0.21	1.2 ± 0.34
Vol%		1.1 ± 0.15	0.4 ± 0.08	0.1 ± 0.04

GGA-PBE (Perdew-Burke-Ernzerhof parametrization of the Generalized Gradient Approximation) [29] level of theory with the Vienna Ab Initio Simulation Package (VASP) software [30–34], with VASP 5.2 recommended PAW (Projector Augmented Wave) potentials [35,36]. These potentials were recently shown to provide a similar precision as all-electron calculations [37]. A $\overline{k}$-point mesh of 30 × 30 × 1 and cut-off energy of 500 eV were used for optimizing the unit cells and atomic positions, and a 40 × 40 × 1 mesh combined with a 650 eV cut-off energy for obtaining the final energies. A convergence criterion of 10^{-8} eV was used for the electronic self-consistent cycle and of 10^{-6} eV for the structural optimization. For electronic convergence, Methfessel-Paxton smearing [38] (σ = 0.2 eV) was used for structure optimization and the tetrahedron method with Blöchl corrections [39] for the final energies.

3. Results

3.1. Aging Response

Hardness measurements of the maraging steel aged for different times at a temperature of 470 ± 5 °C are presented in Fig. 1. A hardness plateau is visible after 20 min of aging and a remarkable increase in hardness can already be observed after 5 min. The very fast aging response is associated with the high Co content [8]. An aging time of 50 min was selected for this work, in order to have an adequate nitriding depth as well.

3.2. Thickness of the Nitrided Layer

The microstructure of the nitrided layer and the substrate, represented with the band slope map derived from the diffraction pattern [40,41], is shown in Fig. 2a. The band slope parameter represents the intensity gradient observed at the margins of the Kikuchi lines in the electron backscatter diffraction pattern (EBSP) [42]. Darker pixels in the map have lower band slope parameter values which correspond to a distorted matrix, in this case the nitrided diffusion layer. Fig. 2b displays the distribution of N through the sample thickness measured with GD-OES. After nitriding, no compound layer was formed at the surface. Only a diffusion zone and a transition zone from this diffusion zone to the core material, with a total thickness of around 20 μm, are visible in the GD-OES depth profile of N. The effective nitrided layer thickness according to the band slope map is around 10 μm, which corresponds to a threshold for N of around 1.2 at.%. Residual stress measurements by the micro-slit milling method were executed on the nitrogen diffusion zone of the same steel grade with different nitriding thicknesses and

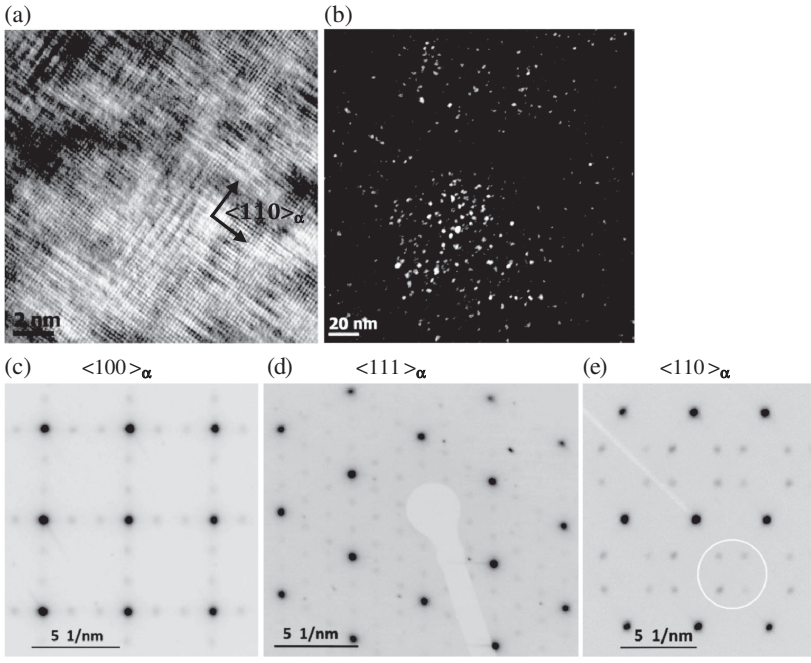

Fig. 4. Maraging steel aged at 470 °C for 50 min: (a) < 100 > $_{\alpha}$ HRTEM image, (b) The dark field micrograph from the circle in (e) showing the presence of precipitates, (c) SAED corresponding to < 100 > $_{\alpha}$ zone axis showing superlattice reflections, (d) < 111 > $_{\alpha}$ zone axis diffraction pattern, (e) < 110 > $_{\alpha}$ zone axis diffraction pattern.

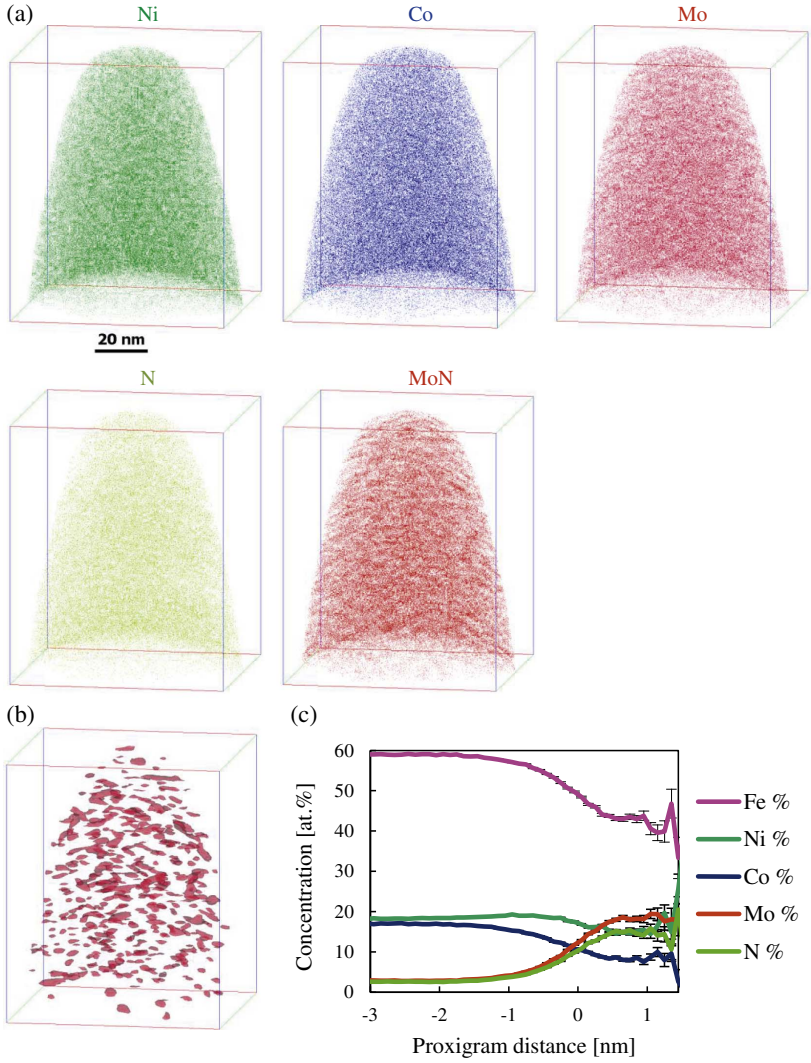

Fig. 5. Sample nitrided at 470 °C for 50 min: 3D reconstruction of the atom positions of (a) Ni, Co, Mo, N and MoN molecules; (b) Isoconcentration surfaces for 7.5 at.% Mo; (c) Proximity histogram according to isosurfaces with 7.5 at.% Mo.

Table 3
Average chemical composition of the precipitates in the maraging steel nitrided at 470 °C for 50 min, based on the volumes in the isoconcentration surfaces of certain at.% Mo.

at.%	all	Inside 7.5 at.% Mo	Inside 9 at.% Mo	Inside 10.5 at.% Mo
Fe	58.4 ± 0.25	46.8 ± 0.69	43.2 ± 0.71	40.7 ± 0.32
Co	16.4 ± 0.13	9.8 ± 0.28	8.6 ± 0.24	7.9 ± 0.91
Mo	3.4 ± 0.10	14.5 ± 0.58	17.9 ± 0.71	20.6 ± 0.50
Ni	18.6 ± 0.25	16.2 ± 0.42	15.0 ± 0.64	13.4 ± 0.55
N	3.0 ± 0.16	12.1 ± 0.69	14.7 ± 0.76	16.8 ± 0.74
$MoN_{x=...}$		0.84 ± 0.03	0.82 ± 0.02	0.80 ± 0.03
Vol%		1.23 ± 0.27	0.26 ± 0.06	0.05 ± 0.01

reported in [43]. Both the microstructure in the aged bulk material and in the first 1–2 μm of the nitrided diffusion zone are studied.

3.3. Microstructure of the Aged, Not Nitrided Maraging Steel

3.3.1. APT Study of the Aged Steel

Table 1 lists the chemical composition of the steel measured both with optical emission spectroscopy and with atom probe tomography. It can be observed that these compositions match well. The three-dimensional reconstruction of the positions of Ni, Co and Mo atoms in the aged sample based on the APT results is presented in Fig. 3a. Significant clustering of Mo atoms is observed, whereas the clustering of Ni is also

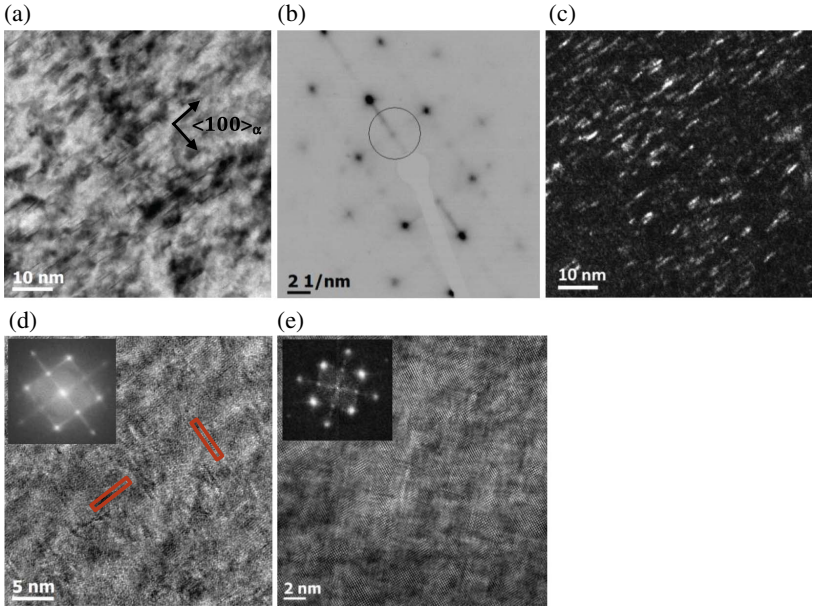

Fig. 6. Specimen nitrided at 470 °C for 50 min: (a) BF image showing nitride platelets embedded in a martensitic matrix; (b) SAED of (a), zone axis < 100 > ; (c) DF image, aperture indicated with circle in (b); (d) and (e) HRTEM and Fourier transform showing two sets of perpendicular platelets embedded in a martensitic matrix, zone axis < 100 > .

Table 4
Atomic coordinates within the P-3 trigonal phase of $(Fe,Ni)_7Mo_2$ and $(Fe,Ni)_8Mo$.

Ni_7Mo_2 *(Ni_8Mo)*	Wyckoff position	$a = a_\alpha \sqrt{6}$ x	$b = a_\alpha \sqrt{6}$ y	$c = a_\alpha \frac{\sqrt{3}}{2}$ z
Fe, Ni *(Mo)*	1a	0	0	0
Fe, Ni	6 g	1/3	0	1/3
Mo *(Fe, Ni)*	2d	1/3	2/3	0

apparent, but less pronounced. Isoconcentration surfaces of 15 at.% Mo are used for visualization of the precipitates, which appear to be randomly distributed in the matrix (Fig. 3b). The same type of nanometer-sized precipitates are observed by TEM as spherical particles (see Section 3.3.2), allowing for proper adjustment of the APT reconstruction parameters to obtain spherical precipitates [44]. The proximity histogram in Fig. 3c, which is the average concentration profile over all precipitates normal to the isoconcentration surface, shows that the precipitates have a high Mo and Ni content, while Fe and Co contents are quite low but do not drop to zero. In order to determine the chemical composition of the precipitates, the volumes in the isoconcentration surfaces of 15, 18 and 21 at.% Mo are considered in Table 2. The average volume of a precipitate is 18.7 nm^3 (or a calculated diameter of 3.3 nm if it is assumed that all precipitates are spherical) and the vol% of precipitates in the measurement is 1.1%, based on the volumes in the isoconcentration surface of 15 at.% Mo. As it can be seen from the result in Table 2, the vol% decreases quickly when higher threshold values are considered, therefore 15 at.% Mo was chosen for an estimation of the dimensions. In addition, due to evaporation aberrations a lot of Fe ions from the matrix are included in the particles and the dimensions are overestimated.

3.3.2. TEM Study of the Aged Material

TEM images were acquired from the sample aged at 470 °C for 50 min. Imaging in high resolution (Fig. 4a) reveals regions having an ordered structure with a periodicity of planes in the < 110 > direction in every third atomic layer. No clear interfaces are visible in this bright field image and the precipitates cannot be distinguished from the matrix, which could be explained by their high density and coherent boundaries. The dark field micrograph (Fig. 4b) taken using superlattice spots, indicated with the circle in Fig. 4e, shows circular precipitates having an average diameter of 2.3 ± 0.7 nm. This is slightly smaller than the diameter deviated from APT measurements. The selected area diffraction patterns in Fig. 4 c–e, reveal superlattice reflection spots, such as the maxima at 1/3 and 2/3 < 110 > directions in the < 100 > bcc pattern of the matrix (Fig. 4c).

3.4. Microstructure of the Nitrided Layer After Simultaneously Aging and Nitriding

3.4.1. APT Study of the Nitrided Zone

Fig. 5a shows the 3D reconstruction of Ni, Co, Mo and N atoms, as well as MoN molecules. Clustering of MoN and a bit less pronounced clustering of Mo can be observed. This can be explained by the rather strong cohesive energy of the MoN pairs [45]. Isoconcentration surfaces of 7.5 at.% Mo are used for visualization of the precipitates in Fig. 5b. In this calculation the MoN molecules are broken down to their constituent atoms. Peak overlap can occur for N_2^+ and Fe^{2+} at 28 Da, which could lead to an underestimation of the actual nitrogen concentration [46,47]. The mass spectra of the volumes inside the isoconcentration surfaces of 7.5, 9 and 10.5 at.% Mo were analyzed. In these nitrides, the observed ion abundances for 27, 28 and 28,5 Da fit to the natural abundances of the isotopes of Fe. Therefore only a negligibly small amount of N_2^+ ions can be hidden beneath the Fe^{2+} peak at

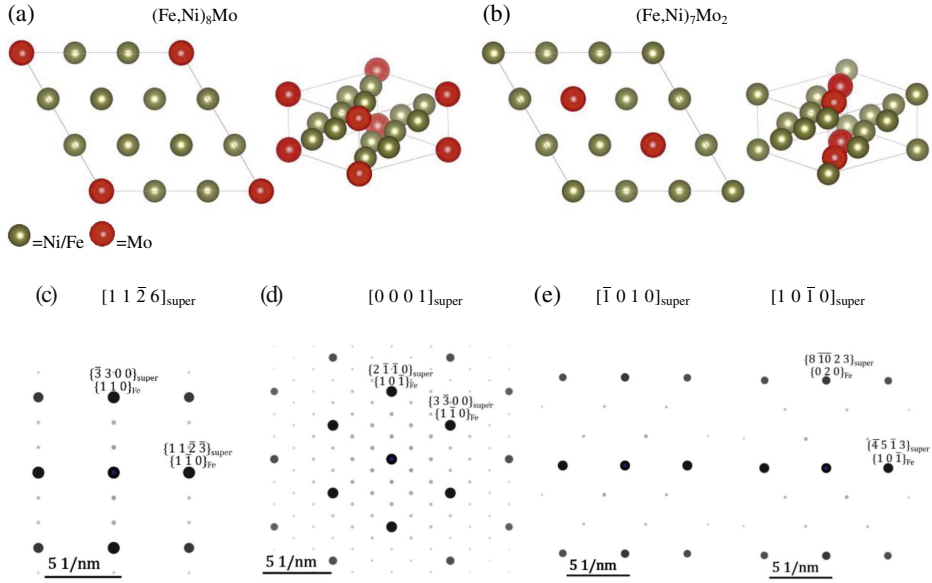

Fig. 7. Reconstructed atomic positions for (a) $(Fe,Ni)_8Mo$: view along c-axis and perspective view, (b) $(Fe,Ni)_7Mo_2$: view along c-axis and perspective view, (c) simulated diffraction spots, zone axis [1 1 $\bar{2}$ 6], (d) simulated diffraction spots, zone axis [0001], (e) simulated diffraction spots, two variants zone axis [$\bar{1}$ 0 1 0] and zone axis [1 0 $\bar{1}$ 0].

28 Da. The proximity histogram (Fig. 5c), in this case the average concentration profile normal to the isoconcentration surfaces of 7.5 at. % Mo, shows that the precipitates are richer in Mo and N and leaner in the other alloying elements and Fe. In order to determine the chemical composition of the precipitates, the volumes in the isoconcentration surfaces of 7.5, 9 and 10.5 at.% Mo are considered in Table 3. Being just an indication for a possible precipitate, the ratio of N to Mo is calculated and is around 0.8. The average volume of a precipitate is 13.12 nm^3 and the vol% of precipitates in the measurement is 1.23%, based on the volumes in the isoconcentration surface of 7.5 at.% Mo.

3.4.2. TEM Study of the Nitrided Zone

TEM images of the nitrided diffusion zone are shown in Fig. 6. The TEM bright field image (Fig. 6a) reveals interrupted lines parallel to the < 100 > directions of the bcc matrix. Both streaks and additional reflections can be found on the 001 diffraction pattern (Fig. 6b). The dark field image from one of the additional reflections also reveals fine platelets on the {100} bcc matrix planes (Fig. 6c). A large density of small precipitates is also observed in HRTEM, as shown in Fig. 6d–e, where two sets of perpendicular platelets embedded in a martensitic matrix are visible. The diameter of the platelets lying on the {100} planes of the martensitic bcc matrix is 3.7 nm ± 2.3 nm. The continuity of atomic planes across the platelets can be observed, indicating full coherency with the Fe-matrix.

4. Discussion

4.1. Atomic Structure of the Intermetallics in the Aged Maraging Steel

A high density of precipitates is observed both by APT and TEM in the maraging steel after only 50 min of aging. This can be explained by the high Co content which reduces the solubility of Mo in the bcc matrix, and therefore increases the driving force for the precipitation of Mo-rich phases [8]. It is reported that during the early stages of aging, short-range ordering results in Fe-Co regions and Ni-rich regions (Ni-Mo-Ti) [48], which facilitates the precipitation of usually coherent and Ni-rich intermetallic compounds Ni_3Mo or Ni_3Ti in a later stage of aging.

The fraction of Fe which is observed with APT in the precipitates of the aged material can differ slightly from the real fraction due to trajectory overlaps and local magnification [49] and is expected to be overestimated but not necessarily zero [50]. The superlattice reflection spots in the SAED patterns in Fig. 4 can be explained in the real lattice by an ordered arrangement of atoms of different atomic scattering powers, where the ordered structure is derived from the bcc lattice. As the atomic scattering factor depends on the atomic number, the components of the alloy can be divided into a group of Fe, Ni and Co and a group of Mo. The observed diffraction patterns were also reported in [3,7,51,52] for similar alloys, and interpreted as the ordered hexagonal ω-phase, sometimes called the S-phase, $(Fe,Ni)_8Mo$ or $(Fe,Ni)_7Mo_2$. The precipitates of the ω-phase are reported to be small, quasi-spherical and a precursor of Ni_3Mo [53]. According to [51], the diffraction spots belong to $(Fe,Ni)_7Mo_2$ with a hexagonal $P6_3/mmc$ structure. However, the current study shows that a better description of this $(Fe,Ni)_8Mo$ or $(Fe,Ni)_7Mo_2$ phase is the trigonal P-3 structure with parameters: a = 0.702 nm and c = 0.248 nm, as described in Table 4 and Fig. 7. The a-axis of the superstructure corresponds to $[11\bar{2}]_\alpha$, the b-axis to $[\bar{2}11]_\alpha$, and the c-axis to $[111]_\alpha$. Yedneral and Perkas [54] proposed a continuous evolution of A_8B, through A_7B_2 up to A_6B_3 or the known A_2B ω-phase, with A = Fe, Ni, Co, and B = Mo. The rhombohedral A_2B ω-phase shows less superlattice spots in the diffraction pattern and does not fit to the experimental diffraction pattern in this work. Both $(Fe,Ni)_8Mo$ and $(Fe,Ni)_7Mo_2$ lead to the same diffraction patterns. Multiple variants of the omega phase were formed, as can be seen in Fig. 7 c and e. Being only an indication for the composition of the precipitates measured with APT, the ratio of Ni to Mo is around 1.6 and the ratio of Fe and Ni to Mo is around 2.2. This is lower than what is expected from the TEM analysis and can be explained by the continuous evolution from A_8B, through A_7B_2 up to A_2B [54], where it seems that the composition of the precipitates is close to A_2B. For higher threshold values

Table 5
Overview of Mo-N-Fe structures and corresponding cohesive energies from DFT calculations, based on the equations in the 2nd column. Structure 1 and 2 are Mo-N monolayers, structure 3–5 correspond to double layers of Mo and N, where structure 5 has a 1–1 stoichiometry. Structure 6–7 correspond to Mo-N triple layers, with structure 7 having the 1–1 stoichiometry. Structure 8 is an ordered structure of Mo-N layers on every fourth layer of Fe.

1. 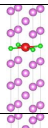	$Fe_{19}Mo(s) + \frac{1}{2}N_2(g) \leftrightarrows Fe_{19}MoN(s)$	$\Delta U = -47\frac{kJ}{mol\ N}$
2. 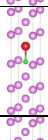	=Fe =Mo =N	$\Delta U = -31\frac{kJ}{mol\ N}$
3. 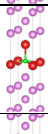	$Fe_{18}Mo_2(s) + \frac{1}{2}N_2(g) \leftrightarrows Fe_{18}Mo_2N(s)$	$\Delta U = -93\frac{kJ}{mol\ N}$
4. 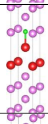		$\Delta U = -25\frac{kJ}{mol\ N}$
5. 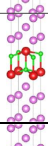	$Fe_{18}Mo_2(s) + N_2(g) \leftrightarrows Fe_{18}Mo_2N_2(s)$	$\Delta U = -76\frac{kJ}{mol\ N}$
6. 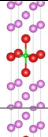	$Fe_{17}Mo_3(s) + \frac{1}{2}N_2(g) \leftrightarrows Fe_{17}Mo_3N(s)$	$\Delta U = -149\frac{kJ}{mol\ N}$
7. 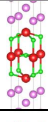	$Fe_{17}Mo_3(s) + \frac{3}{2}N_2(g) \leftrightarrows Fe_{17}Mo_3N_3(s)$	$\Delta U = -60\frac{kJ}{mol\ N}$
8. 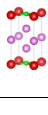	$Fe_{19}MoN(s) \leftrightarrows Fe_3MoN(s) + 16Fe(s)$	$\Delta U = -22\frac{kJ}{mol\ N}$

of Mo, the uncertainty of the Ni content increases (Table 3), which could be linked to small deviations in the chemical composition of the precipitates in the transition state. These observations confirm the existence of the known ω-phase.

4.2. Atomic Structure of the Nitrides

The small precipitates or clusters which are detected in the nitrided diffusion zone are still in the early stage of precipitation. No intermetallics could be observed in the first few micrometers of the nitrided layer. APT shows that the Fe content decreases in the nitrides but is remarkably higher than in the intermetallic precipitates, probably due to the trajectory overlap between the matrix and the very thin plate-like precipitates. In this case, the influence from the matrix on the chemical composition of the precipitates is considerable. It was observed that the ion density is lower inside the particles, which is associated with the higher evaporation field of the precipitates. For high field precipitates, trajectory overlaps of around 1 nm are expected outside the precipitate nearby the interface [55]. Besides, lateral surface diffusion of mainly interstitial atoms on the APT tip can affect the N content of matrix and precipitates. For very fine platelets, the local magnification effect can lead to erroneous detection of large amounts of Fe in the platelets [47]. However, in the very early stage of precipitation the precipitates genuinely still contain a lot of Fe. The observed precipitates could be Mo-nitrides or $Fe_xMo_yN_z$ zones.

Streaks in the diffraction pattern in the < 001 > direction (Fig. 6b) are ascribed to both small dimensions of the scattering object of precipitates or GP zones and irregular spatial distribution between them along the direction parallel to the streaks [56]. The additional reflections in the diffraction pattern can appear due to B2 ordering. The observed precipitates could also be assigned to the FCC-Mo_2N phase, obeying the Baker-Nutting orientation relationship with the matrix: $\{100\}_{nitride}//\{100\}_{\alpha}$ and $< 001 >_{nitride}// < 011 >_{\alpha}$ [20,57]. However, the simulated diffraction pattern does not fit exactly with the observed SAED pattern. Selg et al. [58] concluded that largely coherent Mo_2N-type nitrides develop in maraging steel upon nitriding, surrounded by a tetragonally distorted matrix. Mobile and immobile excess nitrogen is expected in solution-annealed maraging steel which is nitrided. The immobile excess nitrogen is adsorbed at the precipitate/matrix interface, while the mobile excess nitrogen is dissolved in the strained matrix. This excess nitrogen could explain deviation from a specific stoichiometry in the early stages of precipitation. Individual atomic columns composing the platelets in Fig. 6d–e indicate that the platelets consist of a monolayer. However, according to these HRTEM images the platelets could be up to three atomic layers thick but due to the limited resolution they cannot be sharply visualized. The observed structure is expected to be similar to a Mo_2N monolayer which is coherent with the surrounding, tetragonally distorted Fe-matrix. This possible structure was investigated further and is discussed below.

Since TEM and APT do not lead to an unambiguous conclusion regarding the nitrides, DFT calculations have been carried out. The main objective is to obtain optimized structures which correspond to the observed diffraction patterns. Additionally, the relative stabilities of different coordinations of the N atoms can be determined. To isolate a single precipitate in a three-dimensional periodic code, unit cells of 20 layers of Fe in the < 100 > direction were constructed using the ACONVASP software and a number of Fe atoms were replaced with one, two or three consecutive layers of Mo atoms. This number of layers separates the periodic repetition of the Mo precipitates by > 2.5 nm, which is sufficient to cut out all electronic interactions. In a first step, the atomic positions of those structures and the unit cell shape and volume were allowed to relax using a conjugate-gradient algorithm. This results in a fully optimized structure under zero pressure. Secondly, N atoms were introduced into the different octahedral interstitial sites available in the Mo layers, again fully optimizing the unit cell. This enables to determine the energetically most favorable site for N. Finally, Mo-N precipitates of varying thickness with a 1-1 stoichiometry, where the N atoms are placed in the most favorable octahedral positions, were optimized and their cohesive energies were calculated.

When the N atoms are in the octahedral sites in the Mo plane, with two Mo atoms of that plane as nearest neighbors, the difference in cohesive energy ΔU corresponds to 197 $\frac{kJ}{mol\ N}$ in a monolayer, and to 130 $\frac{kJ}{mol\ N}$ in a triple Mo layer. This configuration is highly unfavored, as can be expected on simple geometric grounds. The precipitate plane is coherent with the bulk Fe matrix, which entails that the Mo atoms in that plane are only the lattice parameter of bulk Fe apart. An energetically costly orthorhombic distortion takes place if the N atom is inserted between those Mo atoms. If the two octahedral neighbors of the N atom are coordinated perpendicular to the precipitate, the tetragonal distortion already caused by the Mo precipitate atoms forms an

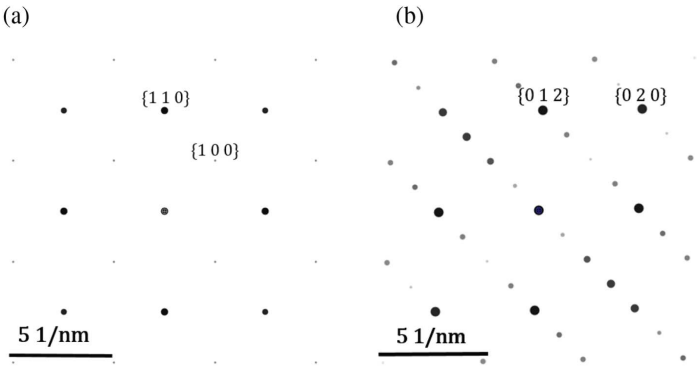

Fig. 8. (a) Simulated diffraction pattern of structure 1 of Table 5, zone axis [001], (b) Simulated diffraction pattern of structure 8 of Table 5, zone axis [100]. Both patterns correspond well to Fig. 6b.

ideal position for the N atom. Table 5 shows the preferential octahedral sites of the interstitial N atoms and their corresponding cohesive energies. For the energetic comparisons, bulk bcc Fe and bcc Fe with N in the octahedral position were also optimized and the enthalpy of solution is calculated to be $\Delta U = 14\ \frac{kJ}{mol\ N}$. It is clear that N has a higher affinity for Mo than for Fe. In the case of a monolayer of Mo, the N prefers to be in the Mo-layer, with Fe as nearest neighbors (cf. Table 5, structure 1). However, a N atom positioned just outside the Mo layer (cf. Table 5, structure 2) is energetically quite similar. The same conclusion can be drawn for the double Mo layer (cf. Table 5, structure 3 and 4 respectively). Structure 6, the triple Mo layer, has the lowest cohesive energy. To assess the driving force for growth of the Mo-N precipitates in the z-direction, the cohesive energy of the single-layer structure (cf. Table 5, structure 1) is compared to the cohesive energy of the double- and triple-layer structure (cf. Table 5, structure 5 and 7 respectively). The combination of two single layers into a double Mo-N layer corresponds to a cohesive energy difference of $\Delta U = -26\ \frac{kJ}{mol\ N}$ ($2\ Fe_{19}MoN \leftrightarrows Fe_{18}Mo_2N_2 + 20\ Fe$). For the combination of three single layers into a triple layer, ΔU ($3\ Fe_{19}MoN \leftrightarrows Fe_{17}Mo_3N_3 + 40\ Fe$) equals $-2\ \frac{kJ}{mol\ N}$. It can be concluded that the driving force to create multiple layers exists but is relatively small, which results in the predominance of single-layer Mo-N precipitates for short nitriding treatments, as evidenced by the TEM results (see Fig. 6d and Fig. 6e).

Fig. 8a shows that the simulated diffraction pattern of the Mo-N monolayer in Fe (structure 1 in Table 5) corresponds well to the SAED patterns in Fig. 6b. Also structures 2 to 7 lead to the simulated diffractions pattern of Fig. 8a. The position of N has a limited impact on the SAED, but the position of the Mo in the Fe-lattice can be linked to B2 ordering and the corresponding additional reflections in the diffraction pattern. However, extra satellites appear in the experimental diffraction pattern which could be explained by an ordered structure of the Mo-N layers which form on every fourth layer of Fe (cf. Table 5, structure 8 and Fig. 8b). There is also an affinity of the Mo layers to form this structure, but the driving force is not very large. A similar structure of single-layered NbN GP zones in steel was reported in [59] with an uncertainty of the position of the N atoms. The compression of the lattice parameter of Fe in the direction perpendicular to the precipitate with the precipitate as nearest neighbor is 2.1% for the Mo-N monolayer. The desired expansion of the nitrided layer as compared to the unnitrided core leads to the compressive macrostress parallel to the surface in the nitrided zone. The distorted Fe-matrix around the Mo-N monolayers corresponds with the microstresses and gives rise to diffraction line broadening (streaks in the SAED). This is also observed as the lower value of the band slope parameter of the EBSD data from the nitrided layer in comparison to the substrate (Fig. 2a).

5. Summary and Conclusions

Two high-resolution techniques, TEM and APT were used to study the precipitates in aged and nitrided Fe-Ni-Co-Mo maraging steel. Ni-Mo type intermetallics were found in the aged bulk material, while Mo-N precipitates were detected in the nitrided zone nearby the surface. These two different types of precipitates are uniformly distributed in the matrix and both have a volume fraction of around 1% in the zone of characterization.

The strengthening intermetallic precipitates formed during the early stages of aging were identified with the aid of TEM as the known ω-type precipitate, with chemical composition of $(Fe,Ni)_8Mo$ or $(Fe,Ni)_7Mo_2$ and a trigonal crystal lattice. However, the APT analysis shows that the (Fe,Ni) to Mo ratio is lower than the one expected in the phase identified by TEM. This can be explained by the continuous evolution of $(Fe,Ni)_8Mo$ through $(Fe,Ni)_7Mo_2$ up to the rhombohedral ω-phase $(Fe,Ni)_2Mo$, where the observed intermetallics are in the transition from $(Fe,Ni)_7Mo_2$ to $(Fe,Ni)_2Mo$, while the crystal structure still corresponds to $(Fe,Ni)_7Mo_2$. The diameter of the spherical precipitates is around 3 nm.

The first few micrometers of the nitrided layer of the simultaneously aged and nitrided maraging steel contain disc shaped precipitates on the {001} martensitic lattice. The diameter of the discs is 3–4 nm, while their thickness is estimated to be one atomic layer. APT reveals the enrichment of the precipitates in Mo and N. However, some influence of the matrix on the chemical composition is present since the precipitates are very small. DFT calculations were performed to compare different configurations of the N atom in Mo-N precipitates of varying thickness. The energetically most favorable position of the N atom is the octahedral position inside the Mo layers, with the nearest neighbor pair oriented perpendicular to the precipitate plane. The low driving force to stack the Mo-N layers agrees with the predominance of single-layer precipitates observed in TEM.

Acknowledgements

The authors acknowledge the financial support of the Dutch Materials Innovation Institute (M2i) under the contract M21.10.11442.

References

[1] W. Sha, A. Cerezo, G.D.W. Smith, Phase chemistry and precipitation reactions in maraging steels: part I. Introduction and study of Co-containing C-300 steel, Metall. Trans. A. 24A (1993) 1221–1232.
[2] S.J. Kim, C.M. Wayman, Precipitation behavior and microstructural changes in

maraging Fe-Ni-Mn-Ti alloys, Mater. Sci. Eng. A128 (1990) 217–230.
[3] J.M. Genin, G. Le Caer, Mössbauer study of precipitation in Fe-Ni-Mo and Fe-Ni-Co-Mo maraging alloys, Scr. Metall. 8 (1974) 15–22.
[4] B. Pennings, M. Tran, M. Derks, A. Brandsma, B. Boulogne, J. Davidson, New push-belt design to increase power density of CVTs featuring a new maraging steel, Proceedings of the Fisita World Automotive Congress, 2004.
[5] W. Sha, G.D.W. Smith, A. Cerezo, Atom probe field-ion microscopy of ageing behaviour of a model Fe-Ni-Co-Mo maraging steel, Surf. Sci. 266 (1992) 378–384.
[6] R. Tewari, S. Mazumder, I.S. Batra, G.K. Dey, S. Banerjee, Precipitation in 18wt% Ni maraging steel of grade 350, Acta Mater. 48 (2000) 1187–1200.
[7] C. Servant, N. Bouzid, O. Lyon, Small-angle X-ray scattering investigation of the martensite unmixing in maraging alloy using synchrotron radiation, Philos. Mag. A 56 (1987) 565–592.
[8] W. Sha, A. Cerezo, G.D.W. Smith, Phase chemistry and precipitation reactions in maraging steels: part III. Model alloys, Metall. Trans. A. 24A (1993) 1241–1249.
[9] J. Fernández de Ara, E. Almandoz, J.F. Palacia, G.G. Fuentes, R.J. Rodriguez, J.A. Garcia, Influence of temperature in arc-activated plasma nitriding of maraging steel in solution annealed and aged conditions, Surf. Coat. Technol. 258 (2014) 754–762.
[10] S.R. Meka, E.J. Mittemeijer, Abnormal nitride morphologies upon nitriding iron-based substrates, JOM 65 (2013) 769–775.
[11] S. Lampman, Heat Treating: Surface Hardening of Steels, 4 ASM, 1991.
[12] M.H. Biglari, C.M. Brakman, E.J. Mittemeijer, S. Van der Zwaag, The kinetics of the internal nitriding of Fe-2at.%Al alloy, Metall. Mater. Trans. A 26 (1995) 765–776.
[13] N.V. Diaz, Nitriding of Iron-based Alloys; Residual Stresses and Internal Strain Fields, PhD thesis (2007).
[14] S.S. Hosmani, R.E. Schacherl, E.J. Mittemeijer, Nitriding behavior of Fe-4wt%V and Fe-2wt%V alloys, Acta Mater. 53 (2005) 2069–2079.
[15] R. Wagner, S.S. Brenner, Morphology and chemistry of internally nitrided Fe-3at.% Mo, Acta Metall. 26 (1978) 197–206.
[16] D. Isheim, E.J. Siem, D.N. Seidman, Nanometer-scale solute segregation at hetero-phase interfaces and microstructural evolution of molybdenum nitride precipitates, Ultramicroscopy 89 (2001) 195–202.
[17] J.H. Driver, J.M. Papazian, The electron and field ion metallography of zones in nitrided Fe-Mo alloys, Acta Metall. 21 (1973) 1139–1149.
[18] D.L. Speirs, W. Robert, R. Grieveson, K.H. Jack, International Symposium on Metallurgical Chemistry, I.S.I, Sheffield, 1971.
[19] D.H. Jack, The structure of nitrided iron-titanium alloys, Acta Metall. 24 (1976) 137–146.
[20] H. Selg, E. Bischoff, S.R. Meka, R.E. Schacherl, T. Waldenmaier, E.J. Mittemeijer, Molybdenum-nitride precipitation in recrystallized and cold-rolled Fe-1at.pct Mo alloy, Metall. Mater. Trans. A 44 (2013) 4059–4070.
[21] G.P. Huffman, H.H. Podgurski, Mössbauer study of nitrided Fe-Mo and Fe-Ti alloys, Acta Metall. 23 (1975) 1367–1379.
[22] J. Takahashi, K. Kawasaki, K. Kawakami, M. Sugiyama, Three-dimensional atom probe analysis of chromium- and copper-added nitriding steel, Surf. Interface Anal. 39 (2007) 232–236.
[23] M.K. Miller, Atom Probe Tomography: Analysis at the Atomic Scal, (2000).
[24] M. Miller, K. Russel, G. Thompson, Strategies for fabricating atom probe specimens with a dual beam FIB, Ultramicroscopy 102 (2005) 287–298.
[25] P. Stadelmann, JEMS Java Electron Microscopy Software, (2004).
[26] P. Hohenberg, W. Kohn, Inhomogeneous electron gas, Phys. Rev. 136 (1964) 864–871.
[27] W. Kohn, L.J. Sham, Self-consistent equations including exchange and correlation effects, Phys. Rev. 140 (1965) 1133–1138.
[28] S. Curtarolo, W. Setyawan, G.L.W. Hart, M. Jahnatek, R.V. Chepulskii, R.H. Taylor, S. Wang, J. Xue, K. Yang, O. Levy, M.J. Mehl, H.T. Stokes, D.O. Demchenko, D. Morgan, AFLOW: an automatic framework for high-throughput materials discovery, Comput. Mater. Sci. 58 (2012) 218–226.
[29] J.P. Perdew, K. Burke, M. Ernzerhof, Generalized gradient approximation made simple, Phys. Rev. Lett. 77 (1996) 3865–3868.
[30] G. Kresse, J. Hafner, Ab initio molecular dynamics for liquid metals, Phys. Rev. B 47 (1993) 558–561.
[31] G. Kresse, J. Hafner, Ab initio molecular-dynamics simulation of the liquid-metal–amorphous-semiconductor transition in germanium, Phys. Rev. B 49 (1994) 14251–14269.
[32] G. Kresse, J. Furthmüller, Efficiency of ab-initio total energy calculations for metals and semiconductors using a plane-wave basis set, Comput. Mater. Sci. 6 (1996) 15–50.
[33] G. Kresse, J. Furthmüller, Efficient iterative schemes for ab initio total-energy calculations using a plane-wave basis set, Phys. Rev. B 54 (1996) 11169–11186.
[34] G. Kresse, M. Marsman, J. Furthmüller, VASP the GUIDE, (2015).
[35] P.E. Blöchl, Projector augmented-wave method, Phys. Rev. B 50 (1994) 17953–17979.
[36] G. Kresse, D. Joubert, From ultrasoft pseudopotentials to the projector augmented-wave method, Phys. Rev. B 59 (1999) 1758–1775.
[37] K. Lejaeghere, G. Bihlmayer, T. Björkman, P. Blaha, S. Blügel, V. Blum, et al., Reproducibility in density functional theory calculations of solids, Science 351 (2016).
[38] M. Methfessel, A.T. Paxton, High-precision sampling for Brillouin-zone integration in metals, Phys. Rev. B 40 (1989) 3616–3621.
[39] P.E. Blöchl, O. Jepsen, O.K. Andersen, Improved tetrahedron method for Brillouin-zone integrations, Phys. Rev. B 49 (1994) 16223–16233.
[40] A. Verdiere, V. Bliznuk, L.A.I. Kestens, R.H. Petrov, Microstructural features controlling very high cycle fatigue of nitrided maraging steel, 6th International Conference VHCF-6, Chengdu, China, 2014.
[41] L. Ryde, Application of EBSD to analysis of microstructure in commercial steels, Mater. Sci. Technol. 22 (2006) 1297–1306.
[42] S.I. Wright, M.M. Nowell, D.P. Field, A review of strain analysis using electron backscatter diffraction, Microsc. Microanal. 17 (2011) 316–329.
[43] C. Mansilla, V. Ocelík, J.T.M.D. Hosson, Local residual stress measurements on nitride layers, Mater. Sci. Eng. A 636 (2015) 476–483.
[44] O. Dmitrieva, P. Choi, S.S.A. Gerstl, D. Ponge, D. Raabe, Pulsed-laser atom probe studies of a precipitation hardened maraging TRIP steel, Ultramicroscopy 111 (2011) 623–627.
[45] A. Deschamps, F. Danoix, F. De Geuser, T. Epicier, H. Leitner, M. Perez, Low temperature precipitation kinetics of niobium nitride platelets in Fe, Mater. Lett. 65 (2011) 2265–2268.
[46] W. Sha, L. Chang, G.D.W. Smith, L. Cheng, E.J. Mittemeijer, Some aspects of atom-probe analysis of Fe-C and Fe-N systems, Surf. Sci. 266 (1992) 416–423.
[47] T. Steiner, S.R. Meka, B. Rheingans, E. Bischoff, T. Waldenmaier, G. Yeli, T.L. Martin, P.A.J. Bagot, M.P. Moody, E.J. Mittemeijer, Continuous and discontinuous precipitation in Fe-1 at.%Cr-1 at.%Mo alloy upon nitriding; crystal structure and composition of ternary nitrides, Philos. Mag. 96 (2016) 1509–1537.
[48] X. Li, Z. Yin, A computer-simulated electron diffraction analysis of precipitates in 18Ni (350) maraging steel, Mater. Lett. 23 (1995) 269–272.
[49] M.K. Miller, M.G. Hetherington, Local magnification effects in the atom probe, Surf. Sci. 246 (1991) 442–449.
[50] A. Morley, G. Sha, S. Hirosawa, A. Cerezo, G.D.W. Smith, Determining the composition of small features in atom probe: bcc Cu-rich precipitates in an Fe-rich matrix, Ultramicroscopy 109 (2009) 535–540.
[51] C. Djega-Mariadassou, L. Bessias, C. Servant, Nanocrystalline precipitates formed by aging of bcc disordered Fe-Ni-Mo alloys, Phys. Rev. B 51 (1995) 8830–8840.
[52] J.B. Lecompte, C. Servant, G. Cizeron, A comparison of the structural evolution occurring during anisothermal or isothermal treatments in the case of nickel and manganese type maraging alloys, J. Mater. Sci. 20 (1985) 3339–3352.
[53] N. Bouzid, C. Servant, O. Lyon, Anomolous small-angle X-ray scattering from a maraging alloy during martensite unmixing, Philos. Mag. B 57 (1988).
[54] A.F. Yedneral, M.D. Perkas, Crystal structure imperfections and martensitic transformations, Fis. Metal. Metalloved 33 (1972) 315.
[55] F. Vurpillot, A. Bostel, D. Blavette, Trajectory overlaps and local magnification in three-dimensional atom probe, Appl. Phys. Lett. 76 (2000) 3127–3129.
[56] D.B. Williams, C. Barry Carter, Transmission Electron Microscopy II, Diffraction, (1996).
[57] G. Miyamoto, A. Yonemoto, Y. Tanaka, T. Furuhara, T. Maki, Microstructure in a plasma-nitrided Fe–18 mass% Cr alloy, Acta Mater. 54 (2006) 4771–4779.
[58] H. Selg, S.R. Meka, M. Kachel, R.E. Schacherl, T. Waldenmaier, E.J. Mittemeijer, Nitriding behaviour of maraging steel: experiments and modelling, J. Mater. Sci. 48 (2013) 4321–4335.
[59] F. Danoix, T. Epicier, F. Vurpillot, D. Blavette, Atomic-scale imaging and analysis of single layer GP zones in a model steel, J. Mater. Sci. 47 (2012) 1567–1571.

Paper III

Error estimates for density-functional theory predictions of surface energy and work function

S. De Waele, K. Lejaeghere, M. Sluydts and S. Cottenier

Physical Review B, **2016**, *94* (23), 235418

S. De Waele performed the surface modeling from which the surface energy and work function were calculated using DFT, interpreted those results and prepared the manuscript.

PHYSICAL REVIEW B **94**, 235418 (2016)

Error estimates for density-functional theory predictions of surface energy and work function

Sam De Waele,[1,2] Kurt Lejaeghere,[1] Michael Sluydts,[1,2] and Stefaan Cottenier[1,2]
[1]*Center for Molecular Modeling, Ghent University, 9052 Zwijnaarde, Belgium*
[2]*Department of Electrical Energy, Metals, Mechanical Constructions and Systems, Ghent University, 9052 Zwijnaarde, Belgium*
(Received 10 July 2016; revised manuscript received 19 September 2016; published 14 December 2016)

Density-functional theory (DFT) predictions of materials properties are becoming ever more widespread. With increased use comes the demand for estimates of the accuracy of DFT results. In view of the importance of reliable surface properties, this work calculates surface energies and work functions for a large and diverse test set of crystalline solids. They are compared to experimental values by performing a linear regression, which results in a measure of the predictable and material-specific error of the theoretical result. Two of the most prevalent functionals, the local density approximation (LDA) and the Perdew-Burke-Ernzerhof parametrization of the generalized gradient approximation (PBE-GGA), are evaluated and compared. Both LDA and GGA-PBE are found to yield accurate work functions with error bars below 0.3 eV, rivaling the experimental precision. LDA also provides satisfactory estimates for the surface energy with error bars smaller than 10%, but GGA-PBE significantly underestimates the surface energy for materials with a large correlation energy.

DOI: 10.1103/PhysRevB.94.235418

I. INTRODUCTION

Due to ever increasing hardware performance and algorithm efficiency, the capabilities of quantum-based computational materials physics continue to grow rapidly. Methods that solve the Schrödinger equation to improve the understanding of materials consequently gain ever more prominence as their reach in system size expands. Density-functional theory (DFT) [1,2] has become one of the most prevalent of these methods. One of the areas in which DFT is being applied, is the modeling of surfaces and interfaces of crystalline solids [3], with an increased emphasis on a computational screening to identify interesting materials without experimental input [4–6]. The usefulness of DFT simulations therefore depends on their *accuracy*, i.e., the deviation with respect to experimental results. A number of studies have attempted to assess the accuracy of DFT-predicted surface properties [7–18]. Most of these studies, however, only consider a limited set of test surfaces, which brings into question the transferability and statistical significance of the accuracy estimate. The present work uses a test set of elemental materials, spanning most of the periodic table, for a statistical analysis of the agreement between DFT-calculated and experimentally measured surface properties. It makes use of the framework established by Lejaeghere *et al.*, who estimated the accuracy of DFT predictions for structural, elastic, and thermal properties of crystalline solids [19,20]. In the same spirit, the objective is to characterize the DFT value as a predictor for the experimental result. This leads to an estimate of the accuracy of DFT-predicted surface properties, the identification of experimental outliers and a protocol to correct calculated quantities *a posteriori* for predictable deviations.

The surface properties considered in this benchmark study are the surface energy and work function of crystalline solids. The surface energy is the energy required to create a surface from the bulk crystal. It is an important thermodynamic quantity governing the equilibrium shape of monocrystals [21–23], brittle fracture [24], or the rate of sintering [25]. The work function is the minimum energy required to extract an electron from the bulk of a material to the surrounding vacuum. It is one of the principal quantities governing thermionic emission [26] and band bending at semiconductor contacts [27]. Because of their fundamental importance, many experimental data are available for both quantities.

Both the work function and surface energy can be derived directly from periodic DFT calculations. This is in contrast to the experimental difficulties encountered when measuring these properties (see Sec. II A). Theoretical predictions of work functions and surface energies therefore offer a convenient and complementary method to cumbersome experiments. Nevertheless, these predictions are not perfect, due to approximations that are meant to make the theory tractable. This work aims to provide a confidence interval for DFT-based surface properties, in order to correctly interpret them with respect to their experimental counterparts.

DFT surface calculations were performed for all group 1 through group 15 elemental materials lighter than Po, except for B, Mn, N, P, and the lanthanides. For N, P, the lanthanides, and materials in groups 16–18, there is very little to no experimental surface information available. A comparison between DFT and experiment is therefore not possible. B and Mn were not considered either, because they both have a very complex unit cell from which surface construction is computationally very cumbersome. For all surfaces both the LDA (in the Perdew-Zunger parametrization) [28] and PBE [29] exchange-correlation functionals were evaluated, as these are two of the most prevalent functionals in the field of solid-state DFT. Additionally, a comparison between both functionals provides insight into how DFT-calculated surface properties depend on the level of theory. In Sec. II the experimental data, details of the calculations and statistical concepts necessary for comparing theory and experiment, are presented. Section III discusses the result of this comparison by evaluating the predictable errors, analyzing the residual errors, and validating the derived correction protocol from theory to experiment.

II. METHODOLOGY

A. Experimental data

The definition of the surface energy is thermodynamically straightforward, but measuring the surface energy of a solid

is extremely difficult and prone to a large imprecision. The experimental challenge is underlined by the myriad of different methods that have been proposed to determine the surface energy. These vary from cleavage experiments [24] for brittle materials, the zero-creep method for more ductile materials [30,31], the analysis of the equilibrium shape of crystallites [22,23], or contact angle measurements of liquid droplets [32]; to less direct solutions such as measuring the elastic modulus [33], the electrical conductivity [34], or even the speed of acoustic waves [35] in submicrometer powder assemblies. These experiments often suffer from a low precision and inaccuracies due to surface contaminants, but more importantly from a benchmark point of view, each method is biased towards a certain class of materials. This inconsistency severely hampers a uniform quantitative comparison across the entire test set of materials evaluated in this work.

Because of the above-described difficulties involved in obtaining the surface free energy of a solid, Tyson and Miller [36] derived a semiempirical approach that uses the liquid surface tension, which can be measured much more accurately. Because the derivation applies to all elemental materials, a consistent database is obtained. Moreover, the transparency of the method by Tyson and Miller makes it possible to estimate a consistent experimental error bar for the surface energies they present, which is necessary for the comparison with DFT predictions. To motivate how the experimental error bars are determined, a short overview of the considerations of Tyson and Miller is necessary.

Tyson and Miller first derived the equality

$$\gamma_{SV} = \gamma_{SL} + \gamma_{LV}, \tag{1}$$

which is valid at melting temperature. γ_{SV} is the solid-vapor interface energy, which is a synonym for the surface free energy being sought for, γ_{SL} is the solid-liquid interface energy, and γ_{LV} the liquid-vapor interface energy (i.e., the surface tension). Although it ignores anisotropic effects of γ_{SL} or γ_{SV}, Eq. (1) adequately represents the average energetic tradeoffs involved in surface formation.

To obtain the relation between the known liquid surface tension γ_{LV} and the desired solid surface energy γ_{SV}, Tyson and Miller then introduced two new ratios, the product of which is the ratio of γ_{SL} and γ_{SV}:

$$\frac{\gamma_{SL}}{\gamma_{gb}}\frac{\gamma_{gb}}{\gamma_{SV}} = \frac{\gamma_{SL}}{\gamma_{SV}} = \alpha, \tag{2}$$

where γ_{gb} is the grain boundary energy for an average high-angle grain boundary. The ratio γ_{SL}/γ_{gb} was determined to be 0.45 ± 0.05 by extrapolation of dihedral angle data of liquid precipitates at grain boundaries in binary alloys [37]. The second ratio γ_{gb}/γ_{LV} was derived from measurements of dihedral angles at thermally etched grain boundaries and estimated to be 0.33 ± 0.04 (see Tyson and Miller). Combining Eqs. (1) and (2), one obtains

$$\frac{\gamma_{SV}}{\gamma_{LV}} = \frac{1}{1-\alpha}. \tag{3}$$

This results in $\gamma_{SV}/\gamma_{LV} = 1.18 \pm 0.03$ as an estimate for a general material. In principle, however, the ratio should be determined for every individual material. This suggests the error margin of ± 0.03 given by Tyson and Miller is somewhat optimistic. Other authors [36] proposed alternative values for the ratio γ_{SV}/γ_{LV} in the range 1.09–1.33, which means a somewhat larger uncertainty of about $\pm 10\%$ should be taken into account for the derived values of γ_{SV} at melting temperature.

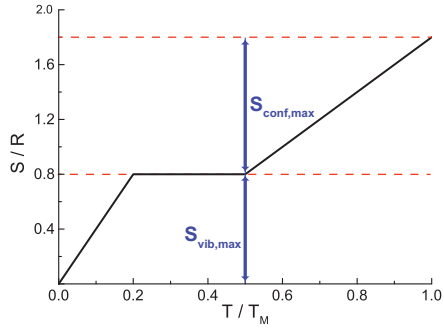

FIG. 1. The surface entropy S as a function of temperature in the simplified model of Tyson and Miller [36]. The first linear increase is due to the activation of surface-related vibrational contributions. The second linear increase is associated with surface roughening.

The conversion from the liquid-vapor to the solid-vapor interface energy is only applicable at the melting temperature T_m. To compare with DFT data, γ_{SV} must be transformed to a surface energy at 0 K. Two entropic contributions were singled out by Tyson and Miller as the most important factors for the temperature dependence of γ_{SV}: the vibrational entropy S_{vib}, and the configurational entropy S_{conf}. The former includes all vibrational modes associated with the surface, whereas the latter aims to describe the surface roughening observed when the material is heated. For both contributions a simplified approximation was proposed [38]. S_{vib} was assumed to increase linearly from 0 to 0.8 R (where R is the universal gas constant) between 0 K and the Debye temperature $T_D \approx 0.2T_m$. Surface roughening, on the other hand, becomes significant from $T = 0.5T_m$ to $T = T_m$ and causes a linear increase in S_{conf} from 0 to R in that temperature interval. The entire temperature-dependent evolution of the surface entropy is depicted in Fig. 1. If the effective [39] surface area A for a surface of general orientation is approximated as $A \approx 1.612N^{1/3}V_m^{2/3}$ [38], with N as Avogadro's number and V_m the molar volume, the temperature-dependent transformation is

$$\begin{aligned}\gamma_{SV}(0) &= \gamma_{SV}(T_m) - \int_{T_m}^{0} \frac{S(T)}{A}dT \\ &\approx \gamma_{SV}(T_m) + \frac{RT_m}{A}.\end{aligned} \tag{4}$$

The transformation of γ_{SV} from T_m to 0 K utilizes a rough approximation for the surface entropy. Other estimates of S_{vib} and S_{conf} suggest a large uncertainty of $\pm 50\%$ should be attached to the RT_m/A value [38]. However, as this term only contributes about 10% of the total surface energy ($RT_m/A \approx 0.1\gamma_{SV}$) [36], the dominant part of the uncertainty remains the conversion from γ_{LV} to γ_{SV}. The total error bar on

the experimental surface energy of a material i is then

$$\sigma_{i,\mathrm{expt}} = \sqrt{(0.1\gamma_{\mathrm{SV}})^2 + (0.5\,\mathrm{R}T_{\mathrm{m}}/A)^2} \approx 0.112\gamma_{\mathrm{SV}}. \quad (5)$$

It must be emphasized that the entire derivation of Tyson and Miller revolves around *averages*. A material-independent conversion from γ_{LV} to γ_{SV} is applied and the temperature effect is estimated by employing a simplified model for the entropy. The only material-specific properties used are surface tension at the melting temperature $\gamma_{\mathrm{LV}}(T_{\mathrm{m}})$ and molar volume V_{m}. This means no crystallographic or anisotropic information is present. Moreover, many materials undergo a phase transformation between 0 K and T_{m}. This begs the question which phase should be associated with the data by Tyson and Miller. A decisive argument to identify the most appropriate surface is the ratio $\gamma_{\mathrm{gb}}/\gamma_{\mathrm{SV}}$. As measurements of this ratio are performed at room temperature, the preferred crystallographic structures are those stable at room temperature. Moreover, work functions are typically measured for those room temperature allotropes as well. Using these when comparing both experimental surface energies and experimental work functions to the DFT-predicted values (see Sec. III), serves to maintain consistency in this accuracy assessment.

Work function measurements are more precise than surface energy measurements. The main source of inaccuracies lies in the presence of surface defects. Adsorbed impurities or structural surface defects can strongly alter the measured work function. For the elemental materials, the work function data compiled by Michaelson [40] forms the largest reference set. However, a rigorous discussion of experimental precision is lacking. A review encompassing fewer elemental materials but a larger amount of data was more recently presented by Kawano [41]. Because more experimental results are available for each material, it is possible to determine reliable experimental error bars for the work functions reviewed by Kawano. The standard deviations on sets of experiments for the same surface are at most 0.18 and 0.25 eV for anisotropic and polycrystalline samples, respectively. For materials with limited experimental data, a safe value of 0.32 eV was applied. There are a number of materials (As, Ba, Bi, Cd, Hg, Mg, Sn, Tl, Zn, and Zr) for which a work function was given by Michaelson, but the data were judged to be of unknown reliability. The accuracy with which the work functions of these materials is predicted by DFT is evaluated, but they are not incorporated in the statistical analysis.

B. DFT calculations for surfaces

A crystalline solid is usually modeled computationally by applying three-dimensional (3D) periodic boundary conditions. A surface of the material is created by inserting a vacuum region within a periodic cell. This essentially mimics a cleavage procedure and creates periodically repeated slabs of N atomic layers, which have two surfaces of an imposed crystallographic orientation (Fig. 2). The surface energy $E_{\mathrm{surf}} = \gamma A$ corresponds to the energy required to create a slab surface of area A. It is obtained from the DFT calculation by subtracting the bulk energy per layer (E_{bulk}) N times from the total slab energy (E_{slab}) and dividing by two to account for the presence of two identical surfaces at both sides of the slab:

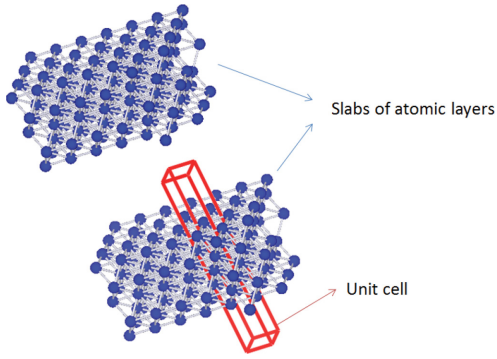

FIG. 2. To model a surface on the atomic scale in a 3D periodic code, slabs of atomic layers are constructed. As an example the {100} surface of a face-centered cubic material is shown. The slab unit cell is indicated by the red box.

$$E_{\mathrm{surf}} = \tfrac{1}{2}(E_{\mathrm{slab}} - N \times E_{\mathrm{bulk}}) = \gamma A. \quad (6)$$

To differentiate the normalized surface energy from E_{surf}, it is usually indicated by γ (as was done in Sec. II A) and expressed in $\mathrm{J/m^2}$.

To correctly model a real surface, no interaction ought to be present between surfaces of neighboring slabs and the center of the slab should behave as bulk material. The first condition is fulfilled by making the vacuum region sufficiently large. The second condition is fulfilled when the work function and surface energy are converged with respect to slab thickness. Using Eq. (6) in this convergence test has a potential computational pitfall, however. Because the bulk and surface energies stem from different DFT calculations, possible numerical discrepancies, caused by different $\vec{k}$-point sampling for example, are enlarged by a factor N, the thickness of the slab [Eq. (6)]. A number of solutions have been proposed to avoid this divergence with respect to slab thickness. Boettger [42] proposed to derive the energy of a bulk layer by subtracting the energy of a slab with $N-1$ layers from that of a slab with N layers. Fiorentini and Methfessel [43] put forward the idea of performing a number of slab calculations and deriving the bulk energy from a linear fit to the energies. Another possible solution is to create a bulk unit cell which matches the orientation of the slab. This would allow for a perfect match in $\vec{k}$-point meshes.

By evaluating all of the above-described approaches to improve convergence of Eq. (6), it was concluded that none of them improved on simply performing a *very precise* bulk and slab calculation. Recently Singh-Miller *et al.* [14] came to the same conclusion when reviewing these different methods. The alternative methods are mainly useful when fine $\vec{k}$ meshing is unfeasible due to hardware limitations. When it is possible to apply highly converged sampling in reciprocal space, however, sticking to a simple bulk calculation is sufficient and avoids additional difficulties. It is, for example, not clear how thick the slab should be when using the Boettger method. Neither

is it easy to determine which thickness range is suitable for deriving the bulk energy from a linear fit, as per the method by Fiorentini and Methfessel.

A calculation of an atomic slab model is inherently limited to a surface of a specific orientation. How does one compare the corresponding anisotropic surface energy prediction by DFT with experimental data? Since Tyson and Miller presented their experimental data as valid for a surface of "general orientation," the ideal solution would be to calculate a number of different orientations sufficiently large to integrate over the two-dimensional orientation space. For materials with cubic symmetry, however, the {100}, {110}, and {111} surfaces actually suffice to perform the integration. By applying the terrace-ledges-kinks (TLK) description of a general surface [44], a ledge (or step) energy can be fitted to the transformation from one orientation to the other, and can subsequently be used to interpolate the surface energy to a general orientation. This approach produces good results for cubic materials because the above-mentioned simple surfaces already cover a total of 26 orientations. For materials with hexagonal, rhombohedral, or tetragonal symmetries a significantly larger number of DFT calculations is needed. Fitting the ledge energy is only valid for interpolating between two simulated orientations with a limited angular separation. Moreover, additional simulations involve more vicinal surfaces, requiring larger slab unit cells and thus a higher computational cost. For the sake of simplicity and consistency across different crystal structures, the basic arithmetic mean of three low-index surfaces was used (see further). Comparing this simple approach with the more accurate results from the TLK approach for the cubic materials, a decrease in surface energy of about −5.5% is observed. This shift is, however, almost completely material independent, ranging from −5.66% to −5.19%. For a comparison to experimental data, the near-constant deviation means the simple arithmetic mean is as valuable as the TLK approach (see Sec. II C).

Whereas the DFT surface energy is derived from the comparison of a bulk and a slab calculation [Eq. (6)], the work function can be directly obtained solely from the slab calculation. The work function is

$$\Phi = V_{\text{vac}} - E_{\text{F}}, \tag{7}$$

where E_{F} is the Fermi energy and V_{vac} corresponds to the local one-electron potential at a point in the vacuum where it becomes constant (i.e., where it is no longer affected by the presence of the surface). To obtain better convergence of the work function with respect to slab thickness, the method of macroscopic averages was proposed by Fall *et al.* [45]. In this method, the Fermi energy from a bulk calculation is used instead. However, for the simple nonpolar slabs in this work, their method does not result in a more reliable work function, provided the slab used for the calculation is sufficiently thick.

For many materials there is only a polycrystalline work function available, which corresponds to a surface containing different facets of varying crystallographic orientation. In a review of photoelectric experiments for obtaining work function data, Helander [46] concluded it is the facet with the lowest anisotropic work function which determines the measurement. This is confirmed by the review by Kawano, where there are both polycrystalline and anisotropic data available for 14 materials. The work functions for polycrystalline samples are on average only 90 meV higher than those of the surface orientation with the lowest work function.

The slab unit cells were constructed from optimized bulk geometries with the use of the ACONVASP software package and are provided in the Supplemental Material [47,48]. For the elemental materials with cubic crystal structures, the {100}, {110}, and {111} surfaces were taken into account. For the hcp and rhombohedral structures, the {0001}, {10$\bar{1}$0}, and {11$\bar{2}$0} surfaces were simulated. The {100}, {110}, and {001} surfaces were selected for the tetragonal materials and the {100}, {010}, and {001} surfaces for orthorhombic Ga. The surface atoms were allowed to relax to acquire an optimized surface structure for all materials. The (2×1){111} and the (2×1){100} surface reconstructions for the diamond structures were also included. There are a number of possible reconstructions for the diamond structures, which were computationally evaluated by Stekolnikov *et al.* [49]. As the (2×1) reconstructions were always either the most stable or at most 6% higher in surface energy, these were the ones included in the present DFT calculations. For materials with more than one atom in the primitive unit cell, some surface orientations have more than one possible termination. In these cases, the energetically most favored termination—the one with the lowest surface energy—was applied to both ends of the slab. For Fe, Co, Ni, and Cr, magnetization of the surface was taken into account.

The Vienna *ab initio* simulation package (VASP) software [50–53] was used with VASP 5.2 recommended PAW potentials [54–56] for all LDA and PBE calculations. These potentials were recently shown to provide a similar precision as all-electron calculations [57]. Convergence tests were performed to determine the most appropriate meshing in reciprocal space, plane-wave cut-off energy, slab thickness, and number of surface layers allowed to relax. To efficiently determine the optimal settings, four electronically different materials were selected for each crystal structure (see Supplemental Material for convergence tests [48]). The most stringent settings required for this group of four materials were applied to all other materials with the same crystal structure. The numerical precision associated with these settings was 60 meV for work functions and 5% for surface energies in the worst cases, significantly lower than the experimental error bars discussed in Sec. II A. The plane-wave cut-off energy was set at 400 eV for all materials except for Li (800 eV) and C (600 eV). A convergence criterion of 10^{-8} eV was used for the electronic self-consistent cycle and of 10^{-6} eV for the structural optimization. The vacuum spacing between slabs was always chosen to be approximately 20 Å wide. The exchange and correlation contributions to the local one-electron potential were not taken into account to determine V_{vac}, as these converge to zero sufficiently far from the surface. During structure relaxations, Methfessel-Paxton smearing of first order [58] ($\sigma = 0.01$ eV) was used. During all other calculations, the tetrahedron method with Blöchl corrections was used [59] for all other calculations. All final slab geometries, settings, DFT results, and experimental data used for comparison are available in the Supplemental Material [48].

C. Statistical analysis

When presenting results of experimental measurements, it is common practice to provide confidence intervals. Guidelines for the determination of such intervals are summarized in the *Guide to the Expression of Uncertainty in Measurement* (GUM) [60]. Published computational results, on the other hand, are rarely accompanied by an error bar. Indeed, determining such an interval is not straightforward, as Civalleri *et al.* [61] illustrated by showing how the comparison of computational methods is affected by the chosen error measure. A formal framework proposed by Irikura *et al.* [62] aims to adhere to international standards as recommended by the GUM by removing the bias in the error. For a DFT-predicted materials property this entails selecting a representative test set and determining the average error. This predictable part of the DFT error can subsequently be distinguished from a material specific error and utilized to transform the calculated result to the expected true value, serving as an *a posteriori* calibration. This decomposition of the computational error has been applied to DFT results [19,20,63] and was recently reviewed by Pernot *et al.* [64]. Note that, whereas the present work discusses computational errors in terms of predictable and material-specific contributions, literature sometimes refers to systematic and random errors. Here the terms systematic and random are avoided, since all computational results are intrinsically deterministic.

To find the predictable error, the discrepancy between the DFT results and experimental data must be analyzed for trends. This boils down to a search for a general transfer function f which maps the computational results X_i onto the experimental values Y_i. The preferred option is a simple model for f with only a few parameters which are intuitively easy to understand. Because of the simple form of f and the complex nature of the errors, there will always remain some amount of scatter ϵ between the transformed DFT results $\hat{Y}_i = f(X_i)$ and the actual experimental results Y_i:

$$Y_i = f(X_i) + \epsilon_i = \hat{Y}_i + \epsilon_i. \tag{8}$$

The residual errors ϵ_i are the material-specific part of the error. They represent a true measure of the inadequacy of the method, as they cannot be removed by correcting for an overall bias. If ϵ_i were zero for all materials i, there would be a perfect mapping between DFT and experiment. This is why an average of three different anisotropic DFT-predicted surface energies is equally valuable as an isotropic surface energy derived by the more accurate TLK approach, as discussed in Sec. II B. The discrepancy between those two methods is entirely material independent and thus predictable. Consequently, the residual errors ϵ_i are the same for both methods.

Determining $\hat{Y} = f(X)$ is most conveniently achieved by proposing a function with p parameters $(\beta_0, \beta_1, \ldots, \beta_p) = \vec{\beta}$ and subsequently minimizing the sum of squares of the residual errors (SSR). For a zero-centered normal distribution of the residual errors ϵ_i, this yields the maximum likelihood estimate (MLE) for $\vec{\beta}$ [65],

$$\mathrm{SSR} = \sum_{i=1}^{n} (\hat{Y}_i - Y_i)^2 = \sum_{i=1}^{n} [f(X_i, \vec{\beta}) - Y_i]^2. \tag{9}$$

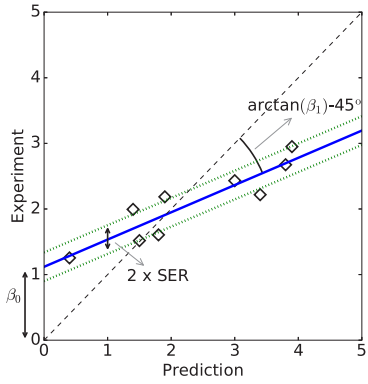

FIG. 3. An illustration of the meaning of the SER. It is a variable, residual error (green dotted line) on top of a predictable deviation (solid blue line).

The SSR is a metric for the total absolute deviation from the proposed model $f(X, \vec{\beta})$. Divided by the statistical degrees of freedom $n_{\mathrm{df}} = n - p$, it also forms an unbiased estimator for the variance σ_ϵ^2 on the ϵ_i. Its square root is referred to as the standard error on the regression (SER) [65] (Fig. 3):

$$\mathrm{SER} = \hat{\sigma}_\epsilon = \sqrt{\frac{\mathrm{SSR}}{n - p}}. \tag{10}$$

When there is an additional uncertainty on the experimental values Y_i, the residual error in Eq. (8) decomposes into $\epsilon_i = \epsilon_{i,\mathrm{DFT}} - \epsilon_{i,\mathrm{expt}}$. If all experimental values are equally precise, Eq. (9) and the fitting procedure can be used unaltered. If, on the other hand, $\epsilon_{i,\mathrm{expt}}$ differs for different X_i the MLE metric to obtain $\vec{\beta}$ slightly changes [65]:

$$\mathrm{SSR} = \sum_{i=1}^{n} \left(\frac{f(X_i, \vec{\beta}) - Y_i}{\sigma_{i,\mathrm{expt}}} \right)^2 = \sum_{i=1}^{n} w_i [f(X_i, \vec{\beta}) - Y_i]^2. \tag{11}$$

The added weights $w_i = 1/\sigma_{i,\mathrm{expt}}^2$ warp the SSR metric, emphasizing more precise experimental data. This in turn alters the interpretation of the SER. Multiplied by the local experimental deviation $\sigma_{i,\mathrm{expt}}$, it is now an estimate of the local residual error ϵ_i. Because the experimental imprecision is likely uncorrelated with shortcomings of the DFT model, one can write

$$\hat{\sigma}_{\epsilon,i}^2 = \sigma_{i,\mathrm{exp}}^2 \mathrm{SER}^2 = \sigma_{i,\mathrm{expt}}^2 + \hat{\sigma}_{i,\mathrm{DFT}}^2. \tag{12}$$

Note how Eq. (12) implies that the SER can never be expected to be smaller than one, as deviations caused by experiment are always present. The SER thus becomes a measure of the relative contribution of the DFT model to the total uncertainty. This confirms the importance of the discussion on experimental errors in Sec. II A. This is not only true for the quantities discussed in this work. Recently, Kirklin *et al.* [66] concluded that the mean absolute error on experimental formation energies was of comparable size

(0.082 eV/atom) to the average absolute difference between DFT and experiment (0.096 eV/atom).

By determining the parameters $\vec{\beta}$, a protocol can be created to transform any DFT-predicted value to the expected experimental one. The SER $\times\, \sigma_{i,\mathrm{expt}}$ obtained via $\vec{\beta}$ then serves as an error bar on this prediction. However, there are a number of important assumptions involved in the application of the least-squares method and the subsequent residual error analysis. First, the value of the derived function $f(X)$ depends on the soundness of the experimental data and the representativity of the test set for a general material. The meticulous determination of material-dependent experimental error bars (Sec. II A) and the large and varied test set should address those concerns. Second, all derived quantities in this section assume a zero-centered normal distribution for the residual errors $(\hat{Y}_i - Y_i)/\sigma_i$. By analyzing the residual errors, this assumption can be evaluated (Sec. III).

III. RESULTS

A. The character of the predictable error

In Sec. II C the transfer function f between theory and experiment, which contains the predictable error, was discussed for a general situation. To determine the most suitable form of f, Bayesian model selection (BMS) was used. The probabilities of different polynomial degrees were compared, by evaluating the model probability as described by Mana *et al.* [67], and are presented in Fig. 4. For the work function data, a linear form $f(X_i) = \hat{Y}_i = \beta_0 + \beta_1 X_i$ is the most likely model. For the surface energy data, on the other hand, adding a quadratic degree of freedom is an equally likely possibility. The possibility of a quadratic dependence is, however, chiefly caused by a different error behavior for some materials classes. The residual errors for the group 1 and group 2 materials are distinctly different from the other materials. Combined with their low surface energies (see Fig. 6), this causes the apparent quadratic dependence. When separate BMS analyses are performed, one for the 10 group 1 and group 2 materials and one for the 33 other materials, the linear form turns out to be the more probable model except for the PBE surface energies for the group 1 and group 2 materials, shown with the red columns in Fig. 4(d). In this case, the influence of the aberrant behavior of Be heavily influences the small group of only ten materials. Because the error on the DFT surface energy for a *general* material is not actually quadratic, but rather consists of two linear contributions, no quadratic term was added to f. This approach serves to make the statistical analysis on the current test transferable to a general material.

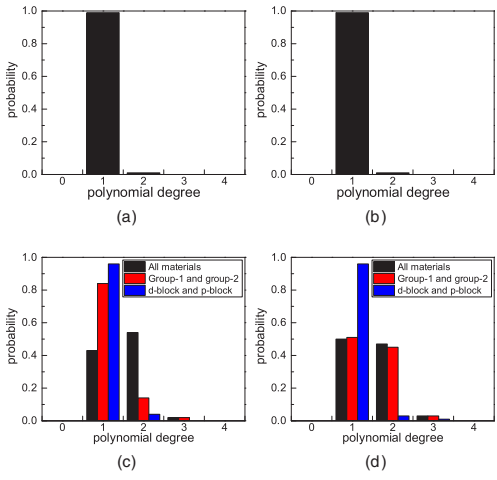

FIG. 4. Results of the Bayesian model selection (BMS) analysis. Left: LDA work functions (a) and surface energies (c). Right: PBE work functions (b) and surface energies (d). A linear fit is clearly the most likely model for both LDA and PBE work functions. For surface energies, the different error character of group 1 and group 2 materials as opposed to the *d* block and *p* block materials result in the quadratic model competing with the linear model.

B. Outlier analysis

In Sec. II C it was stressed that one of the inherent assumptions of the present statistical analysis is the zero-centered normality of the residual errors. Since all data sets contain fewer than 100 materials there are no meaningful quantitative tests available to check for normality. The most effective ways to check for non-normal behavior are then the simple histogram and the quantile-quantile plot (QQ plot). The latter is constructed with Blom's method for normal scores [68]. Both graphical tools also assist in spotting outliers in the data set. Excluding such outliers merely on the grounds of an aberrant residual error is unjustified, however. Indeed, as the residual error contains material-specific inaccuracies of the DFT result, outliers may provide information on the shortcomings of the theoretical prediction.

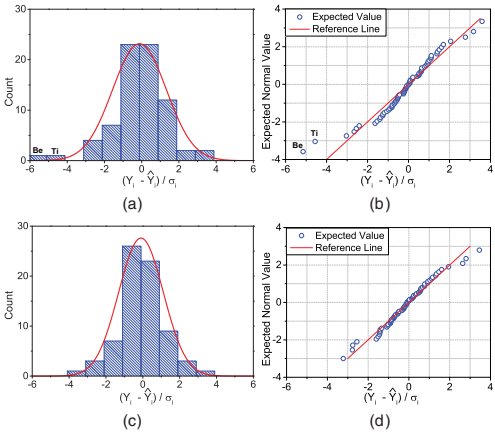

FIG. 5. Analysis of the residual errors for LDA work functions: histograms with fitted normal distributions before (a) and after (c) the removal of the outliers Be and Ti, accompanied by QQ plots before (b) and after (d) outlier removal.

In the histogram and QQ plot of the residuals [69] for the LDA work function (Fig. 5), two clear outliers can be observed: Be and Ti [see also Fig. 6(a)]. The same outliers can also be identified in the PBE work function data set [Fig. 6(b)]. The large residual error is most likely due to the surface crystallography of the samples used to measure the experimental work functions. Section II A stated that for a given material, the lowest anisotropic DFT work function corresponds to the polycrystalline result. This requires of course that the surface orientation with the lowest work function is present in the polycrystalline sample, a condition which seems unfulfilled in the case of Be and Ti. This is especially the case for Be, for which there are alternative work function data available [70,71] that vary significantly from the value of Michaelson. Both materials were therefore excluded from the analysis. Figure 5 demonstrates the importance of removing both outliers. The reduced data in Fig. 5(d) fit significantly better to a normal distribution than the full set in Fig. 5(b). For LDA and PBE the SER drops from 1.46 to 1.23 and 1.49 to 1.29, respectively. This reduction of the SER is not merely a consequence of outlier removal, it also indicates a much improved regression result for the remaining data. The DFT-predicted work functions of Zr and As also show quite a large discrepancy with respect to the experimental values (Fig. 6). These were materials for which the work function was presented as uncertain by Michaelson [40], therefore they carry no weight in the statistical analysis. As such, it is expected that the DFT prediction is more accurate than the uncertain experimental values for those materials.

Among the residual errors for the LDA surface energies, Cr and Ge are two clear outliers (see Fig. 6(c) and the Supplemental Material [48]). For both of these materials, the disagreement between theory and experiment is due to the breakdown of the approach of Tyson and Miller [36] to

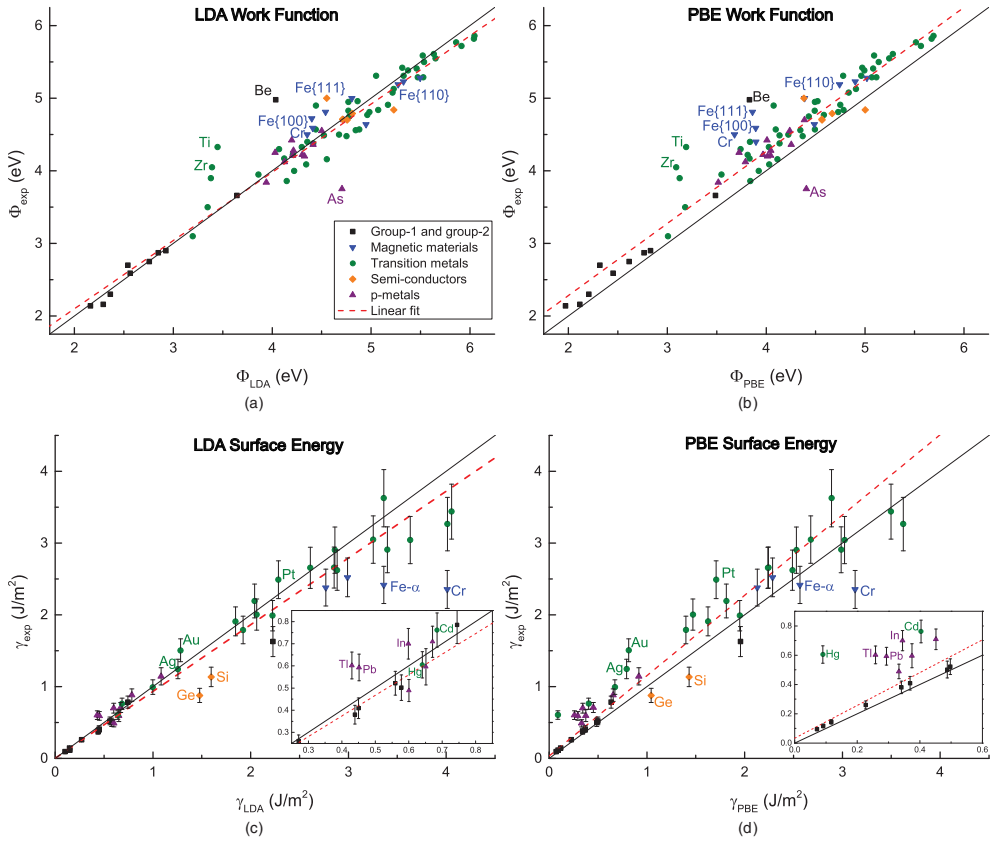

FIG. 6. Linear fits of experimental values to DFT predictions for all four evaluated data sets. Left: LDA work functions (a) and surface energies (c). Right: PBE work functions (b) and surface energies (d). For clarity, an inset is provided of the low surface energy range for both LDA (c) and PBE (d). The data points are color coded per material class [legend in (a)]. The linear fit is indicated by a red dashed line, with the first bisector in black, corresponding to the ideal theory, serving as reference. Materials of particular interest are indicated with a label.

obtain reliable experimental surface energies. Cr is the only material in the present test set which is antiferromagnetic [72]; no magnetic surface effects are included in the derivation by Tyson and Miller however. In the case of Ge, the significant surface reconstruction is probably the cause of the very large residual error. The approach by Tyson and Miller focuses specifically on metals, without taking surface reconstruction into account. For Si, of which the surface energy was also overestimated but not such a significant outlier, it is possible to consult additional experimental results, derived via other methods, to shed some light on this problem. Eaglesham *et al.* [73] derived surface energies for the low-index surface orientations of Si from the equilibrium shape of crystallites, combined with the cleavage energy for the Si{111} plane measured by Jaccodine [74]. With the latter value measured at $-196\,^{\circ}$C and the crystallite equilibrium shapes used to extrapolate the {111} surface energies to the other orientations, the values presented by Eaglesham *et al.* are good candidates for comparison with 0 K DFT values. These experimental values are in much better agreement with the DFT values than the semiempirical results obtained by Tyson and Miller [36]. The DFT surface energies are still larger than the experimental values, but only by about 3%–11% for PBE and 16%–23% for LDA. Moreover, the anisotropy found by Eaglesham *et al.* [73] in the crystallite shape, is reproduced by the DFT calculations. When alternative experimental data for Si{110} are also included into the comparison, it is found that no experimental method renders surface energies as low as the one presented by Tyson and Miller, although they range from 1.43 to 5.38 J/m^2 [75]. From this it can be concluded that the semiempirical derivation used by Tyson and Miller is unsuitable for obtaining the surface energy of the Si and Ge semiconductors. Excluding both Cr and Ge from the test set again ensures zero-centered normality of the residuals and improved regression results with lower SERs. To maintain consistency when comparing the LDA and PBE functionals, Cr and Ge are also removed from the PBE surface energy data set, although in this case they are less distinct outliers. This is not because these materials perform better with PBE than with LDA, but because PBE is less accurate for surface energies than LDA (see Sec. III C).

C. Regression analysis

Table I presents the error estimates resulting from the linear regressions for LDA and PBE work functions and surface energies. All four linear fits are shown in Fig. 6, with data points of particular interest accompanied by a label. The weighted residual errors for the work function and surface energies are indicated with a color code in Fig. 7, with darker shades highlighting larger residual errors. Some experimental work functions were deemed unreliable by Michaelson [40], so these carry zero weight in the regression analysis.

Both LDA and PBE produce very similar residual errors for work functions when compared to experiment. Regardless of the chosen functional, the SER is smaller than $\sqrt{2}$ [see Eq. (12)], which means that the DFT inaccuracy, after correcting for predictable errors, is expected to be smaller than the typical experimental uncertainty. These predictable errors differ somewhat between LDA and PBE, with a simpler

TABLE I. Error estimates from the linear regression between experimental and DFT values, for all four data sets. The coefficients β_0 and β_1 are accompanied by an expected error, obtained from the diagonal elements of the covariance matrix (see the Appendix A). A 95% confidence interval is provided for the SERs (see the Appendix A for derivation).

	β_0 (eV)	β_1	SER
Φ_{LDA}	0.22 ± 0.09	0.94 ± 0.02	$1.22^{1.47}_{1.05}$
Φ_{PBE}	0.30 ± 0.09	0.99 ± 0.02	$1.29^{1.55}_{1.11}$
	β_0 (J/m^2)	β_1	SER
γ_{LDA}	0.00 ± 0.01	0.93 ± 0.02	$1.36^{1.74}_{1.12}$
γ_{PBE}	0.03 ± 0.01	1.12 ± 0.02	$2.34^{2.98}_{1.92}$

character of the predictable error for PBE, as it solely consists of a 0.3 eV constant offset.

Although PBE is the higher level of theory, it does not appear to improve surface energies; LDA is clearly the more accurate functional in this respect, as evidenced by its significantly smaller SER. The predictable error derived from the regression shows an 11% underestimation of the surface energy by PBE ($\beta_1 = 1.12$), but an overestimation of 8% by the LDA functional ($\beta_1 = 0.93$). Such trends are to be expected: creating a surface can be crudely approximated by the breaking of atomic bonds [76] and it is a well-established observation in solid-state DFT that the LDA functional overestimates bond strength, whereas PBE underestimates it [77]. Consequently, the predictable errors on the DFT surface energy are transferable from predictable errors on the DFT cohesive energy [19], a bulk property. Such a connection is also present for the residual error. The Pearson correlation coefficient between the residual errors for the surface energy and the *relative* residual errors [78] for the equilibrium volume is -0.81. This suggests that the error on DFT surface energy predictions very often coincides with an error in predicting the correct equilibrium volume. Such a relation is not observed for work function errors.

The magnetic materials, Fe and especially Cr, are among the worst performing materials, their surface energies being severely overestimated by DFT. This ties in to the discussion of the validity of the approach by Tyson and Miller [36] when magnetic materials are concerned (Sec. III B). The surface energies for Fe, Co, and Ni are slightly improved by using PBE, but it is hard to discern whether this is due to improved DFT modeling or the manner in which the experimental data are derived. The surface energies of Ge and Si are also overestimated by both functionals, even though the DFT values presented in this work are somewhat lower than those presented by previous authors [49,79].

The SER for LDA surface energies is markedly lower than for PBE results, making the former stand out as the functional of choice for predictions of the surface energy. The worse general accuracy of PBE surface energies is mainly due to the poor description of materials in the right part of the d block and of some of the p metals. These materials are labeled in Figs. 6(c) and 6(d), and the trend can be clearly seen in Fig. 7. The loss of accuracy of PBE with respect to LDA for surface

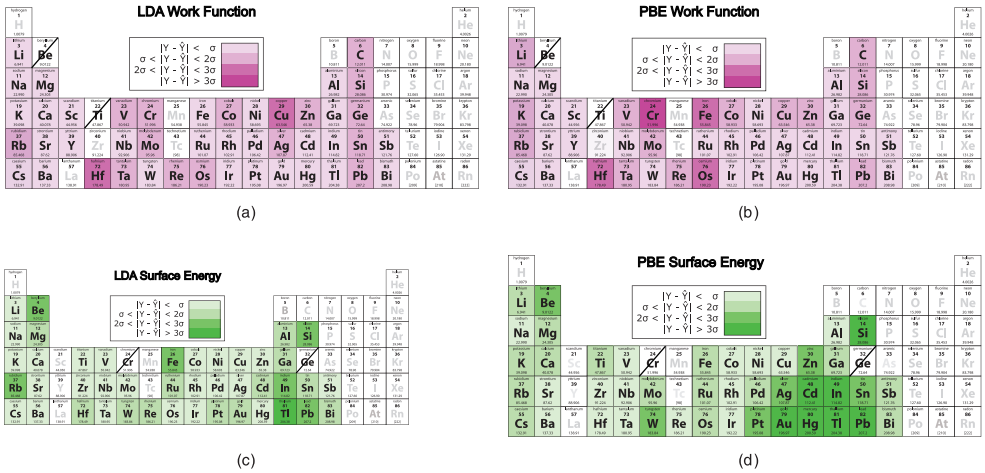

FIG. 7. Overview of the residual errors of the materials for which a comparison with experiment can be made. Top: LDA (a) and PBE (b) work functions. Bottom: LDA (c) and PBE (d) surface energies. A darker shade represents a larger absolute value of the weighted residual error ϵ_i. There are four shades in total, corresponding with the intervals 0–1, 1–2, 2–3, and 3–∞ (see legend). Be and Ti were removed from the work function data set, Cr and Ge were removed from the surface energy data set (see Sec. III B). Materials for which no comparison is made have a gray symbol. Mn, Be, Se, and Te were not calculated because of their crystallographic complexity. There are experimental work function data for Zr and As, but the accuracy of these values is unconfirmed [40].

energies has been discussed by both Kurth *et al.* [80] and Staroverov *et al.* [77], who evaluated the surface energy for a jellium surface. The separate contributions of the exchange and correlation energy to the surface energy were compared to highly accurate random-phase approximation (RPA) calculations that included a short-range GGA correction. They concluded that the reason why LDA provides more accurate surface energies than PBE is entirely fortuitous. Correlation contributions, such as dispersion, are inaccurate for both LDA and PBE, but the overestimation of the exchange contribution to the surface energy within LDA cancels that inaccuracy to a large degree. This explains why materials in the right part of the *d* block suffer from worse surface energy predictions within PBE, as the correlation energy offers a large contribution to the total energy for these materials. This is for example apparent from the extreme case of Hg [81]. In the case of the *p* metals, the overestimation of the exchange energy also corrects for the absence of dispersion contributions. A well-known example where this correction is relevant is the c/a of graphite, which is predicted very accurately by LDA but is overestimated by PBE [82,83]. When, as a test, all materials from group 12 onwards (those with a full *d* shell or a partially occupied *p* shell) and noble metals Pt, Ag, and Au are excluded from the test set, PBE and LDA perform equally well (Table II). For both functionals the SER is reduced to 0.98 and 1, respectively, suggesting their inaccuracy is very similar when the materials with a large correlation energy are excluded. Because these materials are outliers due to theoretical shortcomings in the DFT functionals, and not due to inaccuracies in the experimental result, they were not excluded from the test set.

Due to the deficient description of both exchange and correlation by semilocal functionals, an improved prediction of the surface energy can be achieved by describing both of them at a higher level. One of the possible approaches is quantum Monte Carlo (QMC), which was used by Alfè and Gillan [84] to calculate the surface energy of the MgO {100} surface. By comparing the QMC result to the DFT-LDA and DFT-PBE results, respectively, they concluded that LDA yields a better result. An alternative approach is to use exact exchange (EXX) combined with the many-electron perturbation theory extension known as the random phase approximation (RPA) to go beyond DFT [85,86]. Both Lazar and Otyepka [17] and Schimka *et al.* [87] recently obtained very accurate surface energies by using the EXX+RPA approach. By comparing their highly accurate calculated values with surface energies from cleavage experiments, they suggested the problem of unreliable surface energies as obtained by (semi)local DFT has been solved [77,80].

TABLE II. A comparison between the linear fits of LDA and PBE surface energies to experimental ones when Pt, Ag, Au, and all group 12 through group 15 materials are removed from the data set. Removing these materials with large correlation contributions results in LDA and PBE having a very similar accuracy.

	β_0 (J/m^2)	β_1	SER
γ_{LDA}	0.00 ± 0.01	0.90 ± 0.02	$1.00^{1.37}_{0.79}$
γ_{PBE}	0.02 ± 0.01	1.06 ± 0.03	$0.98^{1.35}_{0.77}$

However, EXX+RPA calculations are computationally very expensive. The current analysis highlights the problematic materials classes for which such an investment would be cost effective.

D. Validation of the model

In the previous section, predictable errors were derived that, when corrected for, enable a better agreement with experiment. These predictable errors remain to be validated. This means that the ansatz that the test set is representative for a general material should be evaluated. In a first step, this can be done internally (within the test set). By leaving one material out of the test set and repeating the linear regression between theory and experiment, the sensitivity of the regression to a single data point can be assessed. None of the four data sets contain a data point of which the removal significantly impacts the parameters $\vec{\beta}$. Not even the PBE surface energy of Hg, the removal of which results in a lowering of the SER to 2.00, alters the regression coefficients more than the expected deviation (Table I).

To externally validate the derived regression results, binary materials can be considered. As an example, DFT-predicted work functions of ZrC{100} [88] and Cu_3Pt{111} [89] are transformed using the regression results from Table I, provided with an error bar and compared to experimental results. The same comparison is made for the surface energy of MgO {100}, although the experimental data in this case originate from cleavage experiments [24,90,91]. The transformed DFT results and the corresponding experimental data are presented in Table III.

The error bars in the first and second column are calculated by propagating the expected error on β_0 and β_1 (which are small), combined with $\sigma_{i,\mathrm{DFT}}$, which is derived from the SER and Eq. (12). To apply Eq. (12), $\sigma_{i,\mathrm{expt}}$ must be known. This is of course not practically possible when DFT is used to *predict* a work function or surface energy. The standard experimental errors that were discussed in Sec. II A can be used for this purpose: $\sigma_{\mathrm{expt}} = 0.32$ eV for work functions and $\sigma_{\mathrm{expt}} = 0.11\gamma$ for surface energies, with γ the transformed DFT result.

For MgO and Cu_3Pt the transformed theoretical results are in excellent agreement with experiment, although the error bar for γ_{PBE} is rather large due to the larger SER. The transformed work function of Cu_3Pt is closer to the experimental value for both LDA and PBE than the bare calculated value. In the case of the surface energy of MgO, it is unclear whether the transformation is an improvement because of the large spread in experimental data. In contrast, the predicted work function of ZrC does not agree all that well with experiment. There is only one experimental value available for the {100} surface, but quite a few more are amassed for polycrystalline ZrC in the Kawano review [41]. They are spread out between 3.2 and 4.48 eV, which indicates that precise ZrC work functions are hard to obtain. In this light, as in the case of As and Zr, the theoretically predicted 4.32 eV might serve as a superior assessment of the ZrC{100} work function.

TABLE III. Comparison of the transformed DFT-predicted surface energy of MgO {100} and work functions of ZrC{100} and Cu_3Pt{111} surfaces to experimental data. Error bars are derived by propagating the error on the coefficients $\vec{\beta}$ and deriving $\sigma_{i,\mathrm{DFT}}$ from the SER. The direct results from DFT calculations are given in parentheses. The experimental error bars on the surface energies are those presented by the original authors. For the work functions, however, no such experimental error bar was given. The general experimental error of ±0.32 eV, derived from the data by Kawano [41], is given here.

	γ_{LDA} (J/m^2)	γ_{PBE} (J/m^2)	γ_{expt} (J/m^2)
MgO	1.16 ± 0.12 (1.25)	1.03 ± 0.24 (0.896)	1.15 ± 0.08 [90] 1.20 ± 0.12 [24] 1.33 ± 0.06 [91]
	Φ_{LDA} (eV)	Φ_{PBE} (eV)	Φ_{expt} (eV)
ZrC{100}	4.31 ± 0.25 (4.35)	4.32 ± 0.29 (4.06)	3.85 ± 0.32 [88]
Cu_3Pt{111}	5.18 ± 0.26 (4.93)	5.22 ± 0.29 (5.32)	5.40 ± 0.32 [89]

IV. CONCLUSION AND OUTLOOK

By comparing 43 experimental surface energies and 73 work functions to their DFT-predicted counterparts, the accuracy of the PBE and LDA functionals was quantified for surface properties. The deviation between the theoretical predictions and experiment was separated into a predictable and a residual contribution. The predictable error was determined with a weighted linear regression, fitting to a linear trend, and is valid for a general material. The residual error, on the other hand, stems from material-specific deviations from the general trend. It was quantified by the standard error on the regression (SER), which is derived from the residual errors for the entire test set. The SER is regarded as a good measure of theoretical inaccuracy and was used to assess the quality of DFT predictions with different functionals. The comparison of the DFT-predicted surface energies and work functions with experimental data is summarized in Fig. 6. The residual errors for both functionals are indicated with a color code in Fig. 7.

Both the LDA and PBE functional yield a SER smaller than $\sqrt{2}$ when the DFT-predicted work functions are compared to experiment. This means that, after correcting for predictable errors, both levels of theory are likely to yield work function results of comparable—even slightly better—quality than experimental results, as the error due to theoretical inaccuracy is expected to be smaller than the one resulting from experimental imprecision. The predictable part of the error has a very simple form for the PBE functional, as it only consists of a 30 meV constant offset. Both LDA and PBE, however, are excellent tools to predict the work function of a crystalline solid.

For surface energy predictions, there is a large discrepancy between the SER of the LDA and PBE functionals. This is mainly caused by poor performance of the PBE functional. Although it is a higher level of theory, it severely underestimates the surface energy of materials for which correlation contributions are important. In contrast, the LDA functional provides more accurate predictions for such materials. This agreement is, however, entirely fortuitous, as was discussed by Kurth *et al.* [80] and Staroverov *et al.* [77]. As such, LDA emerges as a more accurate method for calculating surface energies.

It would be very insightful to extend this research to other functionals, especially for surface energies. Other parametrizations of the GGA, such as the revised PBE (revPBE) [92] or PBEsol functional [93], are tuned for a better prediction of surface properties and could provide more accurate surface energies. More recent GGA functionals, such as the TM functional by Tao and Mo [94], might also provide improved surface energies. However, significant improvements, especially for correlation-governed materials, probably require a higher level of theory. The use of the random-phase approximation (RPA) could solve the severe underestimation of the surface energy for those materials, as was recently suggested in reports by Schimka *et al.* [87] and Lazar and Otyepka [17].

This research was limited to the VASP software package and the use of its recommended PAW potentials. A comparison with different simulation packages, as was performed by Lejaeghere *et al.* [19,57] for bulk properties, could uncover computational shortcomings not associated with the exchange-correlation functional. In addition, the inclusion of spin-orbit coupling, or even of fully relativistic effects, could provide valuable insights into DFT-related shortcomings for the heavier materials.

During this research, over 300 anisotropic work functions and surface energies were calculated. Most predictions, however, cannot be directly compared to experimental data. Moreover, for some materials the experimental values are scarce or unreliable, e.g., the work functions of As, Zr, and ZrC. In such cases, DFT results may provide a reliable estimate, after correcting for predictable errors. In addition, the development of more advanced experimental methods, especially for measuring surface energy, could provide a wealth of information to analyze the DFT shortcomings more precisely.

ACKNOWLEDGMENTS

This work benefited from financial support from the Research Board of Ghent University (BOF) and the Research Foundation Flanders (FWO) (projects No. G.0760.12 and No. G0E0116N). Sam De Waele and Stefaan Cottenier acknowledge financial support from OCAS NV by a funded Ph.D. position and by an OCAS-endowed chair at Ghent University, respectively. The computational resources and services used in this work were provided by the VSC (Flemish Supercomputer Center), funded by the Research Foundation Flanders (FWO) and the Flemish Government department EWI (Economy, Science and Innovation).

APPENDIX: WEIGHTED GENERAL LINEAR REGRESSION

This Appendix serves to provide all the statistical formulas used in this work. The estimators for the parameters $\vec{\beta}$ are found by minimizing Eq. (11). The result can be elegantly contracted in matrix form:

$$\vec{\beta} = (\mathbf{X}^{\mathrm{T}} \cdot \mathbf{W} \cdot \mathbf{X})^{-1} \cdot (\mathbf{X}^{\mathrm{T}} \cdot \mathbf{W} \cdot \vec{Y}).$$

For a fit to a polynomial of degree p, the (i,m) element of $\mathbf{X}$ is X_i^{m-1} (X_i being the ith individual data point) and $\mathbf{W}$ is a square diagonal matrix with dimensions $(p+1) \times (p+1)$ and $\mathbf{W}(i,i) = w_i$. $\vec{Y}$ is the column matrix with experimental values Y_i.

As $\hat{\vec{Y}} = \mathbf{X} \cdot \vec{\beta}$, the residuals $\vec{\epsilon} = \vec{Y} - \hat{\vec{Y}}$ can be expressed in terms of $\mathbf{X}$, $\mathbf{W}$, and $\vec{Y}$ as $\vec{\epsilon} = (1_n - \mathbf{P}) \cdot \vec{Y}$ with the hat matrix $\mathbf{P}$,

$$\mathbf{P} = \mathbf{X} \cdot (\mathbf{X}^{\mathrm{T}} \cdot \mathbf{W} \cdot \mathbf{X})^{-1} \cdot \mathbf{X}^{\mathrm{T}} \cdot \mathbf{W}.$$

From the residuals, the SSR can be obtained as $\mathrm{SSR} = \vec{\epsilon}^{\mathrm{T}}\vec{\epsilon}$.

The covariance matrix $\mathbf{V}$ from which the expected errors on the parameters can be derived for the general linear regression case is

$$\mathbf{V} = (\mathbf{X}^{\mathrm{T}} \cdot \mathbf{W} \cdot \mathbf{X})^{-1}.$$

A confidence interval for the SSE can be determined from SSE/σ^2, which is χ^2 distributed with $n-p$ degrees of freedom. From this, an interval for the SER can be derived.

Algebraically, a weighted linear regression is equivalent to a normal linear regression after the transformation

$$\mathbf{X}' = \mathbf{W}^{1/2} \cdot \mathbf{X},$$

$$\vec{Y}' = \mathbf{W}^{1/2} \cdot \vec{Y}.$$

This allows the use of the BMS algorithm as described by Mana *et al.* [67], where the conditional likelihood of a certain model $\mathbf{M}$, defined by the matrix $\mathbf{X}$, given the data $\vec{Y}$ can be calculated with

$$\mathrm{Prob}(\mathbf{M}|\vec{Y}) \propto \frac{\Gamma\left(\frac{n-l}{2}\right)\Gamma\left(\frac{l}{2}\right)}{|\hat{\vec{Y}}'|^l |\epsilon'|^{(n-l)}} - \frac{\Gamma\left(\frac{n-l}{2}\right)\Gamma\left(\frac{n}{2}\right){}_2F_1\left(\frac{l}{2}, \frac{n-l}{2}; \frac{n+2-l}{2}; \frac{|\epsilon'|^2}{|\hat{\vec{Y}}'|^2}\right)}{|\hat{\vec{Y}}'|^n},$$

where Γ is the gamma function, ${}_2F_1$ is the regularized hypergeometric function, l is the number of parameters that are fitted in the regression ($l = p+1$), and $\hat{\vec{Y}}'$ and ϵ' are the predictions and the residuals resulting from the normal linear regression using $\mathbf{X}'$ and $\vec{Y}'$. If the model search space is restricted, the above equation can be used to assign a probability to each model.

[1] P. Hohenberg and W. Kohn, Phys. Rev. **136**, B864 (1964).
[2] W. Kohn and L. Sham, Phys. Rev. **140**, A1133 (1965).
[3] N. Sukumar, G. Pilania, H. Zhu, and R. Ramprasad, *A Matter of Density: Exploring the Electron Density Concept in the Chemical, Biological, and Materials Sciences* (John Wiley and Sons, New York, 2012).
[4] J. Greeley, T. F. Jaramillo, J. Bonde, I. Chorkendorff, and J. K. Nørskov, Nat. Mater. **5**, 909 (2006).

[5] J. K. Nørskov, F. Abild-Pedersen, F. Studt, and T. Bligaard, Proc. Natl. Acad. Sci. **108**, 937 (2011).
[6] J. M. Kweun, C. Li, Y. Zheng, M. Cho, Y. Y. Kim, and K. Cho, Appl. Surf. Sci. **370**, 279 (2016).
[7] L. Vitos, A. V. Ruban, H. L. Skriver, and J. Kollár, Surf. Sci. **411**, 186 (1998).
[8] C. J. Fall, N. Binggeli, and A. Baldereschi, Phys. Rev. B **61**, 8489 (2000).
[9] I. G. Batyrev, J.-H. Cho, and L. Kleinman, Phys. Rev. B **63**, 172420 (2001).
[10] H. W. Hugosson, O. Eriksson, U. Jansson, A. V. Ruban, P. Souvatzis, and I. A. Abrikosov, Surf. Sci. **557**, 243 (2004).
[11] M. C. Holthausen, J. Comput. Chem. **26**, 1505 (2005).
[12] J. L. F. Da Silva, C. Stampfl, and M. Scheffler, Surf. Sci. **600**, 703 (2006).
[13] M. Ropo, K. Kokko, and L. Vitos, Phys. Rev. B **77**, 195445 (2008).
[14] N. E. Singh-Miller and N. Marzari, Phys. Rev. B **80**, 235407 (2009).
[15] L. Kornblum, P. Shekhter, Y. Slovatizky, Y. Amouyal, and M. Eizenberg, Phys. Rev. B **86**, 125305 (2012).
[16] J. Wang and S.-Q. Wang, Surf. Sci. **630**, 216 (2014).
[17] P. Lazar and M. Otyepka, Phys. Rev. B **91**, 115402 (2015).
[18] J. Depeng and W. Shaoqing, Acta Metall. Sin. **51**, 597 (2015).
[19] K. Lejaeghere, V. Van Speybroeck, G. Van Oost, and S. Cottenier, Crit. Rev. Solid State Mater. Sci. **39**, 1 (2013).
[20] K. Lejaeghere, J. Jaeken, V. Van Speybroeck, and S. Cottenier, Phys. Rev. B **89**, 014304 (2014).
[21] J. C. Heyraud and J. J. Métois, Surf. Sci. **177**, 213 (1986).
[22] C. Bombis, A. Emundts, M. Nowicki, and H. P. Bonzel, Surf. Sci. **511**, 83 (2002).
[23] H. P. Bonzel and M. Nowicki, Phys. Rev. B **70**, 245430 (2004).
[24] J. J. Gilman, J. Appl. Phys. **31**, 2208 (1960).
[25] C. T. Campbell, S. C. Parker, and D. E. Starr, Science **298**, 811 (2002).
[26] O. W. Richardson, *Thermionic Emission from Hot Bodies* (Watchmaker Publishing, Aberdeen, WA, 2003).
[27] Z. Zhang and J. T. Yates, Chem. Rev. **112**, 5520 (2012).
[28] J. P. Perdew and A. Zunger, Phys. Rev. B **23**, 5048 (1981).
[29] J. P. Perdew, K. Burke, and M. Ernzerhof, Phys. Rev. Lett. **77**, 3865 (1996).
[30] T. H. Heumann and J. Johannisson, Acta Metall. **20**, 617 (1972).
[31] V. K. Kumikov, Mater. Sci. Eng. **60**, L23 (1983).
[32] C. Ozcan and N. Hasirci, J. Appl. Polym. Sci. **108**, 438 (2008).
[33] K. Kendall, N. McN.Alford, and J. D. Birchall, Nature (London) **325**, 794 (1987).
[34] K. Kendall, J. Phys. D: Appl. Phys. **23**, 1329 (1990).
[35] K. Kendall, Powder Technol. **66**, 101 (1991).
[36] W. R. Tyson and W. A. Miller, Surf. Sci. **62**, 267 (1977).
[37] W. A. Miller and G. A. Chadwick, Acta Metall. **15**, 607 (1967).
[38] W. Tyson, Canad. Metal. Quart. **14**, 307 (1975).
[39] This does not solely include atoms that are directly at the surface. Rather, it concerns all atoms sufficiently near to the surface that contribute to the surface entropy.
[40] H. B. Michaelson, J. Appl. Phys. **48**, 4729 (1977).
[41] H. Kawano, Prog. Surf. Sci. **83**, 1 (2008).
[42] J. C. Boettger, Phys. Rev. B **49**, 16798 (1994).
[43] V. Fiorentini and M. Methfessel, J. Phys.: Condens. Matter **8**, 6525 (1996).
[44] J. F. Nicholas, in *Structure*, edited by G. Chiarotti (Springer, Berlin, 1993), Vol. 24a, pp. 37–39.
[45] C. J. Fall, N. Binggeli, and A. Baldereschi, J. Phys.: Condens. Matter **11**, 2689 (1999).
[46] M. G. Helander, M. T. Greiner, Z. B. Wang, and Z. H. Lu, Appl. Surf. Sci. **256**, 2602 (2010).
[47] S. Curtarolo, W. Setyawan, G. L. W. Hart, M. Jahnatek, R. V. Chepulskii, R. H. Taylor, S. Wang, J. Xue, K. Yang, O. Levy, M. J. Mehl, H. T. Stokes, D. O. Demchenko, and D. Morgan, Comput. Mater. Sci. **58**, 218 (2012).
[48] See Supplemental Material at http://link.aps.org/supplemental/10.1103/PhysRevB.94.235418 for crystallography information files (.cif's) of all the optimized surfaces and a document containing the experimental data, the DFT results with computational settings and the figures for the statistical analysis of the residuals.
[49] A. A. Stekolnikov, J. Furthmüller, and F. Bechstedt, Phys. Rev. B **65**, 115318 (2002).
[50] G. Kresse and J. Hafner, Phys. Rev. B **47**, 558 (1993).
[51] G. Kresse and J. Hafner, Phys. Rev. B **49**, 14251 (1994).
[52] G. Kresse and J. Furthmüller, Comput. Mater. Sci. **6**, 15 (1996).
[53] G. Kresse and J. Furthmüller, Phys. Rev. B **54**, 11169 (1996).
[54] P. E. Blöchl, Phys. Rev. B **50**, 17953 (1994).
[55] G. Kresse and D. Joubert, Phys. Rev. B **59**, 1758 (1999).
[56] G. Kresse, M. Marsman, and J. Furthmüller, VASP the GUIDE (2015).
[57] K. Lejaeghere, G. Bihlmayer, T. Björkman, P. Blaha, S. Blügel, V. Blum, D. Caliste, I. E. Castelli, S. J. Clark, A. D. Corso, S. d. Gironcoli, T. Deutsch, J. K. Dewhurst, I. D. Marco, C. Draxl, M. Dułak, O. Eriksson, J. A. Flores-Livas, K. F. Garrity, L. Genovese, P. Giannozzi, M. Giantomassi, S. Goedecker, X. Gonze, O. Grånäs, E. K. U. Gross, A. Gulans, F. Gygi, D. R. Hamann, P. J. Hasnip, N. A. W. Holzwarth, D. Iuşan, D. B. Jochym, F. Jollet, D. Jones, G. Kresse, K. Koepernik, E. Küçükbenli, Y. O. Kvashnin, I. L. M. Locht, S. Lubeck, M. Marsman, N. Marzari, U. Nitzsche, L. Nordström, T. Ozaki, L. Paulatto, C. J. Pickard, W. Poelmans, M. I. J. Probert, K. Refson, M. Richter, G.-M. Rignanese, S. Saha, M. Scheffler, M. Schlipf, K. Schwarz, S. Sharma, F. Tavazza, P. Thunström, A. Tkatchenko, M. Torrent, D. Vanderbilt, M. J. v. Setten, V. V. Speybroeck, J. M. Wills, J. R. Yates, G.-X. Zhang, and S. Cottenier, Science **351**, aad3000 (2016).
[58] M. Methfessel and A. T. Paxton, Phys. Rev. B **40**, 3616 (1989).
[59] P. E. Blöchl, O. Jepsen, and O. K. Andersen, Phys. Rev. B **49**, 16223 (1994).
[60] BIPM, IEC, IFCC, ILAC, ISO, IUPAC, IUPAP, and OIML (2008).
[61] B. Kirchner, G. Maroulis, R. Paul, S. Roy, P. Sarkar, A. Savin, G. Wu, and M. Springborg, *Chemical Modelling: Applications and Theory* (Royal Society of Chemistry, London, 2012).
[62] K. K. Irikura, R. D. Johnson, III, and R. N. Kacker, Metrologia **41**, 369 (2004).
[63] G. Hautier, S. P. Ong, A. Jain, C. J. Moore, and G. Ceder, Phys. Rev. B **85**, 155208 (2012).
[64] P. Pernot, B. Civalleri, D. Presti, and A. Savin, J. Phys. Chem. A **119**, 5288 (2015).
[65] N. R. Draper and H. Smith, *Applied Regression Analysis*, 3rd ed., Wiley Series in Probability and Statistics (John Wiley and Sons, New York, 1998).

[66] S. Kirklin, J. E. Saal, B. Meredig, A. Thompson, J. W. Doak, M. Aykol, S. Rühl, and C. Wolverton, npj Comput. Mater. **1**, 15010 (2015).
[67] G. Mana, P. A. Giuliano Albo, and S. Lago, Measurement **55**, 564 (2014).
[68] D. G. Altman, *Practical Statistics for Medical Research*, 1st ed. (Chapman and Hall/CRC, FL, 1990).
[69] Studentized residuals are the preferred choice to check for outliers, whereas the normal residuals are most appropriate for checking for non-normal behavior. The studentized residuals for all the data evaluated in this work were always close to the normal residuals, yielding no different conclusions with respect to outliers.
[70] V. S. Fomenko and G. V. Samsonov, in *Handbook of Thermionic Properties*, edited by V. S. Fomenko and G. V. Samsonov (Springer, New York, 1974), pp. 5–68.
[71] A. K. Green and E. Bauer, Surf. Sci. **74**, 676 (1978).
[72] R. Soulairol, C.-C. Fu, and C. Barreteau, Phys. Rev. B **84**, 155402 (2011).
[73] D. J. Eaglesham, A. E. White, L. C. Feldman, N. Moriya, and D. C. Jacobson, Phys. Rev. Lett. **70**, 1643 (1993).
[74] R. J. Jaccodine, J. Electrochem. Soc. **110**, 524 (1963).
[75] A. Gleizer and D. Sherman, Int. J. Fract. **187**, 1 (2014).
[76] L. Z. Mezey and J. Giber, Jpn. J. Appl. Phys. **21**, 1569 (1982).
[77] V. N. Staroverov, G. E. Scuseria, J. Tao, and J. P. Perdew, Phys. Rev. B **69**, 075102 (2004).
[78] K. Lejaeghere, L. Vanduyfhuys, T. Verstraelen, V. Van Speybroeck, and S. Cottenier, Comput. Mater. Sci. **117**, 390 (2016).
[79] R. Pérez and P. Gumbsch, Phys. Rev. Lett. **84**, 5347 (2000).
[80] S. Kurth, J. P. Perdew, and P. Blaha, Int. J. Quantum Chem. **75**, 889 (1999).
[81] N. Gaston, B. Paulus, K. Rosciszewski, P. Schwerdtfeger, and H. Stoll, Phys. Rev. B **74**, 094102 (2006).
[82] N. Mounet and N. Marzari, Phys. Rev. B **71**, 205214 (2005).
[83] C. Lechner, B. Pannier, P. Baranek, N. C. Forero-Martinez, and H. Vach, J. Phys. Chem. C **120**, 5083 (2016).
[84] D. Alfè and M. J. Gillan, J. Phys.: Condens. Matter **18**, L435 (2006).
[85] H. Eshuis, J. E. Bates, and F. Furche, Theor. Chem. Acc. **131**, 1 (2012).
[86] X. Ren, P. Rinke, C. Joas, and M. Scheffler, J. Mater. Sci. **47**, 7447 (2012).
[87] L. Schimka, J. Harl, A. Stroppa, A. Grüneis, M. Marsman, F. Mittendorfer, and G. Kresse, Nat. Mater. **9**, 741 (2010).
[88] T. C. Tessner and P. R. Davis, J. Vac. Sci. Technol. A **11**, 1 (1993).
[89] U. Schneider, G. R. Castro, H. Busse, T. Janssens, J. Wesemann, and K. Wandelt, Surf. Sci. **269–270**, 316 (1992).
[90] A. R. C. Westwood and D. L. Goldheim, J. Appl. Phys. **34**, 3335 (1963).
[91] P. L. Gutshall and G. E. Gross, J. Appl. Phys. **36**, 2459 (1965).
[92] B. Hammer, L. B. Hansen, and J. K. Nørskov, Phys. Rev. B **59**, 7413 (1999).
[93] M. Fishman, H. L. Zhuang, K. Mathew, W. Dirschka, and R. G. Hennig, Phys. Rev. B **87**, 245402 (2013).
[94] J. Tao and Y. Mo, Phys. Rev. Lett. **117**, 073001 (2016).

Error estimates for density-functinoal theory predictions of surface energy and work function: Supplementary Material

Sam De Waele, Kurt Lejaeghere, Michael Sluydts, Stefaan Cottenier

Physical Review B

Contents

1 Experimental data **1**

2 Computational settings and results **3**

3 Computational precision **7**

4 Statistical analysis for all linear fits **9**

1 Experimental data

All experimental data that were used in the main manuscript are bundled in this section. Work functions for which only one experimental value was found were assigned an experimental error of 0.32 eV. Those that were deemed unreliable by Michaelson [1] have been indicated with an asterisk $^{(*)}$. When no crystallographic orientation is provided, the work function measurement was performed on a polycrystalline sample.

Table 1: The experimental work functions (Φ) and surface energies (γ) and their uncertainties used in the comparison with their DFT-calculated counterparts.

	Φ(eV)	γ(J/m^2)		Φ(eV)	γ(J/m^2)
Li	2.90 ± 0.32	0.522 ± 0.05	Ir	5.27 ± 0.32	3.048 ± 0.33
Na	2.75 ± 0.32	0.261 ± 0.03	Ir {111}	5.77 ± 0.03	
K	2.30 ± 0.32	0.145 ± 0.02	Ir {100}	5.72 ± 0.25	
Rb	2.16 ± 0.32	0.117 ± 0.01	Ir {110}	5.42 ± 0.32	
Cs	2.14 ± 0.32	0.095 ± 0.01	Ni	4.87 ± 0.25	2.380 ± 0.26
Be	4.98 ± 0.32	1.628 ± 0.21	Ni {111}	5.28 ± 0.14	
Mg	3.66 $^{(*)}$	0.785 ± 0.08	Ni {100}	5.23 ± 0.20	
Ca	2.87 ± 0.32	0.502 ± 0.06	Ni {110}	4.64 ± 0.17	
Sr	2.59 ± 0.32	0.409 ± 0.05	Pd	5.24 ± 0.31	2.003 ± 0.22
Ba	2.70 ± 0.32	0.380 ± 0.04	Pd {111}	5.55 ± 0.20	
Sc	3.50 ± 0.32		Pd {100}	5.59 ± 0.26	
Y	3.10 ± 0.32		Pd {110}	5.08 ± 0.23	
Ti	4.33 ± 0.32	1.989 ± 0.21	Pt	5.27 ± 0.26	2.489 ± 0.26
Zr	4.05 $^{(*)}$	1.909 ± 0.20	Pt {111}	5.86 ± 0.18	
Hf	3.90 ± 0.32	2.193 ± 0.23	Pt {100}	5.82 ± 0.13	
V	4.30 ± 0.32	2.622 ± 0.28	Pt{110}	5.61 ± 0.20	

	Φ(eV)	γ($^{J}/_{m^2}$)		Φ(eV)	γ($^{J}/_{m^2}$)
Nb	4.02 ± 0.18	2.655 ± 0.29	Cu	4.51 ± 0.14	1.790 ± 0.19
Nb {111}	3.86 ± 0.33		Cu {111}	4.91 ± 0.05	
Nb {100}	3.95 ± 0.12		Cu {100}	4.57 ± 0.09	
Nb {110}	4.83 ± 0.14		Cu {110}	4.48 ± 0.20	
Ta	4.25 ± 0.06	2.902 ± 0.32	Ag	4.36 ± 0.26	1.246 ± 0.13
Ta {111}	4.00 ± 0.07		Ag {111}	4.56 ± 0.11	
Ta {100}	4.17 ± 0.32		Ag {100}	4.50 ± 0.32	
Ta {110}	4.81 ± 0.16		Ag {110}	4.16 ± 0.26	
Cr	4.50 ± 0.32	2.354 ± 0.27	Au	5.31 ± 0.24	1.506 ± 0.16
Mo	4.60 ± 0.16	2.907 ± 0.32	Au {111}	5.29 ± 0.11	
Mo {111}	4.09 ± 0.23		Au {100}	5.41 ± 0.32	
Mo {100}	4.40 ± 0.13		Au {110}	5.31 ± 0.32	
Mo {110}	4.96 ± 0.11		Zn	4.33$^{(*)}$	0.993 ± 0.10
W	4.55 ± 0.05	3.265 ± 0.37	Zn {0001}	4.90 ± 0.32	
W {111}	4.38 ± 0.12		Cd	4.22$^{(*)}$	0.762 ± 0.08
W {100}	4.57 ± 0.13		Hg	4.49$^{(*)}$	0.605 ± 0.06
W {110}	5.31 ± 0.32		Al	4.23 ± 0.44	1.143 ± 0.12
Re	4.95 ± 0.13	3.626 ± 0.40	Al {111}	4.28 ± 0.11	
Re {0001}	5.13 ± 0.12		Al {100}	4.36 ± 0.32	
Fe	4.66 ± 0.21	2.417 ± 0.26	Al {110}	4.21 ± 0.15	
Fe {111}	4.81 ± 0.32		Ga	4.20 ± 0.32	0.881 ± 0.09
Fe {100}	4.59 ± 0.26		In	4.12 ± 0.32	0.700 ± 0.07
Fe {110}	5.19 ± 0.06		Tl	3.84$^{(*)}$	0.602 ± 0.06
Fe-gamma	4.72 ± 0.25		C {0001}	4.70 ± 0.10	
Ru	4.75 ± 0.33	3.043 ± 0.33	Si	4.60 ± 0.28	1.135 ± 0.14
Ru {0001}	5.39 ± 0.15		Si {111}	4.79 ± 0.15	
Os	4.84 ± 0.07	3.439 ± 0.38	Si {100}	4.71 ± 0.08	
Co	5.00 ± 0.32	2.522 ± 0.27	Si {110}	4.84 ± 0.10	
Rh	4.90 ± 0.32	2.659 ± 0.29	Ge	5.00 ± 0.32	0.877 ± 0.10
Rh {111}	5.50 ± 0.14		Sn	4.42$^{(*)}$	0.709 ± 0.07
Rh {100}	5.29 ± 0.14		Pb	4.25 ± 0.32	0.593 ± 0.06
Rh {110}	4.77 ± 0.08		As	3.75$^{(*)}$	
			Sb	4.55 ± 0.32	0.596 ± 0.08
			Sb {100}	4.70 ± 0.32	
			Bi	4.22$^{(*)}$	0.489 ± 0.05

2 Computational settings and results

The settings and results given in this section apply to the structures supplied in the file "slab_cifs.rar". It is important to note that the number of *layers* is given here. This can differ from the number of atoms in the slab unit cell depending on the crystal structure of the material at hand. The general computational settings that are (almost) material-independent are given first.

Cut-off energy:

400 eV for all materials except for Li (800 eV) and C (600 eV).

Convergence criterion for the electronic self-consistent cycle:

10^{-8} eV

Convergence criterion for the structural optimization:

10^{-6} eV

Precision:

The VASP-tag "PREC" was set to "ACCURATE". This results in a grid spacing of $^1/_{(2\ G_{\mathrm{cut}})}$ for the fast Fourier transformation and $^1/_{(4\ G_{\mathrm{cut}})}$ for the description of the augmentation charges, where G_{cut} is the cut-off electronic wave vector. Projection operators were applied in reciprocal space.

Table 2: The material-dependent computational settings and results for the DFT-calculated work functions (Φ) and surface energies (γ). The integration grid in reciprocal space ($\vec{k}$-mesh), thickness of the slab and the number of layers free to relax have the largest impact on computational precision. The PAW potentials used follow the VASP 5.2 recommendations.

		$\vec{k}$-mesh	Layers in slab	Free layers	Φ_{PBE}(eV)	Φ_{LDA}(eV)	γ_{PBE}($^{\mathrm{J}}/_{\mathrm{m}^2}$)	γ_{LDA}($^{\mathrm{J}}/_{\mathrm{m}^2}$)	PAW file
Li	{111}	31x31	22	4	2.830	2.925	0.537	0.599	Li_sv 23 Jan 2001
	{100}	39x39	19	1	3.018	3.135	0.463	0.520	
	{110}	47x47	15	1	3.225	3.359	0.493	0.561	
Na	{111}	25x25	22	4	2.614	2.756	0.249	0.295	Na_pv 05 Jan 2001
	{100}	33x33	19	1	2.651	2.796	0.221	0.264	
	{110}	39x39	15	1	2.815	2.962	0.210	0.253	
K	{111}	27x27	22	4	2.206	2.362	0.130	0.162	K_sv 06 Sep 2000
	{100}	21x21	16	1	2.217	2.372	0.116	0.145	
	{110}	33x33	15	1	2.358	2.52	0.106	0.133	
Rb	{111}	19x19	22	4	2.118	2.291	0.101	0.166	Rb_sv 06 Sep 2000
	{100}	25x25	19	1	2.115	2.291	0.091	0.151	
	{110}	29x29	15	1	2.239	2.412	0.081	0.134	
Cs	{111}	19x19	22	4	1.978	2.168	0.080	0.113	Cs_sv 08 Apr 2002
	{100}	25x25	19	1	1.970	2.161	0.072	0.101	
	{110}	21x21	15	1	2.070	2.245	0.061	0.087	
Be	{0001}	21x21	18	3	5.321	5.556	1.803	2.089	Be 06 Sep 2000
	$\{10\bar{1}0\}$	29x17	20	2	4.484	4.644	1.938	2.211	
	$\{12\bar{3}0\}$	17x17	15	2	3.830	4.035	2.128	2.381	
	$\{12\bar{3}1\}$	21x21	20	5	4.482	4.679	2.461	2.751	
Mg	{0001}	21x21	18	3	3.705	3.871	0.448	0.644	Mg 05 Jan 2001
	$\{10\bar{1}0\}$	25x25	16	5	3.652	3.814	0.581	0.736	
	$\{12\bar{3}0\}$	13x13	15	2	3.487	3.643	0.688	0.853	

		$\vec{k}$-mesh	Layers in slab	Free layers	Φ_{PBE}(eV)	Φ_{LDA}(eV)	γ_{PBE}($^{\mathrm{J}}/_{\mathrm{m}^2}$)	γ_{LDA}($^{\mathrm{J}}/_{\mathrm{m}^2}$)	PAW file
Ca	{111}	19x19	15	3	2.923	3.012	0.465	0.560	Ca_pv 06 Sep 2000
	{100}	19x19	17	3	2.765	2.848	0.458	0.539	
	{110}	21x13	15	3	2.810	2.949	0.540	0.634	
Sr	{111}	15x15	13	3	2.522	2.668	0.350	0.437	Sr_sv 07 Sep 2000
	{100}	15x15	13	4	2.452	2.563	0.346	0.414	
	{110}	21x13	13	3	2.550	2.663	0.410	0.498	
Ba	{111}	21x21	22	4	2.319	2.575	0.390	0.495	Ba_sv Ba 06 Sep 2000
	{100}	27x27	19	1	2.323	2.54	0.321	0.412	
	{110}	33x33	15	1	2.385	2.584	0.313	0.410	
Sc	{0001}	21x21	18	3	3.334	3.556	1.271	1.458	Sc_sv 07 Sep 2000
	$\{10\bar{1}0\}$	29x17	20	2	3.563	3.772	1.207	1.391	
	$\{12\bar{3}0\}$	13x13	15	2	3.180	3.346	1.264	1.445	
	$\{12\bar{3}1\}$	21x21	20	5	3.416	3.389	1.385	1.584	
Y	{0001}	21x21	18	3	3.178	3.443	1.007	1.148	Y_sv 06 Sep 2000
	$\{10\bar{1}0\}$	29x17	20	2	3.315	3.471	0.974	1.126	
	$\{12\bar{3}0\}$	13x13	15	2	3.005	3.196	1.017	1.164	
Ti	{0001}	21x21	13	2	4.420	4.674	1.952	2.211	Ti_pv 07 Sep 2000
	$\{10\bar{1}0\}$	29x17	20	2	3.896	4.226	2.016	2.000	
	$\{12\bar{3}0\}$	11x11	15	3	3.190	3.446	1.880	2.176	
	$\{12\bar{3}1\}$	19x19	12	3	3.512	3.797	2.031	2.320	
Zr	{0001}	21x21	18	3	4.179	4.455	1.576	1.782	Zr_sv 07 Sep 2000
	$\{10\bar{1}0\}$	29x17	20	2	3.837	4.164	1.650	1.856	
	$\{12\bar{3}0\}$	13x13	15	2	3.089	3.391	1.651	1.898	
Hf	{0001}	21x21	14	3	4.339	4.581	1.726	1.937	Hf_pv 06 Sep 2000
	$\{10\bar{1}0\}$	29x17	20	2	3.939	4.207	1.867	2.081	
	$\{12\bar{3}0\}$	13x13	15	2	3.123	3.378	1.845	2.101	
V	{111}	23x23	22	3	3.872	4.227	2.705	3.098	V_pv 07 Sep 2000
	{100}	27x27	18	1	3.741	4.068	2.380	2.815	
	{110}	35x35	13	1	4.744	5.017	2.379	2.740	
Nb	{111}	25x25	25	4	3.838	4.146	2.345	2.715	Nb_pv 08 Apr 2002
	{100}	33x33	16	1	3.547	3.859	2.302	2.736	
	{110}	21x21	11	1	4.489	4.770	2.068	2.381	
Ta	{111}	25x25	22	4	3.923	4.221	2.742	3.058	Ta_pv 07 Sep 2000
	{100}	39x39	15	1	3.830	4.121	2.490	2.881	
	{110}	33x33	19	1	4.728	4.982	2.354	2.648	
Cr (AFM)	{111}	31x31	22	2	3.741		3.411		Cr_pv 07 Sep 2000
	{100}	41x41	19	1	3.681		3.130		
	{110}	25x25	15	1	4.803		2.849		
Cr (NM)	{111}	31x31	22	2	4.090	4.392	3.570	4.082	Cr_pv 07 Sep 2000
	{100}	41x41	19	1	4.017	4.355	3.748	4.192	
	{110}	25x25	15	1	4.824	5.127	3.313	3.760	
Mo	{111}	27x27	22	4	4.030	4.343	2.998	3.443	Mo_pv 08 Apr 2002
	{100}	35x35	19	1	3.835	4.355	3.190	3.637	

		$\vec{k}$-mesh	Layers in slab	Free layers	Φ_{PBE}(eV)	Φ_{LDA}(eV)	γ_{PBE}($^{\mathrm{J}}/_{\mathrm{m}^2}$)	γ_{LDA}($^{\mathrm{J}}/_{\mathrm{m}^2}$)	PAW file
	{110}	41x41	15	1	4.519	4.862	2.772	3.117	
W	{111}	21x21	21	4	4.134	4.414	3.555	3.958	W_pv 06 Sep 2000
	{100}	33x33	19	1	4.096	4.440	4.034	4.427	
	{110}	31x31	15	1	4.777	5.050	3.282	3.655	
Tc	{0001}	21x21	18	3	4.636	5.005	2.226	2.714	Tc_pv 06 Sep 2000
	$\{10\bar{1}0\}$	29x17	20	2	4.472	4.810	2.543	3.041	
	$\{12\bar{3}0\}$	13x13	15	2	4.239	4.560	2.662	3.199	
	$\{12\bar{3}1\}$	21x21	20	5	4.082	4.420	2.852	3.419	
Re	{0001}	17x17	15	3	4.907	5.227	2.639	3.089	Re 17 Jan 2003
	$\{10\bar{1}0\}$	29x17	12	2	4.680	4.986	2.913	3.381	
	$\{12\bar{3}0\}$	9x9	11	2	4.492	4.769	3.111	3.613	
Fe-α	{111}	31x31	22	3	3.862	4.541	2.712	3.472	Fe 06 Sep 2000
	{100}	41x41	19	2	3.894	4.410	2.530	3.442	
	{110}	47x47	12	0	4.743	5.275	2.455	3.173	
Fe-γ	{111}	27x27	15	3	5.205	5.507	2.467	3.296	Fe 06 Sep 2000
	{100}	25x25	13	3	4.739	5.180	1.906	3.840	
	{110}	33x21	18	3	3.897	4.721	2.410	3.814	
Ru	{0001}	21x21	18	3	4.993	5.372	2.675	3.239	Ru 06 Sep 2000
	$\{10\bar{1}0\}$	29x17	20	2	4.784	5.148	2.986	3.584	
	$\{12\bar{3}0\}$	13x13	15	2	4.430	4.780	3.405	4.076	
	$\{12\bar{3}1\}$	21x21	20	5	4.383	4.739	3.328	4.003	
Os	{0001}	21x21	18	3	5.302	5.638	2.997	3.494	Os_pv 20 Jan 2003
	$\{10\bar{1}0\}$	29x17	20	2	5.062	5.386	3.403	3.956	
	$\{12\bar{3}0\}$	13x13	15	2	4.782	5.071	4.091	4.719	
Co	{0001}	21x21	18	3	4.925	5.386	2.128	2.768	Co 06 Sep 2000
	$\{10\bar{1}0\}$	29x17	20	2	4.703	5.136	2.267	2.954	
	$\{12\bar{3}0\}$	13x13	15	2	4.389	4.806	2.461	3.253	
	$\{12\bar{3}1\}$	21x21	20	5	4.328	4.764	2.622	3.408	
Rh	{111}	25x25	14	3	5.138	5.536	2.000	2.558	Rh 06 Sep 2000
	{100}	23x23	14	3	5.068	5.472	2.340	2.960	
	{110}	27x17	14	3	4.583	4.961	2.388	3.045	
Ir	{111}	25x25	15	3	5.514	5.860	2.297	2.817	Ir 06 Sep 2000
	{100}	23x23	14	3	5.565	5.914	2.850	3.435	
	{110}	27x17	19	3	4.970	5.314	2.881	3.512	
Ni	{111}	29x29	11	3	5.020	5.497	1.916	2.506	Ni 06 Sep 2000
	{100}	27x27	13	3	4.901	5.328	2.209	2.855	
	{110}	33x21	15	3	4.488	4.949	2.262	2.945	
Pd	{111}	25x25	14	3	5.244	5.651	0.253	0.402	Pd 05 Jan 2001
	{100}	23x23	14	3	5.090	5.521	0.305	0.470	
	{110}	27x17	16	3	4.834	5.216	0.322	0.483	
Pt	{111}	25x25	15	3	5.691	6.046	1.434	1.984	Pt 05 Jan 2001
	{100}	23x23	15	3	5.673	6.040	1.834	2.405	
	{110}	27x17	20	3	5.281	5.633	1.858	2.465	
Cu	{111}	25x25	13	3	4.749	5.170	1.271	1.761	Cu 05 Jan 2001

		$\vec{k}$-mesh	Layers in slab	Free layers	Φ_{PBE}(eV)	Φ_{LDA}(eV)	γ_{PBE}($^{\mathrm{J}}/_{\mathrm{m}^2}$)	γ_{LDA}($^{\mathrm{J}}/_{\mathrm{m}^2}$)	PAW file
	{100}	23x23	13	3	4.492	4.880	1.420	1.951	
	{110}	27x17	22	3	4.369	4.751	1.508	2.054	
Ag	{111}	25x25	14	3	4.345	4.843	0.717	1.145	Ag 06 Sep 2000
	{100}	23x23	15	3	4.223	4.676	0.802	1.268	
	{110}	27x17	19	3	4.113	4.552	0.858	1.352	
Au	{111}	21x21	13	3	5.114	5.528	0.699	1.123	Au 06 Sep 2000
	{100}	19x19	13	3	5.082	5.460	0.857	1.334	
	{110}	27x17	22	3	4.961	5.329	0.882	1.389	
Zn	{0001}	21x21	18	3	4.075	4.442	0.308	0.506	Zn 06 Sep 2000
	$\{10\bar{1}0\}$	29x17	20	2	4.334	4.702	0.747	1.102	
	$\{12\bar{3}0\}$	13x13	15	2	4.026	4.299	0.965	1.389	
	$\{12\bar{3}1\}$	21x21	20	5	4.126	4.432	0.943	1.356	
Cd	{0001}	21x21	18	3	3.811	4.208	0.207	0.373	Cd 06 Sep 2000
	$\{10\bar{1}0\}$	29x17	20	2	4.085	4.493	0.442	0.746	
	$\{12\bar{3}0\}$	13x13	15	2	3.902	4.209	0.562	0.935	
Hg-α	{001}	13x13	23	3	4.497	4.732	0.129	0.740	Hg 06 Sep 2000
	{100}	9x15	26	7	4.235	4.627	0.013	0.652	
	{110}	21x13	17	2	4.134	4.522	0.127	0.530	
Hg-β	{001}	23x23	19	7	4.332	4.953	0.075	0.512	Hg 06 Sep 2000
	{100}	21x25	22	4	4.482	4.842	0.090	0.510	
	{110}	19x19	14	7	4.260	4.673	0.087	0.369	
Al	{111}	35x35	19	3	4.047	4.216	0.816	0.972	Al 04 Jan 2001
	{100}	33x33	19	3	4.255	4.415	0.940	1.106	
	{110}	39x25	21	3	4.045	4.207	0.998	1.173	
Ga	{001}	11x11	18	2	4.014	4.328	0.572	0.735	Ga_d 06 Sep 2000
	{100}	7x11	13	1	4.225	4.556	0.503	0.576	
	{010}	13x13	16	5	4.608	4.961	0.891	1.042	
In	{001}	13x13	22	1	3.881	4.216	0.306	0.498	In_d 06 Sep 2000
	{100}	17x11	21	1	3.791	4.125	0.366	0.536	
	{110}	13x13	22	1	3.921	4.301	0.362	0.762	
Tl	{0001}	19x19	16	2	3.561	3.981	0.264	0.428	Tl_d 06 Sep 2000
	$\{10\bar{1}0\}$	23x13	20	1	3.556	3.975	0.234	0.403	
	$\{12\bar{3}0\}$	13x13	16	3	3.516	3.941	0.277	0.459	
	$\{12\bar{3}1\}$	21x21	20	5	3.517	3.948	0.296	0.488	
Graphite	{0001}	23x23	17	1	4.565	4.759	0.119	0.431	C 08 Apr 2002
+D3	{0001}	23x24	17	1	4.459		0.163		
Diamond	{111}	9x17	14	3	4.357	4.541	4.050	4.501	C 08 Apr 2002
	{100}	7x13	14	3	5.626	5.626	5.198	5.697	
	{110}	11x11	12	3	5.299	5.563	5.437	5.903	
Si	{111}	9x17	14	3	4.667	4.811	1.361	1.513	Si 05 Jan 2001
	{100}	7x13	14	3	4.563	4.712	1.406	1.572	
	{110}	7x7	12	2	5.002	5.229	1.528	1.705	
Ge	{111}	9x17	14	3	4.381	4.551	0.890	1.156	Ge_d 06 Sep 2000
	{100}	7x13	14	3	4.482	4.722	1.003	1.269	

		$\vec{k}$-mesh	Layers in slab	Free layers	Φ_{PBE}(eV)	Φ_{LDA}(eV)	γ_{PBE}($^{\mathrm{J}}/_{\mathrm{m}^2}$)	γ_{LDA}($^{\mathrm{J}}/_{\mathrm{m}^2}$)	PAW file
	{110}	11x11	12	3	4.743	4.993	1.235	2.007	
Sn-α	{111}	9x17	14	3	4.148	4.372	0.540	0.700	Sn_d 06 Sep 2000
	{100}	7x13	14	3	4.231	4.494	0.628	0.804	
	{110}	9x9	12	2	4.398	4.706	0.786	0.998	
Sn-β	{001}	11x11	19	3	4.015	4.260	0.507	0.732	Sn_d 06 Sep 2000
	{100}	7x13	16	1	3.954	4.199	0.369	0.576	
	{101}	15x15	14	4	4.009	4.280	0.421	0.624	
	{110}	11x15	16	2	4.217	4.493	0.478	0.705	
Pb	{111}	21x21	22	3	3.763	4.080	0.253	0.402	Pb_d 06 Sep 2000
	{100}	19x19	15	3	3.796	4.101	0.305	0.470	
	{110}	25x25	15	3	3.727	4.029	0.322	0.483	
As	{001}	17x17	18	1	4.407	4.706	0.093	0.336	As 06 Sep 2000
	{100}	11x5	19	4	4.525	4.865	0.539	0.808	
	{110}	17x13	17	3	4.756	4.939	0.657	0.857	
Sb	{001}	17x17	20	2	4.238	4.501	0.162	0.427	Sb 06 Sep 2000
	{100}	11x5	19	5	4.388	4.721	0.475	0.734	
	{110}	13x9	17	3	4.414	4.618	0.488	0.793	
Bi	{001}	17x17	20	2	4.066	4.367	0.198	0.395	Bi_d 06 Sep 2000
	{100}	11x5	19	5	3.968	4.305	0.293	0.655	
	{110}	13x9	17	1	4.140	4.394	0.508	0.751	

3 Computational precision

The aim of this section is to provide an overview of the computational imprecision for those materials for which extensive convergence testing was performed.

Table 3: The precision associated with the settings chosen for the test materials. Both $\Delta\Phi$ and $\Delta\sigma$ are in meV - σ being the surface energy per surface atom. The imprecision caused by the choice of cut-off energy was only evaluated for the first four materials, because of its negligible contribution.

		$\vec{k}$-points		Layers		Cut-off		Free Layers		Total	
Element	Slab	$\Delta\Phi$	$\Delta\sigma$	$\Delta\Phi$	$\Delta\sigma$	$\Delta\Phi$	$\Delta\sigma$	$\Delta\Phi$	$\Delta\sigma$	$\Delta\Phi$	$\Delta\sigma$
Al	{111}	10	4	25	4	0.1	2	4	0	27	6
	{100}	18	3	30	4	0.1	2	0	0	35	5
	{110}	10	5	20	20	0.1	2	3	2	23	21
Au	{111}	15	4	1	2	0.3	2	4	1	16	5
	{100}	6	2	6	4	0.3	2	10	1	13	5
	{110}	3	5	10	2	0.3	2	1	0	10	6
Cu	{111}	15	4	1	2	0.5	2	4	0	16	5
	{100}	5	2	15	1	0.5	2	3	0	16	15
	{110}	5	2	10	6	0.5	2	1	0	11	7
Sr	{111}	5	2	10	0	0.1	1	4	1	12	2
	{100}	10	2	5	1	0.1	1	1	0	11	2

	{110}	7	2	20	2	0.1	1	1	0	21	3
	{111}	4	1	25	15			4	4	26	16
Nb	{100}	7	2	10	10			7	13	14	17
	{110}	5	4	5	4			10	5	12	8
	{111}	10	1	35	5			5	1	37	5
K	{100}	4	2	15	2			1	0	16	3
	{110}	5	0	15	0			1	0	16	0
	{111}	3	1	60	10			10	3	61	10
V	{100}	3	1	8	4			10	5	13	6
	{110}	5	1	2	4			3	1	6	4
	{111}	4	1	35	10			10	8	37	13
W	{100}	6	1	20	6			6	9	22	11
	{110}	5	1	3	25			1	1	6	25
	{0001}	6	0.5	6	2			3	0	9	2
Ti	$\{10\bar{1}0\}$	5	2	9	4			8	1	13	5
	{110}	4	0	14	3			6	5	16	6
	{0001}	6	2	30	1			3	1	31	2
Tl	$\{10\bar{1}0\}$	5	3	40	8			3	0	40	9
	{110}	3	3	20	5			5	1	21	6
	{0001}	8	3	5	3			2	10	10	11
Re	$\{10\bar{1}0\}$	10	1	9	10			5	2	14	10
	{110}	4	6	25	8			15	10	29	14
	{0001}	3	5	4	1			0	0	5	5
Mg	$\{10\bar{1}0\}$	6	3	30	3			6	5	31	7
	{110}	9	0	50	5			3	4	51	6

4 Statistical analysis for all linear fits

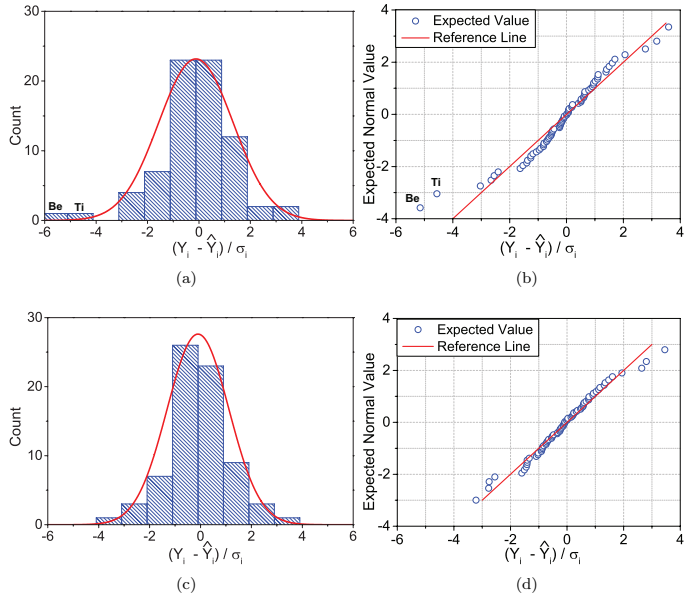

Figure 1: Histograms of the residuals for LDA work functions before [**a**] and after [**c**] outlier removal (Be and Ti), accompanied by QQ-plots before [**b**] and after [**d**] outlier removal.

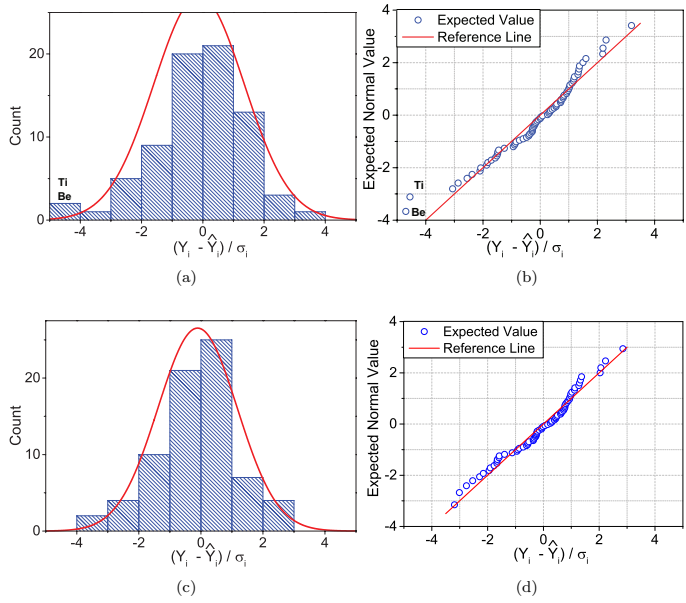

Figure 2: Histograms of the residuals for PBE work functions before [**a**] and after [**c**] outlier removal (Be and Ti), accompanied by QQ-plots before [**b**] and after [**d**] outlier removal.

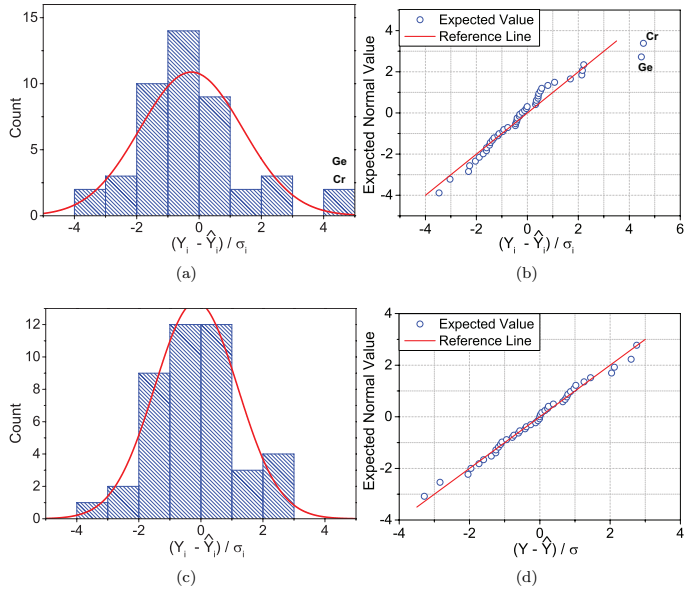

Figure 3: Histograms of the residuals for LDA surface energies before [**a**] and after [**c**] outlier removal (Cr and Ge), accompanied by QQ-plots before [**b**] and after [**d**] outlier removal.

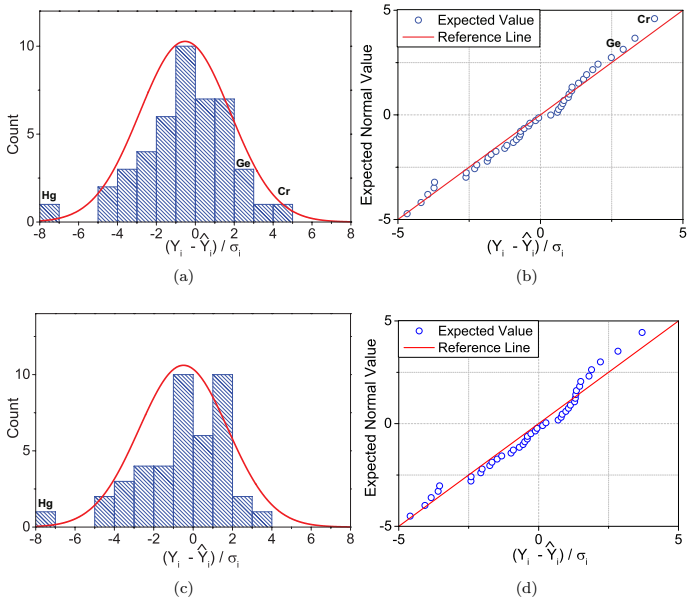

Figure 4: (Color online) Histograms of the residuals for PBE surface energies before [**a**] and after [**c**] outlier removal (Cr and Ge), accompanied by QQ-plots before [**b**] and after [**d**] outlier removal. Hg, for which the PBE surface energy is underestimated considerably, is not visible in the QQ-plots.

References

[1] H. B. Michaelson, "The work function of the elements and its periodicity," *Journal of Applied Physics*, vol. 48, pp. 4729–4733, Nov. 1977.

B

List of Publications

Publications in international peer–reviewed journals

1. **Error estimates for density-functional theory predictions of surface energy and work function**
   Sam De Waele, Kurt Lejaeghere, Michael Sluydts and Stefaan Cottenier
   Phys. Rev. B, **2016**, *94* (23), 235418
   IF: 3.836. Number of citations: 22

2. **Precipitation in simultaneously nitrided and aged Mo–containing maraging steel**
   An Verdiere, Christina Hofer, Sam De Waele, Vitaliy Bliznuk, Sophie Pimig, Stefaan Cottenier, Minh Duc Tran, Bert Pennings, Leo A.I. Kestens and Roumen H. Petrov *Materials Characterization*, **2017**, *131*, 21–30
   IF: 3.460 . Number of citations: 3

3. **A first-principles reassessment of the Fe-N phase diagram in the low-nitrogen limit**
   Sam De Waele, Kurt Lejaeghere, Elke Leunis, Lode Duprez and Stefaan Cottenier, *J. Alloys Compd.*, **2019**, *775*, 758–768
   IF: 3.779. Number of citations: 1

Conference contributions

Oral presentations

1. **A density–functional theory investigation of γ'–Fe_4N and α''–$Fe_{16}N_2$ precipitates in an Fe–N solid solution**
   Sam De Waele, Kurt Lejaeghere, Lode Duprez, Rogert Hubert, Elke Leunis and Stefaan Cottenier
   EUROMAT 2017, Thessaloniki, Greece, September 21, 2017

2. **Error quantication for density-functional theory calculations of surface energy and work function**
   Sam De Waele, Kurt Lejaeghere, Michael Sluydts, Stefaan Cottenier
   Workshop on Precision Quantification in DFT, Louvain–la–Neuve, Belgium, May 24, 2019

Poster presentations

1. **A density–functional theory investigation of Fe_4N and $Fe_{16}N_2$ precipitates in an Fe–N solid solution**
   Sam De Waele, Kurt Lejaeghere, Lode Duprez, Rogert Hubert, Elke Leunis and Stefaan Cottenier
   ADIS 2016, Tegernsee, Germany, October 3 – October 7, 2016

2. **Error estimates for density–functional theory predictions of surface energy and work function**
   Sam De Waele, Kurt Lejaeghere, Michael Sluydts, Stefaan Cottenier
   ADIS 2016, Tegernsee, Germany, October 3 – October 7, 2016

3. **A density–functional theory investigation of Fe_4N and $Fe_{16}N_2$ precipitates in an Fe–N solid solution**
   Sam De Waele, Kurt Lejaeghere, Lode Duprez, Rogert Hubert, Elke Leunis and Stefaan Cottenier
   SPR–KKR Hands–On Course, Daresbury, United Kingdom, November 14 – November 17, 2016

Master's thesis

Error bar assessment for *ab initio* prediction of surface properties
Sam De Waele

Master's thesis performed at the Center for Molecular Modeling (CMM), Ghent University, 2014–2015

Supervisors: prof. dr. ir. Veronique Van Speybroeck and prof. dr. ir. Stefaan Cottenier

Appendices

a

Thermodynamic Data for the Ternary compounds

This appendix contains the thermodynamic data for the research presented in Chapter 4. First, the solute interactions for all configurations as described in Section 4.3.2 are presented. Then, the 0 K energy of formation for the ternary compounds are listed in Table a.2 for the γ' structures and Table a.3 for the α'' structures. For the latter, only the formation energy for the most stable structure given a certain stoichiometry is presented.

Formation energy of solute complexes

The solute interactions are determined using the supercell approach. This means that they are derived from the DFT calculations for a pure 128 atom bcc Fe supercell (Fe), one 128 atom Fe supercell with an interstitial nitrogen impurity (Fe_N), one supercell with 127 Fe atoms and a ternary solute X (Fe_X) and one supercell with both impurities ($Fe_{X\text{-}N}$):

$$E_f = E_{Fe_{X\text{-}N}} + E_{Fe} - E_{Fe_X} - E_{Fe_N} \tag{a.1}$$

For each ternary element X, three interaction energies with nitrogen are given, as they are listed in Figure 4.5.

Ternary element X	E_f (eV)
Ti	0.149
	-0.312
	-0.103
V	0.076
	-0.032
	0.045
Nb	0.674
	-0.148
	-0.026
Cr	-0.035
	0.098
	0.105
Mo	0.612
	0.078
	0.066
Mn	-0.271
	-0.098
	0.073

Co	0.222
	0.202
	0.038
Ni	0.312
	0.234
	0.030
Pd	1.168
	0.315
	-0.030
Pt	1.502
	0.608
	0.033
Cu	0.418
	0.167
	-0.071
Al	0.295
	0.241
	-0.071
Si	0.397
	0.734
	0.031

Table a.1: Solute interaction energies between a nitrogen impurity in three different configurations with respect to a ternary solute X.

Energy of formation of Ternary structures at 0 K

The formation energies of the crystals in this section use the elements in a ferrite matrix as thermodynamic reference. As such, it is derived from:

$$E_f = E_{\mathrm{Fe}_{4-x}\mathrm{X}_x N} - (4-x)E_{\mathrm{Fe}} - xE_{\mathrm{X}_{sol}} - E_{\mathrm{N}_{sol}} \tag{a.2}$$

for the γ' structures, and

$$E_f = E_{\mathrm{Fe}_{8-y}\mathrm{X}_x N} - (8-y)E_{\mathrm{Fe}} - yE_{\mathrm{X}_{sol}} - E_{\mathrm{N}_{sol}} \tag{a.3}$$

For the α'' structures. For the former, the energy of formation is included for all 6 ternary structures and the binary compound X_4N. As a reference, the formation energy for Fe_4N is given as well. For the α'' structures, however,

only the 9 most stable structures in the series $Fe_{8-y}X_yN$ are included for each element. Here as well, the formation energy of $Fe_{16}N_2$ is included as a reference.

Ternary element X	E_f (eV)
Fe4N	-0.296
Ti	-0.744
	-0.926
	-0.603
	-1.590
	-1.638
	-0.610
	-0.839
Zr	-1.556
	-1.459
	-1.729
	-3.572
	-4.044
	-3.264
	-4.807
Hf	-1.432
	-1.080
	-1.069
	-1.073
	-3.266
	-2.240
	-3.277
V	0.230
	-0.378
	0.046
	-0.251
	-0.147
	0.226
	0.435
Nb	-0.391
	-0.664
	-0.671
	-1.380
	-1.323
	-1.485
	-1.447
Ta	-0.336

	-0.499
	-0.216
	-1.029
	-0.622
	-0.848
	-0.851
Cr	0.269
	-0.359
	0.275
	-0.273
	-0.178
	-0.088
	-0.035
Mo	0.471
	-0.086
	-0.117
	-0.257
	-0.152
	-0.533
	-0.441
W	0.692
	0.144
	0.359
	0.456
	0.947
	0.208
	0.733
Mn	-0.375
	-0.574
	-0.465
	-0.849
	-1.120
	-1.555
	-1.961
Tc	0.484
	-0.021
	0.157
	-0.009
	-0.113
	-0.083
	-0.454

Re	0.949
	0.549
	0.974
	1.053
	2.093
	1.236
	1.524
Ru	0.040
	-0.027
	0.329
	0.245
	0.398
	0.514
	0.512
Os	0.504
	0.576
	1.275
	1.659
	2.755
	2.140
	2.896
Co	-0.093
	-0.152
	0.076
	-0.035
	0.283
	0.374
	0.811
Rh	-0.455
	0.052
	0.124
	0.508
	1.026
	0.930
	1.570
Ir	0.002
	0.729
	1.302
	2.051
	3.802

	3.442
	4.845
Ni	-0.498
	-0.469
	-0.528
	-0.278
	0.111
	-0.434
	-0.129
Pd	-1.151
	-0.094
	-0.946
	0.109
	0.502
	-0.820
	-0.599
Pt	-0.722
	0.711
	0.601
	1.989
	3.740
	2.137
	3.934
Cu	-0.942
	-0.261
	-1.138
	0.015
	0.395
	-1.380
	-1.509
Ag	-1.780
	-0.165
	-2.551
	-0.468
	-0.841
	-3.735
	-4.697
Au	-1.446
	0.581
	-0.803

	1.162
	1.991
	-0.672
	-0.249
Al	-0.638
	0.330
	0.917
	0.844
	1.648
	2.291
	3.104
Si	0.559
	1.762
	3.489
	4.113
	6.639
	6.268
	8.302

Table a.2: Formation energy for all ternary γ' phases. For each ternary element X, there are 7 structures included: I.A, I.C, II.AC, II.CC, III.A, III.C and IV. The E_f are presented in that order.

Ternary element X	E_f (eV)
Fe16N2	-0.386
Ti	-0.656
	-1.044
	-1.289
	-1.781
	-0.322
	1.067
	2.173
	2.736
Zr	-1.190
	-2.234
	-3.688
	-5.324
	-4.165
	-4.421
	-4.719

	-5.871
Hf	-0.938
	-2.026
	-2.494
	-3.615
	-3.184
	-1.867
	-2.720
	-3.497
V	-0.283
	-0.260
	0.102
	0.065
	0.696
	1.283
	2.070
	2.858
Nb	-0.593
	-1.369
	-1.222
	-1.932
	-1.629
	-1.540
	-1.366
	-1.323
Ta	-0.600
	-1.395
	-1.273
	-1.887
	-0.967
	-0.520
	-0.285
	-0.259
Cr	-0.123
	-0.230
	-0.007
	0.155
	0.392
	0.436
	0.556
	0.670

Mo	-0.104
	-0.361
	-0.072
	-0.251
	-0.307
	-0.565
	-0.279
	0.023
W	0.047
	-0.373
	0.147
	0.230
	0.240
	0.188
	0.725
	1.174
Mn	-0.529
	-0.657
	-0.983
	-1.849
	-2.258
	-2.626
	-2.830
	-2.319
Tc	0.104
	0.109
	-0.321
	-0.743
	-0.696
	-0.949
	-1.082
	-1.432
Re	0.431
	0.539
	0.492
	0.670
	0.776
	0.694
	0.905
	0.860
Ru	-0.073

	0.117
	0.094
	-0.163
	-0.251
	-0.553
	-0.882
	-1.296
Os	0.257
	0.733
	0.657
	0.800
	0.963
	1.003
	1.032
	1.022
Co	-0.186
	-0.026
	0.139
	0.325
	0.466
	0.495
	0.960
	1.378
Rh	-0.216
	-0.129
	0.076
	0.041
	0.219
	0.585
	1.055
	1.548
Ir	0.094
	0.508
	0.963
	1.438
	2.168
	2.841
	3.952
	5.363
Ni	-0.381

	-0.520
	-0.690
	-0.882
	-0.894
	-0.993
	-0.758
	-0.544
Pd	-0.724
	-1.112
	-1.404
	-1.723
	-1.986
	-2.226
	-2.188
	-2.266
Pt	-0.344
	-0.385
	-0.016
	0.414
	1.105
	2.477
	3.257
	5.254
Cu	-0.786
	-1.403
	-1.659
	-1.992
	-2.558
	-2.834
	-3.429
	-3.968
Ag	-1.146
	-2.373
	-3.520
	-5.423
	-6.982
	-8.666
	-10.333
	-12.077
Au	-1.126

	-1.797
	-2.061
	-3.024
	-4.338
	-3.732
	-4.350
	-4.158
Al	-0.637
	-0.676
	-0.359
	0.087
	1.262
	2.826
	3.985
	6.047
Si	0.001
	0.551
	1.394
	2.613
	4.538
	5.861
	9.281
	14.325

Table a.3: Energy of formation for all ternary α'' phases. For each ternary element X, there are 8 structures included for each possible stoichiometry in the primitve cell of the α'' structure. The iron content thus decreases from 0.875 to 0 for each element.

b

Overview of computational resources

The calculations performed for this thesis were carried out on the infrastructure of the Flemish Supercomputer Center (VSC). More specifically, the Tier–2 cluster in Ghent and the Tier–1 cluster (in both Ghent and Leuven). In this Appendix we present an overview of the Tier–1 projects with the total amount of core days (the use of one processor core for a period of 24 hours) and the total use time on the Ghent Tier–2 clusters.

Tier–1 projects

- **2016:** Error estimates for ab initio predictions of surface energy and work function. 16 000 core days.
- **2016:** Error estimates for ab initio predictions for point defects in the Fe-N system. 48 352 core days.
- **2017:** Analysis of the off-stoichiometry of Fe_3N_{1+y} with Density-Functional Theory in the Fe–N system. 120 960 core days.
- **2017:** Analysis of the off-stoichiometry of Fe_3N_{1+y} with Density-Functional Theory. 96 768 core days.
- **2018:** Assessing DFT reproducibility using a systematic benchmark set: Chemical variety. 61 936 core days.
- **2019:** The influence of ternary alloying elements on the thermodynamic balance between iron-nitride compounds in nitrided steels. 125 748 core days.

Tier–2 Usage

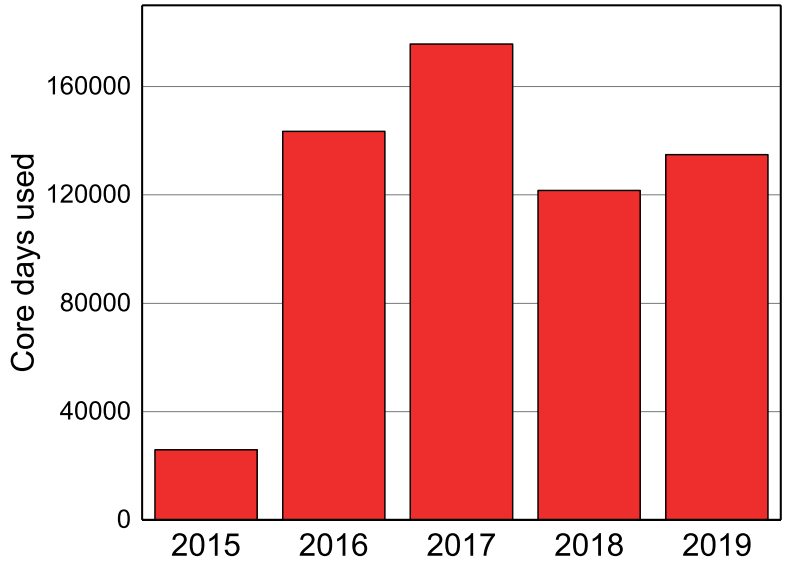

(a) Tier–2 usage year-by-year in total core days used.

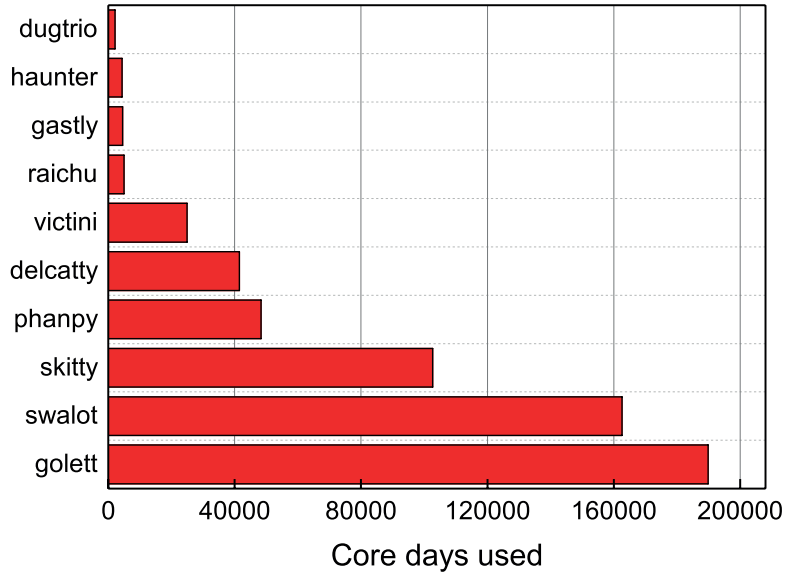

(b) Tier–2 usage per cluster in total core days used.

Figure b.1: Overview of the use of the Tier–2 cluster in Ghent from 2015–2019

C

Supporting information for the Fe-N binary thermodynamics

Free energy of Fe_4N: LDA and PBE comparison

As referenced in the main manuscript of paper III, the difference between the free energy of Fe_4N calculated with the LDA and PBE functionals is shown in Fig.c.1. The difference in free energy between LDA and PBE is shown up to 450 K, above which LDA Fe_4N becomes mechanically unstable.

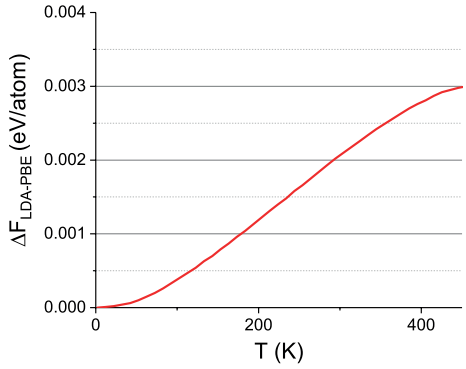

Figure c.1: (Color online) Difference in free energy between the LDA and PBE exchange-correlation functional. Above 450 K, LDA Fe_4N becomes mechanically unstable.

Magnetic contributions

In Table 1, a comparison between VASP and SPR-KKR is presented for the local magnetizations of the iron atoms at the VASP equilibrium lattice constants.

To illustrate the impact of the exchange interactions, the convergence of the mean-field Curie temperature ($T_{C,MF}$) with respect to the cut-off radius for the interactions is shown in Figure c.2.

	lattice constants (Å)	$M_{\text{VASP}}(\mu_B)$	$M_{\text{KKR}}(\mu_B)$
Fe	2.84 (2.87)[183]	2.18 (2.22)[184]	2.33 (2.22)[184]
Fe_4N	3.80 (3.80)[185]	2.50 (2.25)[185]	2.43 (2.25)[185]
$Fe_{16}N_2$	5.70 (5.72)[23]	2.40 (2.48 - 3.5)[186]	2.42 (2.48 - 3.5)[186]
	6.23 (6.29)[23]		

Table c.1: Lattice parameters for Fe, Fe_4N and $Fe_{16}N_2$. Magnetic moments for all three compounds at those lattice parameters for both the VASP code and the SPR-KKR code.

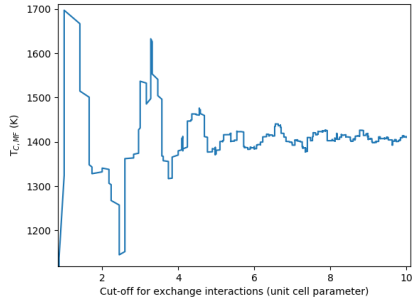

(a) Fe ($a = 2.861$)

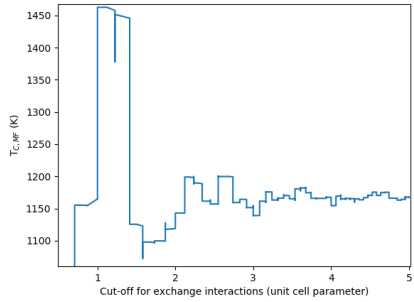

(b) Fe_4N ($a = 3.812$)

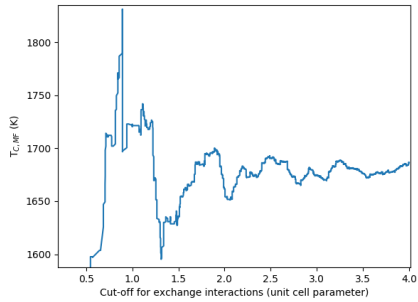

(c) $Fe_{16}N_2$ ($a = 5.742$)

Figure c.2: Calculated mean-field Curie temperatures T_C for Fe, Fe_4N and $Fe_{16}N_2$ as a function of cut-off radius for the exchange interactions. The size of the cut-off radius is relative to the lattice parameter a.

d

List of utilized software

Vienna Ab Initio Simulation Package (VASP)

The Vienna Ab Initio Simulation Package (VASP) is used to perform simulations at the atomic scale. The crystallographic unit cell is the basic input for these simulations, besides the computational settings. From there, the electronic structure, *i.e.* the density, is calculated, along with the energy of the input system, the forces on the atoms and the stress tensor of the unit cell. From those forces and the stress the tensor, the input crystal structure can be optimized towards an equilibrium structure, where all forces on the atoms and stresses are zero.

In this dissertation, we used VASP to perform DFT calculations with the aim of obtaining energies, optimizing structures and calculating forces on perturbed structures. The latter are the input necessary to obtain a phonon spectrum.

Phonopy

Phonopy is a python-based open source package to perform phonon calculations. It can be used to obtain phonon band structures, phonon density of states, the group velocity and thermal properties derived from phonon frequencies. These can be derived within the harmonic approximation or the quasiharmonic approximation. An interface with a calculator that determines the forces on the atoms is required.

We used phonopy to set up the supercells in which the atomic displacements are applied. An important step with respect to computational efficiency, as the software only performs symmetrically inequivalent atomic displacements. Thus the minimum amount of calculations is determined to obtain the phonon spectrum for a given unit cell. After the forces on the atoms in the supercells was calculated (VASP), phonopy is used to combine these forces into the dynamical matrix and diagonalize it for the given $\boldsymbol{q}$–points.

Spin-Polarized Relativistic Korringa-Kohn-Rostoker (SPR–KKR)

The Spin-Polarized Relativistic Korringa-Kohn-Rostoker (SPR–KKR) software package has been developed at LMU MÜNCHEN. Like VASP, it is capable of performing DFT calculations to obtain the electronic structure of

a material. Because it employs a scattering formalism, the package places a strong emphasis on response functions and spectroscopic properties.

The SPR–KKR package is more suited to obtain the Heisenberg exchange constants compared to VASP. Indeed, it has a built-in subroutine for obtaining these constants, as they are directly deducible within the KKR-Green's function formalism. Therefore, in this dissertation this software was used to obtain the Heisenberg exchange constants for all magnetic materials.

ALPS

The Algorithms and Libraries for Physics Simulations is a broad open source effort based on C++ libraries to deliver simulations codes for strongly correlated quantum mechanical systems. It enables to perform both classical and quantum Monte Carlo simulations for solving a variety of Hamiltonians.

We use it to determine the magnetic heat capacity for a range of temperatures for ferromagnetic compounds. The input takes the form of a graph for the Heisenberg exchange constants, which is set up from the SPR–KKR output data. From there, for each desired temperature a classical Monte Carlo simulation is performed for a sufficient amount of steps to obtain the heat capacity at that temperature.

Bibliography

[1] American Iron and Steel Institute, "Profile of the american iron and steel institute," https://www.steel.org/~/media/Files/AISI/About%20AISI/Profile%20Brochure%20F-singles_CX.ashx, [Online; accessed 28-July-2019].

[2] World Steel Association, "Steel Statistical Yearbook," http://www.worldsteel.org/steel-by-topic/statistics/steel-statistical-yearbook.html (), [Online; accessed 29-June-2019].

[3] "World aluminium: Primary aluminium production," http://www.world-aluminium.org/statistics/, [Online; accessed 29-June-2019].

[4] M. Kühnel and T. Kraus, "The global cfrp market 2016 by carbon composites," https://www.carbon-composites.eu/media/2307/cfrp-market-report-ec-2016-kuehnel-freigabe.pdf, [Online; accessed 15-July-2019].

[5] MetalMiner, "Metalminer prices," https://agmetalminer.com/metal-prices/, [Online; accessed 9-July-2019].

[6] World Steel Association, "Steel Statistical Yearbook 2018," https://www.worldsteel.org/en/dam/jcr:e5a8eda5-4b46-4892-856b-00908b5ab492/SSY_2018.pdf (), [Online; accessed 29-June-2019].

[7] Accenture, "Steel demand beyond 2030," https://www.oecd.org/industry/ind/Item_4b_Accenture_Timothy_van_Audenaerde.pdf, [Online; accessed 22-June-2019].

[8] Steel Market Development Institute, "Impact of life cycle emissions when lightweighting with advanced high-strength steel vs. aluminum," http://tiny.cc/bkbodz (), [Online; accessed 29-June-2019].

[9] Steel Market Development Institute, "Fuel economy and emissions," https://www.autosteel.org/autosteel_org/document-types/research-reports/2016-roadmap/fuel-economy-and-emissions (), [Online; accessed 26-June-2019].

[10] B. De Cooman, *Materials Design: The Key to Modern Steel Products*, GRIPS' sparkling world of steel (GRIPS media) ISBN: 978-3-937057-13-2.

[11] Wikimedia Commons, "Fe-C phase diagram," https://commons.wikimedia.org/wiki/File:Iron_carbon_phase_diagram.svg, [Online; accessed 31-July-2019].

[12] D. J. Schaeffler, "Introduction to advanced high-strength steels," http://tiny.cc/88fodz, [Online; accessed 29-June-2019].

[13] D. Pye, *Practical Nitriding and Ferritic Nitrocarburizing* (ASM International, 2003) ISBN: 978-1-61503-249-5.

[14] G. Miyamoto, Y. Tomio, H. Aota, K. Oh-ishi, K. Hono, and T. Furuhara, "Precipitation of nanosized nitrides in plasma nitrided Fe-M (M = Al, Cr, Ti, V) alloys," *Materials Science and Technology* **27**, 742 (2011).

[15] E. J. Mittemeijer, in *Thermochemical Surface Engineering of Steels*, edited by E. J. Mittemeijer and M. A. J. Somers (Woodhead Publishing, 2015) pp. 313 – 340.

[16] M. A. J. Somers and T. L. Christiansen, in *Thermochemical Surface Engineering of Steels*, edited by E. J. Mittemeijer and M. A. J. Somers (Woodhead Publishing, 2015) pp. 557 – 579.

[17] O. Singh, H. K. Malik, R. P. Dahiya, and P. K. Kulriya, "Tuning of mechanical and structural properties of 20 MC 5 steel using N ion implantation and subsequent annealing," *Journal of Alloys and Compounds* **710**, 253 (2017).

[18] W. Dal'Maz Silva, J. Dulcy, J. Ghanbaja, A. Redjaïmia, G. Michel, S. Thibault, and T. Belmonte, "Carbonitriding of low alloy steels: Mechanical and metallurgical responses," *Materials Science and Engineering: A* **693**, 225 (2017).

[19] H. Du, N. Lange, and J. Ågren, "Formation of compound layers on iron during gas nitriding," **11**, 301 (1995).

[20] E. A. d. S. d. Almeida, C. E. d. Costa, and J. C. G. Milan, "Study of the nitrided layer obtained by different nitriding methods," *Matéria (Rio de Janeiro)* **20**, 460 (2015).

[21] Arcor Nitrocarburizing, "Technical information," `http://surface-heat.com/technical-information-arcor-nitrocarborizing`, [Online; accessed 3-July-2019].

[22] E. H. v. Du Marchie van Voorthuysen, D. O. Boerma, and N. C. Chechenin, "Low-temperature extension of the Lehrer diagram and the iron-nitrogen phase diagram," *Metallurgical and Materials Transactions A* **33**, 2593 (2002).

[23] H. A. Wriedt, N. A. Gokcen, and R. H. Nafziger, "The Fe-N (Iron-Nitrogen) system," *Bulletin of Alloy Phase Diagrams* **8**, 355 (1987).

[24] X. C. Xiong, *Élaboration et genèse des microstructures dans les "aciers" fer-azote* (Vandoeuvre-les-Nancy, INPL, 2008).

[25] M. Gouné, T. Belmonte, A. Redjaïmia, P. Weisbecker, J. M. Fiorani, and H. Michel, "Thermodynamic and structural studies on nitrided Fe-1.62%Mn and Fe-0.56%V alloys," *Materials Science and Engineering. A, Structural Materials: Properties, Microstructure and Processing* **351**, 23 (2003).

[26] C. Domain, C. S. Becquart, and J. Foct, "*Ab initio* study of foreign interstitial atom (C, N) interactions with intrinsic point defects in α-Fe," *Physical Review B* **69**, 144112 (2004).

[27] T. Courtney, *Mechanical Behavior of Materials*, McGraw-Hill series in materials science and engineering (Waveland Press, 2005).

[28] R. Borrelly and D. Benkirat, "Sensibilité du pouvoir thermoélectrique à l'état microstructural du fer et du fer-azote," *Acta Metallurgica* **33**, 855 (1985).

[29] S. Malinov, A. J. Böttger, E. J. Mittemeijer, M. I. Pekelharing, and M. A. J. Somers, "Phase transformations and phase equilibria in the Fe-N system at temperatures below 573 K," *Metallurgical and Materials Transactions A* **32**, 59 (2001).

[30] K. H. Jack, "The synthesis and characterization of bulk α''-$Fe_{16}N_2$," *Journal of Alloys and Compounds* **222**, 160 (1995).

[31] P. Ferguson, U. Dahmen, and K. H. Westmacott, "Morphological aspects of α''-$Fe_{16}N_2$ precipitation in α-Fe," *Scripta Metallurgica* **18**, 57 (1984).

[32] P. Ferguson and K. H. Jack, "A lattice imaging study of nitrogen precipitation in α-iron and Fe-2.17 at.% Mn," *Philosophical Magazine A* **50**, 221 (1985).

[33] A. Van Gent, F. C. Van Doorn, and E. J. Mittemeijer, "Crystallography and tempering behavior of iron-nitrogen martensite," *Metallurgical Transactions A* **16**, 1371 (1985).

[34] U. Dahmen, P. Ferguson, and K. H. Westmacott, "A TEM study of α''-$Fe_{16}N_2$ and γ'-Fe_4N precipitation in iron-nitrogen," *Acta Metallurgica* **35**, 1037 (1987).

[35] L. Cheng and E. J. Mittemeijer, "The tempering of iron-nitrogen martensite; dilatometric and calorimetric analysis," *Metallurgical Transactions A* **21**, 13 (1990).

[36] G. Hinojosa, J. Oseguera, O. Salas, and P. S. Schabes-Retchkiman, "Microscopical characterization of α''-$Fe_{16}N_2$ obtained by plasma assisted processes," *Scripta Materialia* **34**, 141 (1996).

[37] X. C. Xiong, A. Redjaïmia, and M. Gouné, "In situ transmission electron microscopy investigations of the kinetics of α''-$Fe_{16}N_2$ precipitation during the ageing of nitrogen-ferrite," *Scripta Materialia* **63**, 1232 (2010).

[38] Y. Hong, C. L. Wu, L. Tian, N. Li, Q. Xu, and J. H. Chen, "Microstructure and property evolution of Fe-N ferrite undergoing early-stages of precipitation," *Materials Science and Engineering: A* **696**, 198 (2017).

[39] K. H. Jack, "Results of further X-ray structural investigations of the iron-carbon and iron-nitrogen systems and of related interstitial alloys," *Acta Crystallographica* **3**, 392 (1950).

[40] M. A. J. Somers, N. M. v. d. Pers, D. Schalkoord, and E. J. Mittemeijer, "Dependence of the lattice parameter of γ' iron nitride, Fe_4N_{1-x} , on nitrogen content; accuracy of the nitrogen absorption datairon nitride, Fe_4N_{1-x} , on nitrogen content; accuracy of the nitrogen absorption data," *Metallurgical Transactions A* **20**, 1533 (1989).

[41] M. Wada, A. Fujii, T. Komazaki, and T. Mori, "Fim observation of nitrogen GP zones in iron," *Acta Metallurgica* **37**, 2349 (1989).

[42] A. Böttger, L. Cheng, E. Frikkee, T. H. d. Keijser, and E. J. Mittemeijer, "Occurrence of incoherent α''-$Fe_{16}N_2$ at room temperature in iron-nitrogen martensite observed by neutron and X-ray diffraction," *Journal of Physics: Condensed Matter* **2**, 9237 (1990).

[43] A. M. Vredenberg, C. M. Pérez-Martin, J. S. Custer, D. O. Boerma, L. de Wit, F. W. Saris, N. M. van de Pers, T. H. de Keijser, and E. J. Mittemeijer, "Synthesis and stability of nitride layers in iron by mega-electronvolt nitrogen implantation," *Surface and Coatings Technology* **51**, 79 (1992).

[44] L. Torchane, P. Bilger, J. Dulcy, and M. Gantois, "Control of iron nitride layers growth kinetics in the binary Fe-N system," *Metallurgical and Materials Transactions A* **27**, 1823 (1996).

[45] P. B. Friehling and M. A. J. Somers, "Growth kinetics of the compound layer on gaseous nitriding of iron: The effect of the surface reaction," *Mass and Carge Transport in Inorganic Devices: Fundamentals to Devices (Part B)* (2000).

[46] M. Keddam, B. Bouarour, R. Kouba, and R. Chegroune, "Growth kinetics of the compound layers: Effect of the nitriding potential," *Physics Procedia* Proceedings of the JMSM 2008 Conference, **2**, 1399.

[47] E. J. Mittemeijer, "Fundamentals of nitriding and nitrocarburizing - heat treating society," (2013).

[48] M. Gouné, T. Belmonte, J. M. Fiorani, S. Chomer, and H. Michel, "Modelling of diffusion-precipitation in nitrided alloyed iron," *Thin Solid Films* International Conference on Metallurgic Coatings and Thin Films, **377-378**, 543 (2000).

[49] H. Liu, Y. Gao, J. Z. Liu, Y. M. Zhu, Y. Wang, and J. F. Nie, "A simulation study of the shape of β' precipitates in Mg-Y and Mg-Gd alloys," *Acta Materialia* **61**, 453 (2013).

[50] P. Hohenberg and W. Kohn, "Inhomogeneous electron gas," *Physical Review* **136**, B864 (1964).

[51] W. Kohn and L. Sham, "Self-consistent equations including exchange and correlation effects," *Physical Review* **140**, 1133.

[52] ICAMS, http://www.icams.de/content/, [Online; accessed 12-July-2019].

[53] N. D. Mermin, "Thermal properties of the inhomogeneous electron gas," *Physical Review* **137**, A1441 (1965).

[54] F. Körmann, A. Dick, T. Hickel, and J. Neugebauer, "Rescaled Monte Carlo approach for magnetic systems: *ab initio* thermodynamics of bcc iron," *Physical Review B* **81**, 134425 (2010).

[55] A. Dick, F. Körmann, T. Hickel, and J. Neugebauer, "*Ab initio* based determination of thermodynamic properties of cementite including vibronic, magnetic, and electronic excitations," *Physical Review B* **84**, 125101 (2011).

[56] N. P. Lavery, S. Mehraban, C. Pleydell-Pearce, S. G. R. Brown, D. J. Jarvis, W. Voice, and M. Brunnock, "Combinatorial development and high throughput materials characterisation of steels," *Ironmaking & Steelmaking* **42**, 727 (2015).

[57] H. Knoll, S. Ocylok, A. Weisheit, H. Springer, E. Jägle, and D. Raabe, "Combinatorial alloy design by laser additive manufacturing," *Steel research international* **88**, 1600416 (2017).

[58] R. Zhang, W. Zheng, X. Veys, G. Huyberechts, H. Springer, and M. Selleby, "Prediction of martensite start temperature for lightweight Fe-Mn-Al-C steels," *Journal of Phase Equilibria and Diffusion* **39**, 476 (2018).

[59] N. Van Steenberge, L. Duprez, and S. Claessens, "Combinatorial metallurgical screening: what is in it for high temperature applications?" (2018).

[60] G. Hautier, "Finding the needle in the haystack: Materials discovery and design through computational ab initio high-throughput screening," *Computational Materials Science* **163**, 108 (2019).

[61] W. Kohn, "Nobel lecture. NobelPrize.org. nobel meadia ab 2019. mon 15 jul 2019." https://www.nobelprize.org/prizes/chemistry/1998/kohn/lecture/.

[62] M. Born and R. Oppenheimer, "Zur quantentheorie der molekeln," *Annalen der Physik* **389**, 457 (1927).

[63] K. Lejaeghere, G. Bihlmayer, T. Björkman, P. Blaha, S. Blügel, V. Blum, D. Caliste, I. E. Castelli, S. J. Clark, A. D. Corso, S. d. Gironcoli, T. Deutsch, J. K. Dewhurst, I. D. Marco, C. Draxl, M. Dułak, O. Eriksson,

J. A. Flores-Livas, K. F. Garrity, L. Genovese, P. Giannozzi, M. Giantomassi, S. Goedecker, X. Gonze, O. Grånäs, E. K. U. Gross, A. Gulans, F. Gygi, D. R. Hamann, P. J. Hasnip, N. a. W. Holzwarth, D. Iuşan, D. B. Jochym, F. Jollet, D. Jones, G. Kresse, K. Koepernik, E. Küçükbenli, Y. O. Kvashnin, I. L. M. Locht, S. Lubeck, M. Marsman, N. Marzari, U. Nitzsche, L. Nordström, T. Ozaki, L. Paulatto, C. J. Pickard, W. Poelmans, M. I. J. Probert, K. Refson, M. Richter, G.-M. Rignanese, S. Saha, M. Scheffler, M. Schlipf, K. Schwarz, S. Sharma, F. Tavazza, P. Thunström, A. Tkatchenko, M. Torrent, D. Vanderbilt, M. J. v. Setten, V. Van Speybroeck, J. M. Wills, J. R. Yates, G.-X. Zhang, and S. Cottenier, "Reproducibility in density functional theory calculations of solids," *Science* **351**, aad3000 (2016).

[64] J. P. Perdew, K. Burke, and M. Ernzerhof, "Generalized gradient approximation made simple," *Physical Review Letters* **77**, 3865 (1996).

[65] P. Janthon, S. A. Luo, S. M. Kozlov, F. Viñes, J. Limtrakul, D. G. Truhlar, and F. Illas, "Bulk properties of transition metals: A challenge for the design of universal density functionals," *Journal of Chemical Theory and Computation* **10**, 3832 (2014).

[66] M. Swart, M. F. Bickelhaupt, and M. Duran, "DFT 2018 poll," `http://www.marcelswart.eu/dft-poll/news2018.pdf`, [Online; accessed 17-July-2019].

[67] C. Kittel, *Introduction to Solid State Physics*, 8th ed. (Wiley, 2004).

[68] G. Kresse and J. Furthmüller, "Efficiency of ab-initio total energy calculations for metals and semiconductors using a plane-wave basis set," *Computational Materials Science* **6**, 15 (1996).

[69] G. Kresse and J. Furthmüller, "Efficient iterative schemes for *ab initio* total-energy calculations using a plane-wave basis set," *Physical Review B* **54**, 11169 (1996).

[70] G. Kresse and D. Joubert, "From ultrasoft pseudopotentials to the projector augmented-wave method," *Physical Review B* **59**, 1758 (1999).

[71] G. Kresse, M. Marsman, and J. Furthmüller, "VASP the GUIDE," (2015).

[72] "Projector augmented-wave method," `https://itp.uni-frankfurt.de/~valenti/TALKS_BACHELOR/paw.pdf`, [Online; accessed 21-July-2019].

[73] U. v. Barth and L. Hedin, "A local exchange-correlation potential for the spin polarized case." *Journal of Physics C: Solid State Physics* **5**, 1629 (1972).

[74] E. Blancá, C. O. Rodriguez, J. Shitu, and D. L. Novikov, "Degree of localization of the exchange-correlation hole and its influence on the ground-state (structural and magnetic) properties of d metals," *Journal of Physics-Condensed Matter* **13**, 9463 (2001).

[75] F. Körmann, A. Dick, B. Grabowski, B. Hallstedt, T. Hickel, and J. Neugebauer, "Free energy of bcc iron: Integrated *ab initio* derivation of vibrational, electronic, and magnetic contributions," *Physical Review B* **78**, 033102 (2008).

[76] D. C. Wallace, *Thermodynamics of Crystals* (Courier Corporation, 1998).

[77] V. Milman, B. Winkler, J. A. White, C. J. Pickard, M. C. Payne, E. V. Akhmatskaya, and R. H. Nobes, "Electronic structure, properties, and phase stability of inorganic crystals: A pseudopotential plane-wave study," *International Journal of Quantum Chemistry* **77**, 895.

[78] A. Y. Liu, A. A. Quong, J. K. Freericks, E. J. Nicol, and E. C. Jones, "Structural phase stability and electron-phonon coupling in lithium," **59**, 4028 (1999).

[79] V. OzolinĂą, C. Wolverton, and A. Zunger, "First-principles theory of vibrational effects on the phase stability of Cu-Au compounds and alloys," **58**, R5897 (1998).

[80] B. Grabowski, T. Hickel, and J. Neugebauer, "Ab initio study of the thermodynamic properties of nonmagnetic elementary fcc metals: Exchange-correlation-related error bars and chemical trends," *Physical Review B* **76**, 024309 (2007).

[81] Z. Mao, W. Chen, D. N. Seidman, and C. Wolverton, "First-principles study of the nucleation and stability of ordered precipitates in ternary Al-Sc-Li alloys," *Acta Materialia* **59**, 3012.

[82] I. A. Abrikosov, A. V. Ponomareva, P. Steneteg, S. A. Barannikova, and B. Alling, "Recent progress in simulations of the paramagnetic state of magnetic materials," **20**, 85 (2016).

[83] C. M. Fang, M. H. F. Sluiter, M. A. van Huis, C. K. Ande, and H. W. Zandbergen, "Origin of predominance of cementite among iron car-

bides in steel at elevated temperature," *Physical Review Letters* **105**, 055503.

[84] R. Lizárraga, F. Pan, L. Bergqvist, E. Holmström, Z. Gercsi, and L. Vitos, "First Principles Theory of the hcp-fcc Phase Transition in Cobalt," **7**, 1 (2017).

[85] Q. Han, T. Birol, and K. Haule, "Phonon Softening due to Melting of the Ferromagnetic Order in Elemental Iron," **120**, 187203 (2018).

[86] B. Grabowski, P. Söderlind, T. Hickel, and J. Neugebauer, "Temperature-driven phase transitions from first principles including all relevant excitations: The fcc-to-bcc transition in Ca," *Physical Review B* **84**, 214107.

[87] F. Birch, "Finite elastic strain of cubic crystals," *Physical Review* **71**, 809 (1947).

[88] A. A. Maradudin, *Theory Of Lattice Dynamics In The Harmonic Approximation* (1971).

[89] A. Togo and I. Tanaka, "First principles phonon calculations in materials science," *Scripta Materialia* **108**, 1 (2015).

[90] N. M. Rosengaard and B. Johansson, "Finite-temperature study of itinerant ferromagnetism in Fe, Co, and Ni," *Physical Review B* **55**, 14975 (1997).

[91] M. Pajda, J. Kudrnovský, I. Turek, V. Drchal, and P. Bruno, "*Ab initio* calculations of exchange interactions, spin-wave stiffness constants, and curie temperatures of Fe, Co, and Ni," *Physical Review B* **64**, 174402 (2001).

[92] M. Ležaić, P. Mavropoulos, and S. Blügel, "First-principles prediction of high Curie temperature for ferromagnetic bcc-Co and bcc-FeCo alloys and its relevance to tunneling magnetoresistance," *Applied Physics Letters* **90**, 082504 (2007).

[93] A. V. Ruban, S. Khmelevskyi, P. Mohn, and B. Johansson, "Temperature-induced longitudinal spin fluctuations in Fe and Ni," *Physical Review B* **75**, 054402 (2007).

[94] G. Y. Gao, K. L. Yao, E. Şaşioğlu, L. M. Sandratskii, Z. L. Liu, and J. L. Jiang, "Half-metallic ferromagnetism in zinc-blende **CaC**, **SrC** and **BaC** from first principles," *Physical Review B* **75**, 174442 (2007).

[95] F. Körmann, A. Dick, T. Hickel, and J. Neugebauer, "Role of spin quantization in determining the thermodynamic properties of magnetic transition metals," *Physical Review B* **83**, 165114 (2011).

[96] J. Korringa, "On the calculation of the energy of a Bloch wave in a metal," *Physica* **13**, 392 (1947).

[97] W. Kohn and N. Rostoker, "Solution of the Schrödinger equation in periodic lattices with an application to metallic lithium," *Physical Review* **94**, 1111 (1954).

[98] H. Ebert *et al.*, "The munich SPR-KKR package," .

[99] H. Ebert, D. Ködderitzsch, and J. Minár, "Calculating condensed matter properties using the KKR-Green's function method–recent developments and applications," *Reports on Progress in Physics* **74**, 096501 (2011).

[100] A. I. Liechtenstein, M. I. Katsnelson, and V. A. Gubanov, "Exchange interactions and spin-wave stiffness in ferromagnetic metals," *Journal of Physics F: Metal Physics* **14**, L125 (1984).

[101] N. Metropolis, A. W. Rosenbluth, M. N. Rosenbluth, A. H. Teller, and E. Teller, "Equation of state calculations by fast computing machines," *The Journal of Chemical Physics* **21**, 1087 (1953).

[102] A. F. Albuquerque, F. Alet, P. Corboz, P. Dayal, A. Feiguin, S. Fuchs, L. Gamper, E. Gull, S. Gürtler, A. Honecker, R. Igarashi, M. Körner, A. Kozhevnikov, A. Läuchli, S. R. Manmana, M. Matsumoto, I. P. McCulloch, F. Michel, R. M. Noack, G. Pawłowski, L. Pollet, T. Pruschke, U. Schollwöck, S. Todo, S. Trebst, M. Troyer, P. Werner, and S. Wessel, "The ALPS project release 1.3: Open-source software for strongly correlated systems," *Journal of Magnetism and Magnetic Materials* **310**, 1187 (2007).

[103] B. Bauer, L. D. Carr, H. G. Evertz, A. Feiguin, J. Freire, S. Fuchs, L. Gamper, J. Gukelberger, E. Gull, S. Guertler, A Hehn, R. Igarashi, S. V. Isakov, D. Koop, P. N. Ma, P. Mates, H. Matsuo, O. Parcollet, G. Pawłowski, J. D. Picon, L Pollet, E. Santos, V. W. Scarola, U. Schollwöck, C. Silva, B. Surer, S. Todo, S. Trebst, M. Troyer, M. L. Wall, P Werner, and S. Wessel, "The ALPS project release 2.0: open source software for strongly correlated systems," *Journal of Statistical Mechanics: Theory and Experiment* **2011**, P05001 (2011).

[104] P. W. Anderson, "Theory of magnetic exchange interactions: Exchange in insulators and semiconductors," *Solid State Physics* **14**, 99 (1963).

[105] H. Nyquist, "Thermal agitation of electric charge in conductors," *Physical Review* **32**, 110 (1928).

[106] H. B. Callen and T. A. Welton, "Irreversibility and generalized noise," *Physical Review* **83**, 34 (1951).

[107] A. W. Sandvik and J. Kurkijärvi, "Quantum Monte Carlo simulation method for spin systems," *Physical Review B* **43**, 5950 (1991).

[108] P. Henelius and A. W. Sandvik, "Sign problem in Monte Carlo simulations of frustrated quantum spin systems," *Physical Review B* **62**, 1102 (2000).

[109] A. Glensk, B. Grabowski, T. Hickel, and J. Neugebauer, "Understanding anharmonicity in fcc materials: From its origin to ab initio strategies beyond the quasiharmonic approximation," *Physical Review Letters* **114**, 195901 (2015).

[110] T. Hickel, B. Grabowski, F. Körmann, and J. Neugebauer, "Advancing density functional theory to finite temperatures: methods and applications in steel design," *Journal of Physics: Condensed Matter* **24**, 053202 (2012).

[111] F. Körmann, B. Grabowski, B. Dutta, T. Hickel, L. Mauger, B. Fultz, and J. Neugebauer, "Temperature dependent magnon-phonon coupling in bcc fe from theory and experiment," *Physical Review Letters* **113**, 165503 (2014).

[112] H. Göhring, O. Fabrichnaya, A. Leineweber, and E. J. Mittemeijer, "Thermodynamics of the Fe-N and Fe-N-C systems: The Fe-N and Fe-N-C phase diagrams revisited," *Metallurgical and Materials Transactions A* **47**, 6173 (2016).

[113] S. Shang and A. J. Böttger, "A combined cluster variation method and ab initio approach to the γ'-Fe[N]/γ'-Fe_4N_{1-x} phase equilibrium," *Acta Materialia* **53**, 255 (2005).

[114] H. Grabke, "Zur fehlordnung des γ'-eisennitrids," *Berichte der Bunsengesellschaft für physikalische Chemie* **73**, 596 (1969).

[115] J. P. Perdew and A. Zunger, "Self-interaction correction to density-functional approximations for many-electron systems," *Physical Review B* **23**, 5048 (1981).

[116] K. Kunc and R. M. Martin, "Ab initio force constants of GaAs: A new approach to calculation of phonons and dielectric properties," *Physical Review Letters* **48**, 406 (1982).

[117] M. Methfessel and A. T. Paxton, "High-precision sampling for Brillouin-zone integration in metals," *Physical Review B* **40**, 3616 (1989).

[118] Q. Chen and Z. Jin, "The Fe-Cu system: A thermodynamic evaluation," *Metallurgical and Materials Transactions A* **26**, 417 (1995).

[119] P. D. Desai, "Thermodynamic properties of iron and silicon," *Journal of Physical and Chemical Reference Data* **15**, 967 (1986).

[120] F. C. Nix and D. MacNair, "The thermal expansion of pure metals: Copper, gold, aluminum, nickel, and iron," *Physical Review* **60**, 597 (1941).

[121] K. Lejaeghere, J. Jaeken, V. Van Speybroeck, and S. Cottenier, "*Ab initio* based thermal property predictions at a low cost: An error analysis," *Physical Review B* **89**, 014304 (2014).

[122] K. Tagawa, E. Kita, and A. Tasaki, "Synthesis of fine Fe_4N powder and its magnetic characteristics," *Japanese Journal of Applied Physics* **21**, 1596 (1982).

[123] E. L. P. y. Blancá, J. Desimoni, N. E. Christensen, H. Emmerich, and S. Cottenier, "The magnetization of γ'-Fe_4N: theory vs. experiment," *Physica Status Solidi (B)* **246**, 909 (2009).

[124] W. Zhou, L.-J. Qu, Q.-M. Zhang, and D.-S. Wang, "Interaction and charge transfer in the iron nitride Fe_4N," *Physical Review B* **40**, 6393 (1989).

[125] D. Li, J. W. Roh, K. J. Jeon, Y. S. Gu, and W. Lee, "First principles calculations of the magnetic properties of Fe-N systems," *Physica Status Solidi (B)* **245**, 2581 (2008).

[126] T. Gressmann, M. Wohlschlögel, S. Shang, U. Welzel, A. Leineweber, E. J. Mittemeijer, and Z. K. Liu, "Elastic anisotropy of γ'-Fe_4N and elastic grain interaction in γ'-Fe_4N_{1-y} layers on α-Fe: First-principles calculations and diffraction stress measurements," *Acta Materialia* **55**, 5833 (2007).

[127] J. F. Adler and Q. Williams, "A high-pressure X-ray diffraction study of iron nitrides: Implications for earth's core," *Journal of Geophysical Research: Solid Earth* **110**, B01203 (2005).

[128] C. L. Yang, M. M. Abd-Elmeguid, H. Micklitz, G. Michels, J. W. Otto, Y. Kong, D. S. Xue, and F. S. Li, "Pressure effects on the electronic properties and the magnetic ground state of γ'-Fe_4N," *Journal of Magnetism and Magnetic Materials* **151**, L19 (1995).

[129] K. Lejaeghere, V. Van Speybroeck, G. Van Oost, and S. Cottenier, "Error estimates for solid-state density-functional theory predictions: An overview by means of the ground-state elemental crystals," *Critical Reviews in Solid State and Materials Sciences* **39**, 1 (2013).

[130] D. J. Singh and J. Ashkenazi, "Magnetism with generalized-gradient-approximation density functionals," *Physical Review B* **46**, 11570 (1992).

[131] T. Takahashi, J. Burghaus, D. Music, R. Dronskowski, and J. M. Schneider, "Elastic properties of γ'-Fe_4N probed by nanoindentation and ab initio calculation," *Acta Materialia* **60**, 2054 (2012).

[132] J. A. Rayne and B. S. Chandrasekhar, "Elastic constants of iron from 4.2 to 300 K," *Physical Review* **122**, 1714 (1961).

[133] J. J. Adams, D. S. Agosta, R. G. Leisure, and H. Ledbetter, "Elastic constants of monocrystal iron from 3 to 500 K," *Journal of Applied Physics* **100**, 113530 (2006).

[134] J. Leese and A. E. Lord, "Elastic stiffness coefficients of single–crystal iron from room temperature to 500°C," *Journal of Applied Physics* **39**, 3986 (1968).

[135] D. Dever, "Temperature dependence of the elastic constants in α–iron single crystals: relationship to spin order and diffusion anomalies," *Journal of Applied Physics* **43**, 3293 (1972).

[136] F. Körmann, Y. Ikeda, B. Grabowski, and M. H. F. Sluiter, "Phonon broadening in high entropy alloys," *npj Computational Materials* **3**, 36 (2017).

[137] J. Weber, "Fluctuation dissipation theorem," *Physical Review* **101**, 1620 (1956).

[138] R. G. Harrison, "Calculating the spontaneous magnetization and defining the Curie temperature using a positive-feedback model," *Journal of Applied Physics* **115**, 033901 (2014).

[139] L. Ke, K. D. Belashchenko, M. van Schilfgaarde, T. Kotani, and V. P. Antropov, "Effects of alloying and strain on the magnetic properties of $Fe_{16}N_2$," *Physical Review B* **88**, 024404 (2013).

[140] J. Crangle and G. M. Goodman, "The magnetization of pure iron and nickel," *Proceedings of the Royal Society of London A* **321**, 477 (1971).

[141] Y. Sugita, H. Takahashi, M. Komuro, K. Mitsuoka, and A. Sakuma, "Magnetic and Mössbauer studies of single–crystal $Fe_{16}N_2$ and Fe–N martensite films epitaxially grown by molecular beam epitaxy (invited)," *Journal of Applied Physics* **76**, 6637 (1994).

[142] S. Yamamoto, R. Gallage, Y. Ogata, Y. Kusano, N. Kobayashi, T. Ogawa, N. Hayashi, K. Kohara, M. Takahashi, and M. Takano, "Quantitative understanding of thermal stability of α''-$Fe_{16}N_2$," *Chemical Communications* **49**, 7708 (2013).

[143] M. Widenmeyer, T. C. Hansen, and R. Niewa, "Formation and decomposition of metastable α''–$Fe_{16}N_2$ from in situ powder neutron diffraction and thermal analysis," *Zeitschrift für anorganische und allgemeine Chemie* **639**, 2851 (2013).

[144] Y. Sugita, "Giant magnetic moment and other magnetic properties of epitaxially grown $Fe_{16}N_2$ single–crystal films (invited)," *Journal of Applied Physics* **70**, 5977 (1991).

[145] H. V. Keer, *Principles of the Solid State* (New Age International, 1993).

[146] X. C. Xiong, A. Redjaïmia, and M. Gouné, "Transmission electron microscopy investigation of acicular ferrite precipitation in γ'-Fe_4N nitride," *Materials Characterization* **61**, 1245 (2010).

[147] T. Gladman, "Precipitation hardening in metals," *Materials Science and Technology* **15**, 30 (1999).

[148] J. D. Kamminga and G. C. A. M. Janssen, "Calculation of nitrogen depth profiles in nitrided Fe-Mn and Fe-V," *Surface and Coatings Technology* PSE 2004, **200**, 909 (2005).

[149] D. H. Jack and K. H. Jack, "Invited review: Carbides and nitrides in steel," *Materials Science and Engineering* **11**, 1 (1973).

[150] M. A. J. Somers, R. M. Lankreijer, and E. J. Mittemeijer, "Excess nitrogen in the ferrite matrix of nitrided binary iron-based alloys," *Philosophical Magazine A* **59**, 353 (1989).

[151] H. Selg, E. Bischoff, S. R. Meka, R. E. Schacherl, T. Waldenmaier, and E. J. Mittemeijer, "Molybdenum-Nitride precipitation in recrystallized and cold-rolled Fe-1 at. pct Mo alloy," *Metallurgical and Materials Transactions A* **44**, 4059 (2013).

[152] R. S. E. Schneider and H. Hiebler, "Influence of increased nitriding temperatures on the hardness profile of low-alloy steels," *Journal of Materials Science* **33**, 1737 (1998).

[153] H. H. Podgurski and F. N. Davis, "Thermochemistry and nature of nitrogen absorption in nitrogenated Fe–Ti alloys," *Acta Metallurgica* **29**, 1 (1981).

[154] R. E. Schacherl, P. C. J. Graat, and E. J. Mittemeijer, "The nitriding kinetics of iron-chromium alloys; the role of excess nitrogen: Experiments and modelling," *Metallurgical and Materials Transactions A* **35**, 3387 (2004).

[155] S. R. Meka, E. Bischoff, R. E. Schacherl, and E. J. Mittemeijer, "Unusual nucleation and growth of γ' iron nitride upon nitriding Fe-4.75 at.% Al alloy," *Philosophical Magazine* **92**, 1083 (2012).

[156] M. Mekata, "Magnetic study on Mn_4N and its related compounds," *Journal of the Physical Society of Japan* **17**, 796 (1962).

[157] M. Meinert, "Exchange interactions and Curie temperatures of the tetrametal nitrides Cr_4N, Mn_4N, Fe_4N, Co_4N, and Ni_4N," *Journal of Physics: Condensed Matter* **28**, 056006 (2016).

[158] M. H. Biglari, C. M. Brakman, E. J. Mittemeijer, and S. Van Der Zwaag, "The kinetics of the internal nitriding of Fe-2 at. pct Al alloy," *Metallurgical and Materials Transactions A* **26**, 765 (1995).

[159] H. H. Podgurski and R. A. Oriani, "Nitrogenation of Fe-Al alloys. III: Absorption of hydrogen in nitrogenated Fe-Al alloys," *Metallurgical Transactions* **3**, 2055 (1972).

[160] G. W. Wiener and J. A. Berger, "Structure and magnetic properties of some transition metal nitrides," *JOM* **7**, 360 (1955).

[161] R. J. Arnott and A. Wold, "The preparation and crystallography of FeNiN and the series $Fe_{4-x}Ni_xN$," *Journal of Physics and Chemistry of Solids* **15**, 152 (1960).

[162] S. K. Chen, S. Jin, T. H. Tiefel, Y. F. Hsieh, E. M. Gyorgy, and D. W. J. Jr, "Magnetic properties and microstructure of Fe_4N and $(Fe,Ni)_4N$," *Journal of Applied Physics* **70**, 6247 (1991).

[163] R. N. Panda and N. S. Gajbhiye, "Magnetic properties of nanocrystalline γ-Fe–Ni–N nitride systems," *Journal of Applied Physics* **86**, 3295 (1999).

[164] D. Andriamandroso, S. Matar, G. Demazeau, and L. Fournes, "Morphological and magnetic properties of Ru, Os and Ir-substituted Fe_4N," *IEEE Transactions on Magnetics* **29**, 2 (1993).

[165] J. v. Appen and R. Dronskowski, "Predicting new ferromagnetic nitrides from electronic structure theory: $IrFe_3N$ and $RhFe_3N$," *Angewandte Chemie International Edition* **44**, 1205 (2005).

[166] X. G. Ma, J. J. Jiang, P. Liang, J. Wang, Q. Ma, and Q. K. Zhang, "Structural stability and magnetism of γ'-Fe_4N and $CoFe_3N$ compounds," *Journal of Alloys and Compounds* **480**, 475 (2009).

[167] C. A. Kuhnen and A. V. dos Santos, "Ground-state and thermal properties of substituted iron nitrides," *Journal of Alloys and Compounds* **297**, 68 (2000).

[168] H. Y. Wang, E. Y. Jiang, and P. Wu, "Enhancement of the thermal stability of $Fe_{16}N_2$ by Ti addition," *Journal of Magnetism and Magnetic Materials* International Conference on Magnetism (Part II), **177–181, Part 2**, 1285 (1998).

[169] D. Benea, O. Isnard, and V. Pop, "Electronic structure and magnetic properties of the $Fe_{16}N_2$ doped with Ti," *Journal of Magnetism and Magnetic Materials* **420**, 75 (2016).

[170] X. Zhao, C.-Z. Wang, Y. Yao, and K.-M. Ho, "Large magnetic anisotropy predicted for rare-earth-free $Fe_{16-x}Co_xN_2$ alloys," *Physical Review B* **94**, 224424 (2016).

[171] J. M. Sanchez, F. Ducastelle, and D. Gratias, "Generalized cluster description of multicomponent systems," *Physica A: Statistical Mechanics and its Applications* **128**, 334 (1984).

[172] F. Ducastelle, *Order and phase stability in alloys* (Amsterdam ; New York : North-Holland ; New York, NY, USA : Sole distributors for the USA and Canada, Elsevier Science Pub. Co, 1991).

[173] D. D. Fontaine, in *Solid State Physics*, Vol. 47, edited by H. E. a. D. TURNBULL (Academic Press) pp. 33–176.

[174] A. Seko, Y. Koyama, and I. Tanaka, "Cluster expansion method for multicomponent systems based on optimal selection of structures for density-functional theory calculations," *Physical Review B* **80**, 165122 (2009).

[175] A. van de Walle and G. Ceder, "Automating first-principles phase diagram calculations," *Journal of Phase Equilibria* **23**, 348 (2002).

[176] A. van de Walle, M. D. Asta, and G. Ceder, "The Alloy Theoretic Automated Toolkit: A user guide," **26**, 539 (2002).

[177] A. van de Walle, "Multicomponent multisublattice alloys, nonconfigurational entropy and other additions to the Alloy Theoretic Automated Toolkit," **33**, 266 (2009).

[178] P. E. Blöchl, "Projector augmented-wave method," *Physical Review B* **50**, 17953 (1994).

[179] S. R. Meka, A. Chauhan, T. Steiner, E. Bischoff, P. K. Ghosh, and E. J. Mittemeijer, "Generating duplex microstructures by nitriding; nitriding of iron based Fe–Mn alloy," *Materials Science and Technology* **32**, 883 (2016).

[180] P. Jessner, M. Gouné, R. Danoix, B. Hannoyer, and F. Danoix, "Atom probe tomography evidence of nitrogen excess in the matrix of nitrided Fe–Cr," *Philosophical Magazine Letters* **90**, 793 (2010).

[181] J.-D. Kamminga, T. Klaver, K. Nakata, B. Thijsse, and G. Janssen, "The interaction of N with atomically dispersed Ti, V, Cr, Mo, and Ni in ferritic steel," *Journal of Computer-Aided Materials Design* **10**, 1 (2003).

[182] Y. You and M. F. Yan, "Interactions of foreign interstitial and substitutional atoms in bcc iron from ab initio calculations," *Physica B: Condensed Matter* **417**, 57 (2013).

[183] W. P. Davey, "Precision measurements of the lattice constants of twelve common metals," *Physical Review* **25**, 753 (1925).

[184] M. Acet, H. Zähres, E. F. Wassermann, and W. Pepperhoff, "High-temperature moment-volume instability and anti-Invar of Fe_4N," *Physical Review B* **49**, 6012 (1994).

[185] B. C. Frazer, "Magnetic structure of Fe_4N," *Physical Review* **112**, 751 (1958).

[186] Y. Shi, Y. Du, and G. Chen, "Correlation of electronic structure and magnetic moment in $Fe_{16}N_2$: First-principles calculations," *Scripta Materialia* **68**, 976 (2013).

This research was enabled by an OCAS-endowed PhD position. We further acknowledge support from the Research Foundation Flanders (FWO) through project Nr. G0E0116N.

The computational resources (Stevin Supercomputer Infrastructure) and services used in this work were provided by the VSC (Flemish Supercomputer Center), funded by Ghent University, FWO, and the Flemish Government – department EWI.